RÉPUBLIQUE FRANÇAISE
Liberté Égalité Fraternité

Université de Toulouse

Doctorat de l'Université de Toulouse

préparé à l'ISAE-SUPAERO

Investigation of the Efects of Inlet Distortion on the Stability of Multi-Stage High-Pressure Compressors via Body-Force Modelling

---

Thèse présentée et soutenue, le 24 mars 2026 par

Chiara CREA

École doctorale
MEGEP - Mécanique, Energétique, Génie civil, Procédés

Spécialité
Dynamique des fuides

Unité de recherche
ISAE-ONERA EDyF Energétique et Dynamique des Fluides

Thèse dirigée par
Guillaume DUFOUR

Composition du jury
M. Antoine DAZIN, Président, Rapporteur, Arts et Métiers ParisTech
M. Vassilios PACHIDIS, Rapporteur, Cranfeld University
M. Ernesto BENINI, Examinateur, Università degli Studi di Padova
M. Julien MARTY, Examinateur, ONERA
Mme Clémence RANNOU, Examinatrice, Direction Générale de l'Armement
M. Guillaume DUFOUR, Directeur de thèse, ISAE-SUPAERO

Membres invités
M. Sébastien COCHON, Safran Aircraft Engines
M. Raphaël BARRIER, ONERA

Acknowledgements

These last three years have been incredibly rich and instructive, both professionally and personally. I am grateful to all the people who have crossed my path and shared in this journey with me.

I would first like to express my sincere gratitude to Professor Pachidis and Professor Dazin for taking the time to review my thesis and for their thoughtful and insightful reports. I am also very grateful to Professor Benini and Dr. Rannou for agreeing to examine this work and for the engaging discussions during my thesis defence.

Je tiens également à remercier mon encadrement de thèse : après près de cent cinquante points hebdomadaires, nous voilà enfin arrivés au terme de cette aventure. Merci à Guillaume pour la direction rigoureuse et l'accompagnement constant, qui m'ont permis de toujours mettre mes idées en perspective et de me guider dans mes choix scientifiques et méthodologiques. Merci à Sébastien pour avoir donné vie à ce projet, pour ses précieux conseils techniques et pour son intérêt constant, qui a été un moteur essentiel pour mener cette thèse à terme. Merci à Raphael pour son regard constructif et son approche positive, ainsi que pour les suggestions pratiques qui ont enrichi mon travail. Et merci à Julien pour les longues matinées passées à discuter de nos idées et à résoudre ensemble des problèmes–faire passer des cas à 1 mld de points n'est pas facile–ainsi que pour son soutien constant face aux difficultés de la thèse. C'est grâce à votre expertise, vos conseils et votre encouragement que ce travail a pu se concrétiser.

Cette expérience doctorale n'aurait certainement pas été la même sans le soutien de mes coéquipiers. Je remercie l'équipe YRKV1 de Safran qui m'a accueillie au début de la thèse et qui a permis le bon démarrage de ce projet, tout en continuant à me suivre de loin. Un grand merci également à l'équipe H2T de l'ONERA dans laquelle j'ai passé trois années riches en rencontres, discussions et bons repas partagés. Un merci tout particulier va à la formidable équipe des doctorants qui m'a accueillie : merci à Cyril et Hugues pour les sessions de support Body-Force du vendredi après-midi, qui permettaient de souffler après une semaine intense. Merci à Johan, Victor, Masa, Rémi et Hugo pour les discussions, les soirées jeux et pour avoir transformé les difficultés de la thèse en défis collectifs. Et aux nouveaux arrivés : Matias–même si tu commences à vieillir–Adrian, Hugo et Stefanos, je vous souhaite bon courage pour la suite et vous encourage à profiter pleinement de cette expérience.

Je souhaite également remercier toutes les personnes qui m'ont accompagnée tout au long de cette aventure, qu'elles soient en Italie, en France ou ailleurs dans le monde. C'est aussi grâce à leur soutien inconditionnel que j'ai pu croire en ce résultat.

Un remerciement particulier va à ma famille. Grazie per avermi incoraggiato in ogni scelta, anche se mi ha portato sempre un po' più lontana da voi. La consapevolezza del vostro supporto mi ha permesso di affrontare ogni cambiamento e ogni nuova sfida con risolutezza e coraggio. Grazie per dimostrarmi cosa significa avere nel mondo qualcuno che sarà sempre dalla mia parte.

Enfin, un grand merci à toi, Alessandro. Merci pour ces années partagées, si riches en émotions et en changements. Merci pour ta présence constante et ton écoute, et pour avoir été ma force tranquille tout au long de ce parcours. La fin de ce chapitre marque le début de nouvelles expériences, et j'ai hâte de continuer cette aventure à tes côtés.

Summary

Aviation is undergoing a transformative shift towards sustainability, with modern aero-engine design focused on meeting ambitious environmental targets. These objectives drive the need for propulsion systems that enhance fuel efficiency, reduce emissions, minimise noise, and maintain cost-effectiveness. In response, engine architectures are evolving towards more advanced configurations, such as boundary layer ingestion and ultra-compact nacelles, improving overall aircraft performance. However, these innovations introduce complex flow disturbances at the compressor inlet, resulting in inlet distortion, a non-uniform distribution of velocity, temperature, and pressure, which can lead to significant operational challenges, including flow separation, reduced performance, lower stall margin, and even compressor stall or surge.

This research examines the aerodynamic effects of inlet distortion on high-pressure compressors, with a focus on how distortion patterns propagate through multi-stage architectures and influence compressor robustness. The study addresses the challenge of predicting inlet distortion impacts early in the design process. Conventional tools, assuming uniform inlet conditions, often underestimate performance penalties, while blade-resolved simulations are computationally expensive. To overcome these limitations, the research enhances a Body-Force modelling framework: an efficient, reduced-order approach that captures key flow phenomena like distortion propagation and swirl transport, offering a practical alternative to high-fidelity CFD simulations.

The research begins with the evaluation of an existing Body-Force model, which is well-established for simpler compressor configurations, and develops targeted modifications to enhance its accuracy and applicability to high-pressure compressors. The enhanced model is validated against high-fidelity reference data from both blade-resolved simulations and experimental data from two distinct compressor test cases. By applying the model to these cases, the research assesses the impact of inlet distortion on compressor robustness, focusing on how distortion patterns propagate across multiple stages and contribute to stall margin reduction and the onset of instability. The results demonstrate that the model accurately predicts distortion-induced effects, including performance degradation, altered flow distribution, and changes in stall margins. Additionally, the study provides insights into the model's capabilities in relation to varying geometric features and highlights how these features influence the compressor's sensitivity to distorted inflow.

The enhanced Body-Force model proves to be an efficient tool for early-stage design, facilitating more informed decision-making in the development of robust, distortion-resilient compressors. By simulating inlet distortion effects with high computational efficiency, the model enables early-stage distortion and parametric studies at a reasonable cost, ultimately improving compressor operations. This research provides valuable insights into the impact of inlet distortion on compressor robustness, enhancing the understanding of how future aero-engine designs can address the evolving environmental and operational challenges.

RÉSUMÉ

Le secteur de l'aviation traverse une transformation vers la durabilité, avec des moteurs aéronautiques de plus en plus conçus pour répondre à des objectifs environnementaux ambitieux. Ces défis imposent des exigences strictes sur les systèmes de propulsion, qui doivent améliorer l'efficacité énergétique, réduire les émissions, limiter le bruit et assurer la rentabilité. Les nouvelles configurations, telles que l'ingestion de la couche limite et les nacelles ultra-compactes, optimisent la performance des aéronefs mais génèrent des distorsions d'entrée susceptibles d'affecter gravement les performances des compresseurs, entraînant des risques de séparation du flux, de baisse de performance, voire des instabilités.

Cette recherche se concentre sur les effets des distorsions d'entrée dans les compresseurs haute pression (HPC), en étudiant leur propagation à travers les architectures multi-étages et leur influence sur la robustesse des compresseurs. Les outils de préconception, en raison de leurs hypothèses simplificatrices, ne permettent pas de prédire pleinement les effets des distorsions, tandis que les simulations détaillées sont coûteuses en ressources de calcul. Pour remédier à cela, létude adopte et perfectionne un modèle Body-Force, une approche réduite efficace pour simuler la propagation des distorsions dans des configurations simples, et offrant ainsi une alternative pratique aux simulations CFD de haute fidélité.

Le travail débute par lévaluation dun modèle Body-Force existant, conçu pour des configurations de compresseurs simples, afin den analyser la pertinence pour les HPC. Ce modèle est ensuite amélioré pour accroître sa précision et ladapter aux exigences spécifiques des compresseurs haute pression. Il est validé par des données expérimentales et des simulations aubes-maillées provenant de deux cas tests distincts. Lapplication du modèle à ces cas permet danalyser limpact des distorsions dentrée sur la robustesse des compresseurs, notamment la manière dont les motifs de distorsion se propagent à travers les étages et influencent la réduction de la marge de décrochage ainsi que lapparition des instabilités. Les résultats montrent que le modèle prédit précisément la dégradation des performances, la modification du flux et lévolution de la marge de décrochage. Létude fournit également des informations sur linfluence des caractéristiques géométriques sur la sensibilité du compresseur aux distorsions.

L'amélioration du modèle Body-Force constitue un outil puissant pour la conception en phase précoce, permettant une prise de décision éclairée dans le développement de compresseurs robustes et résistants aux distorsions. Grâce à sa grande efficacité computationnelle, le modèle facilite les études paramétriques et les évaluations des distorsions à un coût raisonnable, améliorant ainsi les performances globales du compresseur. Cette recherche apporte des éclairages précieux sur l'impact des distorsions d'entrée sur la robustesse des compresseurs et permet de mieux comprendre comment les moteurs d'avion de demain pourront répondre aux défis environnementaux et opérationnels à venir. En offrant une alternative plus accessible aux simulations CFD coûteuses, elle ouvre la voie à une conception plus rapide et plus flexible des systèmes de propulsion aérospatiaux.

Table of Contents

Page

List of Tables **xv**

List of Figures **xvii**

Nomenclature **xxv**

Introduction **1**

1 Literature review **7**
- 1.1 Fundamentals of High-Pressure Compressors . . . 8
  - 1.1.1 Functional Role in Aero-Engines . . . 8
  - 1.1.2 Basic Operating Principles . . . 10
  - 1.1.3 Performance and Operability Characterization . . . 12
- 1.2 Inlet Flow Distortion in High-Pressure Compressors . . . 21
  - 1.2.1 Classification and Physical Origins of Inlet Distortion . . . 21
  - 1.2.2 Impact on Compressor Operation . . . 23
  - 1.2.3 Design Considerations . . . 29
- 1.3 Numerical Modelling of Compressors under Inlet Distortion . . . 31
  - 1.3.1 Challenges in Numerical Modelling of Inlet Distortions . . . 31
  - 1.3.2 Overview of Existing Modelling Approaches . . . 31
  - 1.3.3 Body-Force Modelling: Theory, Applications and Limitations . . . 34
- Conclusion . . . 42

2 Test Cases and Numerical Framework **43**
- 2.1 Compressor Test Cases Overview . . . 44
  - 2.1.1 The CREATE Compressor Test Case . . . 46
  - 2.1.2 The IHPC Compressor Test Case . . . 49
- 2.2 Numerical Framework and Methodology . . . 51
  - 2.2.1 The elsA CFD Solver . . . 51
  - 2.2.2 Numerical Parameters . . . 54
  - 2.2.3 Blade-Resolved Simulation Framework . . . 55
  - 2.2.4 Body-Force Simulation Framework . . . 58
- 2.3 Data Post-Processing . . . 61
  - 2.3.1 Post-Processing of Experimental Data . . . 61
  - 2.3.2 Post-Processing of Numerical Data . . . 65
- Conclusion . . . 66

3 Generation and Analysis of High-Fidelity Reference Simulations for the Compressor Test Cases **67**
3.1 High-Fidelity Simulations of the CREATE Compressor . . . 68
3.1.1 Numerical Blade-Resolved Configurations . . . 68
3.1.2 Validation against Experimental Data . . . 73
3.1.3 Characterization of the Flow Field in the CREATE Compressor . . . 75
3.2 High-Fidelity Simulations of the IHPC Compressor . . . 80
3.2.1 Numerical Blade-Resolved Configurations . . . 80
3.2.2 Validation against Experimental Data . . . 84
3.2.3 Characterization of the Flow Field in the IHPC Compressor . . . 87
Conclusion . . . 89

4 Development of an Enhanced Body-Force Model for Multi-Stage High-Pressure Compressor Modelling **91**
4.1 Body-Force Numerical Configurations . . . 92
4.1.1 Body-Force CREATE Configurations . . . 92
4.1.2 Body-Force IHPC Configurations . . . 92
4.2 Assessment of the Hall-Thollet Model for High-Pressure Compressors . . . 93
4.3 Modifications to the Hall-Thollet Model for High-Pressure Compressors . . . 99
4.3.1 Calibration Strategy Development . . . 99
4.3.2 Near-Wall Clipping Technique . . . 106
4.3.3 Integration of Secondary Losses . . . 109
4.3.4 Final Modified Model . . . 113
Conclusion . . . 115

5 Investigation of Inlet Distortion Effects on the CREATE Compressor via Body Force Methodology **117**
5.1 Validation of the Modified Body Force Model on the CREATE Compressor . . . 118
5.1.1 Global Performance Analysis . . . 119
5.1.2 Local Flow Analysis . . . 123
5.2 Impact of Radial Distortion on the CREATE Compressor . . . 128
5.2.1 Impact on the Flow Field . . . 128
5.3 Impact of Circumferential Distortion on the CREATE Compressor . . . 131
5.3.1 Impact on the Flow Field . . . 131
5.3.2 Impact on Stability Parameters . . . 134
5.4 Considerations on CPU Time Gain . . . 138
Conclusion . . . 139

6 Investigation of Inlet Distortion Effects on Aerodynamics and Stability of the IHPC Compressor via Body Force Methodology **141**
6.1 Validation of the Modified Body Force Model on the IHPC Compressor . . . 142
6.1.1 Global Performance Analysis . . . 142
6.1.2 Local Flow Analysis . . . 145
6.2 Impact of Circumferential Inlet Distortion on the IHPC Compressor . . . 151
6.2.1 Impact on the Flow Field . . . 152
6.2.2 Impact on the Stability of the IHPC Compressor . . . 157
6.3 Considerations on CPU Time Gain . . . 165

Conclusion 167

7 Impact of Design Parameters on the Stability of the IHPC Compressor Under Inlet Distortion 169
7.1 Scope and Hypotheses of the Design Study 170
7.2 Analysis of the Impact of Solidity Variations 171
7.2.1 Geometrical Modification Specifications 171
7.2.2 Evaluation under Clean Inflow 172
7.3 Analysis of the Impact of Aspect-Ratio Variations 180
7.3.1 Geometrical Modification Specifications 180
7.3.2 Evaluation under Clean Inflow 180
7.3.3 Evaluation under Circumferential Distortion 185
7.4 Discussion on the Model Capability 190
Conclusion 193

Conclusions and Perspectives 195

A Mesh Sensitivity Study on the CREATE Compressor 201
A.1 Assessment of the Single-Blade-Passage Mesh 201
A.2 Mesh Modifications for Unsteady Simulations 202
A.3 Mesh Sensitivity Study for Body-Force Calculations 203

B Row-by-Row Performance Predictions of the CREATE Compressor via Body-Force Methodology 205

C Row-by-Row Performance Predictions of the IHPC Compressor via Body-Force Methodology 209

Bibliography 215

French Summary I

List of Tables

Table		Page
2.1	Comparison of the CREATE and IHPC compressor configurations.	45
2.2	Main parameters of the CREATE compressor at nominal conditions [141].	46
2.3	Number of blades in the CREATE compressor.	47
2.4	Number of blades per row in the IHPC compressor.	49
2.5	Main parameters of the IHPC compressor at nominal conditions.	49
2.6	Mesh refinement details for CREATE and IHPC compressors for a single-blade passage.	56
3.1	Number of blades per row in the IHPC compressor: full annulus (2π) and quasi-periodic sector.	82
4.1	Mesh size for each configuration of the CREATE compressor.	93
4.2	Mesh size for each configuration of the IHPC compressor.	93
4.3	Target performance parameters for each calibration coefficient.	103
5.1	Calibration coefficients for each blade of the full-height CREATE compressor configuration.	118
5.2	Calibration coefficients for each blade of the CREATE compressor in the P2D configuration.	119
5.3	Relative prediction errors of global performance metrics for the unmodified and modified Body-Force models compared to blade-resolved RANS simulations, at peak efficiency (PE) and near-stall (NS) operating points.	121
5.4	Maximum absolute relative errors of the Body-Force model with respect to blade-resolved URANS simulations for stagnation pressure, stagnation temperature, and entropy at the compressor outlet, for varying inlet distortion intensities.	133
5.5	Computational cost at convergence for each case, normalised by SBP case.	139
6.1	Calibration coefficients for each blade row of the IHPC compressor configuration.	142
6.2	Relative prediction errors of global performance metrics for the unmodified and modified Body-Force models compared to blade-resolved RANS simulations, at peak efficiency (PE) and near-stall (NS) operating points.	144
6.3	Values of the performance ratio PR and their relative changes ΔPR for experimental and Body Force cases at the last stable operating point near stall.	162
6.4	Computational cost at convergence for each case, normalised by $T_{CPU}/(N_{cores}N_{jobs})$ of the blade-resolved SBP case.	166

7.1 Values of the performance ratio PR and their relative changes ΔPR with respect to the base geometry case under clean inflow. 190

A.1 Characteristics of single-blade-passage mesh grids for the CREATE compressor. . . 201
A.2 Grid sensitivity study results on CREATE compressor performance at peak efficiency. 202
A.3 Mesh details for Body-force calculations of CREATE. 203

List of Figures

Figure **Page**

1.1 Schematic of a turbofan engine and its main components [168]. 9
1.2 Schematic of a simplified Brayton cycle. 10
1.3 Schematic of velocity triangles in a typical compressor stage and evolution of flow quantities across the stage. 11
1.4 Schematics of a compressor map showing pressure ratio vs. mass flow with efficiency contours, iso-speed lines, and stability limits [169]. 14
1.5 Illustration of stage matching on the efficiency-mass flow characteristics for three compressor stages. Mismatched (left) and properly matched (right) configurations. 15
1.6 Schematics illustrating: (a) the rotating stall mechanism within a rotor row, (b) part-span stall cells, and (c) full-span stall cell. 16
1.7 Time-resolved hot-wire probe signals from six circumferential positions around the annulus, used to identify spike and modal stall inception mechanisms [14]. . . 17
1.8 Schematic of compressor map illustrating rotating stall and surge instability regions. 18
1.9 Representative near-wall secondary flow structures in axial compressors. (a) Passage and corner vortices. (b) Tip-leakage vortex. 20
1.10 Scheme of inlet distortion patterns: (a) radial, (b) circumferential, (c) rotating, (d) swirl. 22
1.11 Effects of inlet radial distortion on compressor performance and secondary flow structures. Adapted from [92]. 24
1.12 Comparison of hub separation in a transonic axial compressor stage with clean inflow (no screen) and two distortion screens (Cases 1 and 2) [119]. 25
1.13 Effects of azimuthal distortions on the compressor flow distribution [99]. 27
1.14 Stall margin (SM) as a function of angular extension of the distortion grid [5]. . . . 28
1.15 Comparative effects of radial and circumferential distortions on the surge pressure ratio [129]. 29
1.16 Compressor geometry and performance trends in GE compressors, 1950s-1980s [165]. 30
1.17 Schematics of (a) the metal blockage definition and (b) the normal/parallel force decomposition in the Hall-Thollet model [155]. 37
1.18 K_{Mach} schematic [155]. 38
1.19 Axial velocity contours in a compressor subject to a 120° total pressure distortion [56]. 39
1.20 Work coefficient (left) and mass flow rate (right) downstream of the fan rotor under stratified BLI distortion [155]. 40
1.21 Total pressure and giration angle distributions downstream of the fan rotor under boundary layer ingestion (BLI). Bladed simulation (left) and recalibrated Body-Force (right) [55]. 41

2.1 Meridional view of the 3.5-stage CREATE compressor [141]. 46
2.2 Schematic representation of the CREATE test rig [141]. 47
2.3 Schematic meridional view of the 4.5-stage IHPC compressor. 49
2.4 O6H mesh block names and topology for a rotor blade. 56
2.5 Detailed views of the blade-resolved mesh applied to one rotor blade. 57
2.6 Radial and axial mesh renement of the Body-Force mesh applied to one rotor blade. 59
2.7 Comparison of boundary condition schemes between blade-resolved (a) and Body-Force (b) simulations. Color coding: inflow (red), outflow (blue), rotor-stator interfaces (green), and no-slip walls (gray). 60
2.8 Schematic overview of the coupling framework between the elsA solver and the Body-Force co-processing module. 61
2.9 Total pressure distribution measured at the IHPC compressor inlet under clean and distorted inflow conditions. 63
2.10 Relative total pressure difference between clean and distorted inflow conditions at the IHPC compressor inlet. 64

3.1 Domain of the $2\pi/16$ periodic sector configuration of the CREATE compressor, and single-blade-passage highlighted in red. 69
3.2 Inlet boundary condition characterization for the CREATE single-blade-passage case: radial profiles of total pressure (red) and enthalpy (blue), normalised by their respective mean values. 70
3.3 Radial distortion profile and resulting inlet map for the $2\pi/16$ periodic sector configuration of the CREATE compressor un radial distortion. 72
3.4 Computational domain of the single-blade-passage P2D configuration of CREATE, compared to the single-blade-passage 3D case. 72
3.5 Boundary condition setup for the single-blade-passage P2D case for the CREATE configuration. 73
3.6 Azimuthal total pressure distortion features for the P2D simulations of CREATE. . 74
3.7 Compressor map of total-to-total pressure ratio and isentropic efficiency vs. corrected mass flow for experimental data (red circles) and blade-resolved single-blade-passage (green crosses). 75
3.8 Mass flow-averaged radial profiles of total pressure and total temperature along the compressor channel are presented. Results from the SBP and experimental data are compared at multiple axial locations. 76
3.9 Flow field characteristics at 50% channel height in the CREATE compressor. 77
3.10 Detailed view of the flow field at 50% channel height in the first stage of the CREATE compressor. 77
3.11 Entropy distribution at 50% channel height in the first and third stages of the CREATE compressor. 78
3.12 Entropy distribution at 97% channel height of the CREATE compressor. 79
3.13 Skin friction lines on the first rotor blade of the CREATE compressor. 79
3.14 Entropy distribution on an iso-X plane at the outlet of the first rotor blade of CREATE. 80
3.15 Full-annulus computational domain of the IHPC compressor. 81
3.16 Inlet boundary condition characterization for the IHPC single-blade-passage case: radial proles of total pressure (red) and enthalpy (dark red), normalised by their respective mean values. 82

3.17 Azimuthal total pressure distortion features for the full-annulus IHPC simulations. 84
3.18 Compressor map of total-to-total pressure ratio vs. corrected mass flow with experimental data (red circles), single-blade-passage simulations (green crosses), $2\pi/4$ sector simulations (blue diamonds), full-annulus 2π simulations (white triangles). 85
3.19 Mass flow-averaged radial profiles of total pressure and total temperature along the compressor channel. Experimental data are shown as red dots. Results from single-blade-passage, $2\pi/4$, and full-annulus 2π simulations are compared at multiple axial stations. 86
3.20 Entropy flow field at 50% h/H for the IHPC compressor. 87
3.21 Flow field characteristics at the first and fourth rotors of the IHPC compressor at 50% h/H. Contours of iso-$M_{rel} = 1$ line in black. 88
3.22 Entropy distribution at the blade-to-blade cut at 97% h/H, for the first to the fourth rotor blades in the IHPC compressor. 88
3.23 Skin friction lines on the first rotor blade of the IHPC compressor. 89

4.1 Performance characteristics of the 3-stages CREATE compressor. 94
4.2 Total-to-total pressure ratio of the CREATE compressor rows. 95
4.3 Radial profiles of total pressure and total temperature for the CREATE compressor. 96
4.4 Performance characteristics of the 4.5-stages IHPC compressor. 98
4.5 Radial profiles of total temperature for the IHPC compressor. 99
4.6 Lift ratio of a cascade of thin flat plates, illustrating its dependence on stagger angle and space-to-chord ratio [38]. 101
4.7 Influences of K_n and K_f on the performance maps of the first rotor of the isolated first-stage CREATE configuration. 102
4.8 Influence of K_n and K_f on the performance maps of the first rotor of the isolated first-stage CREATE configuration. 103
4.9 Influences of K_D on the isentropic efficiency maps of the first rotor of the single-stage CREATE configuration. 105
4.10 Workflow of the calibration strategy. 106
4.11 View of the normal force component for the 2° Body-Force sector of CREATE. . . . 108
4.12 Schematic of the total pressure loss distribution [135]. 110
4.13 Workflow of the modified Body-Force Model. 114

5.1 Comparison of global performance metrics for the 3-stage CREATE compressor: blade-resolved reference (SBP - bladed), Body-Force with original Hall-Thollet model (BF - HT), and Body-Force with the enhanced model (BF - new). 120
5.2 Comparison of performance metrics for the second rotor row of the CREATE compressor: blade-resolved reference (SBP - bladed), Body-Force with original Hall-Thollet model (BF - HT), and Body-Force with the enhanced model (BF - new). . . 121
5.3 Comparison of π_{tt} characteristics of the CREATE compressor: blade-resolved reference (SBP - bladed), Body-Force with original Hall-Thollet model (BF - HT), Body-Force with the enhanced model (BF - new) and Body-Force with the clipping only (BF - clip). 122
5.4 Spanwise profiles of total pressure (top row) and total temperature (bottom row) at stations downstream of each rotor and at the compressor outlet for the CREATE compressor at peak efficiency. 124

5.5 Spanwise profiles of absolute flow angle (top row) and entropy rise (bottom row) at stations downstream of each rotor and at the compressor outlet for the CREATE compressor at peak efficiency. 125
5.6 Meridional views of absolute flow angle at the peak efficiency point for CREATE. . 125
5.7 Meridional views of total pressure at the peak efficiency point for CREATE. 126
5.8 Meridional views of total temperature at the peak efficiency point for CREATE. . . 126
5.9 Radial profiles of total pressure and total temperature for the CREATE compressor at NS. 127
5.10 Radial profiles of total pressure and total temperature for the CREATE compressor under radial distortion. Relative variations with respect to the clean inflow case. . 129
5.11 Meridional views of total temperature at the peak efficiency operating point for the CREATE compressor in presence of radial distortion. 130
5.12 Radial profiles of total temperature for the CREATE compressor under clean and distorted inflow. Relative variations with respect to the blade-resolved approach. . 131
5.13 Azimuthal profiles of stagnation pressure, stagnation temperature, and entropy at the compressor outlet, at 50% h/H, for clean inflow, 4% and 10% total pressure deficit. Results from blade-resolved simulations (grey), filtered data (black), and Body-Force model (red) are compared. 132
5.14 Evolution of stagnation pressure and temperature across the axial stations of the compressor under 10% circumferential distortion. 134
5.15 Azimuthal profiles of swirl angle, flow coefficient and relative flow angle across different axial stations, for the 10% distortion case. 135
5.16 Entropy field of the blade-resolved (left) and Body-Force (right) P2D cases at 4% distortion. 135
5.17 Azimuthal profiles of stability parameters DH and DLI for all blade rows under 10% inlet total pressure distortion, predicted by the Body-Force model. 136
5.18 Azimuthal profiles of stability parameters DH and DLI for stator S3 under 4% and 10% total pressure distortions, at peak efficiency (PE) and near-stall (NS) operating points, with the blade-resolved (BR) and Body-Force (BF) approaches. 137

6.1 Comparison of global performance metrics for the 4.5-stage IHPC compressor: blade-resolved reference ($2\pi/4$ - bladed), Body-Force with original Hall-Thollet model (BF - HT), and Body-Force with the enhanced model (BF - new) at PE. . . . 143
6.2 Comparison of global performance metrics for the second rotor of the IHPC compressor: blade-resolved reference ($2\pi/4$ - bladed), Body-Force with original Hall-Thollet model (BF - HT), and Body-Force with the enhanced model (BF - new) at PE. 145
6.3 Mass flow-averaged radial distribution of entropy loss at PE. Bladed-resolved ($2\pi/4$ - bladed), and Body Force data using the original (BF - HT) and the modified model (BF - new) at PE. 146
6.4 Mass flow-averaged radial distribution of entropy loss at PE. Bladed-resolved ($2\pi/4$ - bladed), and Body Force data using the original (BF - HT), the modified model (BF - new), and the model with rotor tip losses only (BF - ω_{rt}) at PE. 147
6.5 Mass flow-averaged radial distribution of total pressure and temperature at PE. Bladed-resolved ($2\pi/4$ - bladed) , and Body Force data using the original (BF - HT) and the modified model (BF - new) at PE. 148

6.6 Meridional views of total temperature at the peak efficiency operating point for the IHPC compressor. . . . 149
6.7 Meridional views of entropy rise at the peak efficiency operating point for the IHPC compressor. . . . 149
6.8 Mass flow-averaged radial distribution of entropy loss at PE. Bladed-resolved ($2\pi/4$ - bladed) , and Body Force data using the original (BF - HT) and the modified model (BF - new) at NS. . . . 150
6.9 Azimuthal total pressure distortion features for the full-annulus IHPC simulations. 151
6.10 Compressor outlet flow quantities at 50% channel height. Body Force (red), filtered bladed data (black), and unfiltered bladed data (gray) shown for distortion case only et PE. . . . 152
6.11 Azimuthal profiles of total pressure (left) and total temperature (right) at 50% h/H, comparing bladed URANS and Body Force results for distorted inflow at different stations at PE. . . . 153
6.12 Azimuthal profiles of flow coefficient (Φ) and relative flow angle (β) at the compressor inlet, at 50% h/H and at PE. . . . 154
6.13 2D contour of total temperature showing azimuthal and radial variation downstream of each rotor, comparing the Body Force (right) and Bladed (left) results at PE. . . . 155
6.14 Blade-to-blade entropy field at 50%h/H for the 3.5% distortion case at PE. . . . 156
6.15 Body-force azimuthal profiles of total pressure (top), total temperature (middle), and entropy rise (bottom) at 50% h/H at the compressor outlet, shown for the distortion cases $k_{3.5}$ and $k_{7.5}$ at the PE and NS points. . . . 158
6.16 Entropy flow field at 25% channel height for the critical near-stall point with 7.5% distortion. Vertical black lines mark the leading and trailing edges of the fourth stator (S4). . . . 159
6.17 Map of absolute flow angle (left), axial velocity (middle), and entropy rise (right) at the outlet plane of stator S4, for the critical near-stall point with 7.5% distortion. 160
6.18 Compressor map from Body Force under clean and distorted inlet conditions (3.5% and 7.5%) compared with experimental data. . . . 161
6.19 Azimuthal distribution of flow angle α and axial velocity V_x at the outlet for last stable operating points at 0% (CLN), 3.5%, and 7.5% distortion, and the first critical point at 7.5% distortion. . . . 163
6.20 Azimuthal distribution of DH and DLI at the outlet of S4 at 50% h/H for the last stable operating points with 0%, 3.5%, and 7.5% distortion, and the first critical point at 7.5% distortion. . . . 164

7.1 Solidity modification of the first rotor row: base geometry in blue, and modified geometry in white. . . . 171
7.2 Comparison of the 4.5-stage compressor performance for the solidity variation via the blade-resolved and Body-Force approaches. . . . 172
7.3 Comparison of the first rotor row performance for the solidity variation via the blade-resolved and Body-Force approaches. . . . 173
7.4 Comparison of the 3-stage CREATE compressor performance for the solidity variation via the blade-resolved and Body-Force approaches. . . . 174

7.5 Comparison of the relative Mach number fields for the IHPC and CREATE first rotor rows at peak-efficiency conditions, at 95% h/H. Iso-$M_{rel} = 1$ contour line in black. . . . 175
7.6 Comparison of the isolated first rotor row performance at 80% speed for the solidity variation via the blade-resolved and Body-Force approaches. Plots rescaled to address errors in the reference dataset prediction. . . . 177
7.7 Skin friction lines and contour on the IGV blade at 90% part speed at PE. . . . 178
7.8 Comparison of the 4.5-stage compressor performance at 90% speed for the solidity variation via the blade-resolved and Body-Force approaches. . . . 179
7.9 Comparison of the first rotor row performance at 90% speed for the solidity variation via the blade-resolved and Body-Force approaches. . . . 179
7.10 Aspect-ratio modification of the first rotor row: base (grey) and modified (blue) geometry. . . . 181
7.11 Comparison of the 4.5-stage compressor performance for the aspect-ratio variation via the blade-resolved and Body-Force approaches. . . . 182
7.12 Comparison of the first rotor row performance for the aspect-ratio variation via the blade-resolved and Body-Force approaches. . . . 183
7.13 Comparison of radial profiles of total pressure, total temperature, entropy and absolute flow angle downstream of the first rotor at the peak efficiency point. . . . 183
7.14 Comparison of radial profiles of axial, azimuthal, radial flow velocity and magnitude of flow velocity downstream the first rotor at the peak efficiency point. . . . 184
7.15 Comparison of radial profiles of axial, azimuthal, radial flow velocity and magnitude of flow velocity downstream the first rotor at the near stall point. . . . 185
7.16 Azimuthal profiles of DH (left) and DLI (right) of R1 at the peak efficiency point for both the baseline and modified geometries, obtained using the Body-Force approach. . . . 186
7.17 Azimuthal profiles of DH (left) and DLI (right) of R1 at the stable near stall point for both the baseline and modified geometries, obtained using the Body-Force approach. . . . 187
7.18 Azimuthal profiles of DH (left) and DLI (right) of S4 at the peak efficiency and stable near stall point for both the baseline and modified geometries, obtained using the Body-Force approach. . . . 188
7.19 Two-dimensional entropy contours at the compressor outlet for the geometries at varying aspect ratio at the peak-efficiency point for the $k_{3.5}$ distortion. . . . 189
7.20 Two-dimensional total pressure contours at the compressor outlet for the geometries at varying aspect ratio at the peak-efficiency point for the $k_{3.5}$ distortion. . . . 189
7.21 2D entropy contours at the critical operating point near stall for the 75% c case. . . . 191
7.22 Field of M_{rel} and P_s at the peak-efficiency operating point at 95%h/H. . . . 192
7.23 Field of M_{rel} at the peak-efficiency operating point at 95%h/H, for the part-speed cases. . . . 194

A.1 Normalised entropy field in the wake of the first rotor, across the rotor-stator interface. . . . 203
A.2 Total-to-total pressure ratio of the CREATE compressor computed using four different Body-force meshes. Noticeable differences occur mainly in the choke region at high mass flow rates. . . . 204

B.1 Performance metrics for the first rotor row of the CREATE compressor. 206
B.2 Performance metrics for the first stator row of the CREATE compressor. 206
B.3 Performance metrics for the second rotor row of the CREATE compressor. 207
B.4 Performance metrics for the second stator row of the CREATE compressor. 207
B.5 Performance metrics for the third rotor row of the CREATE compressor. 208
B.6 Performance metrics for the third stator row of the CREATE compressor. 208

C.1 Comparison of performance metrics for the inlet guide vane (IGV) of the IHPC compressor. 209
C.2 Performance metrics for the first rotor row (R1) of the IHPC compressor. 210
C.3 Performance metrics for the first stator row (S1) of the IHPC compressor. 210
C.4 Performance metrics for the second rotor row (R2) of the IHPC compressor. 211
C.5 Performance metrics for the second stator row (S2) of the IHPC compressor. 211
C.6 Performance metrics for the third rotor row (R3) of the IHPC compressor. 212
C.7 Performance metrics for the third stator row (S3) of the IHPC compressor. 212
C.8 Performance metrics for the fourth rotor row (R4) of the IHPC compressor. 213
C.9 Performance metrics for the fourth stator row (S4) of the IHPC compressor. 213

NOMENCLATURE

Acronyms

AR	Aspect-Ratio
BC	Boundary Conditions
BF	Body-Force
BL	Boundary Layer
BLI	Boundary Layer Ingestion
BR	Blade-Resolved
CFD	Computational Fluid Dynamics
CL	Choke Limit
CPU	Central Processing Unit
CREATE	Compresseur de Recherche pour l'Étude des effets Aérodynamiques et TEchnologiques
DH	De Haller number
DLI	Lieblein diffusion factor
DNS	Direct Numerical Simulations
EXP	Experimental data
HPC	High-Pressure Compressor
HPT	High-Pressure Turbine
HT	Hall-Thollet
IGV	Inlet Guide Vane
IHPC	Industrial High Pressure Compressor
LDA	Laser Doppler Anemometry
LE	Leading Edge
LES	Large Eddy Simulations
LMFA	Laboratoire de Mécanique des Fluides et Acoustique
LPC	Low-Pressure Compressor
LPT	Low-Pressure Turbine
NS	Near Stall
P2D	Pseudo-2D
PE	Peak Efficiency
PR	Performance Ratio
PSn	Pseudo-stage n
PTA	Profile Transformation Approach
Rn	Rotor n
RANS	Reynolds-Averaged Navier-Stokes
Sn	Stator n

SBP	Single-blade-passage
SL	Surge Limit
SLC	Streamline Curvature
SM	Stall Margin
TE	Trailing Edge
TLV	Tip Leakage Vortex
URANS	Unsteady Reynolds-Averaged Navier-Stokes

Constants

Symbol	Definition	Value	Unit
γ	Heat capacity ratio	1.4	$-$
R_{gas}	Specific gas constant	287.05	$J \cdot kg^{-1} \cdot K^{-1}$

Variables

Latin Symbol	Definition	Unit
b	blockage	$-$
B	Bladespan	m
c	Blade chord	m
C_L	Lift coefficient	$-$
C_f	Skin friction coefficient	$-$
$\vec{f}$	Body force per unit mass	$m \cdot s^{-2}$
h	Specific enthalpy	$J \cdot kg^{-1}$
H	Enthalpy	J
h/H	Channel height	$-$
k_{ij}	Local distortion coefficent at radial position i and azimuthal position j	$-$
k_j	Averaged distortion coefficent at azimuthal position j	$-$
$k_{j,new}$	Corrected averaged distortion coefficent at azimuthal position j	$-$
K_{Mach}	Compressibility correction	$-$
m	Meridional streamline	$-$
$\dot{m}$	Mass flow rate	kg/s
M	Mach number	$-$
$\vec{n} = (n_x, n_r, n_\theta)$	Normal vector to the blade camber line	$-$
N_{blades}	Number of blades	$-$
N_{rows}	Number of bladed rows	$-$
p, P	Pressure	Pa
Q_{corr}	Corrected mass flow rate	$-$
r	Radius	m
Re	Reynolds number	$-$
Re_x	Chordwise reynolds number	$-$
s	Blade pitch	$-$
S	Entropy	$J \cdot K^{-1}$

S_b	Blockage source term	$kg \cdot m^{-3} \cdot s^{-1}$
Δt	Time step	s
T	Temperature	K
t	Blade thickness	$-$
tc	Tip clearance	m
$\overline{tc}$	Tip clearance over bladespan	$-$
T_{ref}	Reference time	s
V	Absolute flow velocity	m/s
W	Relative flow velocity	m/s
X	Generic quantity	$-$

Greek Symbol	**Definition**	**Unit**
α	Absolute flow angle	rad
β	Relative flow angle	rad
β_1	Blade metallic angle at leading edge	rad
β_2	Blade metallic angle at trailing edge	rad
β_s	Blade stagger angle	rad
δ	Local three-dimensional flow deviation angle	rad
δ_1	Boundary layer thickness	m
δ_1^*	Boundary layer displacement thickness	m
$\overline{\delta_1^*}$	Boundary layer displacement thickness over bladespan	$-$
η	Compressor efficiency	$-$
Φ	Flow coefficient	$-$
π	Pressure ratio	$-$
Ψ	Pressure rise coefficient	$-$
τ	Temperature ratio	$-$
ω	Shaft speed	rpm
$\overline{\omega}$	Total pressure loss coefficient	$-$
ρ	Flow density	kg/m^3
σ	Blade solidity	$-$
$\Delta\theta$	Azimuthal shift of flow path	rad
$\Delta\theta_r$	Rotation component of the azimuthal shift of flow path	rad
$\Delta\theta_s$	Stagger component of the azimuthal shift of flow path	rad
ζ	Swirl angle	rad

Subscripts and superscripts

Subscripts	**Definition**
$\bullet_0$	At reference conditions
$\bullet_{CLN}$	Clean inflow
$\bullet_{DIST}$	Distorted inflow
$\bullet_{hb}$	Hub
$\bullet_{in}$	Inlet
$\bullet_{is}$	Isentropic
$\bullet_m$	Meridian direction

$\bullet_n$	Normal force direction
$\bullet_{out}$	Outlet
$\bullet_p$	Parallel force direction
$\bullet_r, \bullet_{rel}$	Relative
$\bullet_{ref}$	Reference
$\bullet_s$	Static
$\bullet_{sh}$	Shroud
$\bullet_{st}$	total-to-static
$\bullet_t$	Total
$\bullet_{tt}$	Total-to-total
$\bullet_x, \bullet_r, \bullet_\theta$	Cylindrical coordinates
$\bullet_x, \bullet_y, \bullet_z$	Cartesian coordinates

Superscripts	**Definition**
$\bullet^{\eta_{max}}$	At maximal isentropic efficiency point
$\bullet^n$	At iteration n
$\bullet^{n+1}$	At iteration n+1
$\bullet^{pivot}$	At pivot point
$\bullet^w$	Relative reference frame



INTRODUCTION

Environmental Context and Regulatory Drivers

Modern aero-engine design is increasingly shaped by stringent environmental targets and regulatory frameworks established by national and international aviation authorities, aimed at significantly reducing the sector's carbon footprint. The global aviation community has committed to ambitious emissions reductions by 2030 [80], with the ultimate objective of achieving net-zero carbon emissions by 2050 [79], in alignment with international climate goals. These mandates impose complex requirements on propulsion systems, which must simultaneously deliver improved fuel efficiency, reduced emissions, lower noise, enhanced operability, and cost-effectiveness across the engine lifecycle.

To address these multifaceted demands, contemporary engine architectures are evolving towards more aerodynamically advanced and tightly integrated configurations. Emerging propulsion concepts, such as boundary layer ingestion (BLI) [101], S-duct inlets [107], and ultra-compact nacelles [124], are developed to improve aircraft-level performance by reducing drag, enabling more compact installations, and lowering fuel burn and emissions. In parallel, compressor designs are trending toward higher aerodynamic loading and tighter stage-matching tolerances to meet performance objectives. While these innovations offer clear performance and environmental benefits, they also introduce highly non-uniform and unsteady flow conditions at the compressor inlet. Such configurations can induce adverse flow phenomena, such as separation, swirl, secondary flows, and strong gradients, leading to spatially and temporally distorted inflow profiles.

In addition to distortion generated by integrated propulsion configurations, real-world operating scenarios, such as crosswind conditions, aircraft maneuvers, bleed air extraction, and ingestion of hot or recirculated gases, can introduce transient and unpredictable distortions [114], further complicating the compressor's operating environment. Consequently, compressor inlets are inherently distorted under realistic operating conditions due to the variety of distortion mechanisms. This scenario presents new aerodynamic challenges that must be thoroughly understood and addressed during both design and operation.

Impact of Inlet Distortion on Compressor Performance

Inlet distortion refers to the non-uniform distribution of flow properties, such as velocity, temperature, pressure, and flow direction, at the compressor inlet, relative to the idealised uniform conditions typically assumed in design. These non-uniformities may be present in the radial and circumferential directions, and often exhibit significant unsteadiness arising

from upstream flow interactions or ingestion phenomena [107]. Such distortions impose spatially and temporally varying aerodynamic loads on compressor blades, causing localised overloading that can lead to flow separation, reduced pressure rise capability, and a lowered stall margin, which represents the safety buffer before the onset of aerodynamic instability [41, 114, 166].

In severe cases, such conditions can lead to compressor stall or surge, with serious implications for engine operability and flight safety. From an industrial and operational standpoint, distortion-induced instabilities contribute to increased maintenance demands, reduced engine service life, and potential mission interruptions. These effects highlight the critical importance of accurately predicting and mitigating distortion-related phenomena.

The impact of inlet distortion is especially significant in high-pressure compressors (HPC), which operate under demanding aerodynamic loads and within a highly complex flow environment [1]. Inlet distortions, whether induced by airframe integration or operational conditions, can propagate through multiple stages of the HPC, where they interact with complex flow structures such as shock waves, tip leakage flows, secondary vortices, and blade wakes [128]. The multi-stage nature of HPCs amplifies these effects, as distortion patterns evolve through successive stages due to nonlinear aerodynamic coupling and flow mixing.

To mitigate the adverse effects associated with inlet distortion, modern compressor designs incorporate features aimed at enhancing aerodynamic robustness and maintaining stable operation across a range of inflow conditions. Aerodynamic shaping of blades and vanes plays a critical role in managing non-uniform inflows: optimisations in blade sweep, stagger angle, solidity and aspect ratio can improve stall margin and reduce aerodynamic losses under distorted flow conditions. In addition, mitigating strategies, such as the use of bleed air systems and wall treatments, are employed to regulate internal compressor flows, suppress instabilities, and support consistent performance. Achieving such robustness, particularly during early development stages, requires reliable prediction of compressor behaviour under realistic, distorted operating conditions. Consequently, computational tools are essential for assessing the impact of distortion and guiding design decisions prior to costly physical testing.

Modelling the Effects of Inlet Distortion

The dynamic nature of distortion propagation and its highly three-dimensional behaviour make modelling and prediction especially challenging, necessitating the use of advanced numerical methods capable of capturing the relevant physical phenomena.

Early-stage compressor design typically relies on simplified computational tools that assume uniform inlet flow [96]. These include mean-line and throughflow solvers, which provide rapid estimates of performance and are widely used for preliminary design. However, such methods inherently neglect the complex, non-axisymmetric flow features introduced by distortion and therefore tend to underestimate performance penalties and the risk of aerodynamic instabilities. As a result, designs based solely on these tools may prove inadequate under realistic operational conditions. At the other end of the spectrum, high-fidelity computational fluid dynamics (CFD) simulations, such as Unsteady Reynolds-Averaged Navier-Stokes (URANS), typically used for these applications, can resolve detailed, three-dimensional, unsteady flow features with high accuracy, including the dynamics of inlet distortion [12, 25, 88]. Despite their predictive accuracy, the extensive computational cost and long turnaround

times of such simulations restrict their practical use to the later stages of the design process, rather than for iterative concept development or parametric exploration.

To address this gap, a range of reduced-order modelling techniques has been developed over the years. These methods aim to capture the essential physics governing the compressor response to inlet distortion while maintaining tractable computational costs [67]. Representative approaches include the Parallel Compressor model [108], the Actuator Disk model [81], and extended throughflow methods [4, 34, 49]. While these approaches offer useful tools for early-stage performance assessment and system-level studies, their reliance on idealised assumptions often limits their applicability to highly integrated, multi-stage compressors. In particular, these models typically simplify or neglect key flow features such as swirl transport, inter-stage coupling, and distortion evolution. As such, their predictive fidelity remains limited, motivating the development of more advanced yet computationally efficient modelling strategies.

Body-Force Modelling for Efficient and Accurate Compressor Simulation

Within the family of reduced-order approaches, Body-Force models have received growing attention due to their favourable balance between physical accuracy and computational cost. These models approximate blade-induced aerodynamic effects by introducing distributed momentum and energy source terms into the governing equations, thereby eliminating the need to resolve individual blade geometries [55, 156]. The source terms incorporated into the Navier-Stokes equations are generally formulated locally, allowing distorted inlet conditions to be analysed through steady-state simulations, significantly reducing the computational cost with respect to unsteady blade-resolved computations.

Body-Force methods therefore offer a practical means of capturing the impact of inlet distortion on compressor performance with greater fidelity than uniform-inlet tools. Previous studies have shown that these models can reproduce key flow phenomena such as distortion propagation and swirl transport, with results that compare favourably to experimental data and high-fidelity simulations [3, 156]. Their computational efficiency also makes them well suited for parametric studies, multi-disciplinary optimisation, and design space exploration [42, 55].

Nonetheless, extending Body-Force modelling approaches to high-pressure, multi-stage compressors remains a significant challenge. HPCs are characterised by highly loaded blade rows, strong inter-stage aerodynamic interactions, and non-linear flow behaviour [29]. Many existing Body-Force models rely on empirical correlations and simplified coefficients calibrated for different operating regimes or geometries, which may not generalise well to HPC applications. These simplifications often fail to capture secondary flow structures, tip leakage effects, and non-linear blade-flow interactions, leading to a loss of predictive fidelity under realistic distorted inflow conditions. Furthermore, the evolution of distortion through successive stages introduces additional complexity, as flow structures interact and transform in ways that are not readily predicted by existing models.

These limitations highlight the need for advanced Body-Force modelling frameworks that can accurately reproduce the nuanced behaviour of compressors under distorted inflow while retaining computational efficiency. Developing such models would provide a valuable capability for distortion-aware design and early-stage analysis, enabling more robust and efficient compressor systems in future aero-engine architectures.

Research Objectives

The primary objective of this research is to investigate the aerodynamic effects of inlet flow distortion on high-pressure compressors and to assess compressor robustness under realistic, non-uniform inflow conditions. Emphasis is placed on understanding how various distortion patterns propagate through multi-stage compressor architectures, contribute to performance degradation, and interact with key geometric and aerodynamic parameters. This work aims to advance the fundamental understanding necessary to inform the development of compressors with enhanced resilience to inlet distortion, improving operability and performance across a broad range of inflow scenarios.

To achieve this, the study adopts and further develops an existing Body-Force modelling framework as an efficient yet physically representative alternative to fully blade-resolved simulations. This approach provides sufficient fidelity to capture critical flow phenomena such as swirl transport and distortion evolution while significantly reducing computational expense. The enhanced Body-Force formulation is applied to investigate distortion transport and performance degradation across multiple compressor stages, as well as to explore the impact of key geometric features on compressor sensitivity to inlet distortion.

The proposed model is rigorously validated against both experimental data and high-fidelity reference simulations of representative high-pressure compressor cases. Its formulation remains independent of specific inlet conditions, enabling systematic investigation across a broad spectrum of distortion configurations.

By enabling detailed parametric studies at a fraction of the computational cost associated with full-annulus, blade-resolved unsteady simulations, the enhanced Body-Force model provides a practical and versatile tool for early-stage analyses that account for inlet distortion effects. Ultimately, this research seeks to deepen the understanding of distortion-compressor interactions and to establish a foundation to inform the future development of distortion-resilient compressor designs.

Thesis Structure

The structure of this thesis reflects the methodological progression of the research, from foundational theory and reference data generation through model development and validation to practical application and final analysis.

Chapter 1 provides the theoretical background and literature review, covering the fundamentals of high-pressure compressors, the effects of inlet flow distortion, and the numerical approaches available for distortion analysis. Particular attention is given to Body-Force modelling techniques, highlighting their current capabilities and known limitations, and identifying the reference model adopted for further development in this thesis.

Chapter 2 introduces the two compressor test cases investigated throughout the thesis. It outlines their geometric and operational characteristics and presents the experimental dataset used for validation. The numerical methodology is then described, with a focus on the differences between blade-resolved and Body-Force simulation strategies.

Chapter 3 focuses on the generation of high-fidelity blade-resolved simulations, which are used to establish a reference dataset for both compressors. It details the computational configurations and provides an initial characterisation of the flow fields under clean inlet conditions.

Chapter 4 is dedicated to the assessment and enhancement of the Body-Force modelling approach undear clean inflow. It begins with the validation of a baseline Body-Force formulation against the blade-resolved reference data. Based on this comparison, key limitations are identified, and a series of targeted modifications are proposed to enhance model representativeness for high-pressure compressors.

Chapters 5 and 6 exploit the improved Body-Force model to simulate inlet distortion effects on the two compressors: a radial and a simplified circumferential distortion study for the first, and a fully circumferential distortion study for the second. A progressive approach is adopted, with increasing levels of geometric and aerodynamic complexity. For each case, results are validated against the corresponding blade-resolved data, and the model's ability to capture performance degradation and internal flow features is critically assessed.

Chapter 7 explores the impact of geometric design modifications on compressor robustness to inlet distortion. First, the modified configurations are validated under clean conditions using blade-resolved simulations. The Body-Force methodology is then applied to evaluate their performance under distorted inflow, enabling comparative analysis of distortion sensitivity.

Finally, the Conclusion summarises the main findings, discusses their implications for compressor design and modelling, and outlines potential directions for future research in low-order modelling for distortion prediction.

Publications and Conference Presentations

The work presented in this thesis has led to the following publications and presentations at international conferences:

- [26]: Crea, C.; Marty, J.; Barrier, R.; Cochon, S.; Dufour, G. "Body-Force Modelling of a Multi-Stage High-Pressure Compressor Under Inlet Distortion". *International Journal of Turbomachinery Propulsion and Power* 2025, 10, 12.

  https://doi.org/10.3390/ijtpp10020012.

- [27]: Crea, C.; Marty, J.; Barrier, R.; Cochon, S.; Dufour, G. "Body-Force Modelling of a Multi-Stage High-Pressure Compressor Under Inlet Distortion". In Proceedings of the 16th European Turbomachinery Conference, 24–28 March 2025, Hannover (DE).

  https://www.euroturbo.eu/publications/proceedings-papers/etc2025-159.

- [28]: Crea, C.; Marty, J.; Barrier, R.; Cochon, S.; Dufour, G. "Effects of Inlet Distortion on the Stability of a Transonic Multi-Stage High-Pressure Compressor: A URANS-Validated Body-Force Approach". In Proceedings of the AIAA SciTech Forum, 12–16 January 2026, Orlando, FL (USA).

  https://doi.org/10.2514/6.2026-0238.

CHAPTER 1

LITERATURE REVIEW

This chapter establishes the theoretical and methodological framework for studying the effects of inlet flow distortion on high-pressure compressors in aero-engines. It begins with an overview of compressor function, operating principles, and performance characteristics to provide essential background. The phenomenon of inlet distortion is then introduced, with emphasis on radial and circumferential types due to their significant impact on aerodynamic stability and efficiency. The chapter concludes with a review of numerical modelling approaches, focusing in particular on Body-Force methods. Special attention is given to the Hall-Thollet model, which underpins the simulation methodology employed in this thesis.

Contents

1.1 Fundamentals of High-Pressure Compressors **8**
1.1.1 Functional Role in Aero-Engines 8
1.1.2 Basic Operating Principles 10
1.1.3 Performance and Operability Characterization 12
1.1.3.1 Performance Characterization 12
1.1.3.2 Operability Limits 15
1.2 Inlet Flow Distortion in High-Pressure Compressors **21**
1.2.1 Classification and Physical Origins of Inlet Distortion 21
1.2.2 Impact on Compressor Operation 23
1.2.2.1 Radial Distortion Effects 24
1.2.2.2 Circumferential Distortion Effects 26
1.2.3 Design Considerations 29
1.3 Numerical Modelling of Compressors under Inlet Distortion **31**
1.3.1 Challenges in Numerical Modelling of Inlet Distortions 31
1.3.2 Overview of Existing Modelling Approaches 31
1.3.3 Body-Force Modelling: Theory, Applications and Limitations 34
1.3.3.1 Generalities 34
1.3.3.2 The Hall-Thollet Model 36
1.3.3.3 Investigation of Inlet Distortion with Body-Force Models . 39
Conclusion **42**

1.1 Fundamentals of High-Pressure Compressors

This section provides the foundational background necessary to understand the behaviour of high-pressure compressors, especially under distorted inlet conditions. It begins by outlining the functional role of the compressor within a modern aero-engine and its contribution to overall engine performance. Basic principles governing axial compressor stage operation are introduced to establish the aerodynamic context. Subsequently, key performance metrics and definitions are presented to ensure consistency in terminology throughout the thesis. The section concludes with an overview of the primary operability constraints that define the limits of stable and efficient compressor operation.

1.1.1 Functional Role in Aero-Engines

A modern aero-engine comprises several key components operating within a tightly coupled and highly optimised thermodynamic cycle. Among various engine types, turbofan architectures presently dominate commercial and military aviation due to their superior fuel efficiency, reduced acoustic emissions, and effective performance across a broad range of flight conditions. This engine configuration includes a fan, low-pressure compressor (LPC), high-pressure compressor (HPC), combustor, high-pressure turbine (HPT), low-pressure turbine (LPT), and exhaust nozzle, as shown in Figure 1.1. The engine operates on a dual-stream

principle, where the incoming air is divided into two distinct flows: the fan stream, which bypasses the core, and the core stream, which passes through the engine core for compression, combustion, and power generation.

The fan and compressors are responsible for pressurising the incoming air; the combustor converts chemical energy via fuel-air combustion; and the turbines extract mechanical energy to drive the compressors and fan. Among these components, the axial compressor plays a pivotal role, as it governs the aerodynamic and thermodynamic state of the airflow entering the combustor and later alimenting the turbine, directly influencing engine thrust, fuel efficiency, and operational stability.

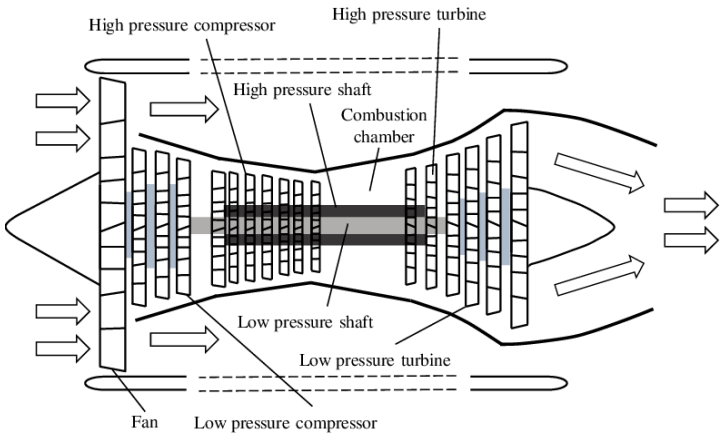

Figure 1.1: Schematic of a turbofan engine and its main components [168].

The thermodynamic cycle governing turbofan engine operation is the Brayton cycle. Ideally, it consists of isentropic compression in the fan and compressor, constant-pressure heat addition in the combustor, isentropic expansion in the turbine, and isentropic flow acceleration through the nozzle. For clarity, the cycle can be modelled using a simplified configuration comprising a single compressor, combustor, turbine, and nozzle, as illustrated in Figure 1.2, and represented on an enthalpy-entropy (h–S) diagram.

In the ideal cycle, ambient air at state 1 is isentropically compressed to state 2, increasing its pressure and temperature. Heat is then added at constant pressure from 2 to 3, and the high-energy gas expands isentropically through the turbine from 3 to 4. The remaining thermal energy is converted into kinetic energy through isentropic acceleration in the nozzle from 4 to 9, generating thrust.

In reality, irreversibilities such as mechanical friction, aerodynamic losses, and heat transfer between the working fluid and engine components cause deviations from the ideal process. These effects increase entropy and are illustrated by the red dashed lines in Figure 1.2. As a result, compression occurs from 1 to a non-ideal outlet state 2′, with higher entropy and higher power consumption than 2. Similarly, pressure losses and heat transfer in the combustor cause a shift from 3 to 3′, and expansion proceeds from 3′ to 4′, and from 4′ to 9′, again with increased entropy and reduced recovered power. These losses increase the required compressor work and reduce turbine work output, lowering the overall thermal efficiency of the cycle, defined as the ratio of the net work output to the heat input.

The compressor plays a pivotal role in the Brayton cycle, as its efficiency significantly affects overall thermodynamic performance. A more efficient compression process results in a

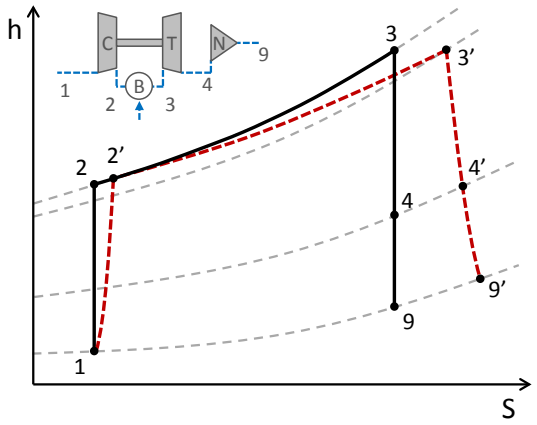

Figure 1.2: Schematic of a simplified Brayton cycle.

smaller enthalpy increase for a given pressure ratio, thereby maximizing the enthalpy difference between states 3 and 9, and minimizing the enthalpy rise between states 1 and 2. This difference determines the net work output of the cycle. The compressor also sets the pressure, temperature, and flow conditions at the combustor inlet, directly influencing fuel consumption, thrust generation, and overall engine efficiency. Accurate prediction of compressor behavior, particularly under off-design conditions such as inlet flow distortion, is therefore essential for reliable engine design and operation.

1.1.2 Basic Operating Principles

In modern turbofan engines, achieving the high overall pressure ratios required for efficient Brayton cycle operation necessitates multiple compressor stages. Compressor stages are limited by aerodynamic and mechanical constraints such as flow instabilities, shock losses, and structural stresses, which degrade efficiency and reliability. To overcome these limitations, high-pressure compressors are typically designed as multi-stage axial-flow machines, with each stage providing a moderate pressure increase while maintaining aerodynamic and mechanical integrity. This staged approach enables the high total pressure ratios essential for efficient engine performance across a wide range of flight conditions.

Axial compressors are preferred over centrifugal designs in aircraft propulsion due to their ability to handle high mass flow rates and pressure ratios with greater efficiency. Unlike centrifugal compressors, which turn the airflow radially outward from the axis of rotation, axial compressors maintain flow parallel to the engine axis. This configuration allows for a more compact engine diameter and improved integration within the airframe. Furthermore, the modular nature of axial compressors facilitates scalability and higher overall efficiencies through the addition of multiple stages, making them the standard in both commercial and military aviation.

Each axial compressor stage typically consists of a rotating blade row (rotor) followed by a fixed blade row (stator). The rotor imparts work to the flow, increasing its total pressure and total temperature by accelerating it. The stator then acts as a diffuser, decelerating the flow to convert kinetic energy into increased internal energy, which is reflected as an increase in static pressure, while also redirecting the flow to match the inlet angle of the next rotor stage.

The aerodynamic behaviour of the flow within a stage is captured by velocity triangles, which describe the vector relationships among blade speed, absolute velocity, and relative velocity at the rotor and stator interfaces, as illustrated in Figure 1.3.

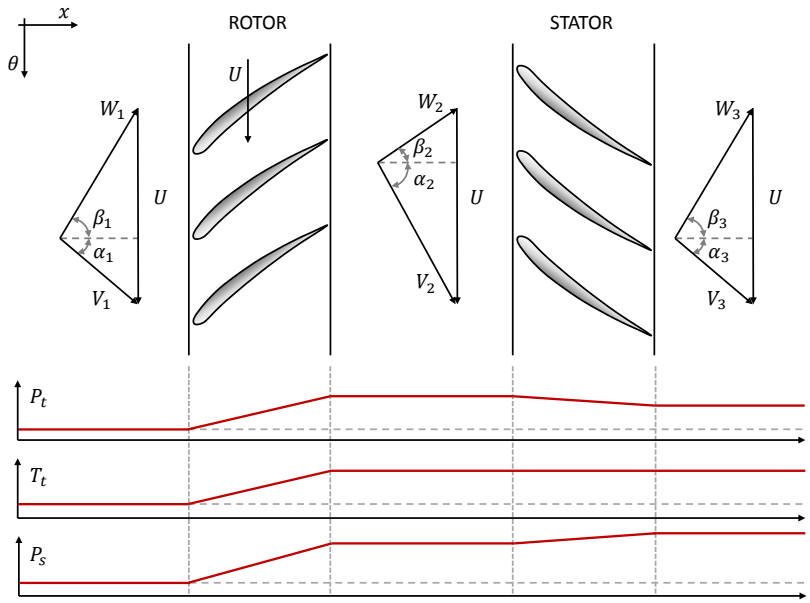

Figure 1.3: Schematic of velocity triangles in a typical compressor stage and evolution of flow quantities across the stage.

At the rotor inlet, the absolute velocity $\vec{V}_1$ forms an angle α_1 with the axial direction. This vector can be decomposed into the blade speed $\vec{U} = \omega R \vec{u}_\theta$, where ω is the angular velocity, R the radius and $\vec{u}_\theta$ the azimuthal unit vector, and the relative velocity $\vec{W}_1$, which forms an angle β_1 relative to the axial direction. The vector relation is given by: $\vec{V}_1 = \vec{W}_1 + \vec{U}$. As the flow passes through the rotor, both the magnitude and angle of the absolute velocity typically increase, while the relative velocity magnitude and angle decrease.

The work imparted by the rotor to the flow is governed by Euler's turbine equation, which relates the total enthalpy rise across the rotor to the change in the tangential component of the absolute velocity:

$$\Delta h_t = U_2 V_{\theta,2} - U_1 V_{\theta,1}, \tag{1.1}$$

where $V_{\theta 1}$ and $V_{\theta 2}$ are the tangential components of the absolute velocity at the rotor inlet and outlet, respectively. In compressors, this work results in an increase in total temperature and total pressure, while static pressure increases more modestly due to aerodynamic compression.

Immediately downstream, the stator decelerates the flow and reorients it to suit the next rotor stage. While total temperature remains constant (in the absence of heat transfer), total pressure may decrease slightly due to aerodynamic losses. The stator reduces the magnitude and angle of the absolute velocity, while increasing the relative velocity and its corresponding angle, thereby aligning the flow with the blade angles of the next rotor. This alignment minimises incidence losses, reduces flow separation, and maximises stage efficiency.

A thorough understanding of these velocity relationships is essential to characterise aerodynamic loading and work transfer in each stage, and to assess how changes in flow conditions influence blade forces and overall compressor performance.

1.1.3 Performance and Operability Characterization

This section provides a general overview of the key challenges associated with compressor operability. It begins by introducing the main performance metrics used in compressor analysis. Subsequently, it discusses the primary flow phenomena that limit the operating range of multi-stage compressors, along with additional mechanisms that may lead to instabilities and further operability constraints under specific operating conditions.

1.1.3.1 Performance Characterization

Performance Metrics To evaluate compressor behavior across different operating conditions, a set of standard performance metrics is commonly employed. These metrics provide a quantitative basis for assessing aerodynamic performance, efficiency, and operability throughout the flight envelope.

The primary performance metric is the total-to-total pressure ratio, π_{tt}, which measures the compressor's ability to increase fluid pressure and directly influences the engine's thermal efficiency. Similarly, the total temperature ratio, τ_{tt}, quantifies the temperature rise due to compression and relates to the work input required. Additionally, the total-to-static pressure ratio, π_{st}, is often used to assess flow deviation and pressure recovery at the compressor outlet. These ratios are defined in Equation (1.2).

$$\pi_{tt} = \frac{P_{t,\text{out}}}{P_{t,\text{in}}}, \quad \tau_{tt} = \frac{T_{t,\text{out}}}{T_{t,\text{in}}}, \quad \pi_{st} = \frac{P_{s,\text{out}}}{P_{t,\text{in}}} \tag{1.2}$$

The isentropic efficiency, η_{is}, compares the actual enthalpy rise across the compressor to that of an ideal, isentropic compression process, for equivalent pressure ratios. This metric quantifies thermodynamic losses due to phenomena such as friction, shock waves, boundary layer separation, and secondary flows. Its expression is given in Equation (1.3).

$$\eta_{is} = \frac{h_{t,\text{out,is}} - h_{t,\text{in}}}{h_{t,\text{out}} - h_{t,\text{in}}} = \frac{\left(\frac{P_{t,\text{out}}}{P_{t,\text{in}}}\right)^{\frac{\gamma-1}{\gamma}} - 1}{\frac{T_{t,\text{out}}}{T_{t,\text{in}}} - 1} \tag{1.3}$$

Here, h_t, P_t, and T_t denote the total enthalpy, pressure, and temperature, respectively. The subscripts $\bullet_{in}$, $\bullet_{out}$, and $\bullet_{out,is}$ refer to the inlet, outlet, and isentropic outlet conditions.

The mass flow rate, $\dot{m}$, is another fundamental quantity that governs aerodynamic performance and overall engine operation. The reduced massflow rate is commonly employed to compare flows across different operating conditions by removing the effect of inlet thermodynamic state and geometry, and is defined in Equation (1.4).

$$\dot{m}_{\text{reduced}} = \frac{\dot{m}\sqrt{R_{gas}\,T_{t,in}}}{P_{t,in}\,A} \tag{1.4}$$

where: $\dot{m}$ is the actual mass flow rate, R_{gas} is the specific gas constant, $T_{t,in}$ is the total inlet temperature, $P_{t,in}$ is the total inlet pressure, and A is the reference area.

Since inlet conditions vary with altitude and flight speed, the corrected mass flow rate, Q_{corr}, is introduced to normalise $\dot{m}$ to a standard set of reference inlet conditions. This normalization allows consistent comparisons across operating points and is defined in Equation (1.5).

$$Q_{\text{corr}} = \dot{m}\sqrt{\frac{T_{t,\text{ref}}}{T_{t,\text{in}}}}\frac{P_{t,\text{in}}}{P_{t,\text{ref}}} \tag{1.5}$$

In this expression, $T_{t,\text{in}}$ and $P_{t,\text{in}}$ represent the inlet total temperature and pressure, respectively, while $T_{t,\text{ref}}$ and $P_{t,\text{ref}}$ denote the reference values, which are chosen as the standard conditions of 273.15 K and 101325 Pa, respectively. All flow quantities employed in the calculation of these performance metrics are derived from the averaged flow field, in accordance with the averaging criteria detailed in Section 2.3.2.

In addition to thermodynamic performance, flow stability metrics are also commonly employed. One such metric is the De Haller number, DH, which is traditionally used to assess the risk of flow separation within a blade row [32]. It is defined as the ratio of the relative flow velocity at the blade outlet to that at the inlet, as shown in Equation (1.6).

$$DH = \frac{W_2}{W_1} \tag{1.6}$$

Here, W_1 and W_2 are the inlet and outlet relative velocities in the blade reference frame. Lower values of DH indicate stronger flow deceleration and higher susceptibility to separation and stall.

Another widely used metric is the Lieblein Diffusion Factor, DLI, which provides a more comprehensive measure of blade row aerodynamic loading [97]. It includes a one-dimensional deceleration term and a component accounting for blade turning. Its formulation is given in Equation (1.7).

$$DLI = 1 - \frac{W_2}{W_1} + \frac{\Delta W_\theta}{2\sigma W_1} \tag{1.7}$$

In this expression, ΔW_θ is the change in the tangential component of the relative velocity across the blade row, and σ is the solidity, defined as the ratio of the chord length c to the blade pitch. The pitch is computed as $2\pi R/N_{blades}$, where R is the local radius and N_{blades} the number of blades. Higher values of DLI indicate stronger aerodynamic loading and greater risk of flow separation and stall.

Compressor Map Compressor performance and stability metrics are fundamental to assessing aerodynamic behavior and ensuring operability across a range of conditions. These metrics are collectively visualised using a compressor map, a key graphical tool that illustrates the compressor's operating envelope.

Figure 1.4 shows a typical compressor map, where pressure ratio is plotted against mass flow rate. The black curves denote iso-speed lines, each corresponding to a specific rotational speed Nn. The corrected rotational speed may also be used, and is defined as $N_{corr} =$

$N/\sqrt{T_{t,in}}$. Green contours represent lines of constant isentropic efficiency, highlighting the variation in performance across the map. The orange line connects the points of maximum efficiency along each iso-speed line and typically represents the nominal (or design) operating conditions.

Operability limits are also indicated: the red curve marks the surge line (SL), beyond which the compressor experiences flow instabilities such as surge at low mass flow rates. Conversely, the blue curve defines the choke line (CL), which corresponds to the maximum flow capacity before aerodynamic blockage occurs.

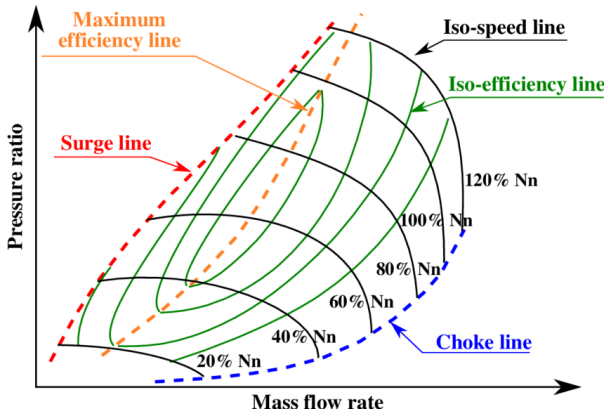

Figure 1.4: Schematics of a compressor map showing pressure ratio vs. mass flow with efficiency contours, iso-speed lines, and stability limits [169].

Stage Matching Stage matching is a fundamental consideration in the design and operation of multi-stage compressors, as it directly influences the overall aerodynamic efficiency and stability of the machine. Building upon the framework provided by individual stage compressor maps, stage matching refers to the alignment of flow parameters between successive stages such that each operates near its respective peak efficiency point. This implies that the thermodynamic and aerodynamic conditions at the outlet of one stage must be compatible with the optimal inlet conditions of the subsequent stage, thereby ensuring that all stages function within their most efficient regions of operation.

Improper stage matching can result in suboptimal performance and reduced stability margins. This concept is illustrated in Figure 1.5, which presents the efficiency-mass flow rate characteristics (gray lines) for three stages of a compressor. The left-hand case depicts a mismatched configuration: while the first stage operates at its design point (A1), corresponding to maximum efficiency, the second stage (A2) at the same mass flow rate deviates significantly from its optimal operating point, moving closer to its stability boundary. Similarly, the third stage does not achieve its peak efficiency. This mismatch reduces the overall efficiency of the compressor and can lead to increased risk of aerodynamic instabilities, such as stall or surge, particularly in the later stages.

In contrast, the right-hand case of Figure 1.5 shows a well-matched configuration, where all three stages operate at or near their respective best-efficiency points under nominal mass flow rate conditions (B1, B2, B3). Such a design ensures that the compressor achieves maximal overall efficiency and maintains robust stability margins. Furthermore, proper stage matching extends the operability of the compressor by preventing any single stage from becoming the limiting factor due to premature stall or choke.

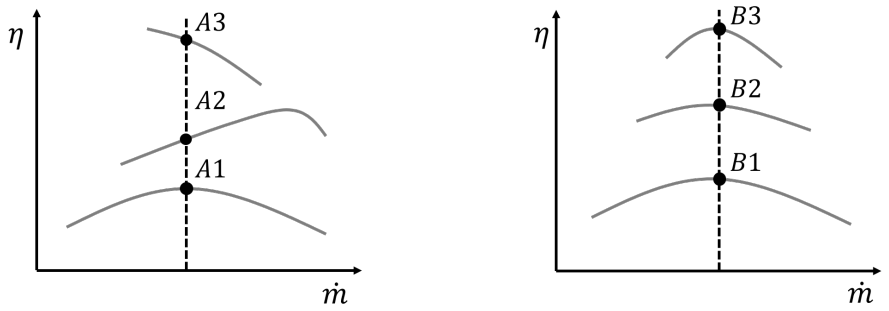

Figure 1.5: Illustration of stage matching on the efficiency-mass flow characteristics for three compressor stages. Mismatched (left) and properly matched (right) configurations.

1.1.3.2 Operability Limits

This section addresses the primary operability limits of multi-stage high-pressure compressors and is divided into two parts. The first part introduces the main physical phenomena that constrain stable compressor operation, namely rotating stall, surge, and choking. These mechanisms define the aerodynamic boundaries of the compressor's operating envelope and must be thoroughly understood to enable robust design and control strategies.

The second part provides a brief overview of secondary flow phenomena that, under certain operating conditions, can contribute to the onset of these instabilities. These include near-wall effects, tip leakage flows, and shock-induced interactions. While generally less critical, such mechanisms can reduce stability margins and serve as precursors to stall, surge, or choking.

Limits of Compressor Operation

Axial compressor operability is constrained by three primary aerodynamic phenomena: rotating stall, surge, and choking, which together define the aerodynamic boundaries of compressor performance.

Stall is a localised flow separation phenomenon that typically originates within individual blade passages and may propagate circumferentially as rotating stall cells. Surge, in contrast, is a global instability characterised by large-amplitude pressure oscillations and flow reversal throughout the entire compressor system. Choking occurs when the flow reaches sonic conditions at one or more critical locations, beyond which no further increase in mass flow is possible. A thorough understanding of these three limiting phenomena, is essential for predicting and preventing compressor instability.

Stall Stall occurs when the angle of incidence between the incoming flow and a rotor blade exceeds a critical threshold, leading to boundary layer separation and partial flow blockage within the affected blade passage. This localised separation disrupts the flow field and causes the fluid to be redirected into adjacent passages. As a result, these neighboring passages are subjected to increased flow angles, which may also induce separation, thereby initiating a chain reaction of flow disturbances. The cumulative effect is the formation of one or more stall cells, regions of reversed or highly disturbed flow, that propagate circumferentially around the compressor annulus, typically in the direction opposite to blade rotation in the

relative frame. This rotating stall phenomenon reduces the effective mass flow capacity of the compressor and often serves as a precursor to surge [31].

Figure 1.6a illustrates this mechanism, showing streamlines approaching the blade leading edge at non-optimal angles of attack, leading to the onset of separation and stall.

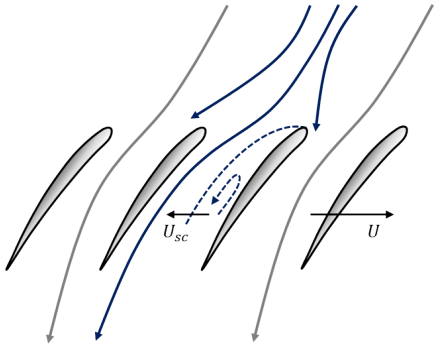

(a) Rotating stall mechanism in a rotor stage.

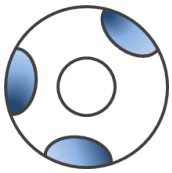

(b) Part-span stall cells.



(c) Full-span stall cell.

Figure 1.6: Schematics illustrating: (a) the rotating stall mechanism within a rotor row, (b) part-span stall cells, and (c) full-span stall cell.

Rotating stall exhibits several defining characteristics. The number of stall cells can vary, ranging from a single cell to multiple cells, which may interact with each other due to differences in their extension and speed, and are typically distributed around the annulus. These cells may span the full height of the blade (full-span stall) or occupy only a portion of the span (part-span stall), thereby influencing the severity and aerodynamic impact of the disturbance. Figures 1.6b and 1.6c illustrate part-span and full-span stall cells, respectively.

Stall inception in axial compressors can occur through two fundamentally different mechanisms: spike-type and modal-type. These mechanisms differ both in their spatial and temporal evolution. Spike-type inception is characterised by a short-duration, abrupt disturbance that originates locally and propagates rapidly into stall. It presents little or no circumferential coherence and is often associated with a localised breakdown of the boundary layer, resulting in a fast-growing flow blockage. In contrast, modal-type inception is marked by a low-frequency, circumferentially coherent disturbance that gradually amplifies over several rotor revolutions before leading to stall. This behavior is associated with a global instability mode that encompasses the full annulus [40, 44, 59, 60].

These distinctions are illustrated in Figure 1.7, which presents time-resolved hot-wire measurements from six probes arranged circumferentially around the annulus. The left subfigure shows a spike-type event characterised by a sudden, localised disturbance in a single probe signal with a distinct phase, rotating at approximately 70% of the blade speed. In contrast, the right subfigure depicts a modal-type inception, where a coherent wave propagates circumferentially, evidenced by a diagonal phase shift across the probes. This indicates a rotating modal structure with a mode speed near 20% of the rotor speed, notably lower than that of the spike-type event [14].

The stall margin (SM) quantifies the operational distance between the compressor's current operating point and the onset of stall, providing a measure of the safety buffer before instability occurs. The stall margin can be defined using various parameters, such as the pressure ratio, the pressure-to-mass flow rate ratio, the flow coefficient, or the rotor tip speed.

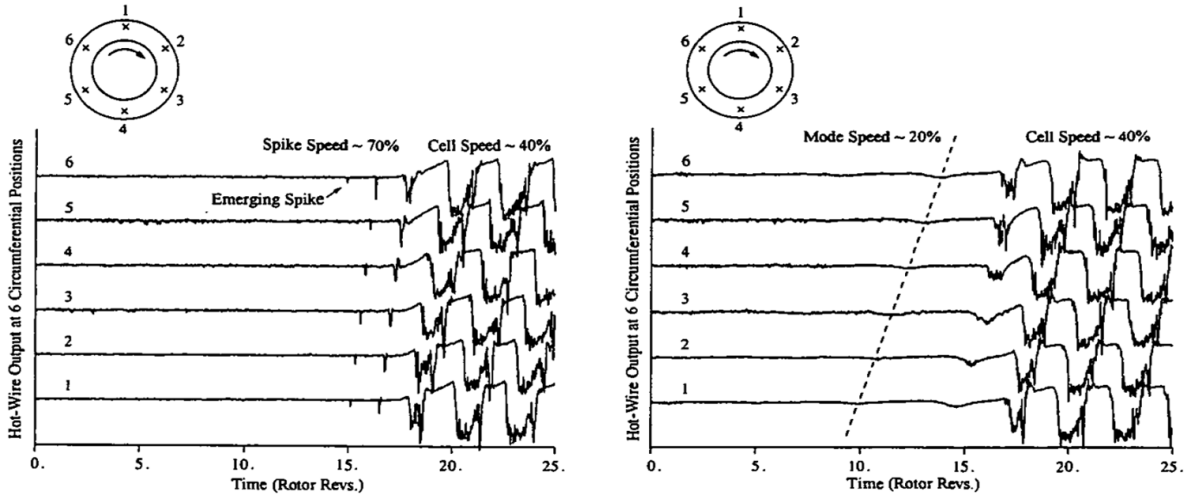

(a) Spike-type stall inception. **(b)** Modal-type stall inception.

Figure 1.7: Time-resolved hot-wire probe signals from six circumferential positions around the annulus, used to identify spike and modal stall inception mechanisms [14].

A higher stall margin indicates greater tolerance to disturbances and operational variability, while a reduced margin increases the likelihood of instability, particularly under transient or off-design conditions.

Surge Surge is a global aerodynamic instability in the compression system, which arises when the compressor mass flow rate decreases below a critical limit for a given pressure ratio. This corresponds to the surge limit indicated with the red dashed line in Figure 1.4. Under these conditions, the compressor is unable to overcome the adverse pressure gradient imposed by the system, resulting in large-scale flow reversal accompanied by unsteady, low-frequency oscillations in flow and pressure throughout the compressor and connected ducting [30, 113, 159]. Surge induces significant mechanical vibrations, which can cause severe damage to engine components and eventually failure.

Surge typically occurs near the low mass flow boundary of the compressor operating map, known as the surge limit. It is often triggered by off-design operating conditions such as rapid throttle changes or inlet flow disturbances, which modify the effective mass flow either globally or locally. The resulting increase in aerodynamic loading promotes flow separation and unstable dynamic interactions between the compressor and downstream components. This interaction causes the flow to oscillate between stalled and recovered states, thereby restricting the stable operating range of the compressor.

Surge can be classified as either partial or deep. Partial surge refers to a milder instability, where the oscillations in mass flow rate and pressure ratio are smaller, and no flow reversal occurs. Deep surge, on the other hand, involves more severe instabilities, where the mass flow rate can become negative, indicating flow reversal and significant disruption to the compressor's operation. Both types of surge exhibit hysteresis behavior, meaning the compressor does not immediately return to stable operation once surge conditions are alleviated. This behavior arises from the coupled dynamics of the compressor flow and system inertia, leading to an

asymmetric relationship between pressure ratio and mass flow rate during the surge cycle, complicating control and prevention strategies.

Figures 1.8a and 1.8b provide schematics of rotating stall and surge regions on the compressor map, respectively, highlighting the distinct operating mechanisms for these phenomena.

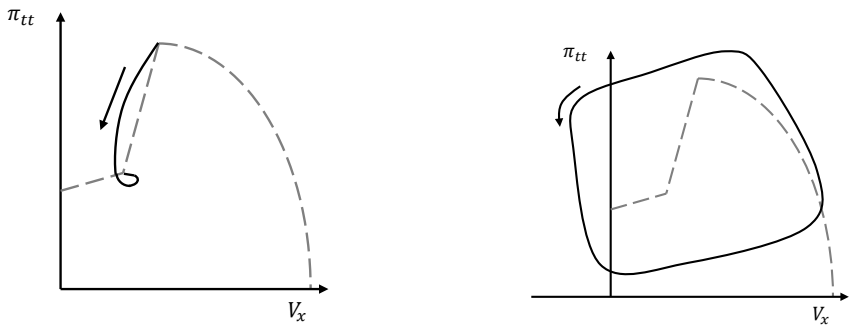

(a) Rotating stall. **(b)** Surge.

Figure 1.8: Schematic of compressor map illustrating rotating stall and surge instability regions.

In summary, stall and surge define critical aerodynamic limits of compressor operation, with stall often serving as an early indicator of impending surge. Accurate prediction and mitigation of these phenomena remain challenging but are essential for safe and efficient compressor performance.

Choking Choking occurs when the flow velocity at the throat of a compressor passage reaches sonic speeds, thereby limiting the maximum achievable mass flow rate. This corresponds to the choke limit indicated with the blue dashed line in Figure 1.4. At this point, the flow becomes constrained, and any further decrease in total-to-static pressure ratio becomes unsustainable due to the formation of shock waves and aerodynamic blockage. This phenomenon establishes a definitive upper limit on the compressor's flow capacity, as the sonic condition prevents further acceleration and can lead to a significant reduction in overall efficiency. Choking is particularly critical in high-speed or transient conditions, where rapid fluctuations in mass flow or pressure may drive the compressor toward this limiting state.

Similarly to stall margin, the choke margin quantifies the operational distance between the compressor's current operating point and the onset of choking. A larger choke margin provides a buffer, enhancing operational flexibility and ensuring that the compressor remains within stable conditions during dynamic loading or transient events, such as rapid throttle changes or variations in engine power demand. Defining an adequate choke margin in the design phase is thus essential to ensure compressor stability and performance across varying operating conditions.

Secondary Flow Phenomena Relevant to Compressor Stability

Secondary flows in axial compressors arise from complex three-dimensional interactions between blade geometry, boundary layers, and pressure gradients. These flows significantly influence aerodynamic losses and stability margins, thereby affecting compressor per-

formance and operability. Moreover, secondary flow phenomena have been shown to play a critical role in triggering flow instabilities such as stall and surge by promoting localised flow separation and unsteady flow patterns [10, 164]. For clarity and focus on stability-relevant mechanisms, secondary flows are categorised as follows in the following: near-wall secondary flows, tip clearance flow, and shock-related phenomena.

Near-Wall Secondary Flows Near-wall secondary flows encompass a range of complex aerodynamic phenomena that arise within the boundary layers adjacent to blade surfaces and endwalls. These flows result from the combined effects of viscosity, adverse pressure gradients, and three-dimensional flow interactions, giving rise to vortical structures and localised separations. Among the most prominent features are passage vortices, cross-flows, corner vortices, and corner separation, all of which play a significant role in modifying the effective flow area, altering local incidence angles, and thereby influencing compressor stability and performance. Among these, the passage and corner vortices are of particular interest in this study due to their dominant role in loss generation and flow separation near endwalls. These structures are schematically illustrated in Figure 1.9a.

Passage vortices originate within blade passages due to the interaction between surface boundary layers and cross-passage pressure gradients. These interactions generate coherent rotational structures that transport low-momentum fluid toward the blade suction side and endwalls, as described in [72]. Additionally, the horseshoe vortex, formed by the aerodynamic pressure differences across the blade surfaces, interacts with the flow in the passage, influencing the development of the passage vortex and contributing to flow separation near the blade tips and endwalls. Cross-flows arise from lateral pressure gradients, either between hub and casing or across adjacent blade rows, and distort the streamwise velocity profile, effectively altering the local flow angles and boundary layer development.

Corner vortices form near the blade-endwall junctions due to the combined influence of leading-edge flow acceleration and boundary layer thickening along the hub or casing. More critically, corner separation occurs in these regions as a result of strong adverse pressure gradients and three-dimensional boundary layer interactions. This leads to the formation of low-momentum, often reversed-flow regions that substantially reduce the effective flow area and increase total pressure losses [50, 170]. Corner separation is particularly detrimental because it introduces highly unsteady flow behavior and promotes early flow blockage, reducing stall margins and increasing the susceptibility to flow instabilities.

These secondary flow structures often interact nonlinearly, compounding their adverse effects. The resulting flow field is highly three-dimensional and spatially non-uniform, particularly in the near-endwall regions. This non-uniformity enhances the compressor's sensitivity to inlet distortions, facilitates premature flow separation, and significantly contributes to the development of instabilities such as rotating stall [61].

Tip Clearance Flow Tip clearance flow is a fundamental secondary flow phenomenon driven by the pressure differential between the pressure and suction sides of rotor blades at the blade tip. The resulting leakage flow passes through the gap between the blade tip and compressor casing, generating a coherent vortical structure known as the tip leakage vortex which convects downstream within the blade passage. This structure is schematically illustrated in Figure 1.9b. The characteristics of this vortex, including its circulation intensity, spatial extent, and trajectory, are strongly influenced by geometric parameters such as tip

clearance size and blade shape, as well as operating conditions including rotational speed and mass flow rate [122].

The presence of the tip leakage vortex adversely affects compressor performance and stability by reducing the effective flow capacity and increasing aerodynamic losses. Furthermore, interactions between the tip leakage vortex and boundary layers on blade and endwall surfaces can induce unsteady flow separation and localised blockage, phenomena known to contribute to stall and surge inception [109, 152]. Approaching stall, increased blade loading amplifies the tip leakage flow, enlarging the vortex and exacerbating losses and blockage. These dynamics restrict the compressor's stable operating range and highlight the critical role of tip clearance flow in stability assessment.

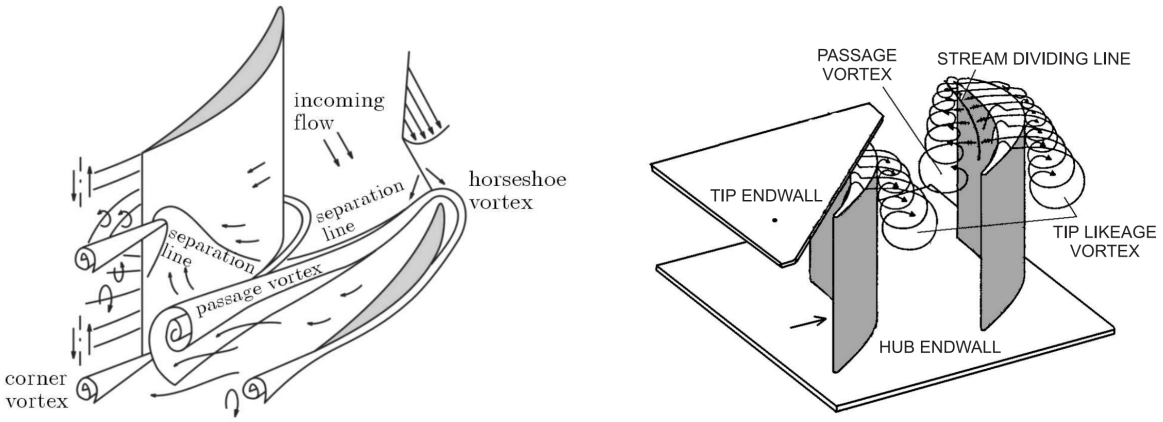

(a) Near-hub secondary flow structures within an axial compressor cascade [110].

(b) Near-shroud secondary flow structures within a turbine cascade [87].

Figure 1.9: Representative near-wall secondary flow structures in axial compressors. (a) Passage and corner vortices. (b) Tip-leakage vortex.

Shock-Related Phenomena Shock wave formation occurs predominantly in transonic compressor stages when the relative flow velocity locally exceeds the speed of sound. Flow acceleration over blade surfaces, particularly near leading edges and blade tip regions, can induce supersonic flow followed by abrupt deceleration through shock waves. These shocks cause sudden increases in static pressure and temperature, accompanied by losses in total pressure, thereby adversely affecting aerodynamic performance [83].

Under certain operating conditions, the flow approaching the compressor blade can be supersonic, causing shock waves to form upstream or at the blade leading edge. These shocks induce abrupt deceleration and pressure rises, altering the incoming flow angle and velocity distribution, which can degrade aerodynamic loading and reduce stage performance.

Interactions between shock waves and boundary layers or secondary flow structures, such as blade wakes and tip leakage vortices, can lead to boundary layer separation and flow unsteadiness [43, 86, 127]. Although high-fidelity numerical studies have shown that direct losses caused by shocks may constitute a relatively small portion of rotor losses, their interactions with boundary layers and secondary vortices can significantly contribute to overall loss and flow distortion [138]. These interactions remain among the primary sources of aerodynamic losses in transonic rotors. The unsteady nature of shock-boundary layer interactions

exacerbates flow non-uniformities, promotes early separation, and increases susceptibility to instabilities such as stall and surge [71].

Effective management of shock-related phenomena is therefore critical in transonic compressor design to preserve stability margins and maintain efficient operation.

In summary, the interplay of near-wall secondary flows, tip clearance vortices, and shock-related phenomena critically influences compressor stability. A thorough understanding of the behavior of these secondary flows and their sensitivity to inlet distortions is essential for advancing compressor design aimed at improved operability and reliability.

1.2 Inlet Flow Distortion in High-Pressure Compressors

Disruptive advancements in engine technology driven by the imperative to improve fuel efficiency, reduce emissions, and enhance overall performance are transforming the design and integration of aeronautical propulsion systems. These innovations often require more compact engine architectures and highly integrated configurations, which result in complex inlet geometries and tighter spatial constraints. Such design evolution exacerbates flow non-uniformities and increases the susceptibility of compressors to inlet distortion. At the same time, increasingly stringent operational conditions, particularly in military applications characterised by rapid throttle transitions, aggressive maneuvers, and operation in adverse environments, impose additional challenges by inducing highly transient and non-uniform inlet flows. The combination of these disruptive technologies and demanding operational profiles creates critical inlet conditions that profoundly affect compressor stability, efficiency, and overall engine reliability, underscoring the need for comprehensive understanding and mitigation of inlet distortion effects.

High-pressure compressors, positioned deep within the engine core, must reliably operate despite encountering varying degrees of inlet distortion throughout their service life. The distortions encountered in these components arise both from upstream flow irregularities and from aerodynamic interactions with upstream engine components, which together generate non-uniform flow patterns that challenge compressor stability and performance.

The following sections first examine the physical characterization of inlet distortion and its effects on turbomachinery operation, with particular emphasis on the degradation of compressor stability due to distortion ingestion. Building on this foundation, the influence of key design parameters on compressor performance and stability will be analysed, specifically considering the presence of inlet distortion. While modifications to design parameters can improve efficiency and performance under uniform flow conditions, they often reduce the compressor's stability margin and its tolerance to distorted inflow. Consequently, it is essential to carefully evaluate these trade-offs to achieve an optimal balance between enhanced performance and robustness to distortion.

1.2.1 Classification and Physical Origins of Inlet Distortion

Any non-uniformity in the inlet flow conditions of a compressor, manifesting as variations in pressure, temperature, or flow angle, is considered a distortion. The impact of such distortions on compressor performance depends on their characteristics, which are commonly classified according to spatial distribution, intensity, and temporal variation [11].

Figure 1.10 provides an overview of the most frequently encountered distortion patterns. Distortions are broadly categorised as either steady or unsteady, based on the temporal fluctuations of the distorted flow properties.

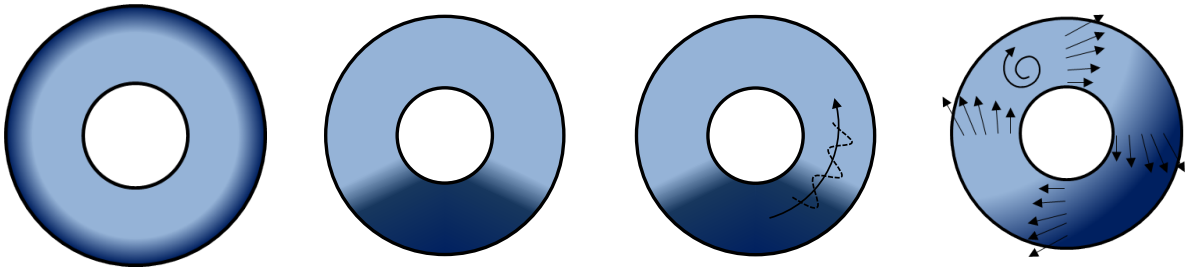

Figure 1.10: Scheme of inlet distortion patterns: (a) radial, (b) circumferential, (c) rotating, (d) swirl.

Steady distortions are characterised by non-uniformities that remain effectively constant over timescales significantly longer than the characteristic response time of the compressor. These steady distortions are typically subdivided into radial distortions, illustrated in Figure 1.10a, where the distortion pattern is axisymmetric but varies along the annulus height [148]; and circumferential distortions, shown in Figure 1.10b, where the distortion is localised over a segment of the annulus circumference [78]. Additionally, combined distortion patterns exhibiting variations in both radial and azimuthal directions may occur.

Regarding unsteady distortions, the most common types include rotational distortion, depicted in Figure 1.10c, characterised by a circumferential distortion pattern rotating azimuthally at a specific frequency [100], and swirl distortion, one of the more complex and recently studied patterns, defined as a non-uniform variation in the angular momentum or flow direction of the incoming airflow, resulting in uneven rotation or twisting of the flow, as schematically shown in Figure 1.10d [24].

These distinct distortion patterns originate from different underlying physical mechanisms. Radial inlet distortion commonly arises from boundary layer development along the walls of the inlet duct, leading to a velocity deficit near the casing and hub regions. Particularly, the thickness and characteristics of the boundary layer vary according to the upstream duct geometry and flow conditions. This non-uniform velocity profile results in a radial gradient of total pressure and axial velocity, which can significantly affect the aerodynamic performance of the downstream compressor and potentially amplifying the severity of an inlet distortion.

Another source of radial distortion is the occurrence of flow separation on the inlet duct walls or hub surfaces. Flow separation generates recirculating regions characterised by low momentum and modified pressure distributions, resulting in pronounced radial variations in the incoming flow field. The onset and extent of these separated regions depend on several factors, including inlet geometry, flow incidence, and Reynolds number, and may evolve with the engine operating point [93].

A further source of radial distortion in compressor inlets arises from flow injection processes such as cooling air introduction or aspiration, which generate localised thermal gradients that induce non-uniformities in temperature, density, and static pressure along the radial direction. These thermal-induced variations modify the inlet flow topology and can degrade compressor stability and performance [153].

Circumferential distortion originates from azimuthal non-uniformities in the inlet flow, typically manifesting as sectors of reduced total pressure. These patterns result from a range of external and geometric factors that introduce asymmetries in the flow approaching the engine. One of the most frequent causes is crosswind ingestion during ground operations, particularly at low forward speed conditions such as taxiing, takeoff, or landing. Crosswinds alter the direction and momentum of the incoming streamlines, creating sectors of reduced total pressure and high incidence on the windward side of the inlet [21].

Another major contributor to circumferential distortion is asymmetric inlet geometry. This includes offset or serpentine ducts, which are commonly employed in embedded engine installations, especially in military aircraft, to achieve better integration within the airframe and reduce radar and infrared signatures. These configurations inherently introduce azimuthally non-uniform pressure and velocity distributions at the engine inlet [107]. Boundary layer ingestion is also a frequent source of circumferential distortion [68]. When the inlet captures low-momentum air from the airframe boundary layer, particularly during low-speed or high-incidence flight, it creates localised pressure deficits along specific azimuthal sectors. Additionally, inlet-airframe interactions can introduce further asymmetries in the incoming flow [156]. Each of these phenomena contributes to circumferential distortion, which can severely influence compressor stability and reduce the overall performance margin of the propulsion system.

Unsteady flow distortions in compressor inlets arise from time-dependent, three-dimensional flow non-uniformities. In multi-spool engines, instabilities originating in upstream compressors may propagate downstream, altering the inlet conditions of subsequent stages [100]. These distortions can be further amplified by tip vortex shedding at high blade loading, which introduces additional swirling structures [167].

Swirl distortion occurs due to non-uniform angular momentum distributions in the incoming flow. It can exhibit both steady and unsteady characteristics. Steady swirl distortion is typically caused by asymmetries in inlet geometry or disturbances from upstream wakes and tip vortices, which impart a consistent rotational motion to the flow. Unsteady swirl distortion, on the other hand, arises from transient disturbances that introduce time-varying swirling motions. Installation effects from adjacent structures can also introduce swirl components by altering the flow path before the compressor inlet [143]. Additionally, ground vortex ingestion can contribute to swirl distortion by drawing in vortical flow generated near the ground during low-altitude operations [3].

In summary, inlet flow distortions present a variety of spatial and temporal characteristics that can be broadly classified into radial, circumferential, rotating, and swirl distortions. However, in real-world applications, these categories are not always clearly separated. Complex interactions between multiple phenomena, combined with varying operational conditions, often result in overlapping and interdependent distortion patterns.

1.2.2 Impact on Compressor Operation

The aerodynamic effects of steady inlet distortions are examined in this section, as these represent the primary focus of the study. Emphasis is placed on their influence on key aspects of compressor operation, including stall margin, efficiency, and overall stability.

1.2.2.1 Radial Distortion Effects

Radial distortion is a common type of inlet distortion that causes uneven flow distribution and aerodynamic loading along the blade span. These variations affect incidence and loading, which in turn alter the flow environment around the compressor blades. Radial distortion is typically classified as either hub or tip distortion, depending on whether it occurs near the inner or outer boundary of the compressor annulus. The compressor's stability and performance response depend on the location and intensity of the distortion. Tip distortion generally reduces stall margin and accelerates stall onset by destabilizing the tip leakage vortex, while hub distortion can either delay stall onset and improve stability, or exacerbate hub corner separation, depending on its intensity [7, 93, 114, 139].

The effects of radially non-uniform inflow on compressor stability can be clearly visualised in Figure 1.11a, which illustrates how tip and hub distortions differently influence the behaviour of tip leakage vortices. Tip distortion destabilises the tip leakage vortex by pushing it toward near-stall conditions, increasing blockage and promoting stall [47, 73, 172]. It also redistributes mass flow from the distorted regions to the undistorted ones, shifting the vortex toward the centerline and increasing its unsteadiness. In contrast, hub distortion constrains the tip vortex closer to the blade tip, weakening it and moving it downstream along the adjacent blade's pressure side, which can delay stall onset and enhance compressor stability. These mechanisms are further clarified by the tip leakage flow visualizations in Figure 1.11b: under uniform inflow, the vortex maintains a baseline position and strength; tip distortion intensifies the vortex and shifts it toward the leading edge, increasing destabilisation; hub distortion, instead, weakens the vortex and shifts it downstream, correlating with improved stability. This figure-guided explanation demonstrates how tip and hub distortions differently modulate secondary flow structures and their impact on compressor operability.

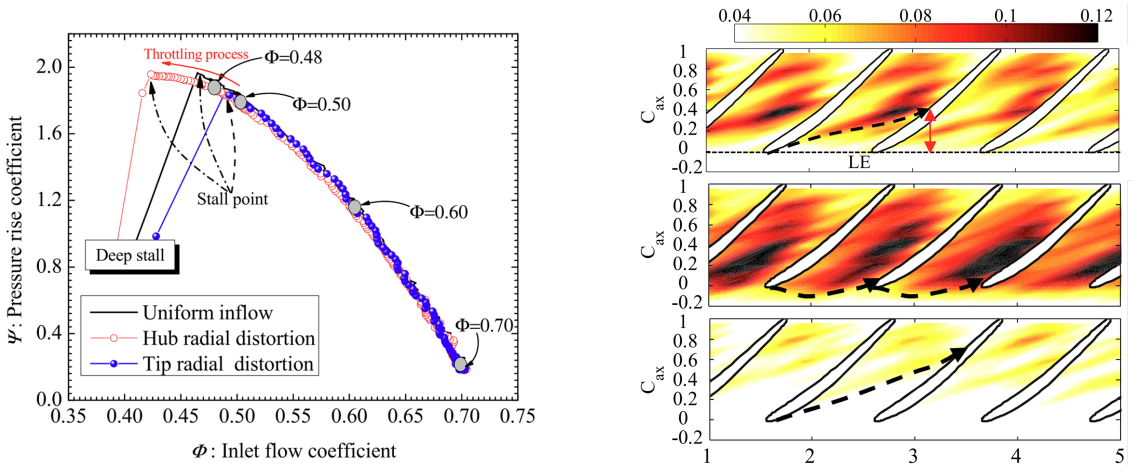

(a) Compressor performance map illustrating operating points under different inlet conditions.

(b) Tip leakage flow visualizations for uniform inflow (top), tip radial distortion (center), and hub radial distortion (bottom) at $\Phi = 0.50$.

Figure 1.11: Effects of inlet radial distortion on compressor performance and secondary flow structures. Adapted from [92].

However, hub distortion can also have adverse effects near the hub wall, where it increases local blade loading and exacerbates near-wall flow separation. This condition promotes hub

corner separation and can accelerate stall onset, potentially shifting the stall inception point from the rotor tip to the stator hub [39, 40, 95].

The radial distribution of blade loading near stall conditions governs the type of instability that initiates: low hub loading at low rotor speeds tends to produce rotor tip-initiated stall, whereas high hub loading at higher speeds can lead to partial surge. Introducing inlet distortion can mitigate hub loading, reduce localised flow blockage, and delay stall onset, provided the distortion produces a favourable blade loading distribution [119]. Conversely, if the distortion increases hub loading, it may exacerbate hub corner separation and degrade overall compressor stability. Figure 1.12 illustrates this behavior for a transonic axial compressor stage, comparing clean inflow (no screen) with two distorted inflow conditions generated by screens of different porosities (Cases 1 and 2). The figure demonstrates that increasing pressure loss coefficients and localised flow blockage progressively reduce hub separation, with the extent of separation decreasing from the clean inflow case to Case 1, and further in Case 2, highlighting the influence of radial distortions on near-hub flow behavior and compressor stability.

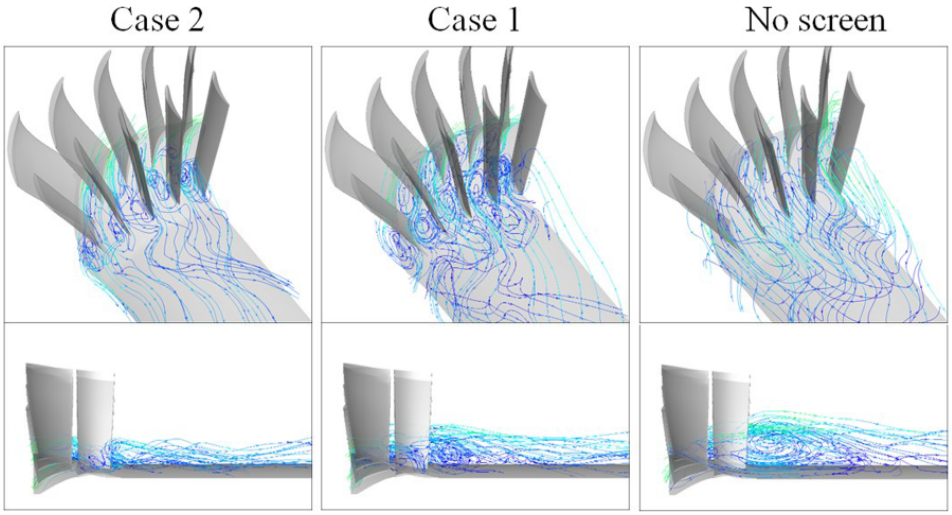

Figure 1.12: Comparison of hub separation in a transonic axial compressor stage with clean inflow (no screen) and two distortion screens (Cases 1 and 2) [119].

Active and passive flow control techniques, such as tip flow injection and casing treatments, have been extensively investigated to mitigate the effects of radial distortion on secondary flows and compressor stability [36, 76, 153]. Tip flow injection has been shown to extend the stable operating range, recover stalled stages through local flow re-energization, and alter stall inception mechanisms by suppressing spike-type stall in favor of modal stall, the latter being generally less abrupt and more manageable [137].

In contrast, hub casing treatments and tailored radial distortion strategies have proven effective in reducing hub corner separation by weakening adverse pressure gradients and modifying hub leakage flow. These approaches enhance near-hub flow uniformity, thereby improving compressor stability and delaying stall onset [19, 119].

In summary, radial distortion has a significant impact on compressor stability by inducing uneven spanwise flow distributions and blade loading, and by altering secondary flow structures such as tip leakage vortices and hub corner separation. These changes affect stall inception mechanisms and reduce the stall margin, ultimately narrowing the compressor's

stable operating range. The location and intensity of the distortion are critical in determining the aerodynamic performance and operability of axial compressors.

1.2.2.2 Circumferential Distortion Effects

Circumferential distortions cause uneven blade loading around the annulus, where some sectors encounter reduced flow momentum, increased incidence angles, or a combination of both. In response to such azimuthal distortions, the compressor flow field redistributes due to the circumferential static pressure gradients that develop. Flow moves from regions of higher static pressure toward regions of lower static pressure, leading to a redistribution of mass flow around the annulus. Regions with local pressure deficits tend to draw in flow from adjacent higher-pressure sectors, while over-pressured regions drive flow outward toward areas of lower pressure, promoting partial rebalancing of the distorted inflow.

This redistribution process reduces localised flow non-uniformities as the distorted flow progresses through subsequent compressor stages, thereby partially mitigating the initial imbalance [64, 99, 108]. Additionally, distortion attenuation occurs across the rotor due to non-uniform aerodynamic work input: the rotor imparts more work in distorted sectors where flow momentum is lower, locally accelerating the flow and further smoothing circumferential variations. Together, flow redistribution and variable work input by the rotor progressively decrease distortion intensity downstream.

However, this flow migration alters local inlet angles at the blade leading edges, changing incidence distributions around the annulus. Elevated incidence in distorted sectors increases local blade loading and aerodynamic work, raising total temperature. Furthermore, blades crossing distortion boundaries experience abrupt shifts in pressure, temperature, and flow angles, which can destabilise the flow and increase the risk of separation and stall onset.

Figure 1.13 illustrates the effects of circumferential distortion on a three-stage compressor. Figure 1.13a shows that the flow coefficient in the distorted region is lower than in the rest of the annulus, indicating a local reduction in velocity and mass flow rate. This reduction results in elevated incidence angles on the blades within the affected sector. As the flow progresses through the compressor, Figure 1.13b demonstrates an attenuation of the pressure deficit from the inlet guide vane (IGV) to the last stator exit, reflecting flow redistribution and partial recovery from the initial distortion. Despite this partial mitigation, the combination of reduced mass flow and increased incidence in distorted regions can compromise compressor stability.

Beyond this, such distortions alter secondary flow structures, including tip leakage vortices and corner separations. As discussed in Section 1.2.2.1, these structures are highly sensitive to changes in flow conditions. A local deficit in pressure, velocity, or mass flow rate can cause the affected region to approach near-stall conditions, exacerbating the behaviour of these structures. This may lead to instabilities driven by separations and tip leakage vortex breakdown. The mechanisms that weaken or strengthen the secondary flow structures are similar to those observed in the case of radial distortions, with the key difference being that the rotor blades perceive the distortion as moving azimuthally. As a result, these structures change in intensity and characteristics cyclically, causing the rotor to experience rapid variations in flow angle, relative velocity, and other associated factors. The combination of these effects tends to weaken the overall robustness of the compressor [61, 98, 151].

It is clear that this distortion also impacts stall inception and stall margin. Specifically, the presence of a circumferential flow distortion reduces stall margin, with instabilities occurring at a higher mass flow rate compared to clean inflow conditions [148].

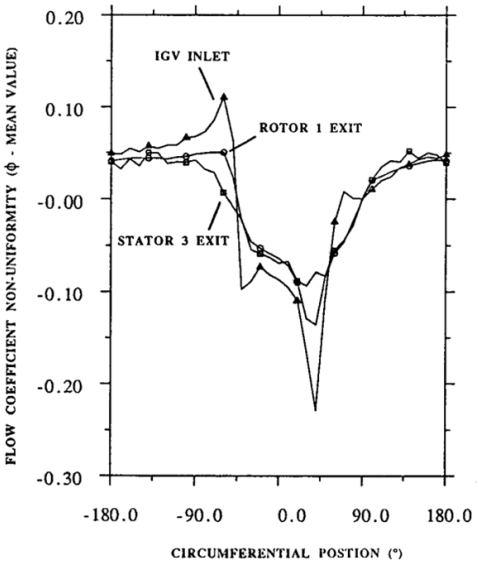

(a) Flow coefficient distribution at the IGV inlet and the stator 1 and stator 3 exits.

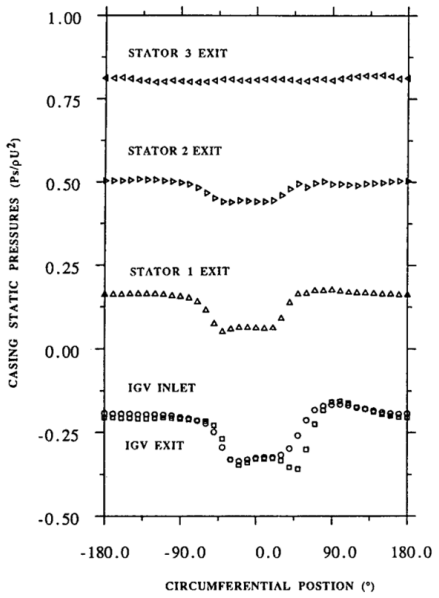

(b) Pressure attenuation across the compressor from the IGV to each stator exit.

Figure 1.13: Effects of azimuthal distortions on the compressor flow distribution [99].

The azimuthal extent and intensity of circumferential distortions are critical factors in determining whether a compressor will eventually experience stall. Severity is typically associated with the deficit of the relevant flow parameter, often total pressure, and its spatial distribution across the annulus. This behaviour has been investigated using distortion grids, where porosity represents the intensity of the distortion. Lower porosity corresponds to more intense distortion, while the angular extension characterises the azimuthal spread of the distortion [5]. Figure 1.14 summarises these findings, showing the stall margin as a function of the angular extent of the distortion grid for different distortion intensities. It is evident that increasing the angular sector of the distortion consistently reduces the stall margin for all distortion intensities. For high-intensity distortions (low porosity), this reduction is more pronounced and continues almost linearly with increasing angular extent, without exhibiting a plateau. In contrast, exceptions arise for lower distortion intensities, which correspond to wider grids (porosity $\geq$ 0.5). In these cases, a plateau in the stall margin is reached at an angular extension of around 90°. This phenomenon, known as the critical angle, was first postulated by Reid [129]. It occurs for a range of low-intensity distortions and states that beyond this critical angle, increasing the angular extent of the grid does not affect the surge margin or the total pressure loss. Both parameters remain constant despite further increases in the distortion's angular spread. It was also found that dividing the total distorted sector into smaller, multiple distorted sectors, while maintaining the same total extension, could improve the stability margin of the compressor, provided each smaller sector remains below the critical threshold [129].

These findings clearly demonstrate that the injected distortion must be both sufficiently wide and intense to significantly degrade the stall margin and trigger the onset of stall.

Once the compressor enters stall conditions, the nature of stall inception can be heavily influenced by the severity and distribution of the circumferential distortion. The intensity and

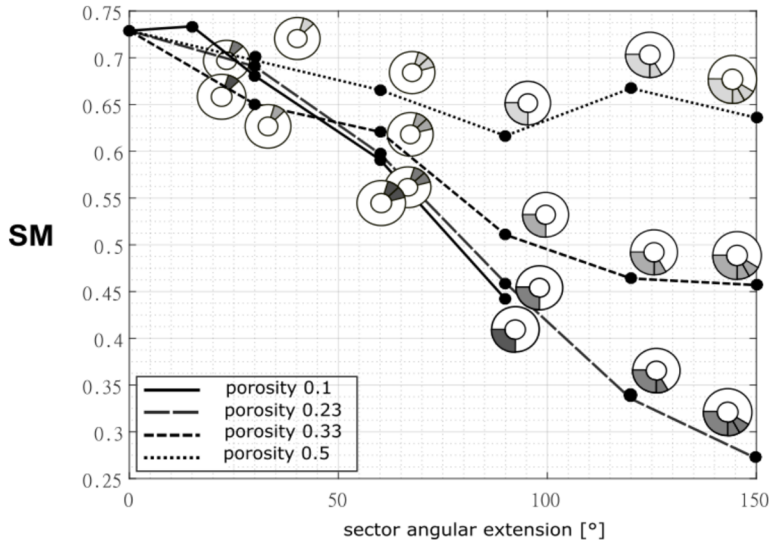

Figure 1.14: Stall margin (SM) as a function of angular extension of the distortion grid [5].

spatial distribution of the distortion determine whether the stall manifests as spike-type or modal-type. High-intensity distortions, typically associated with low porosity grids or narrower grid sectors, tend to favour spike-type stall, which is characterised by localised flow instabilities. In contrast, low-intensity distortions, linked to high porosity grids or wider grid sectors, often lead to modal-type stall, where more global oscillations are observed across the compressor [98, 137, 157]. Thus, at varying inflow conditions, the compressor can also experience a shift from modal-type to spike-type stall. Notably, for weaker distortions, modal oscillations can appear before the onset of spike-type stall, with both types of instabilities possibly occurring concurrently [6]. This complex stall behaviour is influenced by the upstream flow redistribution. At higher distortion intensities, this redistribution can create local flow conditions that exceed normal operating limits, causing secondary flow structures to intensify and destabilise the system. Moreover, the interaction between the distorted inflow and the compressor geometry can modify the velocity triangles and the local work done on the flow, further altering the stall characteristics. The combination of these effects underscores the crucial role that distortion intensity and distribution play in shaping stall behaviour in axial compressors.

In general, circumferential distortions are known to be more critical than radial distortions for compressor operability. A brief example is shown in Figure 1.15, where the surge pressure ratio is highlighted for a clean inflow case and three distorted cases: a 25% hub radial distortion, a 25% tip radial distortion, and a 90° sector circumferential distortion. It is found that the greatest variation in surge pressure ratio occurs for the azimuthal distortion case [129].

To summarise, circumferential distortion affects compressor stability by causing uneven flow distribution across the annulus, resulting in non-uniform blade loading and variations in pressure, velocity, and flow angle. These distortions lead to increased incidence angles and regions of low flow, both of which reduce the stall margin and can trigger earlier stall. The impact of circumferential distortion on compressor performance is highly dependent on its intensity and angular extent, making it a critical factor in maintaining stability and operability, particularly under off-design conditions.

In practical applications, both radial and circumferential distortions must be carefully con-

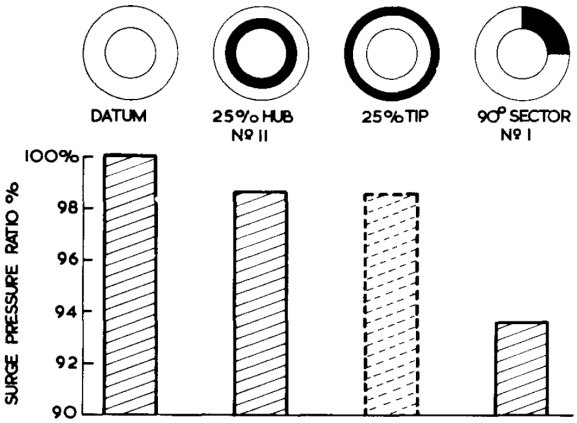

Figure 1.15: Comparative effects of radial and circumferential distortions on the surge pressure ratio [129].

sidered, as they each present unique challenges to compressor stability and efficiency. Often occurring simultaneously in real-world conditions, these distortions create complex, interrelated effects that can significantly reduce compressor operability and stability, especially under off-design conditions. Therefore, understanding their individual effects is a crucial first step toward advancing comprehension of complex flow phenomena in real turbomachinery environments.

1.2.3 Design Considerations

The design of multi-stage high-pressure compressors is a complex, iterative, and multidisciplinary process. It aims to balance aerodynamic performance, structural integrity, and operational robustness. During early design phases, throughflow calculations, meridional solvers, and empirical correlations are typically used to define the annulus and blade geometry, axial velocity distribution, and stage loading. These preliminary analyses establish the compressor flowpath and loading requirements, which are subsequently refined through detailed three-dimensional aerodynamic and mechanical blade design.

A central goal of aerodynamic design is the effective management of blade loading, which represents the aerodynamic work extracted or imparted by each blade row. Blade loading correlates closely with the pressure rise across the blade passage and is influenced by parameters such as the diffusion factor and flow turning angle. Excessive blade loading leads to adverse pressure gradients, boundary layer separation, and shock formation, especially in transonic compressors, reducing performance and stability. Conversely, insufficient loading results in underutilised aerodynamic potential and in reduced compressor efficiency. Therefore, carefully tailoring the spanwise and chordwise distribution of blade loading is crucial to achieving an optimal balance between aerodynamic efficiency and flow stability.

Blade loading capacity primarily depends on blade geometry, notably solidity and aspect ratio, which affect boundary layer behavior, wake dynamics, and secondary flow structures. Historically, from the 1950s to the 1980s, axial compressor designs trended toward increased solidity and decreased aspect ratio by lengthening blade chords. This approach improved performance by enabling higher pressure ratios and efficiency as well as enhanced compressor stability by reducing blade aspect ratio, thereby lowering susceptibility to vibrations, flow

instabilities, and secondary flow effects [29]. Figure 1.16 illustrates these design trends alongside associated gains in aerodynamic loading and pressure ratio [165].

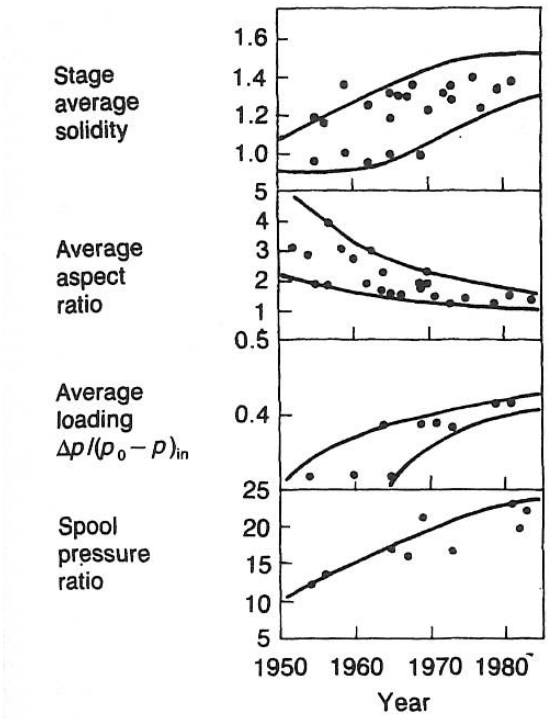

Figure 1.16: Compressor geometry and performance trends in GE compressors, 1950s-1980s [165].

In contrast, recent aero-engine developments driven largely by environmental and integration objectives have prompted a shift toward more compact, lighter, and aerodynamically integrated propulsion systems. This new paradigm favors higher aspect ratio and lower solidity blades in multi-stage compressors. Such designs reduce engine length and weight, improve integration and rotor aerodynamics, and decrease secondary losses relative influence. However, these benefits come at the cost of increased sensitivity to inlet distortion, greater vulnerability to tip clearance flows, and heightened susceptibility to aeroelastic blade excitations.

To better understand these trade-offs, it is essential to analyse the effects of aspect ratio and solidity variations in modern compressors.

Aspect ratio, defined as the blade height to chord length ratio, strongly influences three-dimensional flow phenomena such as secondary flows and tip leakage vortices. Lower aspect ratio blades tend to have higher Reynolds numbers based on chord length, which improves boundary layer stability. They also benefit from reduced relative tip clearance with respect to chord length, mitigating tip leakage intensity and its detrimental effects on operability. However, the longer chords exacerbate secondary flow losses and corner separations, increasing aerodynamic losses and limiting maximum achievable loading [158]. They also pose mechanical challenges, including increased susceptibility to foreign object damage due to thinner leading edges and more complex vibration and aeroelastic behavior. Conversely, higher aspect ratio blades promote more uniform spanwise flow and reduced secondary flow losses, enhancing aerodynamic efficiency and stability.

Solidity, defined as the ratio of blade chord to blade pitch, governs the blade loading distribution and degree of flow diffusion through the blade row. Increasing solidity reduces the aerodynamic load per blade, improving flow attachment and delaying boundary layer separation. This effect enhances stall margin and tolerance to inlet distortion. However, higher solidity increases profile losses due to a larger wetted surface area and greater structural mass, which can negatively impact efficiency and manufacturing costs. Conversely, lower solidity reduces these losses but may compromise operability under distorted inflow conditions [77, 140].

In summary, the interplay between aspect ratio and solidity defines a fundamental design trade-off. Lower aspect ratio combined with higher solidity generally improves robustness against inlet distortion and enhances operability by stabilizing flow and increasing stall margin. In contrast, higher aspect ratio and lower solidity promote aerodynamic efficiency, reduce weight, and enable more compact integration but require careful management of stability and mechanical challenges.

1.3 Numerical Modelling of Compressors under Inlet Distortion

1.3.1 Challenges in Numerical Modelling of Inlet Distortions

It has been presented how inlet distortions can significantly degrade the operability and performance of axial compressors in aero-engines. Accurately predicting these effects remains a central challenge in compressor research. While experimental studies have long been the primary source of distortion data due to their ability to explore a wide operating range rapidly and provide valuable insights [65, 100, 130], advances in computational power have increasingly enabled numerical simulations to complement and extend experimental findings through detailed flow-field analysis.

However, simulating compressors under distorted inlet conditions presents substantial challenges. Compressor flow is inherently three-dimensional and unsteady, and non-uniform inflow further exacerbates its complexity. Even nominally steady distortions, such as radial profiles, can trigger transient, azimuthally extensive instabilities near critical operating conditions. These phenomena elude steady-state methods and cannot be adequately captured using sector-based models or simplified computational domains.

Accurate prediction therefore requires high-fidelity numerical techniques and significant computational resources. In particular, unsteady full-annulus CFD simulations are often essential to resolve time-dependent interactions between rotating blades and distorted inflow, even when the imposed distortion is steady. Such simulations enable localised, non-axisymmetric evaluation of the flow response and capture the evolution of distortion effects across multiple stages. However, their computational cost remains a major constraint, motivating continued efforts to balance simulation fidelity and computational feasibility in compressor modelling and design under inlet distortion.

The next section reviews current modelling strategies developed to meet these challenges, highlighting their respective advantages and limitations.

1.3.2 Overview of Existing Modelling Approaches

A wide range of numerical strategies have been developed to simulate compressor aerodynamics and are adapted to the investigation of distorted inflow conditions. These methods

can be broadly classified according to their fidelity and associated computational cost.

High-fidelity approaches remain the benchmark for accurately capturing the complex, time-dependent interactions between rotating blade rows and non-uniform inflow. They resolve transient flow structures, modal instabilities, and the circumferential transport of low-momentum fluid, all critical to understanding compressor behaviour under inlet distortion. A key distinction among these methods lies in the turbulence length scales resolved directly versus those modelled.

Direct Numerical Simulation (DNS) resolves the complete spectrum of turbulent scales down to the smallest dissipative structures, providing the most detailed representation of turbulence. However, the extreme computational requirements render DNS impractical for industrial applications; its use is currently still limited to academic studies on small computational domains.

Large Eddy Simulation (LES) resolves the large, energy-containing eddies while modelling the smaller subgrid-scale motions, offering a compromise between accuracy and computational cost. Despite this, LES remains expensive for full-scale industrial applications. Several studies have applied LES and derived variants, such as Zonal Detached Eddy Simulation (ZDES) and Delayed Detached Eddy Simulation (DDES), to investigate distortion effects. However these studies are typically restricted to reduced configurations such as fan rotors or fan-intake interactions [103, 118], or intake flows dynamic [20, 111].

Unsteady Reynolds-Averaged Navier-Stokes (URANS) methods model the entire turbulence spectrum without explicitly resolving turbulent scales, substantially reducing computational cost. Consequently, URANS and hybrid URANS-LES approaches are commonly used in both industry and applied research, offering a practical balance of fidelity and efficiency across a wide range of aerodynamic investigations [102, 144]. Numerous studies have employed URANS-based methods to analyse inlet distortion, particularly in fan-intake systems, fan rotors, and outlet guide vanes (OGVs) [57, 89, 171], as well as for intake flow control, boundary layer ingestion [54, 107], or even single-stage and multi-stage compressors [90, 154, 162].

The choice of method ultimately depends on the required accuracy and available computational resources. However, even the less costly high-fidelity approaches, such as URANS, remain computationally demanding for large-scale configurations, including full multi-stage compressors. Consequently, only a very limited number of numerical studies have addressed inlet distortion in full multi-stage axial compressors, with most investigations confined to simplified geometries or reduced-stage models. This highlights that despite recent advances, full-machine simulations under distorted inflow remain largely prohibitive.

At the other end of the spectrum, lower-fidelity approaches offer significant reductions in computational cost and are often employed in preliminary design or parametric studies. These methods rely on simplifying assumptions to approximate the overall aerodynamic behaviour without resolving detailed unsteady flow structures. Common strategies include the parallel compressor model, actuator disk methods, throughflow calculations, and Body-Force models.

The parallel compressor model divides the compressor annulus into independent sectors, each subjected to a different but uniform inlet condition [108, 123]. It enables first-order estimation of compressor performance under circumferential distortion and has been widely used due to its simplicity. However, it neglects interactions between sectors and unsteady flow phenomena, limiting its predictive reliability in complex distortion patterns, such as

combined radial-circumferential inflow non-uniformities [151]. While useful for initial assessments, its strong simplifying assumptions reduce applicability in modern compressor analysis where spatial and temporal variations are critical.

Actuator disk models approximate blade rows as momentum sources distributed over thin surfaces [18, 70, 81], often based on the Rankine-Froude Blade-Element theory [120, 149]. They enable rapid estimation of stagewise pressure rise and flow deviation, useful for preliminary design and system-level studies. Various implementations exist, including adaptive approaches based on local conditions, applied through either boundary conditions or source terms [149]. A key limitation is their dependence on reference blade data, typically from 2D high-fidelity simulations, which affects accuracy under off-design or distorted inflow. Furthermore, actuator disk models do not resolve intra-passage flow phenomena such as blockage, choking, or shocks, and may suffer convergence issues in highly loaded stages. Their inherent assumptions also limit the ability to capture unsteady and non-uniform features associated with inlet distortion.

A different approach was introduced by Marble in 1964 [105], proposing an axisymmetric framework that assumes an infinite number of blades and incorporates their effects through Body-Forces in the equations of motion. He developed thermodynamic relationships linking blade forces with total enthalpy changes and entropy generation within blade passages. From this idea, throughflow models were developed.

Two-dimensional throughflow models solve the axisymmetric Euler or Navier-Stokes equations in the meridional plane to estimate mean flow properties through compressor stages. These models improved from simpler streamline curvature (SLC) methods [34, 49] to employing time-marching techniques [150], enabling better handling of unsteady and viscous effects. Throughflow solvers efficiently capture global performance parameters such as flow turning and pressure rise at significantly reduced computational cost. However, they rely heavily on empirical correlations to account for blade deviation, viscous losses, and aerodynamic blockage, limiting predictive accuracy under complex flow conditions [4, 48]. Importantly, traditional axisymmetric throughflow approaches average circumferential variations and thus cannot resolve non-uniformities or transient circumferential flow features induced by inlet distortions.

To overcome axisymmetric limitations, three-dimensional throughflow approaches were developed. These couple a three-dimensional CFD solver in blade-free volumes with simplified blade row models, such as SLC, within blade passages [45, 66]. Blade effects are introduced as source terms, obtained from blade row models applied on multiple sectors to reconstruct the full annulus [66]. This coupling captures three-dimensional flow phenomena such as instabilities and distortion responses with reasonable computational cost. Despite this, blade forces remain semi-empirical, depending on correlations and assumptions from simplified blade row models, limiting the ability to dynamically respond to changing flow conditions [45, 66].

Body-Force models represent a further evolution by explicitly formulating blade forces as source terms within the governing equations dependent directly on the local flow field [17, 56]. Unlike 3D throughflow methods, where blade forces derive from empirical models for deviation and losses, Body-Force models compute deviation and loss dynamically. Early work by Gong [56] decomposed blade forces into flow-turning and loss components calibrated with empirical data, later refined by other authors [67, 125]. These models improve physical consistency and enable more accurate prediction of complex phenomena such as stall inception and distorted inflow response while maintaining manageable computational cost. Calibration is

typically needed and requires high-fidelity CFD or experimental data, with recent formulations reducing empirical dependence and increasing robustness [67, 155].

Thus, Body-Force models offer the capability to dynamically model blade forces based on local flow conditions, capture complex and non-axisymmetric flow features, and maintain low computational cost. Consequently, they provide an effective compromise between accuracy and efficiency for inlet distortion studies on complex components such as multi-stage high-pressure axial compressors.

1.3.3 Body-Force Modelling: Theory, Applications and Limitations

1.3.3.1 Generalities

As introduced in the preceding section, Body-Force models are categorised as three-dimensional non-axisymmetric throughflow methods. These models simulate the aerodynamic influence of a bladed row by introducing additional source terms into the governing equations of fluid motion, specifically the momentum and energy equations, within the Euler (inviscid) or Navier-Stokes (viscous) frameworks. This approach enables the aerodynamic effects of the blades to be captured without explicitly resolving the detailed blade geometry.

As anticipated, the foundational formulation for Body-Force modelling was developed by Marble [105]. He proposed two orthogonal force components: one normal to the local relative flow direction, $\vec{f}_n$, such that $\vec{f}_n \cdot \vec{W} = 0$, representing the turning effect imparted by the blade row; and one parallel and opposite to the flow, $\vec{f}_p$, such that $\vec{f}_p \times \vec{W} = 0$, accounting for aerodynamic losses manifested as entropy production. These two components are defined in Equation (1.8).

$$\begin{cases} f_n(x,r) = \dfrac{V_m}{r}\dfrac{\partial(rV_\theta)}{\partial m} \\ f_p(x,r) = -\dfrac{T_s V_m}{W}\dfrac{\partial s}{\partial m} \end{cases} \tag{1.8}$$

Here, m denotes the meridional streamline coordinate; r indicates the radial position; V_m and V_θ are the meridional and circumferential velocity components; W is the relative velocity magnitude; T_s the static temperature; and s the entropy per unit mass.

Marble's original formulation assumes axisymmetry, implying that the forces are uniformly distributed in the circumferential direction. While this simplification facilitates analytical treatment, it limits the model's ability to capture azimuthal flow distortions commonly encountered in realistic turbomachinery operating conditions.

To overcome this limitation, a significant step toward a three-dimensional and non-axisymmetric formulation was made by Gong [56], who extended Marble's work by considering the flow as locally axisymmetric within infinitesimal blade sectors. This method allowed the modelling of azimuthal flow variations and their interaction with blade forces, enabling more accurate simulations in the presence of inlet distortions or flow non-uniformities.

The general mathematical framework describing these models is based on the Reynolds-Averaged Navier-Stokes (RANS) equations, incorporating Body-Force source terms. This formulation is succinctly presented in Equation (1.9).

$$\frac{\partial}{\partial t}\begin{pmatrix}\rho\\ \rho\vec{v}\\ \rho e_t\end{pmatrix} + \operatorname{div}\begin{pmatrix}\rho\vec{v}^T\\ \rho\vec{v}\otimes\vec{v}+p\mathbf{I}-\vec{\tau}\\ \rho e_t\vec{v}+p\vec{v}-\vec{\tau}\cdot\vec{v}+\vec{q}\end{pmatrix} = \begin{pmatrix}S_\rho\\ \vec{S}_{\rho\vec{v}}\\ S_{\rho e_t}\end{pmatrix} = \begin{pmatrix}0\\ \rho\vec{f}\\ \rho r\omega f_\theta\end{pmatrix} \tag{1.9}$$

In Equation (1.9), ρ is the fluid density; $\vec{v}$ the velocity vector; e_t the total energy per unit mass; p the pressure; $\vec{\tau}$ the viscous stress tensor; $\vec{q}$ the heat flux vector; and $\mathbf{I}$ the identity tensor. The left-hand side expresses the Navier-Stokes equations in conservative form, encompassing mass, momentum, and energy conservation through temporal and spatial transport mechanisms. The source terms $(S_\rho, \vec{S}_{\rho\vec{v}}, S_{\rho e_t})^T$ model the aerodynamic effects of the blade row. In its baseline formulation $(0, \rho\vec{f}, \rho r\omega f_\theta)^T$, the variable $\vec{f} = (f_x, f_r, f_\theta)^T$ denotes the Body-Force vector components per unit mass. Notably, only the f_θ component contributes to the energy equation, as it is the only component performing mechanical work on the flow [105]. These forces encapsulate effects such as blade turning and loss generation, and they may depend on local flow variables, blade geometry, and calibrated coefficients when required.

The formulation of Body-Force source terms varies according to the modelling strategy adopted. In turbomachinery applications, these source terms are typically derived from circumferentially averaged flow fields. Two principal methodologies are commonly employed to extract forces from blade calculations. The first methodology consists of extracting volumetric force distributions directly from high-fidelity computational fluid dynamics simulations, which are subsequently circumferentially averaged to yield axisymmetric force representations. The second methodology applies Marble's equations [105] to circumferentially averaged two-dimensional CFD data or to one-dimensional radial profiles redistributed azimuthally, thus providing a consistent framework for deriving Body-Force source terms.

The modelling of distributed source terms depends on the role attributed to the blade forces within the simulation framework. One approach employs blade forces to directly impose specified flow deviation. In this context, the target flow deviation and losses are typically obtained from empirical correlations or calibration coefficients and enforced via restoring forces. An iterative feedback mechanism is often implemented to adjust the Body-Force terms until the desired flow behavior is attained.

Alternatively, blade forces may be modelled locally without directly prescribing the resulting flow fields. This approach involves constructing local force expressions either by analogy with canonical reference flows or by extraction from CFD databases. When derived from CFD data, local force distributions may be interpolated or predicted using machine learning algorithms trained on relevant CFD solutions [121].

This work primarily focuses on models that define blade forces locally by analogy with simplified aerodynamic flows, without explicitly prescribing the resulting flow field. Such models require limited input data, are relatively straightforward to implement, and depend only on basic geometric and flow information. Notable contributions in this area include the works of Gong [56], Hall [67], Thollet [155], Peters [125], and others.

Dosne [42] offers a detailed review of these models and groups them based on a few core principles that have been gradually refined over time. Gong's early model [56] includes two contributions to the normal force: one proportional to flow deviation and another based on the pressure gradient in a staggered channel. This formulation represents blade forces and successfully captures compressor performance under inlet distortion. However, it relied on empirical calibration and originally neglected radial flow and blade lean effects. Hall [67]

proposed an analytical formulation for the normal force based on thin-airfoil theory, linking flow deviation to an effective incidence angle. This model naturally incorporates radial effects but requires corrections to account for compressibility and viscous losses. Building on both approaches, Thollet [155] adopted Hall's expression for the normal force, augmented by a compressibility correction, and formulated the parallel force with an off-design term expressed as a function of the squared flow deviation. Additional corrections for blockage and compressibility were introduced to improve the robustness of the model.

These models form a progression of increasingly sophisticated formulations that strike a balance between physical fidelity, computational efficiency, and ease of implementation. Their combination of practicality and accuracy makes them particularly suitable for simulating non-uniform inflows in turbomachinery applications.

From a computational standpoint, Body-Force models offer two principal advantages. The first is a substantial simplification of the mesh topology, along with a reduction in the total number of computational cells, owing to the absence of explicit blade geometry within the domain. The fine-resolution mesh typically required to capture boundary layer development along blade surfaces is no longer necessary, resulting in lighter and more tractable computational grids. This advantage becomes increasingly relevant as the scale and complexity of the configuration increase, particularly in multi-stage turbomachinery applications.

The second advantage lies in the capability to capture steady distortion effects through steady-state simulations. This is enabled by the local formulation of the source terms and the quasi-steady assumption inherent to Body-Force approaches. Specifically, this assumption presumes that circumferential perturbations evolve on a time scale significantly longer than the characteristic aerodynamic time scale of the model, such as the blade passing or convective time scales. As a result, high-frequency phenomena such as rotor and stator interactions are filtered out, while lower-frequency effects associated with distortions having a circumferential length scale larger than one blade pitch can still be resolved [62]. As discussed in Section 1.3.1, conventional CFD approaches require unsteady simulations to capture such distortion-driven phenomena, leading to substantially higher computational costs. In this context, Body-Force models represent a highly attractive alternative for the analysis of steady distortion effects in complex engine architectures. It should be noted that the study of unsteady distortions can also benefit from the Body-Force approach, as the less stringent mesh requirements and the ability to decouple the time step from the wake spatial resolution make them more efficient than fully blade-resolved simulations.

In the remainder of this work, the focus will be placed on the so-called Hall-Thollet model, based on the normal-parallel force formulation. This formulation remains one of the most complete and versatile currently available, requiring only limited geometric input and no prior CFD data. Its analytical and explicit structure, combined with minimal calibration and broad applicability, makes it particularly well-suited for the objectives of this study.

1.3.3.2 The Hall-Thollet Model

The Hall-Thollet Body-Force formulation is here presented in its normal-parallel force decomposition framework.

The equation system introduced in Equation (1.9) can be expanded for this specific formulation, as shown in Equation (1.10).

$$\frac{\partial}{\partial t}\begin{pmatrix}\rho\\ \rho\vec{v}\\ \rho e_t\end{pmatrix} + \text{div}\begin{pmatrix}\rho\vec{v}^T\\ \rho\vec{v}\otimes\vec{v}+p\mathbf{I}-\vec{\tau}\\ \rho e_t\vec{v}+p\vec{v}-\vec{\tau}\cdot\vec{v}+\vec{q}\end{pmatrix} = \begin{pmatrix}S_b\\ S_b\vec{v}+\rho\vec{f}\\ S_b h_t+\rho r\omega f_\theta\end{pmatrix} \tag{1.10}$$

A key distinction with respect to the more general formulation presented in Section 1.3.3.1 is the introduction of the blockage source term S_b. This term, originally derived from the work of Kottapalli [84], accounts for the portion of the blade passage physically occupied by the blade geometry. It is obtained by comparing the azimuthally integrated conservation equations of a bladed configuration and those of an equivalent unbladed Body-Force configuration. The blockage source term S_b, along with the associated local blockage factor b, are defined in Equation (1.11).

$$S_b = \frac{1}{b}\left(\rho\vec{v}\cdot\overrightarrow{\text{grad}}(b)\right) \qquad \text{where} \qquad b = 1-\frac{t}{s} = \frac{\theta_{ps}-\theta_{ss}}{2\pi/N_{blades}} \tag{1.11}$$

The blockage factor b is defined as the fraction of the blade passage not occupied by the blade material. It is a local geometric quantity that depends on the blade tangential thickness t and the blade pitch $s = 2\pi/N_{blades}$, where N_{blades} is the number of blades. Alternatively, b can be expressed in terms of the azimuthal extent between the suction side of one blade and the pressure side of the next, divided by the pitch, as shown in Equation (1.11) as well. The metal blockage definition is schematically presented in Figure 1.17a.

The corresponding source term S_b is also defined locally and depends on the quantity $\rho\vec{v}$, which denotes the local mass flux vector. This term is introduced directly into the mass conservation equation, thereby modifying the mass balance within the computational domain. In particular, its presence may lead to local non-conservation of mass in regions where blade thickness varies abruptly, such as at the leading and trailing edges of blades. In such regions, additional mesh refinement is typically required to prevent spurious mass flow losses. Due to its derivation, the term S_b also appears in the momentum and energy conservation equations, as shown in Equation (1.10) and extensively demonstrated in Thollet's work [155].



(a) Metal blockage definition [155]. **(b)** Normal/parallel force decomposition [155].

Figure 1.17: Schematics of (a) the metal blockage definition and (b) the normal/parallel force decomposition in the Hall-Thollet model [155].

The specific definition of the blade force vector $\vec{f}$ is what distinguishes one Body-Force model from another. In the adopted Hall-Thollet formulation, the blade forces are defined lo-

cally and are decomposed into two components: a normal force f_n, which acts perpendicular to the local flow velocity and accounts for flow turning, and a parallel force f_p, which acts along the flow direction but in the opposite sense, representing entropy production and aerodynamic losses. Moreover, the model relies on geometrical data of the blade camber surface through means of its normal vector distribution $\vec{n} = (n_x, n_r, n_\theta)$. The decomposition and orientation of the two force components of the model are schematically presented in Figure 1.17b.

The normal force component formulation is defined in Equation (1.12).

$$f_n = \frac{W^2}{2sb|n_\theta|} \cdot 2\pi\delta K_{Mach} \tag{1.12}$$

Here, W is the relative velocity magnitude, δ is the local three-dimensional flow deviation angle, and K_{Mach} is a compressibility correction factor based on the Prandtl-Glauert and Ackeret relations, as defined in Equation (1.13) and presented in Figure 1.18.

$$K_{Mach} = \begin{cases} \min\left(\frac{1}{\sqrt{1-M_r^2}}, 3\right) & \text{if } M_r < 1 \\ \min\left(\frac{4}{2\pi\sqrt{M_r^2-1}}, 3\right) & \text{if } M_r > 1 \end{cases} \tag{1.13}$$

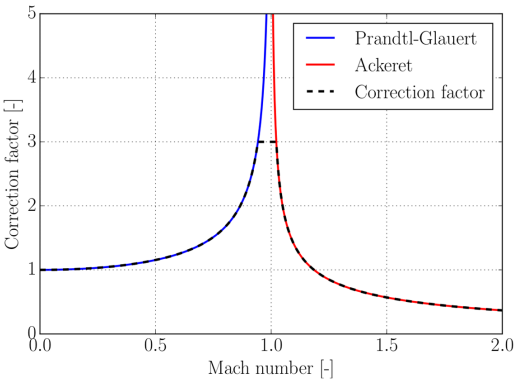

Figure 1.18: K_{Mach} schematic [155].

The inclusion of compressibility correction and blockage effects enabled Thollet to improve the predictive accuracy of the model across a wide range of operating conditions, including both high and low Mach number regimes. These enhancements also allowed for a more accurate estimation of the choke mass flow rate.

The normal force expression given in Equation (1.12) is directly analogous to the lift coefficient $C_L = 2\pi\alpha$, where α denotes the angle of attack. This coefficient originates from the Kutta-Joukowski theorem and is applicable to an isolated, two-dimensional airfoil in an ideal, inviscid, and incompressible flow. In the present blade force formulation, the term $2\pi\delta$ establishes the analogy to this lift coefficient, thereby situating the Hall-Thollet model within the class of Body-Force formulations that utilise aerodynamic analogies based on simplified reference flows.

The parallel force component formulation is presented in Equation (1.14).

$$f_p = \frac{W^2}{2sb|n_\theta|} \left[2C_f + 2\pi K_{Mach}(\delta - \delta^{\eta_{\max}})^2\right] \tag{1.14}$$

This force consists of two distinct contributions. The first term, which is proportional to the skin-friction coefficient C_f, accounts for nominal viscous aerodynamic losses. It is derived by analogy with the friction coefficient of a flat plate in turbulent flow. The coefficient C_f

is modelled as a function of the local chordwise Reynolds number Re_x, using the empirical relation $C_f = 0.00592 Re_x^{-0.2}$, which is derived from the fully-turbulent boundary layer on a flat plate.

The second term accounts for off-design aerodynamic losses and is inspired by the empirical drag formulation for two-dimensional airfoils, where the drag coefficient is commonly expressed as $C_D = C_{D_0} + KC_L^2$. As noted earlier, the lift coefficient in thin airfoil theory is given by $C_L = 2\pi\delta$, where δ denotes the flow deviation angle.

In the present context, the off-design losses are modelled as a quadratic penalty based on the difference between the local deviation δ and its optimal value $\delta^{\eta_{\max}}$, which corresponds to the flow deviation angle at the point of maximum efficiency. The quadratic term $(\delta - \delta^{\eta_{\max}})^2$ is therefore introduced to model the increase in aerodynamic losses as the flow turning departs from this optimal value.

The value of $\delta^{\eta_{\max}}$ is extracted from a single Body-Force simulation at the peak efficiency operating point and remains fixed for all other operating conditions.

As demonstrated by the aerodynamic analogies underlying its formulation, the predictive capabilities of the Hall-Thollet model depend critically on the validity of the adopted correlations and assumptions. Consequently, the accuracy of this model is contingent upon the applicability of these formulations to the configuration under investigation.

1.3.3.3 Investigation of Inlet Distortion with Body-Force Models

Numerous studies have demonstrated the effectiveness of the Hall-Thollet family of Body-Force models in capturing the effects of inlet distortion on turbomachinery operation.

Gong [56] proved the capabilities of his model on a single-stage high-speed compressor subjected to total pressure and total temperature inlet distortions. The model successfully captured key phenomena such as choking and shock wave formation. Figure 1.19 illustrates the axial velocity field at different stations across the compressor when a 120° total pressure distortion is applied far upstream. The predicted flow redistribution due to the inlet distortion, as well as the downstream transmission of the distorted pattern through the bladed rows, agreed well with reference results. A key limitation of this methodology is the reliance on calibration coefficients derived from empirical correlations found in the literature, with fixed values for these coefficients originally suggested by Gong [56].

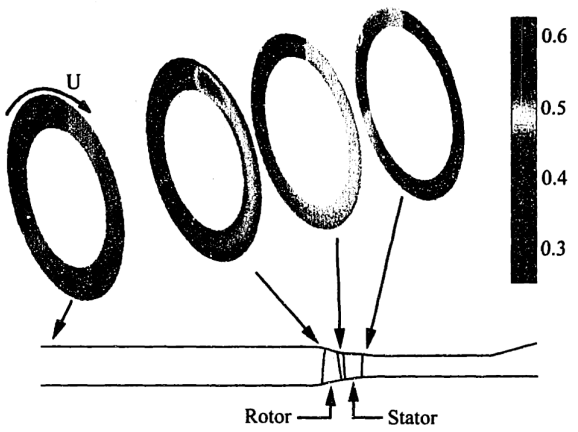

Figure 1.19: Axial velocity contours in a compressor subject to a 120° total pressure distortion [56].

Hall [67], in his original research, investigated the application of his throughflow model to study boundary layer ingestion effects in civil aircraft propulsors. His formulation, composed only of the normal force responsible for flow turning, was coupled with an inviscid solver. The model captured large-scale flow features in a pitchwise-averaged sense, in agreement with reference calculations. It was able to reproduce stagnation enthalpy rise, radial loading distribution, flow redistribution, and velocity non-uniformities. However, the model remained highly simplified, lacking losses modelling, which significantly limited its predictive capabilities for operability and performance estimation.

Thollet [155, 156] applied his model to study fan-intake aerodynamic interactions and boundary layer ingestion. In both cases, the normal-parallel force formulation proved effective in predicting the impact of distortion on the fan flow field, particularly the loss in stage efficiency. The model was also used to perform parametric studies on the characteristics of the injected BLI distortion, demonstrating flexibility and robustness. Figure 1.20 shows the results downstream of the fan rotor in terms of work coefficient and mass flow rate when a stratified BLI pattern is applied. The model captures both the global flow redistribution and the local non-axisymmetric features of the distorted flow. However, the simplified treatment of secondary flows and loss mechanisms reduces its accuracy under highly distorted conditions or close to stall.

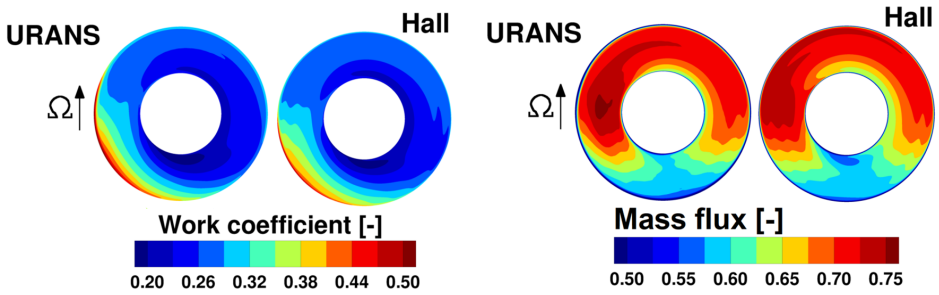

Figure 1.20: Work coefficient (left) and mass flow rate (right) downstream of the fan rotor under stratified BLI distortion [155].

Among the studies building upon Thollet's developments to investigate distortion effects, those of Godard [55], Awes-Cheynis [3] and Hill et al. [74, 75] are of particular interest.

Godard continued the fan-intake interaction work initiated by Thollet, extending the analysis to circumferential inlet distortions. He demonstrated that the Body-Force model could reproduce the stall margin reduction observed in URANS simulations with good fidelity. While the model captured trends in stagnation pressure and isentropic efficiency variations, it systematically underpredicted the stagnation temperature rise, leading to an overestimation of isentropic efficiency. These discrepancies were attributed to limitations in modelling inter-blade flow physics. A corrective coefficient was introduced to partially mitigate this, and a broad parametric study was conducted to identify design trends and blade configurations that improve operability under distorted inflow. Nevertheless, the model still lacks a comprehensive treatment of secondary and shock-related phenomena. Figure 1.21 illustrates the results for a BLI-type distortion, showing good agreement between the recalibrated Body-Force model and blade-resolved URANS simulations.

Awes-Cheynis [3] proposed an Unsteady Body-Force Methodology (UBFM) based on the Hall-Thollet framework, including a calibrated loss formulation derived from reference RANS computations. The approach provides a computationally efficient alternative to full-annulus

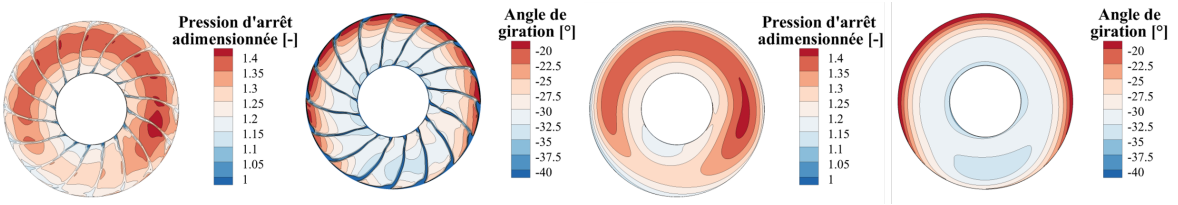

Figure 1.21: Total pressure and giration angle distributions downstream of the fan rotor under boundary layer ingestion (BLI). Bladed simulation (left) and recalibrated Body-Force (right) [55].

URANS, while retaining the ability to capture key phenomena such as rotating stall inception and throttle margin degradation due to unsteady inlet vortices. However, as stated by the author, the methodology tends to underpredict some unsteady flow structures, particularly stall cell patterns, and requires further validation across different architectures and distortion scenarios to fully assess its generalizability.

Hill and Defoe [74, 75] extended the Hall-Thollet approach by incorporating additional compressibility corrections, a camber correction replacing the mass flow blocage term, and a loss model to better capture spanwise work input and choking effects in transonic compressors. Their model accurately predicted both global performance parameters and localised flow features under a wide range of inlet distortion conditions. Notably, it captured nearly linear scaling of inlet blade flow angle variations with distortion intensity, enabling efficient estimation of distortion impacts on operability. Despite these strengths, the model still requires operating-point-specific calibration and lacks an integrated treatment of viscous losses and blockage effects. Furthermore, its applicability to configurations beyond the one studied, a single-stage compressor, remains to be demonstrated.

Additional developments by Guo [63, 64], Magrini [104], and Dosne [42] have further demonstrated the applicability of this category of Body-Force models to multiple configurations, challenging inlet distortions, and diverse modelling objectives. Collectively, these studies have demonstrated the potential of such formulations to address a wide range of aerodynamic and integration challenges, particularly within the context of turbomachinery design and performance prediction.

Another significant contribution is that of Righi [131]. In this PhD work, an unsteady Body-Force methodology is developed and validated for the prediction of stall and surge in low-speed multi-stage compressors, including a dedicated modelling approach for reverse flow [134]. Compared to the previously discussed studies, the formulation relies primarily on empirical correlations to represent the blade forces. A comprehensive set of correlations is presented and assessed across several low-speed configurations, with additional correlations sourced from industrial practice employed in some cases to improve agreement with experimental data. When extended to high-speed compressors, the initial formulation showed limitations in capturing the machine behaviour, particularly under transonic operating conditions. However, more recent work by the same author [132, 133] demonstrates that, with suitable modifications, the approach can be successfully applied to such regimes, although the details of the updated correlations are not disclosed due to industrial confidentiality. Overall, the model proves effective in analysing compressor near-stall behaviour, with a particular emphasis on predicting performance characteristics. Its application to the analysis of detailed local flow, distortion effects and transfer mechanisms, and the sensitivity of compressor robustness to blade geometric variations within the machine, remains to be addressed.

Despite the progress made in this area, several limitations are consistently observed across these works. First, validation has largely been restricted to configurations that differ from those of interest here, such as isolated fan rotors, fan-intake assemblies, fan-IGV or fan-OGV setups, and single-stage compressors. Consequently, the applicability of this class of Body-Force models to more complex architectures, including multi-stage machinery with strong blade-row interactions and highly loaded configurations, remains insufficiently explored. In particular, even when multi-stage machinery is investigated, the effects of inlet distortion on high-pressure compressors have received comparatively limited attention within this modelling framework. Second, to achieve accuracy in complex configurations, these models almost always rely either on empirical correlations, dependent on case-by-case corrective coefficients and often undisclosed formulations, or on calibration processes typically tailored to each specic operating point or speed line and often relying on custom, non-transferable procedures. To date, no simple calibration process that is unique across varying operating points, inlet conditions, and iso-speed lines has been established, with each case requiring a dedicated formulation. Finally, most existing models do not incorporate correction mechanisms to account for secondary ow structures or shock-induced phenomena, which have been proven to be essential for accurate performance predictions.

These limitations continue to restrict the predictive capabilities, robustness, and generalizability of Body-Force models when applied to realistic engine environments. Addressing these challenges constitutes one of the principal motivations for the present work.

Conclusion

This chapter has reviewed the fundamentals of high-pressure compressors and the challenges posed by inlet flow distortion, focusing on existing modelling approaches used to investigate these effects. Body-Force models, particularly the Hall-Thollet model, offer a favorable balance between accuracy and computational efficiency. However, these models are constrained by simplifying assumptions, especially when applied to complex, multi-stage compressor configurations. They often require case-specific calibrations and fail to fully capture key secondary flow phenomena.

The literature underscores a clear need for more efficient, adaptable, and robust tools to study the impact of inlet distortion on compressor performance. This research aims to address these gaps by developing an enhanced Body-Force model capable of better capturing the effects of inlet distortion across multiple compressor stages.

The following chapter will lay the first foundation towards this objective, by presenting the test cases selected for model validation, along with their design characteristics and corresponding experimental data. The computational framework used for both the blade-resolved and Body-Force simulations will also be outlined, setting the stage for further model development and analysis.

CHAPTER 2

TEST CASES AND NUMERICAL FRAMEWORK

This chapter introduces the two test cases examined throughout this thesis: the CREATE and the IHPC high-pressure compressors. Each case is presented with a concise overview of its design characteristics and the associated experimental datasets, which provide reference data for subsequent validation. The chapter then outlines the computational framework employed in the numerical simulations, including the governing equations, the CFD solver, and the key numerical parameters. Special emphasis is placed on the implementation of blade-resolved and Body-Force modelling approaches, highlighting their fundamental differences. Finally, the chapter details the post-processing procedures applied to both experimental and numerical data to establish a consistent basis for the comparative analyses performed in the following chapters.

Contents

2.1 Compressor Test Cases Overview **44**
2.1.1 The CREATE Compressor Test Case 46
2.1.1.1 Overview of the CREATE Compressor 46
2.1.1.2 Available Experimental Data 47
2.1.2 The IHPC Compressor Test Case 49
2.1.2.1 Overview of the IHPC Compressor 49
2.1.2.2 Available Experimental Data 50
2.2 Numerical Framework and Methodology **51**
2.2.1 The elsA CFD Solver 51
2.2.2 Numerical Parameters 54
2.2.3 Blade-Resolved Simulation Framework 55
2.2.3.1 Mesh Characteristics of Blade-Resolved Calculations . . . 55
2.2.3.2 Boundary Conditions of Blade-Resolved Calculations . . . 58
2.2.4 Body-Force Simulation Framework 58
2.2.4.1 Mesh Characteristics of Body-Force Calculations 58
2.2.4.2 Boundary Conditions of Body-Force Calculations 59
2.2.4.3 Body-Force Co-Processing Module 60
2.3 Data Post-Processing **61**
2.3.1 Post-Processing of Experimental Data 61
2.3.2 Post-Processing of Numerical Data 65
Conclusion **66**

2.1 Compressor Test Cases Overview

This study investigates two high-pressure, multi-stage axial compressor configurations: the CREATE and IHPC compressors. These two cases were selected to form a coherent test matrix characterised by increasing geometric, aerodynamic and inflow distortion complexity, enabling a progressive evaluation of the modelling approaches developed in this work. Their selection is motivated by both the availability of experimental datasets and their relevance to academic and industrial research contexts.

The CREATE compressor is a 3.5-stage axial research machine that has been extensively investigated through both experimental and numerical studies. It exhibits complex multistage flow phenomena, characteristic of high-pressure compressor cores, including rotor-stator interactions, three-dimensional separations, and endwall secondary flows. The operating flow regime is low-transonic, with moderate transonic effects that give rise to compressibility-driven interactions, while avoiding the strong shock structures typically associated with higher-speed compressors.

A distinctive feature of the CREATE configuration is its geometric periodicity, achieved through integer blade count ratios between all the blade rows. This enables the use of reduced annular sectors in unsteady numerical simulations of stable operating points, both under clean inlet conditions and in the presence of radial distortion. This approach significantly reduces computational cost while preserving the fidelity of unsteady flow predictions.

The CREATE compressor is also supported by a comprehensive and high-resolution experimental dataset, offering detailed measurements under clean inflow for different operating conditions. However, the lack of data for distorted inlet flow limits its suitability for validation studies focused specifically on inlet distortion effects.

In contrast, the IHPC compressor is a 4.5-stage axial machine derived from a modern industrial core design. It operates in a fully transonic regime, characterised by localised supersonic flow regions, strong shock waves, and significant interactions between shock structures and secondary flows. These features result in complex aerodynamic behavior, including pronounced rotor-stator interactions, elevated turbulence levels, and increased sensitivity to secondary flow and tip leakage effects.

Geometrically, the IHPC compressor reflects contemporary industrial design practices, incorporating features that increase both aerodynamic complexity and the challenges of numerical modelling. These include non-periodic blade row arrangements, variable stator vanes, and complex annulus geometry, all of which contribute to a highly three-dimensional and unsteady flow environment.

Although the experimental dataset available for the IHPC compressor is more limited than that of CREATE, it includes two iso-speed operating lines encompassing both uniform and circumferentially distorted inlet flow conditions. This enables a broader assessment of model robustness across off-design conditions and non-uniform inflow scenarios.

Table 2.1 summarises the principal differences between the CREATE and IHPC compressors, highlighting their respective geometric, aerodynamic, and experimental characteristics.

The inclusion of these two compressor configurations enables a structured approach to the development and validation of the modelling methodology investigated in this work. The CREATE compressor offers a well-instrumented case that balances complexity and computational cost for establishing and benchmarking numerical methods in the context of multistage high-pressure compressor flows. In contrast, the IHPC compressor serves as an industrially representative test case for evaluating the generalizability and robustness of the proposed modelling strategies under more challenging aerodynamic conditions and increased geometric complexity. This dual-case approach ensures that the conclusions drawn in this study are both grounded in experimentally validated data and applicable to the demands of modern compressor design and analysis.

Table 2.1: Comparison of the CREATE and IHPC compressor configurations.

Feature	**CREATE**	**IHPC**
Number of stages	3.5	4.5
Operating regime	Low-transonic	Fully transonic
Aerodynamic complexity	Moderate to high	High
Spatial periodicity	$2\pi/16$	2π
Computational cost	Moderate to high	Very high
Variable geometry	No	Yes
Experimental data	Extensive	Limited
Inlet conditions	Axisymmetric	Axisymmetric + Azimuthal Dist.

2.1.1 The CREATE Compressor Test Case

2.1.1.1 Overview of the CREATE Compressor

The CREATE compressor (i.e. Compresseur de Recherche pour l'Étude des effets Aérodynamiques et TEchnologiques) is a 3.5-stage research compressor designed and built by Safran Aircraft Engines, and tested at the Laboratory for Fluid Mechanics and Acoustics (LMFA) at École Centrale de Lyon.

Multiple studies have been conducted on the CREATE configuration, providing extensive experimental and numerical insights into the richness and complexity of the flow field within this multi-stage high-pressure compressor [22, 23, 106, 116, 141, 142].

CREATE has been designed to be representative of a high-speed compressor located in the central core of a turbojet engine. Its geometric features, rotational speed, and number of stages were selected to encompass a wide range of flow phenomena within the annulus, while maintaining a manageable overall size to minimise both the power requirements of the test rig (2MW) and the computational cost of numerical simulations.

The meridional view of the CREATE compressor is presented in Figure 2.1, together with the labeling of the experimental measurement planes.

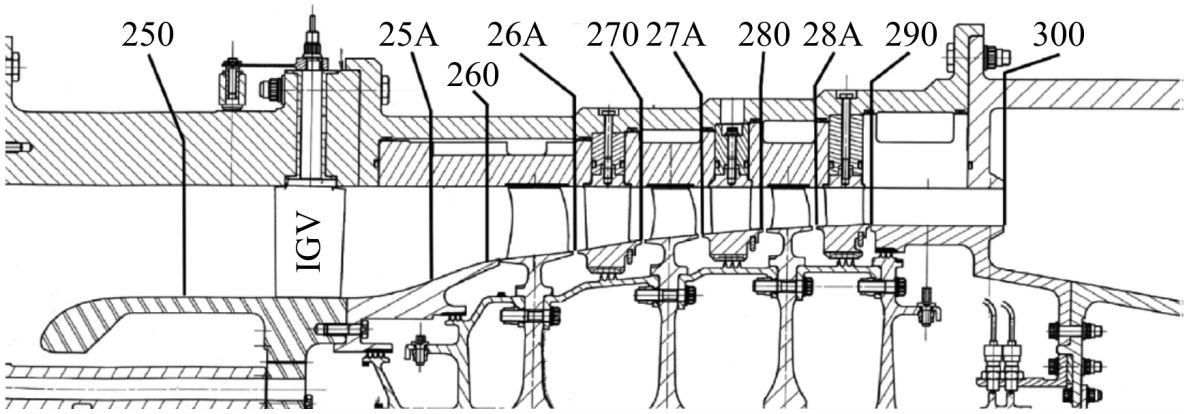

Figure 2.1: Meridional view of the 3.5-stage CREATE compressor [141].

The experimental planes are numbered from 25 to 30. Those located downstream of a rotor are denoted with the final letter "A", while those downstream of a stator end with a "0". An exception is plane 25A, which is positioned at the outlet of the inlet guide vane (IGV).

Key parameters of the CREATE compressor are summarised in Table 2.2. Notably, the first rotor operates slightly transonically, but the remaining rows operate fully in the subsonic regime.

Table 2.2: Main parameters of the CREATE compressor at nominal conditions [141].

Parameter	Value
Shroud external diameter	0.52 m
Shaft rotational speed	11 543 rpm
Blade speed at Rotor 1 tip	313 m/s
Rotational Mach number at Rotor 1 tip	0.92
Mass flow rate	12.7 kg/s

As anticipated, the compressor can be reduced to a periodic sector of $2\pi/16 = 22.5°$ thanks to the collaborative number of blades at the different rows. Table 2.3 summarises the number of blades present in the complete configuration, as well as the ones in the reduced periodic sector.

Table 2.3: Number of blades in the CREATE compressor.

Sector	IGV	R1	S1	R2	S2	R3	S3
2π	32	64	112	80	112	80	112
$2\pi/16$	2	4	7	5	7	5	7

Each rotor row includes a tip clearance (tc) and a hub fillet, while the stator rows, where no mechanical gaps are required, are equipped with hub and shroud fillets to improve structural integrity, reduce secondary flow effects and improve aerodynamic behavior.

2.1.1.2 Available Experimental Data

The CREATE compressor test rig operates as an open-loop system, as illustrated in Figure 2.2, drawing ambient air through a settling chamber into the compressor. The compressor shaft is driven by a 2 MW electric motor coupled with a gearbox. Downstream of the compressor, a butterfly-type throttle valve regulates the mass flow rate, which is measured by a Venturi nozzle located before the exhaust. To reduce electrical power consumption during testing, the total pressure at the inlet is lowered using a nozzle within the settling chamber. This reduction is accounted for through a standardization procedure applied to the experimental measurements [141].

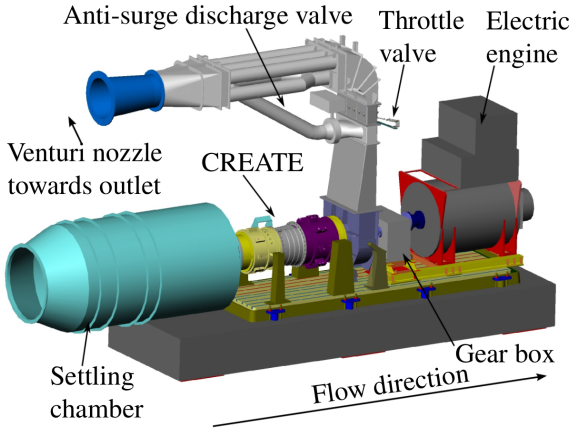

Figure 2.2: Schematic representation of the CREATE test rig [141].

The experimental campaign was conducted at the LMFA laboratory as anticipated, utilising multiple measurement techniques. These include steady-state measurements, high-frequency casing pressure recordings, and velocity measurements using Laser Doppler Anemometry (LDA).

High-frequency casing pressure measurements are time-resolved pressure data collected near the blade tips at the compressor casing. These data provide valuable information on unsteady pressure fluctuations caused by blade passing and flow instabilities, enabling the analysis of transient flow phenomena at both stable and unstable operating points.

Laser Doppler Anemometry is a non-intrusive optical technique that determines local velocity components by measuring the Doppler shift of laser light scattered by tracer particles seeded within the flow. During the test campaign, LDA was utilised to characterise the axial and circumferential velocity components at various inter-row planes, providing detailed velocity profiles across the whole compressor.

Steady-state measurements were taken at inter-stage planes ranging from 250 to 290, including static casing pressure, total pressure, total temperature, and flow angle, recorded at both peak efficiency and loaded operating points. These quantities enable the calculation of additional flow parameters, as detailed in Section 2.3.1. At plane 250, data were collected at a single circumferential position, while at the other planes measurements covered four stator blade passages. Computational studies have confirmed that this sampling adequately captures the dominant flow physics [141].

Inlet conditions were also characterised: total temperature was monitored by ten probes within the settling chamber, and total pressure was measured upstream of the inlet guide vanes at plane 250 using a Kiel probe. At the compressor outlet, plane 300, the flow was surveyed using probe racks comprising thirty measurement points arranged at six circumferential and five spanwise positions, enabling detailed mapping of total pressure and temperature fields. Where multiple measurements were available, data were averaged to produce representative values for performance assessment.

The experimental campaign involved multiple clocking configurations achieved by varying the relative circumferential positions of the stator rows. The present work analyses data from a single configuration, clocking condition 3 as described in a previous work [141]. For this configuration, two operating points were studied: peak efficiency (PE) and near-stall (NS).

High-frequency casing pressure and LDA data are not used here, as steady-state measurements provide sufficient validation of the reference RANS blade-resolved numerical simulations against experimental results. Therefore, the experimental data for the CREATE compressor at the peak efficiency (PE) and near-stall (NS) operating points considered in this work consist of the following:

- Planes 250 to 290: static pressure, total pressure, total temperature, and flow angle measured using three-hole probes over four stator passages.
- Inlet (settling chamber): total temperature measured using ten thermocouples.
- Plane 250: total pressure measured using a Kiel probe.
- Plane 300: total pressure and total temperature measured using probe racks.
- Downstream of the compressor: mass flow rate.

In summary, the extensive experimental dataset available for the CREATE compressor provides a comprehensive characterization of the flow field under steady operating conditions. These measurements serve as a robust basis for validation of numerical simulations and further analysis of the compressor aerodynamics.

2.1.2 The IHPC Compressor Test Case

2.1.2.1 Overview of the IHPC Compressor

The IHPC compressor is a 4.5-stage high-pressure axial compressor developed and tested by Safran Aircraft Engines. It is designed to replicate the aerodynamic operating conditions encountered in modern industrial engines.

Figure 2.3 shows a meridional view of the IHPC compressor, indicating the locations of experimental measurements. Planes highlighted in blue correspond to inlet, outlet, and inter-row sections, the latter located at the leading edge (LE) of the stators and spanning the full channel height, while planes highlighted in red denote casing measurements at both the hub and shroud walls.

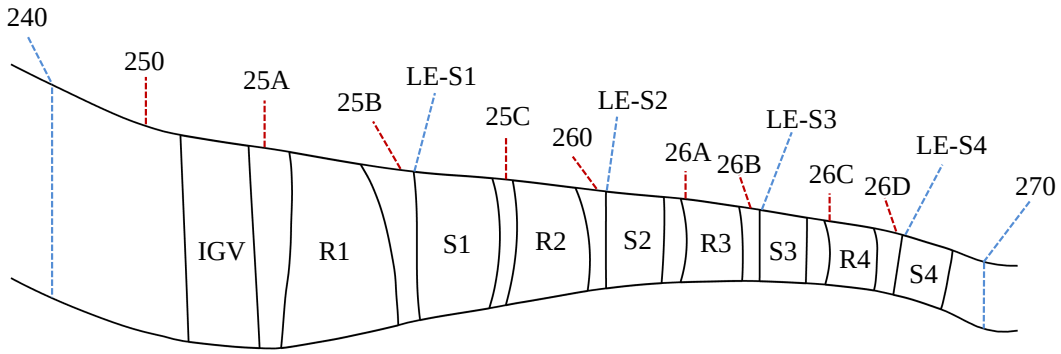

Figure 2.3: Schematic meridional view of the 4.5-stage IHPC compressor.

Unlike the CREATE compressor, the IHPC compressor does not feature an integer blade count ratio between all the rows across the stages; therefore, spatial periodicity cannot be exploited to reduce the computational domain. The number of blades for each blade row is listed in Table 2.4.

Table 2.4: Number of blades per row in the IHPC compressor.

Sector	IGV	R1	S1	R2	S2	R3	S3	R4	S4
2π	36	28	49	40	84	52	90	56	78

Some key parameters of the IHPC compressor are summarised in Table 2.5. These parameters characterise the geometric and operating conditions of the machine.

Table 2.5: Main parameters of the IHPC compressor at nominal conditions.

Parameter	Value
Shaft rotational speed	18 813 rpm
Rotational Mach number at Rotor 1 tip	> 1
Mass flow rate	5.2 kg/s

The IHPC compressor features two rows of variable stator vanes: the inlet guide vane (IGV) and the first stator row (S1). These vanes can be reoriented for different iso-speed lines to optimise their angle of attack relative to the incoming flow, and that of the first rotor row.

To accommodate the associated actuation mechanisms, both IGV and S1 include partial hub and shroud gaps.

In addition, each rotor row features a tip clearance (tc) and a hub fillet. The stator rows, except for the IGV and S1 which include partial gaps, are equipped with both hub and shroud fillets to improve structural integrity and to mitigate secondary flow effects, similar to the CREATE compressor.

2.1.2.2 Available Experimental Data

A comprehensive experimental campaign was performed on this compressor under both clean and distorted inlet conditions. Data acquisition points were distributed throughout the compressor, focusing primarily on the inlet and outlet planes, the leading edges of the stator rows, and wall surfaces.

At the inlet plane (station 240), six circumferentially arranged rakes equipped with combined total pressure and total temperature probes were deployed. Each rake contained six probes evenly spaced along the channel height, providing a total of 36 measurement points distributed over the full annulus. In addition, five static pressure sensors mounted on the shroud captured local pressure variations.

At the outlet plane (station 270), total pressure and total temperature measurements were obtained using separate probe rakes. Five total pressure rakes and five total temperature rakes were positioned circumferentially, each comprising five probes spanning the channel height. Complementary static pressure data were recorded via five sensors on the hub and shroud surface, enabling detailed mapping of pressure distributions at the compressor exit.

Localised measurements at the leading edges of the four stator rows included ten total pressure probes arranged over five radial and two azimuthal locations. Additionally, five total temperature probes were installed at five radial positions along a single azimuthal location. These data provide detailed insight into flow conditions at the stator inlets.

Static pressure measurements along the hub and shroud walls throughout the bladed rows further characterise the circumferential and axial pressure distribution within the compressor.

Global mass flow rates were provided for each operating point along two iso-speed lines, complementing the spatially resolved measurements.

Only steady-state data acquired at the inlet plane (station 240), outlet plane (station 270), and stator leading edges were utilised in this study. No internal flow angle or velocity profiles within the compressor annulus were available, limiting the detailed flow characterization compared to the previous compressor case.

Multiple iso-speed lines were tested during the experimental campaign; however, only one featured inlet distortion. To enable direct comparison, the same iso-speed line was selected among those tested under clean inlet conditions. Differences in ambient conditions between the clean and distorted iso-speed line experiments are thus accounted for in the subsequent analyses.

As part of the inlet distortion investigations, a distortion grid spanning an azimuthal extent of 105° was installed at an angular position of 270°, featuring a porosity of 0.76. This grid excluded the lower 5% of the channel height to mitigate excessive pressure deficits near the hub. Radial and azimuthal total pressure measurements recorded at the inlet plane allow to quantify the effective total pressure deficit imposed on the incoming flow, as detailed in Section 2.3.

The specific measurements employed in this work are summarised as follows:

1. Total pressure and total temperature measurements at inlet plane 240.
2. Total pressure and total temperature measurements at outlet plane 270.
3. Total pressure and total temperature measurements at the leading edges of the four stator rows.
4. Global mass flow rate values corresponding to each operating point.

2.2 Numerical Framework and Methodology

The core methodology of this work relies on computational fluid dynamics (CFD) simulations. This section presents the numerical framework used throughout the study. First, the CFD solver and its turbomachinery-specific boundary conditions are introduced. Next, the key numerical parameters employed in the simulations are outlined. This is followed by a description of the blade-resolved numerical setup, including mesh generation, boundary condition specification, and other relevant modelling choices. Finally, the Body-Force framework is briefly presented and compared to the blade-resolved approach.

2.2.1 The elsA CFD Solver

The computational fluid dynamics (CFD) simulations in this study were performed using the elsA solver, developed by ONERA and co-owned by ONERA and Safran [13]. elsA is an industrial-grade, robust flow solver designed to resolve the three-dimensional, viscous, compressible Navier-Stokes equations using a cell-centered finite volume approach. It supports both structured and unstructured grids, making it well suited for a wide range of aerodynamic configurations and mesh topologies.

Intended for high-fidelity aerodynamic analyses, elsA enables the simulation of both internal and external flows with applications spanning turbomachinery, rotorcraft, and fixed-wing aircraft. Its modular architecture and extensive physical modelling capabilities provide versatility for advanced CFD studies.

Depending on the upstream inflow conditions imposed on the compressor, the simulations conducted here employ either a steady-state Reynolds-Averaged Navier-Stokes (RANS) or an unsteady RANS (URANS) approach.

For rotating machinery simulations, elsA offers a suite of specialised boundary conditions tailored to various physical and numerical requirements. At rotor-stator interfaces, methods such as the mixing plane condition, phase-lag (chorochronic) approach, profile transformation approach (PTA), and sliding mesh technique are available. These approaches differ in their handling of unsteady interactions and computational cost, allowing selection based on the simulation goals and configuration.

At outlet boundaries, elsA provides options including radial equilibrium and valve law conditions, enabling control over downstream flow profiles and supporting varying levels of physical fidelity in the treatment of mass flow, pressure, and swirl distributions.

Furthermore, a periodicity condition can be imposed at azimuthal boundaries for simulations modelling a sector of the machine instead of the full 360° annulus.

The boundary conditions most relevant to the present study are briefly described in the following.

Mixing Plane Condition The mixing plane condition is employed to connect two adjacent bladed rows rotating at different angular velocities, typically at a rotor-stator interface. It is primarily applied in steady-state simulations to maintain a time-invariant flow field. This boundary condition enforces a circumferential averaging of the flow variables, i.e. a pitch-wise average, from one side of the interface, which is then imposed on the opposite side. On the upstream side (left of the mixing plane), one flow variable is prescribed, analogous to an outlet boundary condition. On the downstream side (right of the mixing plane), four flow variables are imposed, analogous to an inlet boundary condition. Consequently, the flow crossing the interface is smoothed and rendered axisymmetric, thereby eliminating detailed unsteady fluctuations.

As a result, unsteady flow phenomena such as wakes, shocks, and potential interactions between rotors and stators are smoothed out across the mixing plane interface. While this simplification reduces the fidelity of the flow field by neglecting time-dependent effects, it enables the use of single-blade channel simulations, where only one blade per row is modelled. This approach significantly reduces computational cost when analysing turbomachinery at steady operating conditions.

One important limitation of the mixing plane approach is its tendency to reflect a substantial portion of incoming flow disturbances, including shock waves. These reflections can introduce artificial energy losses and degrade simulation accuracy, especially in high-speed flows or when the mixing plane is placed close to the blade rows.

For investigations where transient effects are important and higher accuracy is required, more advanced and computationally intensive methods such as the sliding mesh technique or the PTA approach should be used.

Profile Transformation Approach Condition The Profile Transformation Approach (PTA), originally proposed by Fourmaux in 1994 [46] and comprehensively detailed in Gout's work [58], is a method designed to model the rotor-stator interface in unsteady simulations where the blade count ratio between adjacent rows is close, but not exactly equal to an integer.

The key idea behind PTA is to reduce the computational domain to a carefully selected number of blade passages per row such that an instantaneous spatial periodicity can be approximately enforced on the azimuthal boundaries. This allows for the application of periodic boundary conditions in cases where strict periodicity would otherwise not hold.

More specifically, let N_1 and N_2 denote the number of blades on the first and second rows, respectively. Two integers K_1 and K_2 are chosen to be as small as possible while satisfying the condition that the ratios N_1/K_1 and N_2/K_2 are approximately equal. This selection ensures that the azimuthal extent of the computational domain for each row corresponds to nearly the same physical angle, enabling a near-periodic matching of flow fields at the interface. The same procedure is applied for subsequent rows in multi-stage compressors.

Although the flow is generally not spatially periodic between the azimuthal boundaries of an arbitrary group of passages due to the difference in blade counts, a careful choice of K_1 and K_2 greatly reduces the time lag associated with the mismatch, thereby allowing the enforcement of a simple spatial periodicity condition on the azimuthal boundaries.

At the rotor-stator interface, a coordinate transformation is applied in which one domain is azimuthally compressed while the other is expanded. This rescaling aligns the blade passages between rows with differing blade counts by adjusting the azimuthal coordinate of the exchanged flow variables. Importantly, this transformation does not affect the blade geome-

tries and their relative azimuthal positions within a row, which remain unchanged. As a result, the physical integrity of the quantities exchanged across the interface is preserved, enabling accurate and consistent coupling between the two rows despite the mismatch in blade counts.

The simulation time step is consequently adjusted using a correction coefficient D_m, defined in Equation ((2.1)). This coefficient depends on the ratio between the actual number of blades N_i in the full annulus and the simulated number of blades in the reduced sector K_i for each blade row i, as well as on the total number of rows N_{rows}:

$$D_m = \frac{1}{N_{rows}} \sum_{i=1}^{N_{rows}} \frac{N_i}{K_i} \tag{2.1}$$

Accordingly, the reference time for one revolution within the computational domain, T_{ref}, and the corresponding physical time step, Δt, are given by Equation ((2.2)). Here, N_{it} denotes the number of iterations per revolution, and $D_{m,ideal}$ is calculated as the ratio between 360° and the simulated sector angle.

$$T_{ref} = T_{rev} \frac{D_{m,ideal}}{D_m}, \quad \Delta t = \frac{T_{ref}}{N_{it}} \tag{2.2}$$

As an example, the first stage of the IHPC compressor, with 28 rotor and 49 stator blades, can be modeled using $K_1 = 7$ and $K_2 = 12$ passages. The rotor and stator domains then span 90° and $(360°/49) \times 12 \approx 88°$, respectively. The resulting correction coefficient $D_m = 4.04$, close to the ideal value of 4, corresponds to an average azimuthal extent of $360°/D_m \approx 89°$. The rotor flow is thus contracted from 90° to 89°, and the stator flow expanded from 88° to 89°, yielding a quasi-periodic coupling at the rotor-stator interface.

Sliding Mesh Condition The sliding mesh method can be considered a particular case of the Profile Transformation Approach (PTA) applicable when the blade counts of adjacent rows are cooperative, meaning their ratio is an integer, or when a full-annulus simulation is performed. In such cases, the computational domains of both rows can be discretised with an integer number of blade passages, enabling exact spatial and temporal periodicity across the rotor-stator interface.

In contrast to the PTA, which requires a coordinate transformation to enforce approximate periodicity when blade counts are non-matching, the sliding mesh approach resolves the actual unsteady relative motion between rows by explicitly rotating one domain with respect to the other over time. This allows for a high-fidelity representation of time-dependent flow phenomena such as blade wakes, shock interactions, and rotor-stator potential effects, without relying on any spatial or temporal averaging assumptions.

In this configuration, the corrective coefficient is $D_m = 1$, and the reference time corresponds directly to the physical time of one full revolution of the turbomachinery ($T_{ref} = T_{rev}$).

Outflow Condition The radial equilibrium condition is a fundamental assumption used to define the pressure and flow distribution at the outlet of turbomachinery. It is based on the balance of centrifugal forces, pressure gradients, and radial acceleration within the flow field, ensuring that the flow variables vary smoothly in the radial direction and are invariant in the azimuthal direction. This condition allows for the determination of radial profiles of static pressure and velocity components, consistent with the swirling flow exiting the rotor or stator.

In practice, a simplified form of the radial equilibrium equation is often employed, assuming negligible radial velocity and axial variations, which reduces the governing equations to a balance between the radial pressure gradient and the centrifugal force due to swirl. This approximation facilitates efficient boundary condition implementation while retaining the essential physics needed to predict the flow's radial variation downstream of the row. The simplified radial equilibrium implemented in elsA is presented in equation (2.3), with p the static pressure, r the radius, ρ the flow density, and V_θ the azimuthal flow velocity component.

$$\frac{\partial p}{\partial r} = \frac{\rho V_\theta^2}{r} \tag{2.3}$$

The radial pressure gradient defined in equation (2.3) provides the variation of static pressure with radius. To determine the absolute static pressure across the outlet plane, a reference value, called the pivot pressure p_{pivot}, is prescribed at a chosen pivot radius at the outlet plane, typically at the hub. This pivot pressure serves as the boundary condition for integrating the radial equilibrium equation, yielding the complete radial static pressure profile consistent with the swirling flow at the outlet.

To enable control of the operating point, the radial equilibrium condition in elsA is often combined with a valve law that prescribes a relationship between the outlet pivot pressure and the mass flow rate. During the simulation, the valve law dynamically adjusts the pivot pressure based on iteration progress or prescribed rules, allowing the outlet pressure profile to adapt to flow changes. This dynamic adjustment improves numerical stability and ensures physically consistent boundary conditions, facilitating stable convergence, particularly at near stall conditions.

In this work, the valve law used to update the pivot pressure is given by Equation (2.4), where $\dot{m}$ denotes the mass flow rate, and n the iteration number. The law gradually drives the ratio $p_{pivot}/\dot{m}$ toward the target reference value $p_{ref}/\dot{m}_{ref}$, with ω as a relaxation factor controlling the update rate:

$$p_{pivot}^{n+1} = p_{pivot}^{n} + \omega \left(p_{ref} \frac{\dot{m}^n}{\dot{m}_{ref}} - p_{pivot}^{n} \right) \tag{2.4}$$

This iterative update allows the outlet boundary condition to adapt naturally throughout the simulation, improving numerical stability and ensuring convergence to physically consistent flow and pressure fields. Additionally, adjusting the target reference value $p_{\text{ref}}/\dot{m}_{\text{ref}}$ enables control over the simulated operating point.

2.2.2 Numerical Parameters

The key numerical parameters employed in this study are presented herein.

Turbulence Model This study employs the *k-l* Smith turbulence model [146], a two-equation turbulence model that solves transport equations for the turbulent kinetic energy k and a turbulence length scale l. This approach is known to provide good predictions near walls, and is well-suited for compressible flows with complex boundary layers.

The choice of this model in the present work is further justified by its extensive use in studies employing Body-Force methodologies, where it has demonstrated reliability and effectiveness [3, 85].

Spatial Scheme The spatial discretization employed in this study uses a second-order upwind Roe scheme with an approximate Riemann solver [136] and a Van Albada flux limiter [160], ensuring stable second-order spatial accuracy. Additionally, the scheme is enhanced by the Harten correction [69], which reduces non-physical oscillations in the solution, especially in high-gradient regions. These parameters are typically associated with the above-mentioned *k-l* Smith turbulence model.

Temporal Scheme Steady-state calculations employ a local time-stepping approach based on the Courant-Friedrichs-Lewy (CFL) condition, in which the time step is adjusted locally according to the flow velocity and grid spacing. This accelerates convergence by allowing larger time steps in regions of slower flow while maintaining numerical stability in regions with higher velocities. In the present work, the CFL number is gradually increased from 1 to 30 over 300 iterations, providing a controlled ramp that ensures rapid convergence without compromising stability.

Unsteady calculations employ the second-order implicit Gear scheme [51] for temporal discretization. To ensure numerical stability and achieve a balance between computational efficiency and solution accuracy, each physical time iteration includes 12 Newton sub-iterations, which reduce residuals by approximately two orders of magnitude. This process ensures rapid convergence. The time step and iteration count are further informed by the investigation conducted by Schreiber [141] on the CREATE compressor, which tested several iteration counts per period of the $2\pi/16$ sector: 210, 420, 840, and 1680 iterations. The study found that 210 iterations led to numerical instability, while higher iteration counts produced comparable compressor performance metrics. The differences between these higher counts were limited to minor variations in tip leakage vortex velocities and velocity fluctuations. Based on these findings, the current study adopts 420 iterations per period, corresponding to a minimum of 60 iterations per blade passage, as an effective compromise between computational cost and solution fidelity. The total number of iterations per revolution in the investigated configurations thus depends on the maximum number of blade passages and is provided in Sections 3.1.1 and 3.2.1, with respect to each test case.

2.2.3 Blade-Resolved Simulation Framework

Among the modelling approaches employed in this study, the blade-resolved method involves explicitly modelling the blades within the computational domain, which are then meshed and simulated. This section presents the numerical framework for the blade-resolved cases, including mesh characteristics and the boundary conditions adopted. Further details regarding mesh size and specific features for each calculation will be provided in Sections 3.1.1 and 3.2.1, where the reference blade-resolved simulations are discussed in detail.

2.2.3.1 Mesh Characteristics of Blade-Resolved Calculations

The meshes for the blade-resolved calculations of both test cases were generated using the NUMECA AutoGrid5 mesh generation software [115]. AutoGrid5 is a structured mesh generation tool developed by NUMECA, which is now part of Cadence. It is specifically designed for turbomachinery applications and automates the creation of high-quality, multi-block, structured grids around complex blade geometries, enabling precise resolution of flow features within rotating machines.

The meshes of the configurations studied in this work are thus structured, multi-block grids. The mesh topology around each bladed row predominantly follows a O6H configuration. A simplified O4H topology is applied when the axial spacing between rows is insufficient to accommodate the full O6H layout or when the mesh quality near the interface surface is already satisfactory without the additional blocks of the O6H mesh. The O4H topology consists of an O-grid surrounding the blade surface (referred to as the skin block), complemented by four additional H-grids named inlet, outlet, up, and down, which occupy the regions adjacent to the blade. In the O6H mesh, two further blocks called upstream and downstream are incorporated to improve mesh quality and provide smooth connectivity at the rotor-stator interfaces. These block are illustrated for a rotor in Figure 2.4. It should be noted that the block names such as inlet, outlet, up, and down are purely geometric labels used to describe the mesh topology surrounding the blade row and do not correspond to physical boundary conditions like flow inlet or outlet boundaries.

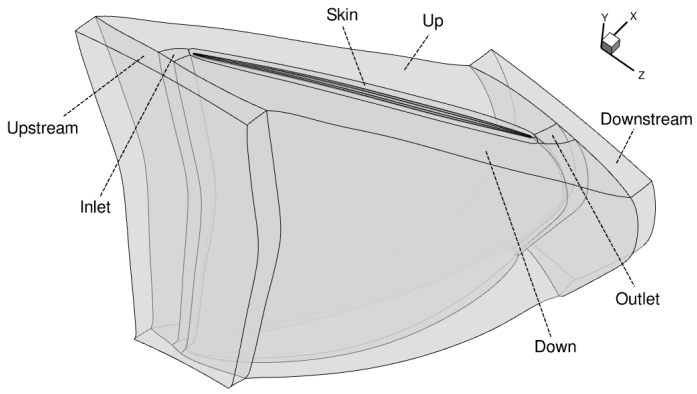

Figure 2.4: O6H mesh block names and topology for a rotor blade.

The mesh refinement details are summarized in Table 2.6. The N_x values in the table represent the number of cells in the axial direction, spanning from the upstream to the downstream grids of an intermediate row. The N_θ values denote the number of azimuthal cells per blade passage, while N_r represents the number of radial mesh cells.

In the radial direction, the rotor meshes consist of approximately 101 cells for the CREATE compressor and 125 cells for the IHPC compressor, with the stator meshes containing 93 cells for CREATE and 121 cells for IHPC. In the axial direction, the CREATE compressor uses 151 cells for rotors and 141 cells for stators, while the IHPC compressor employs 159 cells for rotors and 141 cells for stators. Azimuthally, both compressors feature between 80 and 90 cells per blade passage for rotors and between 60 and 80 cells for stators.

Table 2.6: Mesh refinement details for CREATE and IHPC compressors for a single-blade passage.

Compressor	**Row**	$\mathbf{N}_r$	$\mathbf{N}_x$	$\mathbf{N}_\theta$
CREATE	Rotor	101	151	80–90
	Stator	93	141	80–90
IHPC	Rotor	125	159	80–90
	Stator	121	141	80–90

The mesh criteria were established based on a trade-off between accuracy and computa-

tional cost, informed by a mesh sensitivity study on the CREATE compressor, presented in Appendix A. These criteria were applied unchanged to the IHPC configuration wherever feasible. When direct transposition was not possible, the IHPC compressor mesh was further refined to ensure that the minimum refinement standards identified in the CREATE study were met or exceeded. The increased mesh refinement for the IHPC compressor is justified by the greater complexity of the blade geometry, technological effects, and channel configuration, which necessitated modifications to maintain the mesh quality requirements established in the CREATE study.

The mesh quality achieved is considered optimal for the purposes of this study and satisfies the constraints commonly accepted in the field. The skewness is low, with a minimum skewness angle above 35°, ensuring good cell shape. The expansion ratio is typically below 2, but reaches 2 locally in critical areas such as fillet radii and blade gaps due to their geometric complexity. The spanwise angular deviation remains below 40°, maintaining smooth mesh variation along the blade span. Additionally, the dimensionless wall distance, y^+, is approximately 1 across all blade rows, which is considered sufficient to accurately resolve the near-wall flow.

Figure 2.5 illustrates the resulting mesh applied to a single rotor blade. Figure 2.5a shows the global 3D mesh highlighting the overall mesh structure. Figure 2.5b presents the mesh distribution on the blade surface, demonstrating the refinement applied across the blade. Figures 2.5c and 2.5d focus on the leading and trailing edge mesh, respectively, showing the detail in these critical regions.

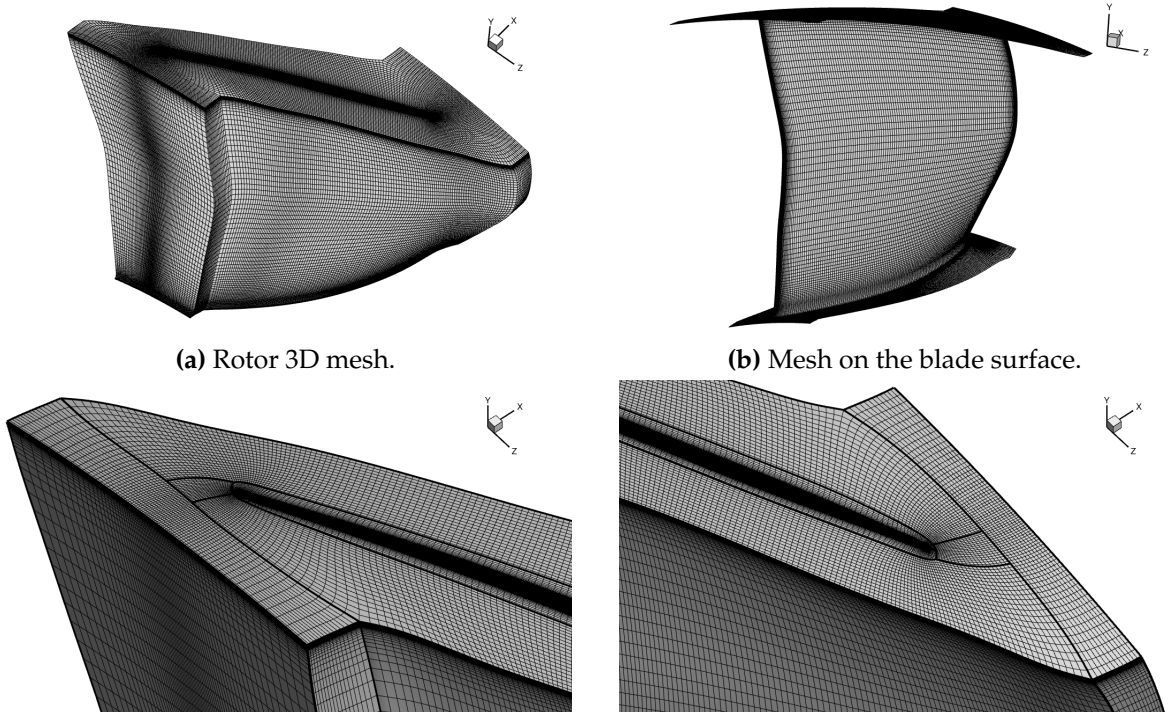

(a) Rotor 3D mesh.

(b) Mesh on the blade surface.

(c) Mesh at leading edge.

(d) Mesh at trailing edge.

Figure 2.5: Detailed views of the blade-resolved mesh applied to one rotor blade.

2.2.3.2 Boundary Conditions of Blade-Resolved Calculations

The boundary conditions applied to the blade-resolved calculations are described below.

Inflow Condition All simulations employ subsonic inflow boundary conditions. A spatially varying inflow map is imposed to prescribe the desired inlet flow characteristics. These maps are primarily derived from experimental data to replicate test conditions accurately; however, for specific distortion studies, they may also be synthetically generated, and this is specified when done. More details on the characteristics of the flow injected at the inlet of the numerical domain are presented in Sections 3.1.1 and 3.2.1.

Each inlet map is defined by seven quantities: total pressure, total enthalpy, the turbulent variables k and l for the turbulent kinetic energy and turbulent length scale, and the components of the unit normal vector in the x-, y-, and z-directions. These quantities are determined from the absolute flow angle α and the geometric angle ϕ, defined by the hub and shroud geometry at the inlet, which together specify the flow direction. These parameters fully specify the thermodynamic state, turbulence characteristics, and flow orientation at the inlet.

Outflow Condition The outflow boundary condition is based on a simplified radial equilibrium formulation, with a pivot point at the compressor hub, and is combined with a valve law to control the mass flow rate. This approach enables a realistic distribution of static pressure at the outlet while maintaining numerical stability. Both the radial equilibrium and valve law formulations are described in detail in Section 2.2.1.

Wall Condition All blade, hub, and shroud walls are treated as adiabatic, no-slip walls, which is a standard assumption in aerodynamic simulations where heat transfer effects are not explicitly resolved. In simulations where the domain is reduced to a streamline tube representation, the physical hub and shroud walls are replaced by upper and lower boundaries, on which a slip condition is imposed to allow for radial flow development without introducing artificial wall friction. This is further described in Section 3.1.1.3.

Rotor-Stator Interface Condition The rotor-stator interfaces are modeled using one of the following approaches: the mixing plane for steady-state calculations, the profile transformation approach for unsteady calculations of non-periodic sectors, or the sliding mesh for unsteady calculations of periodic sections or full-annulus. Detailed descriptions of these methods are provided in Section 2.2.1. The choice of approach depends on the configuration of the study, as detailed in Sections 3.1.1 and 3.2.1.

2.2.4 Body-Force Simulation Framework

This section details the numerical setup for the Body-Force simulations and highlights the differences compared to the blade-resolved simulation approach.

2.2.4.1 Mesh Characteristics of Body-Force Calculations

The mesh used for Body-Force calculations features a significantly simpler topology compared to that of blade-resolved simulations. It was generated using the pre-processing module of the MOLA computational chain [9]. The Body-Force mesh generation within MOLA

involves two additional modules: Ersatz, an internal software owned by ONERA, and Cassiopee [8]. The Ersatz module extracts the geometric features of the numerical domain from a reference AutoGrid blade-resolved mesh. Subsequently, the Cassiopee module regenerates a structured mesh that preserves the shape of the hub, shroud, and of the volume swept by each blade. Additionally, the geometric information required by the co-processing Body-Force calculation module is embedded into the mesh tree for later use, in accordance with the CGNS standard [126] adopted in this work.

The generated mesh is a structured H-grid of the annulus channel, with slight refinement along the axial direction at the blade leading and trailing edges to ensure mass conservation, as discussed in Section 1.3.3.2. Additionally, since the Body-Force calculations solve the viscous RANS equations, further refinement is applied near the hub and shroud walls to accurately capture the boundary layer. Finally, the distribution of cells along the azimuthal direction is uniform. A detail of the radial and axial refinement of the Body-Force mesh is presented in Figure 2.6. A sensitivity analysis was performed to assess the adequacy of the implemented Body-Force mesh; the results are presented in Appendix A.

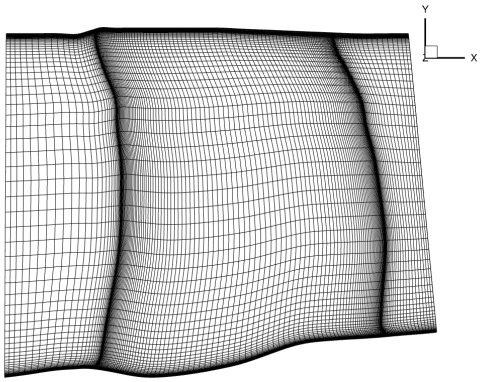

Figure 2.6: Radial and axial mesh renement of the Body-Force mesh applied to one rotor blade.

2.2.4.2 Boundary Conditions of Body-Force Calculations

Inflow and Outflow Conditions The inflow and outflow boundary conditions applied in the Body-Force simulations are identical to those described previously for the blade-resolved calculations.

Wall Conditions The wall boundary conditions differ from those in the blade-resolved simulations, as no blades are present or explicitly meshed in the Body-Force calculations. The remaining wall conditions remain unchanged: the hub and shroud have adiabatic no-slip boundary conditions, except in cases where reduced streamline tube configurations are simulated, in which the slip condition is applied as appropriate.

Rotor-Stator Interface Condition In Body-Force calculations, since the blades are not explicitly modelled and the simulations are performed under steady-state conditions in the absolute frame, there is no need to explicitly model the rotor-stator interface. Consequently, the flow is treated as continuous through the channel without any interface discontinuities.

Summary of Boundary Conditions Differences The blade-resolved and Body-Force calculations thus present some important differences in terms of boundary conditions. These are illustrated in Figure 2.7. In particular, subfigure 2.7a shows the boundary conditions for blade-resolved simulations, while subfigure 2.7b presents those for Body-Force simulations. The locations of the inflow boundary condition is indicated in red, the outflow condition in blue, the rotor-stator interfaces in green, and no-slip walls in gray.

It is also noteworthy that the azimuthal extent of the Body-Force numerical domain for a single-blade-passage calculation is significantly smaller than that used in the blade-resolved configuration. This reduction helps lower the computational cost of the Body-Force calculations and is enabled by the inherent axisymmetry of the Body-Force solution when an axisymmetric inflow condition is imposed, assuming the operating point remains within the stable regime.

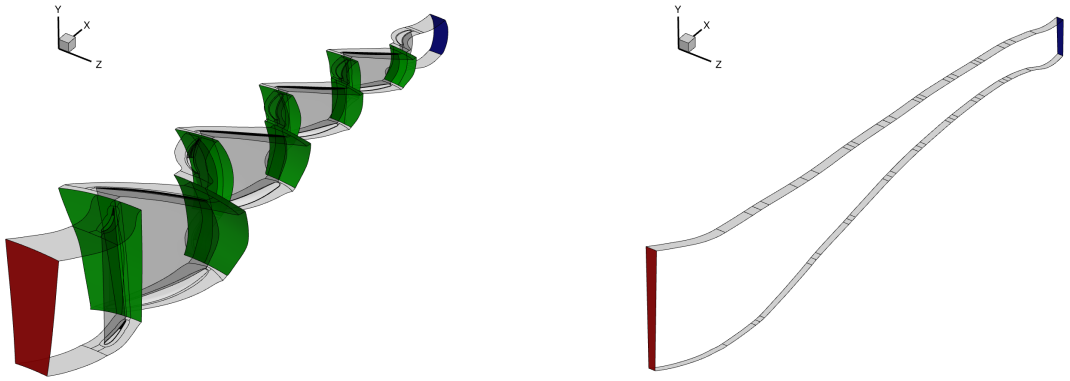

(a) Scheme of BCs for blade-resolved cases. **(b)** Scheme of BCs for Body-Force cases.

Figure 2.7: Comparison of boundary condition schemes between blade-resolved (a) and Body-Force (b) simulations. Color coding: inflow (red), outflow (blue), rotor-stator interfaces (green), and no-slip walls (gray).

2.2.4.3 Body-Force Co-Processing Module

The Body-Force source terms are computed within an independent module and a coupling is set up with the CFD solver to take into account their effects.

The coupling between the flow solver and the external body-force source term computation is achieved through the MOLA framework [9]. The CFD solver elsA solves the RANS equations and provides MOLA with the necessary flow field variables at the end of each iteration. Within MOLA, a dedicated co-processing Python module uses these variables to compute and update the body forces. These forces are then introduced as source terms in the RANS equations for the subsequent iteration.

This co-processing approach enables flexible and modular integration of the source terms within the solver, allowing complex or customised force models to be implemented without modifying the core solver. However, invoking an external module at each iteration increases runtime due to communication overhead between elsA and the Python-based co-processing module. For maximum computational efficiency, the source terms computation could be implemented directly within elsA, though this would reduce flexibility and limit potential applications due to the increased complexity of integration.

To balance computational cost and accuracy, the update frequency of the source terms can be adjusted by recomputing the body forces only every few iterations instead of at every iteration, which reduces computational requirements. Furthermore, the application of source terms can be delayed for a certain number of initial iterations, which may improve numerical stability during the early stages of convergence. In the present work, the source terms are updated at every iteration, starting from the first.

A schematic representation of the interaction between the solver (elsA) and the Body-Force co-processing module employed in this study is shown in Figure 2.8. The figure also depicts the pre-processing workflow, as described in Section 2.2.4. Different components and data are color-coded for clarity: the MOLA modules are highlighted in green, the elsA solver in blue, and the exchanged input and output data at each step in orange.

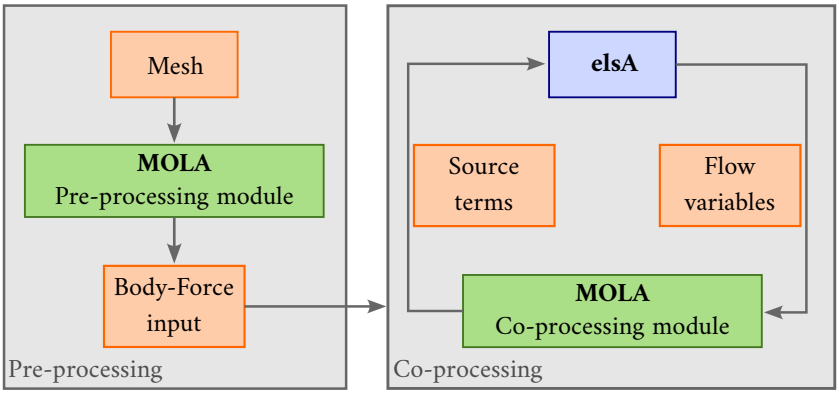

Figure 2.8: Schematic overview of the coupling framework between the elsA solver and the Body-Force co-processing module.

2.3 Data Post-Processing

This section provides a brief overview of the post-processing procedures applied to both the experimental datasets and the numerical simulation results.

2.3.1 Post-Processing of Experimental Data

As previously mentioned, the experimental campaigns conducted on the two investigated compressors yielded different types of datasets. Nevertheless, the post-processing approach described below is applicable to both test campaigns, wherever the relevant quantities are available.

The experimental measurements of static pressure P_s, total pressure P_t, total temperature T_t, and flow angle α are used to derive key flow parameters including the Mach number M, density ρ, and axial velocity V_x.

The Mach number is obtained from the ratio of total to static pressure by applying the isentropic flow relation in Equation (2.5) and solving for M.

$$\frac{P_t}{P_s} = \left(1 + \frac{\gamma - 1}{2} M^2\right)^{\frac{\gamma}{\gamma-1}} \quad \Rightarrow \quad M = \sqrt{\left[\left(\frac{P_t}{P_s}\right)^{\frac{\gamma-1}{\gamma}} - 1\right] \frac{2}{\gamma - 1}} \tag{2.5}$$

Here, γ is the specific heat ratio of the working fluid.

Subsequently, the static temperature T_s is calculated from the measured total temperature T_t and the Mach number M using Equation (2.6).

$$T_s = \frac{T_t}{1 + \frac{\gamma-1}{2} M^2} \tag{2.6}$$

The flow density ρ is determined via the perfect gas law of Equation (2.7), where R_{gas} is the specific gas constant.

$$\rho = \frac{P_s}{R_{gas} T_s} \tag{2.7}$$

The magnitude of the flow velocity V is calculated from the Mach number and the static temperature using Equation (2.8).

$$V = M\sqrt{\gamma R_{gas} T_s} \tag{2.8}$$

Finally, knowing that the experimental probes are placed perpendicularly to the compressor axis, the axial velocity component V_x is found by accounting for the absolute flow angle α as shown in Equation (2.9).

$$V_x = V\cos(\alpha) \tag{2.9}$$

In addition to local flow quantities, integral quantities were derived from these data to characterise the overall flow behavior. To do so, an averaging procedure has been chosen as follows.

Mass-Weighted Averaging Total quantities, denoted here as X_t, were averaged using a mass flow weighting criterion to account for the local contribution of mass flow rate, as defined in Equation (2.10), where r is the radial coordinate.

$$\overline{X}_t = \frac{\iint X_t \rho V_x \, dA}{\iint \rho V_x \, dA} = \frac{\int_{r_{\min}}^{r_{\max}} X_t \rho V_x \, r \, dr}{\int_{r_{\min}}^{r_{\max}} \rho V_x \, r \, dr} \tag{2.10}$$

Surface Averaging Static quantities, denoted as X_s, were averaged based on a purely geometric surface area weighting, as shown in Equation (2.11).

$$\overline{X}_s = \frac{\iint X_s \, dA}{\iint dA} = \frac{\int_{r_{\min}}^{r_{\max}} X_s \, r \, dr}{\int_{r_{\min}}^{r_{\max}} r \, dr} \tag{2.11}$$

Mass Flow Rate Calculation The total mass flow rate $\dot{m}$ through the measurement plane was computed according to Equation (2.12).

$$\dot{m} = \iint \rho V_x \, dA = 2\pi \int_{r_{\min}}^{r_{\max}} \rho V_x \, r \, dr \tag{2.12}$$

Due to limitations of the experimental instrumentation, measurements could not be taken sufficiently close to the endwalls; typically data coverage extends between approximately 5% and 95% of the normalised channel height h/H. To perform the integrals over the entire annulus height, the axial mass flux ρV_x was assumed to be zero at the walls (i.e. at 0% and 100% h/H), consistent with the no-slip condition at the wall boundaries.

Wherever possible, the calculated mass flow rates were validated against independent measurements obtained from the Venturi nozzle, showing good agreement within experimental uncertainty.

Distortion Deficit Calculation The total pressure measurements at the IHPC compressor inlet, under both clean and distorted inflow conditions, are presented in Figure 2.9. The dataset consists of a 6×6 matrix of discrete probe locations, corresponding to the vertices of the polygon shown in the figure. The azimuthal (j-index) and radial (i-index) positions are indicated. Although the visualizations in Figure 2.9a and Figure 2.9b display continuous spatial variations, these maps are interpolated for graphical clarity and do not directly represent the measured data.

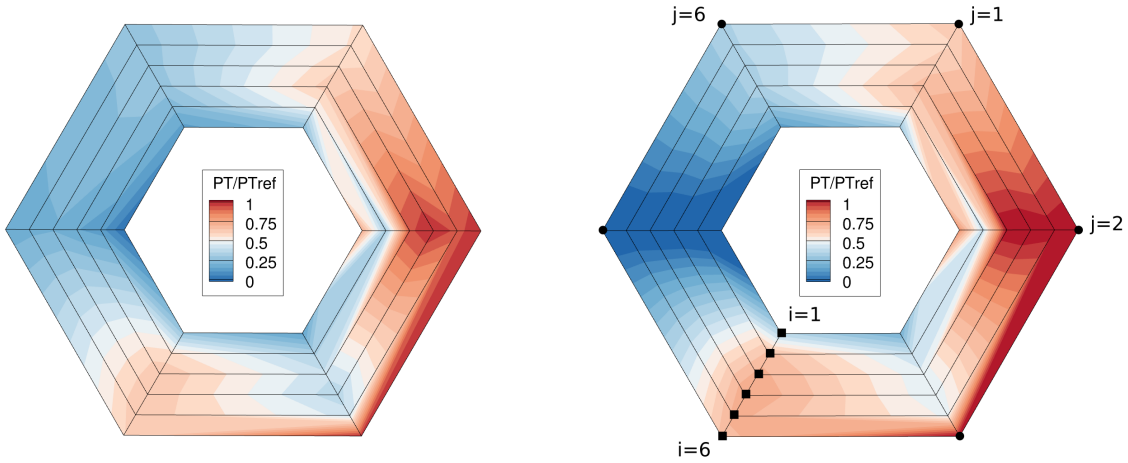

(a) Clean inflow case. **(b)** Distorted inflow case.

Figure 2.9: Total pressure distribution measured at the IHPC compressor inlet under clean and distorted inflow conditions.

These contour maps reveal the spatial distribution of total pressure at the inlet, highlighting the azimuthal non-uniformities. Even under clean inflow conditions, certain asymmetries are present, likely due to secondary effects, such as the structural support struts or the upstream S-shaped duct geometry.

To isolate the specific impact of the distortion grid, Figure 2.10 shows the relative difference in total pressure between the distorted and clean inflow cases, normalised by the clean case values at each probe location. The variation of total pressure is plotted along the circumferential direction indexed by j for each radial position i. This difference defines a local dis-

tortion coefficient k_{ij}, which quantifies the percentage change in total pressure at each radial and azimuthal location, as shown in Equation (2.13). This coefficient aids in characterising the distortion effect and supports the correction methodology described later.

$$k_{ij} = 1 - \frac{P_{t,DIST,ij}}{P_{t,CLN,ij}} \, [\%] \tag{2.13}$$

Here, $P_{t,CLN,ij}$ and $P_{t,DIST,ij}$ represent the total pressures measured under clean and distorted inflow conditions, respectively.

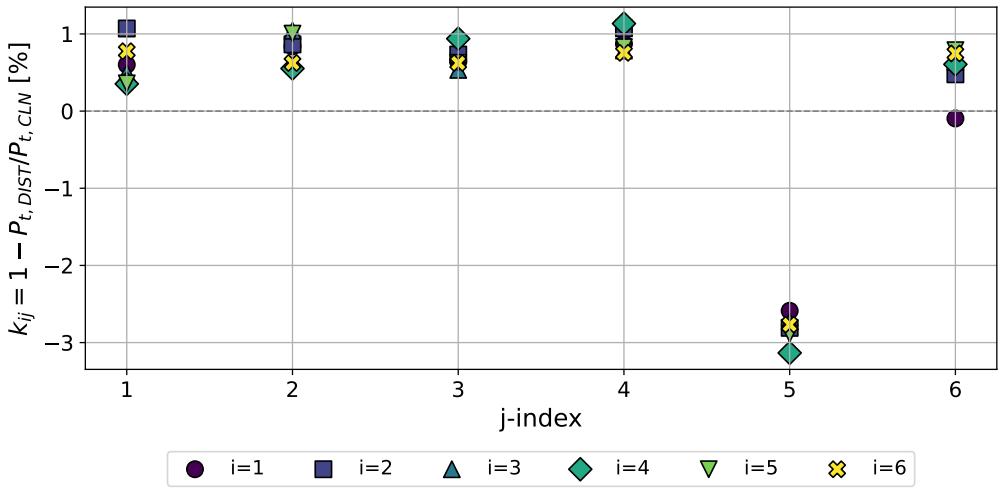

Figure 2.10: Relative total pressure difference between clean and distorted inflow conditions at the IHPC compressor inlet.

Two key features are evident from the data. First, a significant pressure deficit is recorded consistently across all radial positions at the azimuthal index $j = 5$. Second, non-zero differences are observed in the undistorted sectors, indicating small variations in operating conditions between the two experimental setups. This systematic offset necessitates a correction procedure to accurately isolate the distortion effect.

The radial variation of the measured distortion was relatively small at a fixed azimuthal position. To further characterise the distortion, the local distortion coefficient k_{ij} was averaged radially at each azimuthal position. The resulting azimuthal average distortion coefficient k_j is given by:

$$k_j = \frac{1}{N_r} \sum_{i=1}^{N_r} k_{ij} \tag{2.14}$$

where N_r is the number of radial probe positions, equal to six.

To eliminate the baseline offset between the two test cases and isolate the effect of the distortion grid, a reference average was computed using only the undistorted azimuthal sectors. Let $U = \{1, 2, 3, 4, 6\}$ denote the set of undistorted azimuthal indices. The corrected distortion coefficient $k_{j,\text{new}}$ is then defined by subtracting the mean value over the undistorted region:

$$k_{j,\text{new}} = k_j - \frac{1}{N_u} \sum_{j \in U} k_j \tag{2.15}$$

where N_u is the number of elements in the undistorted set U, i.e. five.

This correction ensures that the mean distortion in the unaffected regions is zero, isolating the deficit introduced by the distortion grid. For the distorted probe rake located at $j = 5$, the corrected distortion coefficient was found to be $k_{j=5,\text{new}} = -3.5\%$, representing the relative pressure deficit induced by the distortion grid compared to the clean inflow baseline.

The corrected distortion deficit $k_{j,\text{new}}$ serves as the basis for defining the inlet distortion map in the numerical simulations, which is further detailed in Section 3.2.1. This quantitative characterisation is crucial for ensuring consistency between the experimental and computational representations of the inflow conditions.

2.3.2 Post-Processing of Numerical Data

The post-processing of numerical data follows the same approach as for experimental data, where applicable, to ensure consistent comparison. It may vary slightly based on the nature of the results and the type of simulation performed.

For steady-state simulations, the analysis is performed on the final converged flow field. In the case of unsteady simulations, once convergence is reached, a full revolution of the compressor is simulated. The time-averaged solution over this full revolution, provided by the CFD code elsA, is used for subsequent analysis. When instantaneous flow fields from unsteady simulations are presented, this is explicitly stated; otherwise, the time-averaged solution is assumed by default.

For ease of interpretation, the three-dimensional flow field is typically reduced to lower-dimensional representations: two-dimensional (2D), one-dimensional (1D), or global (0D).

The 2D data are extracted as planar sections of the three-dimensional domain taken along iso-h/H lines, where h/H denotes the normalised channel height, going from 0 at the hub to 1 at the shroud; or at inter-plane stations perpendicular to the rotation axis. These planar sections can be directly analysed without further processing.

Another 2D representation consists of meridional views of the flow field, obtained by performing a mass-flow-weighted average over the azimuthal direction of the 3D solution onto a meridional plane. These views are used exclusively for stable operating points with azimuthally uniform inlet conditions.

One-dimensional data, representing radial variations of flow quantities within the compressor channel, are derived using a mass flow rate-weighted average for total quantities and a surface average for static quantities. These azimuthal averages provide a single representative value for each radial position, encompassing all azimuthal locations. This averaging procedure is occasionally applied in cases with non-uniform inlet conditions and is explicitly specified when used.

Finally, global data are obtained through mass flow-weighted averaging or surface averaging, similar to the approach used for experimental data, applied to 2D cuts. This yields single representative values for the entire configuration.

All data are presented in dimensionless form. Performance metrics are normalised with respect to selected reference operating points, such as the peak-efficiency condition $(X/X_{|PE})$ or the choke condition $(X/X_{|choke})$. Spanwise profiles are normalised by the mean value of

the corresponding reference profile: the experimental mean $(X/\overline{X}_{exp})$ when available, the mean of the highest-fidelity blade-resolved data $(X/\overline{X}_{ref})$ otherwise, or, when only Body-Force data are available, the mean of the reference Body-Force case $(X/\overline{X}_{ref})$. Meridional flow fields are normalised in the range between 0 and 1. Finally, in distortion studies, azimuthal profiles are normalised by the mean profile obtained under clean inflow conditions $(X/\overline{X}_{CLN}$ or $X/X_{CLN})$.

Conclusion

This chapter has laid the methodological and numerical groundwork for the investigations presented in this thesis. Two compressor configurations were introduced: one academic and one industrial. These were selected to span a range of geometric and aerodynamic complexities, covering operating regimes from high subsonic to fully transonic. The associated experimental datasets, which differ in richness and resolution, were also described. These datasets serve as validation references for blade-resolved calculations and support a detailed characterisation of the annulus flow field under varying conditions.

The numerical framework employed throughout this work was then presented. This includes the CFD solver elsA and its turbomachinery-specific features, the selected numerical parameters and boundary conditions, and a detailed comparison between blade-resolved and Body-Force modelling approaches. Finally, the post-processing strategies used to analyse both experimental and numerical results were described. These ensure consistent metrics for performance evaluation and flow field analysis. Particular attention was given to the derivation of the distortion deficit from the industrial compressor's experimental data.

With this foundation established, the thesis proceeds along two complementary paths that build on the approaches introduced here. Chapter 3 presents the blade-resolved simulations for the test cases introduced in this chapter, detailing the numerical configurations, validating the results against experimental data, and briefly characterising the resulting flow fields. These high-fidelity results serve both as reference benchmarks for the Body-Force calculations and as a basis for understanding key flow features. Chapter 4 builds upon these results to assess the baseline performance of the Body-Force model identified in Chapter 1 and explores a series of targeted modifications aimed at improving its predictive accuracy in the context of high-pressure, multi-stage compressors.

CHAPTER 3

GENERATION AND ANALYSIS OF HIGH-FIDELITY REFERENCE SIMULATIONS FOR THE COMPRESSOR TEST CASES

This chapter presents the reference blade-resolved, high-fidelity (U)RANS simulations performed as part of this work. It is divided into two parts, focusing respectively on the CREATE and IHPC compressors. For each case, the numerical configurations developed and analysed are described in detail, including their specific roles within the thesis and their relation to the numerical methods introduced earlier. The blade-resolved numerical results under clean inflow conditions are then validated against available experimental data to assess their accuracy and reliability. Finally, a concise characterisation of the flow field in each compressor is provided, highlighting the key aerodynamic features and flow phenomena relevant to the subsequent analyses.

Contents

3.1 High-Fidelity Simulations of the CREATE Compressor **68**
3.1.1 Numerical Blade-Resolved Configurations 68
3.1.1.1 Single Blade Passage Configuration 69
3.1.1.2 Periodic Sector Configuration 71
3.1.1.3 Periodic Sector Configuration 72
3.1.2 Validation against Experimental Data 73
3.1.3 Characterization of the Flow Field in the CREATE Compressor . . . 75
3.2 High-Fidelity Simulations of the IHPC Compressor **80**
3.2.1 Numerical Blade-Resolved Configurations 80
3.2.1.1 Single Blade Passage Configuration 81
3.2.1.2 Quasi-Periodic Sector Configuration 82
3.2.1.3 Full-Annulus Configuration 83
3.2.2 Validation against Experimental Data 84
3.2.3 Characterization of the Flow Field in the IHPC Compressor 87
Conclusion **89**

3.1 High-Fidelity Simulations of the CREATE Compressor

3.1.1 Numerical Blade-Resolved Configurations

Blade-resolved high-fidelity (U)RANS simulations form the core reference dataset for this thesis. Available experimental data for each compressor are used to validate the simulations, ensuring they accurately reproduce the operating behavior of the investigated machines. Once validation is confirmed and the numerical results show good agreement with the experimental data, the detailed flow field information from the simulations can be reliably used. These high-fidelity simulations thus serve as the primary reference for comparison, validation, and informing the Body-Force analyses in the following chapters.

The CREATE test case has been extensively studied through multiple numerical configurations, each developed and analysed in this work to address key objectives: validation of mesh grid sensitivity and numerical setup against experimental data under clean inflow conditions, creation of a reference database for Body-Force methodology assessment under clean inflow, and investigation of inlet distortion effects through both radial and circumferential distortion scenarios.

To fulfil these objectives, the compressor performance under clean inflow conditions is initially investigated using a single-blade-passage configuration with a mixing-plane interface. As introduced in Section 2.2.3, this setup models one blade passage per row with a steady-state approach, significantly reducing computational cost. It serves as the first validation step against experimental data and establishes the baseline for later comparisons with Body-Force simulations under clean inflow.

Building on this, the spatial periodicity of the CREATE compressor, corresponding to a $2\pi/16$ azimuthal sector as described in Section 2.1.1, is leveraged by simulating that sector

using a sliding mesh approach detailed in Section 2.2.1. This configuration enables investigation of unsteady flow phenomena within the compressor annulus, assessment of radial inlet distortion effects, and development of the methodology required for full-annulus simulations with very large computational meshes. This configuration is depicted in Figure 3.1, with the single-blade-passage case highlighted in red.

Finally, to investigate azimuthal distortion effects while managing computational expense, a P2D full-annulus configuration employing a sliding mesh approach is considered. This setup balances the need for azimuthal resolution with reduced computational cost compared to fully three-dimensional simulations.

In the following sections, each configuration is described in terms of geometry, mesh characteristics, time step when relevant, and boundary conditions, including the inflow conditions and corresponding inlet maps for each case.

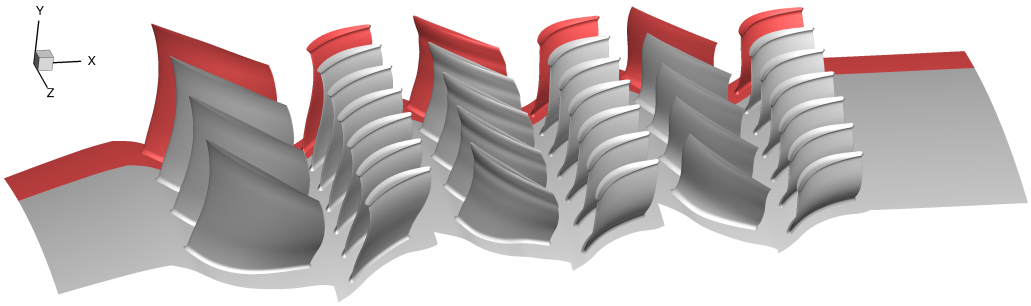

Figure 3.1: Domain of the $2\pi/16$ periodic sector configuration of the CREATE compressor, and single-blade-passage highlighted in red.

3.1.1.1 Single Blade Passage Configuration

Geometry The single-blade-passage (SBP) configuration employed in the CREATE numerical setup replicates the geometry of the experimental axial compressor, with targeted simplifications introduced to reduce computational cost. Specifically, the inlet guide vane (IGV) is excluded from the computational domain, but accounted for in the inflow condition. As a result, the numerical model includes only the blade rows from the first rotor (R1) to the third stator (S3). All technological effects, except the fillets ant tip gaps, are neglected. The numerical domain for this configuration is highlighted in red in Figure 3.1.

Mesh For this configuration, the mesh employed is slightly coarser than that defined by the mesh criteria presented in Section 2.2.3. The final meshing strategy outlined there was developed to meet the requirements of unsteady simulations, where accurately capturing rotor-stator interactions and resolving blade wakes is essential. In contrast, the single-blade-passage CREATE configuration was generated prior to this refinement step and therefore uses a slightly coarser mesh. Nonetheless, it remains sufficiently fine for the steady mixing-plane approach adopted in this case. The final mesh contains approximately 8.82×10^6 cells. Further details on the single-blade-passage mesh and its later refinement for unsteady simulations are provided in Appendix A.

Boundary Conditions The boundary conditions for this case correspond to those described in Section 2.2.3, with a mixing-plane interface applied at the rotor-stator boundaries, to perform steady-state calculations.

Inflow Conditions In the absence of the IGV, appropriate inflow boundary conditions must be applied at the domain inlet to ensure consistency with the physical system. These boundary conditions are derived from experimental measurements taken immediately downstream of the IGV in the test rig, at experimental plane 25A, as defined in Figure 2.1. The corresponding data are imposed directly at the computational inlet, which coincides with the region upstream of the first rotor row.

The inflow is specified using an axisymmetric inlet map derived from azimuthally averaged experimental data across the annulus radius. For the CREATE configuration, this map is discretised into fifteen radial points, corresponding to the experimental resolution. This approach enables the simulation to incorporate realistic inflow conditions without explicitly modelling the upstream duct and the inlet guide vane. All seven inlet flow quantities are prescribed as non-uniform radial profiles. These include total pressure, total temperature, the three velocity unit vectors along the x-, y-, and z- directions, the turbulent kinetic energy k, and the integral length scale l. Figure 3.2 shows the inlet total pressure and total enthalpy profiles imposed in the single-blade-passage configuration. A noticeable increase in total temperature near the hub is present, corresponding to a heated mass flow introduced during the experiment. Although the upstream duct and IGV are not modelled, this feature is accurately reproduced in the simulation thanks to the use of experimental data at the inlet, allowing key physical effects to be retained despite the simplified domain.

The described map serves as the baseline inlet condition for all CREATE simulations performed under clean inflow, whether using a single-blade-passage (SBP), a $2\pi/16$ periodic sector, or a full-annulus 360° configuration.

Initialisation Field The single-blade-passage calculation is initialised using a meridional field.

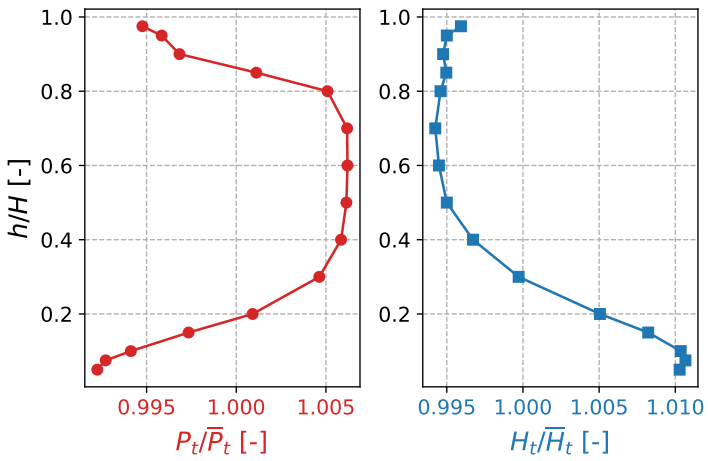

Figure 3.2: Inlet boundary condition characterization for the CREATE single-blade-passage case: radial profiles of total pressure (red) and enthalpy (blue), normalised by their respective mean values.

3.1.1.2 Periodic Sector Configuration

Geometry The $2\pi/16$ periodic sector configuration of the CREATE compressor is constructed by azimuthally replicating the single-blade-passage (SBP) domain. The number of blade passages matches the periodicity defined by the actual blade count, ensuring a geometrically accurate representation of the rotor-stator arrangement. The blade count for this configuration has been previously detailed in Table 2.3.

This configuration retains the features of the single-blade-passage setup, including the exclusion of the inlet guide vane (IGV) and the application of the clean baseline inlet map for the study of undistorted inflow conditions. A schematic of the three-dimensional computational domain of the periodic sector is shown in Figure 3.1, with the single-blade-passage domain highlighted in red.

Mesh The mesh employed for this configuration adheres to the criteria outlined in Section 2.2.3, which were developed specifically to resolve the complex unsteady flow phenomena inherent in rotor-stator interactions and blade wake dynamics. The overall mesh comprises 64.27×10^6 cells.

Time Step The criterion of 60 time steps per blade passage outlined in Section 2.2.2 corresponds here to 6720 physical time iterations per revolution, yielding a time step of 7.74×10^{-7} s. This criterion also corresponds to a maximum of 105 time steps in the first rotor row per blade passage.

Boundary Conditions Boundary conditions are consistent with those described in Section 2.2.3, with a sliding mesh condition applied at the rotor-stator interfaces. This approach exploits the perfect multiple relationship between the number of rotor and stator blades, enabling accurate modelling of relative blade row motion and associated unsteady phenomena.

Inflow Conditions In addition to the baseline clean inflow map, a modified inlet condition is introduced to investigate the impact of radial inlet total pressure distortion on compressor flow dynamics. Although such distortion could be applied on the single-blade-passage configuration, its effects on unsteady phenomena are more comprehensively captured in the periodic sector domain due to the enhanced spatial and temporal resolution and the capture of unsteady phenomena.

The radial distortion profile is based on industrial data representing the total pressure distribution downstream of an S-duct intake, but was not tested during the experimental campaign. This dimensionless profile is applied multiplicatively to the mean total pressure of the clean inlet map to generate the distorted inlet map. The radial distortion profile and the resulting inlet map are illustrated in Figure 3.3. In particular, Figure 3.3a shows the comparison between the radial profile of total pressure for the clean and the radially distorted cases, where the latter exhibits more pronounced variations especially at the shroud.

Initialisation Field The $2\pi/16$ sector calculations are initialised with the converged solution of the single-blade-passage calculation at the peak efficiency point, duplicated by the number of blade passages of the $2\pi/16$ configuration.

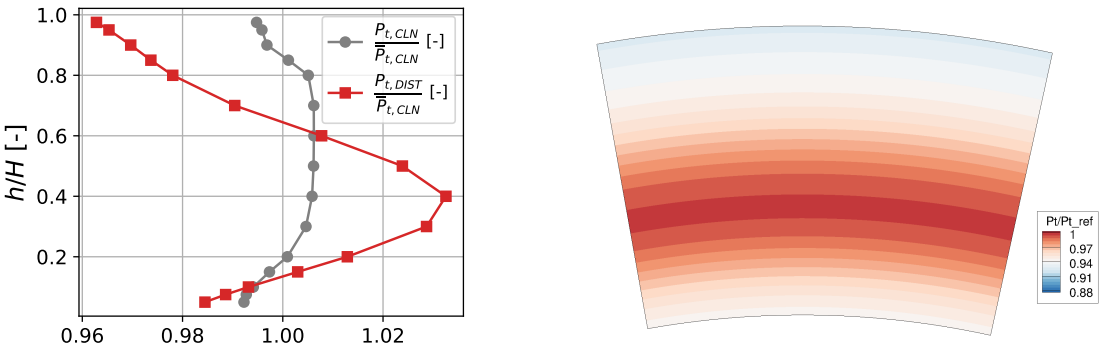

(a) Inlet radial profile of total pressure distortion. **(b)** Inlet total pressure map of radial distortion.

Figure 3.3: Radial distortion profile and resulting inlet map for the $2\pi/16$ periodic sector configuration of the CREATE compressor un radial distortion.

3.1.1.3 Periodic Sector Configuration

Geometry The Pseudo-2D (P2D) configuration was developed to study the impact of azimuthal distortions on the compressor flow field, while significantly reducing computational costs. This approach provides a practical alternative to the full three-dimensional 360° configuration, which would require a mesh size exceeding one billion cells.

The numerical domain of the P2D configuration differs from the previously described cases. It is constructed by isolating a narrow streamtube centered around the mid-span region, approximately at 50% of the channel height, and extending vertically over about 5% of the channel height. The domain for the single-blade-passage P2D configuration is shown in gray in Figure 3.4, while the 3D single-blade-passage case is represented in white.

Additionally, as illustrated in Figure 3.4, the mesh block upstream of the first rotor has been split. Since the first row of the domain is rotating, but the distortion must be applied at a stationary inlet, a non-rotating mesh block is positioned at the inlet, with a rotor-stator interface between this block and the first rotor. This setup ensures that the distortion map can be correctly applied in the simulation as a steady distortion in the absolute frame.

To enable the study of azimuthal flow distortions and to capture circumferential interactions, this configuration is subsequently extended to a full annulus configuration through periodic replication of the single-blade-passage.

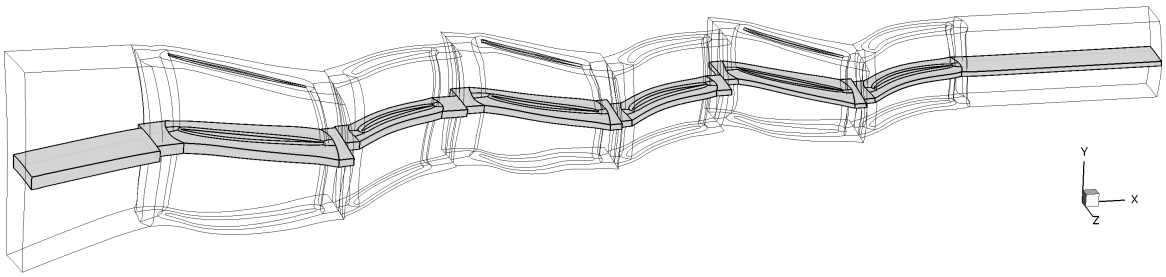

Figure 3.4: Computational domain of the single-blade-passage P2D configuration of CREATE, compared to the single-blade-passage 3D case.

Mesh The blade-to-blade and axial mesh discretisation for the P2D configuration is identical to that used in the $2\pi/16$ periodic sector case, ensuring consistent resolution of flow structures in the circumferential and axial directions. In the radial direction, however, the mesh is reduced to only four cells of uniform height. The obtained spanwise resolution corresponds to the mesh distribution at mid-span in the $2\pi/16$ configuration, thereby maintaining consistency in grid topology within the extracted streamtube. The overall mesh size is of 53.99×10^6 mesh cells across the full-annulus.

Time Step As for the periodic sector configuration, 6720 physical time iterations are performed per revolution, yielding a time step of 7.74×10^{-7} s.

Boundary Conditions The boundary conditions applied in this setup are those described in Section 2.2.4. A sliding mesh interface is implemented at the rotor-stator boundaries to resolve unsteady interactions, while slip wall conditions are imposed at both the hub and shroud boundaries. The overall boundary condition setup is depicted in Figure 3.5 for an isolated blade passage for clarity. The BCs are: the inlet in red, the outlet in blue, the row interfaces in green, the no-slip walls in gray and the slip walls in orange.

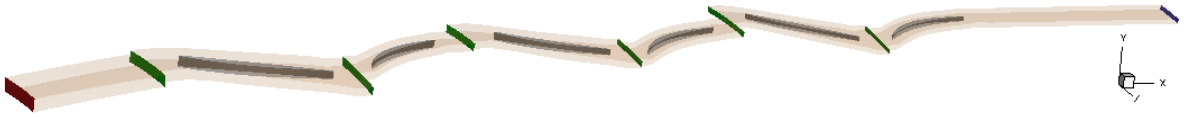

Figure 3.5: Boundary condition setup for the single-blade-passage P2D case for the CREATE configuration.

Inflow Conditions For the clean inlet condition, total pressure, total temperature, turbulent kinetic energy k, and integral length scale l are prescribed as uniform values. These are extracted from the clean inlet map used for the single-blade-passage configuration, at 50% h/H. The inlet velocity vector is aligned accordingly, with unit magnitude and direction matching the local flow orientation at mid-span.

To investigate the effects of azimuthal distortion, two additional inlet maps are generated. These introduce a circumferential sector of 120° with a total pressure deficit, imposed as a percentage reduction relative to the clean inlet value. Two distortion amplitudes are considered: -4% and -10%. The azimuthal distortion profile is applied to the clean inlet total pressure value, while other inlet quantities remain unchanged. The applied total pressure profiles and the two-dimensional representations of the -4% distortion map are presented in Figure 3.6.

Initialisation Field The P2D calculations are initialised with the converged solution of the single-blade-passage P2D case at the peak efficiency point, which is itself initialised with a meridional field. The single-blade-passage P2D solution is thus duplicated over the full annulus to initialise the complete configuration.

3.1.2 Validation against Experimental Data

The single-blade-passage configuration previously presented is investigated to validate the numerical results against the available experimental data.

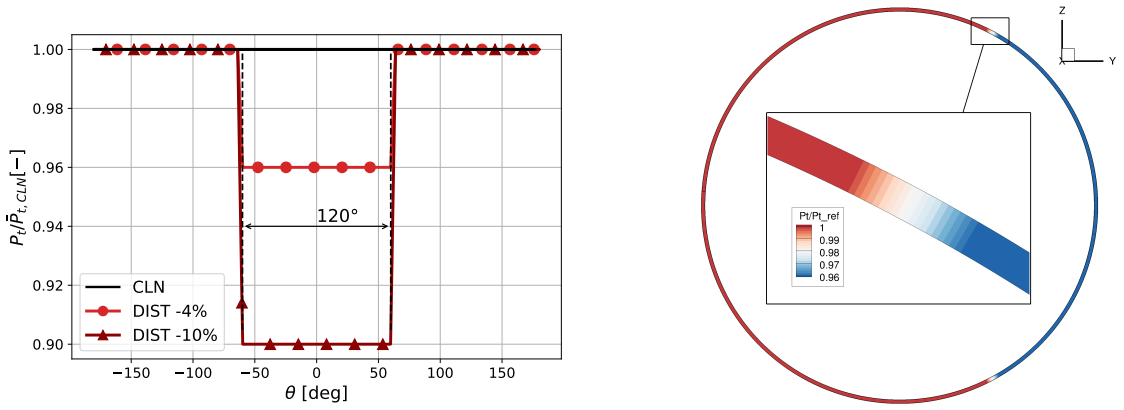

(a) Azimuthal profiles of total pressure of the -4% and -10% azimuthal distortion cases.

(b) Two-dimensional total pressure inlet map of the -4% azimuthal distortion case.

Figure 3.6: Azimuthal total pressure distortion features for the P2D simulations of CREATE.

Global Performance An initial assessment is performed through the analysis of the integral performance of the compressor. Figure 3.7 shows the total-to-total pressure ratio and the isentropic efficiency plotted against the corrected mass flow rate for the complete three-stage compressor, as well as for each individual stage, comprising a rotor followed by its corresponding stator.

The data presented include experimental results (shown in red) and numerical results from the single-blade-passage simulations (shown in green). Specifically, the experimental data correspond to the peak efficiency (PE) operating point, which serves as the reference for the normalization of the total-to-total pressure ratio, the isentropic efficiency, and the corrected mass flow rate, and the near stall (NS) operating point.

The numerical predictions exhibit a good degree of accuracy in capturing the total-to-total pressure ratio for both the overall compressor and individual stage performance, with deviations limited to within 2-3% relative to the experimental measurements at iso-corrected mass flow rates. Likewise, the isentropic efficiency is accurately predicted for the full compressor configuration, with a maximum deviation of approximately 2%.

Minor discrepancies arise at the stage level, where the numerical model tends to underestimate the isentropic efficiency of the first stage while overestimating that of the second stage. These opposing deviations partially compensate for each other, resulting in good aggregated performance. However, the error in isentropic efficiency is of less than 0.05 percentage points in the absolute efficiency value. This level of agreement is considered satisfactory for the purpose of the study, and it demonstrates the reliability of the numerical predictions not only in terms of global performance but also on a stage-by-stage basis. Overall, the performance of the experimental compressor is well reproduced, providing confidence that the simulations serve as a reliable reference for subsequent developments.

Local Flow Behaviour A further investigation is carried out through the analysis of the radial profiles of flow quantities along the channel height at various axial stations within the compressor. Figure 3.8 shows the evolution of total pressure and total temperature, with experimental data plotted in red and single-blade-passage numerical predictions in green. The profiles are presented downstream of each rotor and at the compressor outlet.

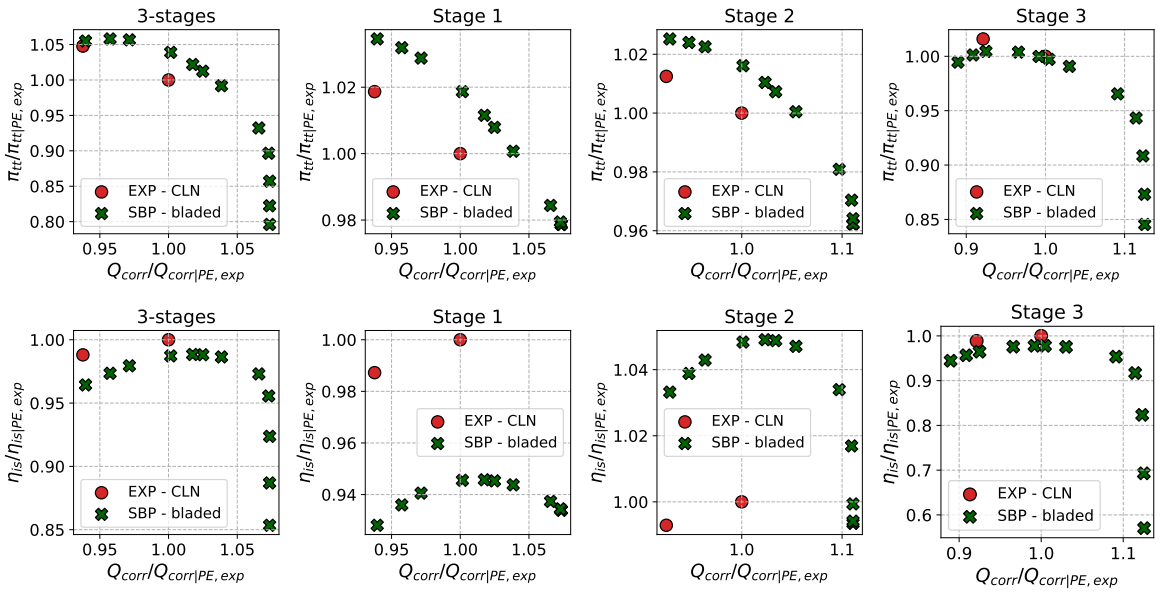

Figure 3.7: Compressor map of total-to-total pressure ratio and isentropic efficiency vs. corrected mass flow for experimental data (red circles) and blade-resolved single-blade-passage (green crosses).

Overall, the numerical predictions show very good agreement with the experimental data. The total pressure distribution is accurately reproduced, with a maximum deviation of approximately 2.5% at the compressor outlet. The total temperature profiles are also well captured at the hub and at mid span, although a noticeable offset appears near the shroud, becoming significant at certain axial stations. These discrepancies may arise from the absence of technological effects in the numerical domain or from a high sensitivity of the simulation to secondary flows, which may be overestimated. Despite these local differences, the overall agreement between numerical and experimental data remains strong and is representative of the compressor behaviour, supporting the validity of the numerical results and justifying their use in the remainder of this thesis. Although only numerical data are employed in the following sections, their demonstrated consistency with the experimental measurements ensures a robust and reliable connection to the physical configuration.

3.1.3 Characterization of the Flow Field in the CREATE Compressor

This section presents a concise characterization of the flow field within the CREATE compressor, focusing on representative features of the main flow under nominal, undistorted conditions. The results employed here are issued from a URANS calculation of the $2\pi/16$ periodic sector of the machine, at the peak efficiency operating point.

Mid-Span Flow An initial assessment of the flow field is conducted through a cut at 50% channel height of the three-dimensional computational domain. This plane is selected to minimise the influence of secondary flow phenomena and endwall effects, providing a clearer view of the core aerodynamic behavior.

Figure 3.9 illustrates the relative Mach number distribution and the axial momentum field along the mid-span plane.

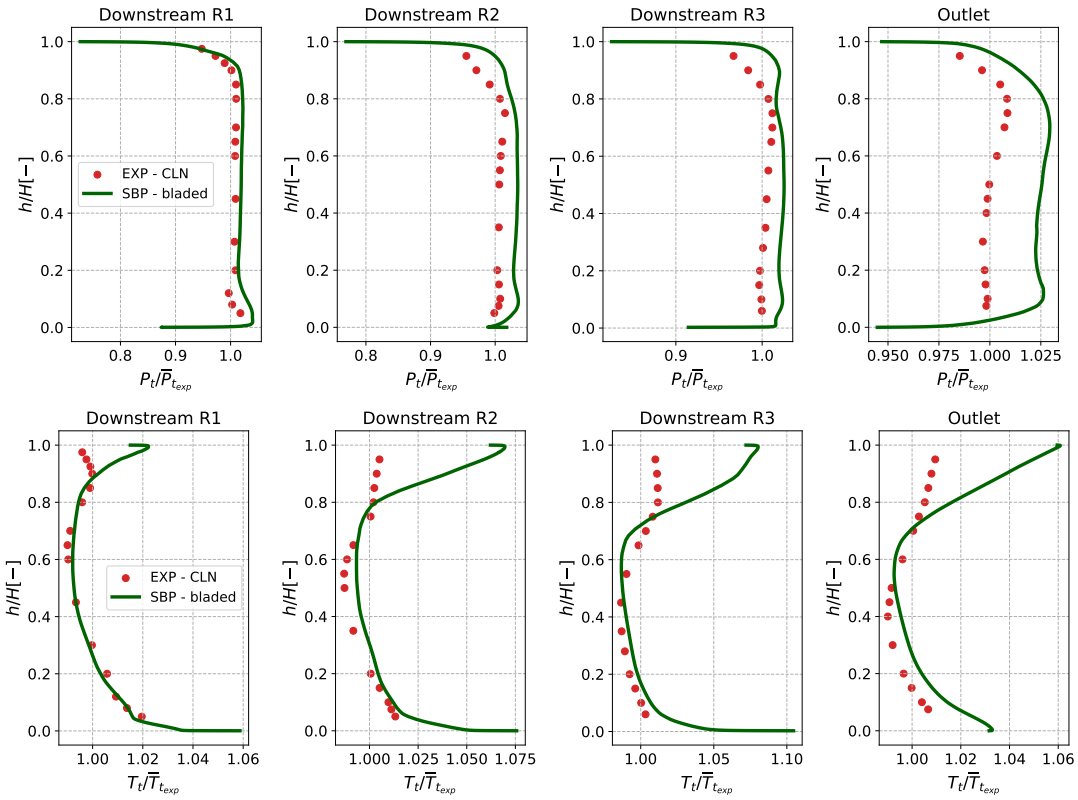

Figure 3.8: Mass flow-averaged radial profiles of total pressure and total temperature along the compressor channel are presented. Results from the SBP and experimental data are compared at multiple axial locations.

Figure 3.9a illustrates the relative Mach number distribution at 50% channel height. A pronounced acceleration occurs on the suction side of each rotor blade, with the first rotor reaching locally transonic conditions near the leading edge, as indicated by the $M_{\text{rel}} = 1$ iso-line. In the downstream stages, the intensity of this suction-side acceleration gradually decreases, and the flow remains predominantly subsonic, reflecting the progressive rise in static pressure throughout the compressor. Beyond the leading-edge acceleration region, the flow decelerates along the remainder of the blade span, a behaviour associated with the diffusion imposed by the blade passages. The blade geometry and stagger angles guide the flow, ensuring a smooth redistribution of velocity and pressure within each stage.

The axial momentum distribution, shown in Figure 3.9b, increases steadily through the compressor. This rise is primarily due to the density increase from compression, while annulus convergence helps maintain an approximately uniform axial velocity. As the flow passes through each rotor-stator pair, the blades' work further raises static pressure and density, resulting in a net gain in axial momentum. Local deviations occur in the blade wakes, where viscous effects create momentum deficits; these are recovered downstream as the flow is re-accelerated by the following blade row.

To examine the first stage in more detail, Figures 3.10a and 3.10b show the relative Mach number and static pressure distributions at 50% channel height. Near the rotor leading edge, high relative Mach numbers correspond to low static pressure regions, indicating strong acceleration as enthalpy is converted into kinetic energy. Approximately one-third along the

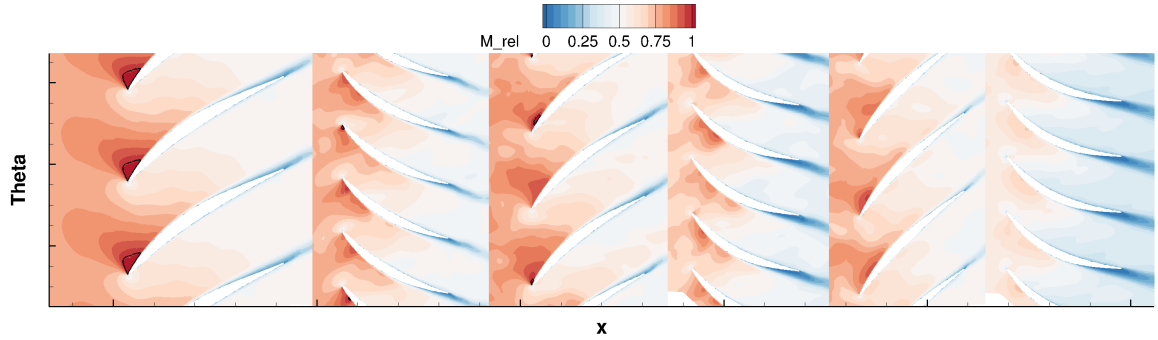

(a) Relative Mach number field at 50% channel height. The $M_{\text{rel}} = 1$ iso-line is shown in black.

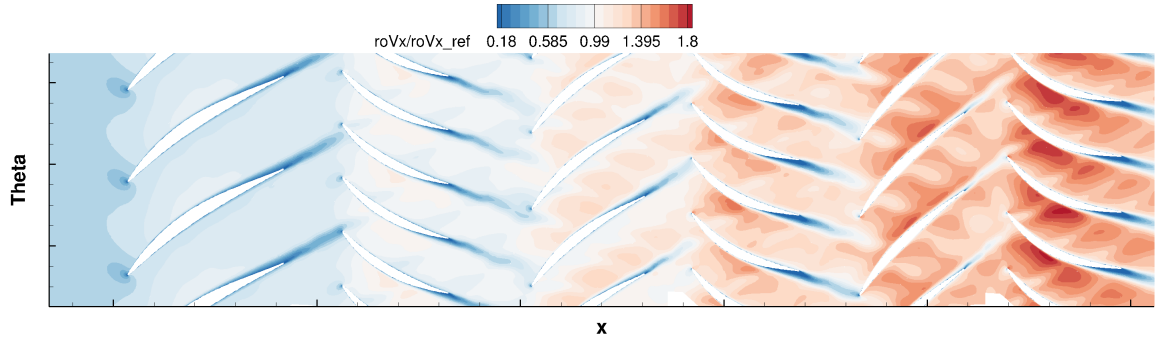

(b) Axial Momentum field at 50% channel height. Blade wakes appear as low-momentum regions.

Figure 3.9: Flow field characteristics at 50% channel height in the CREATE compressor.

blade chord, the flow decelerates and static pressure rises, reflecting the diffusion within the rotor passage. The stator further increases static pressure by gradually converting the remaining kinetic energy into static enthalpy, demonstrating its diffusive role in recovering pressure from the flow.

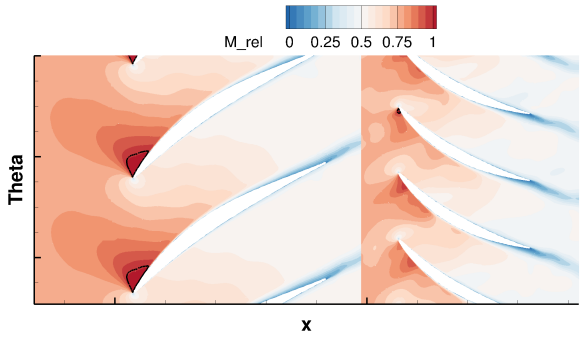

(a) Relative Mach number field at 50% channel height. The $M_{\text{rel}} = 1$ iso-line is shown in black.

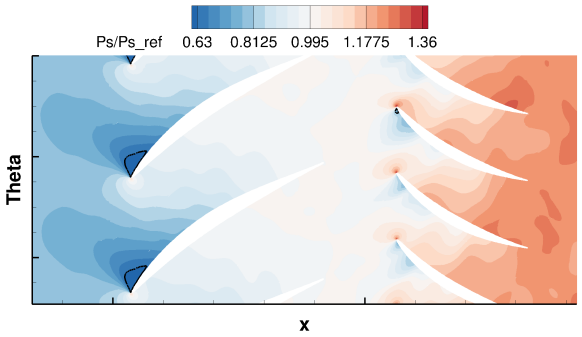

(b) Static pressure field at 50% channel height. The $M_{\text{rel}} = 1$ iso-line is shown in black.

Figure 3.10: Detailed view of the flow field at 50% channel height in the first stage of the CREATE compressor.

To conclude the analysis of the mid-span flow, Figure 3.11 presents the entropy distribution at 50% channel height for the first stage (Figure 3.11a) and the third stage (Figure 3.11b) of the CREATE compressor. In both cases, increased entropy levels are observed in the viscous

wakes of the blades, indicating aerodynamic losses.

In the first stage, a distinct interaction between the rotor wake and the downstream stator is evident, highlighting the effect of rotor-stator interaction on entropy generation. In the third stage, the entropy field exhibits a more complex structure resulting from the accumulated influence of multiple upstream blade rows. The wake mixing and diffusion from previous stages produce a broadened and less coherent loss pattern, which continues to impact the downstream rows. This results in elevated and spatially distributed entropy levels, representative of compounded mixing and loss mechanisms.

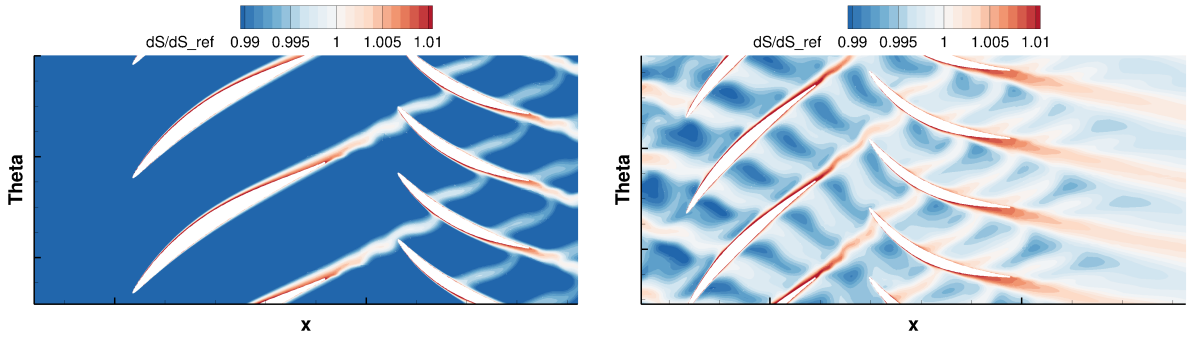

(a) First stage entropy distribution at 50% channel height.

(b) Third stage entropy distribution at 50% channel height.

Figure 3.11: Entropy distribution at 50% channel height in the first and third stages of the CREATE compressor.

Secondary Flows At the endwalls, specific secondary flow phenomena, introduced in Chapter 1, play a significant role in the overall aerodynamic behaviour of the compressor.

Near the casing, each rotor blade generates a tip leakage vortex (TLV) due to the finite tip gap. The entropy distribution at 97% of the channel height, shown in Figure 3.12, illustrates the pronounced effects of these vortices. The entropy field clearly indicates the presence of tip leakage vortices originating from each rotor blade, which interact with the pressure side of adjacent blades, leading to elevated entropy levels and associated aerodynamic losses. The intensity of these losses increases with the relative tip-clearance-to-chord ratio, which itself grows from the upstream to the downstream rows, a trend consistently observed from the front to the rear stages of axial compressors [122]. Furthermore, the trajectory of the TLVs becomes more aligned with the leading edge line as the tip clearance-to-chord ratio increases, suggesting a potential source of instability at higher tc/c values.

Near the hub, several vortical structures develop, with one of the most significant phenomena in the CREATE configuration being extensive corner separation. This can be visualized by the skin friction line patterns on the first rotor blade, as shown in Figure 3.13.

Subfigure 3.13a, depicting the suction side, reveals a large region near the hub where the skin friction lines delineate a clear corner separation, extending up to approximately 50% of the channel height at the trailing edge. This highlights the potential influence of vortex-induced interactions on the blade surface. In contrast, subfigure 3.13b, showing the pressure side, presents a more regular skin friction pattern. However, slight deviations near the blade tip are observed, likely caused by the interaction with the tip leakage vortex (TLV) from the

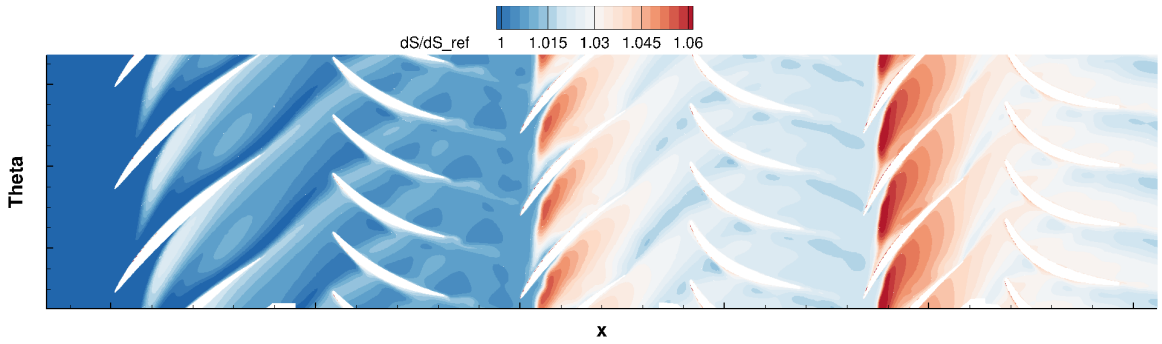

Figure 3.12: Entropy distribution at 97% channel height of the CREATE compressor.

adjacent blade passage. These observations globally align with entropy and velocity-based evidence of secondary flows and their effect on the blade boundary layers.

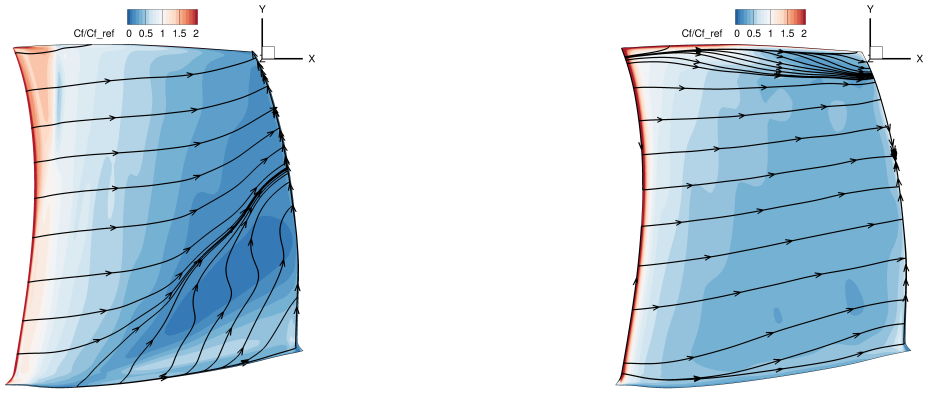

(a) Suction side of first rotor.

(b) Pressure side of first rotor.

Figure 3.13: Skin friction lines on the first rotor blade of the CREATE compressor.

The influence of secondary flow structures is further illustrated in the entropy distribution downstream of the first rotor. Figure 3.14 presents the entropy field on an iso-X plane located just downstream of the rotor's trailing edge.

Three distinct loss mechanisms are evident in this distribution. Near the casing, elevated entropy levels indicate tip leakage losses, generated by the tip leakage vortex formed at the rotor tip gap. A vertical band of increased entropy, aligned with the rotor wake, reflects losses due to viscous dissipation within the blade boundary layer and wake. Additionally, a stronger concentration of losses is observed along the lower half of the wake, closer to the hub. This is associated with the passage vortex and the separation it induces on the suction side of the rotor. These features highlight the spatial development of secondary losses and their significant contribution to overall stage inefficiency.

The analysis of the flow field confirms the presence and significance of secondary flow phenomena throughout the CREATE compressor. Tip leakage vortices, passage vortices, and rotor-stator interactions all contribute to the complex flow topology observed at various spanwise locations. These features make the CREATE compressor a representative high-pressure compressor configuration and provide important context for the subsequent analysis.

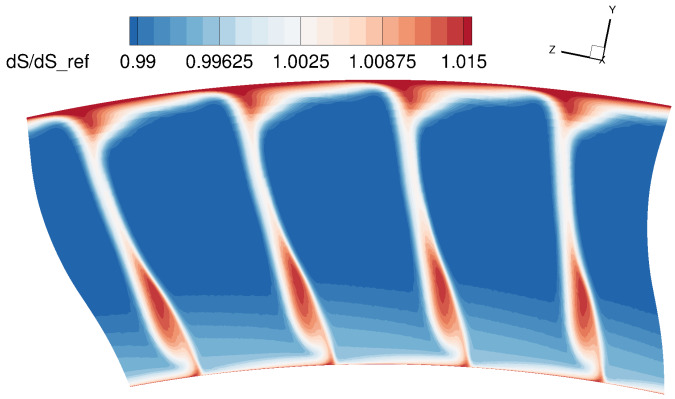

Figure 3.14: Entropy distribution on an iso-X plane at the outlet of the first rotor blade of CREATE.

3.2 High-Fidelity Simulations of the IHPC Compressor

3.2.1 Numerical Blade-Resolved Configurations

Similarly to the previous compressor, blade-resolved high-fidelity numerical simulations of the IHPC compressor are developed and validated against available experimental data. This validation ensures the reliability of the simulations, which form the basis for all subsequent analyses and discussions in this thesis.The main objectives of the IHPC numerical study are threefold: to perform an initial validation of the numerical setup against experimental results, to provide a dataset under clean inflow conditions for assessing the Body-Force model capabilities, and to investigate the compressor's response to azimuthal inlet distortion.

To achieve the first goal, the IHPC compressor is first investigated using a single-blade-passage, mixing-plane configuration. This setup allows a rapid preliminary assessment of numerical predictions and addresses the first objective. However, due to shock wave reflections at the mixing-plane interfaces, a limitation discussed in Section 2.2.1, this configuration showed significant discrepancies with experimental data and was therefore considered insufficient.

To overcome these limitations and fulfill the first two objectives, a quasi-periodic azimuthal sector configuration was developed. Since the IHPC compressor lacks exact spatial periodicity, the Profile Transformation Approach (PTA) [46] introduced in Section 2.2.1 was applied to generate the computational domain. Unsteady RANS simulations were performed on this sector, which then became the reference configuration for validation and comparison with the reduced-order Body-Force model under clean inflow.

Finally, addressing the third objective, a full-annulus three-dimensional configuration of the entire compressor was simulated. Enabled by the substantial computational resources provided by GENCI [52], this setup allows a comprehensive investigation of the compressor's behaviour under azimuthal inlet distortion. The numerical domain of the full-annulus compressor is depicted in Figure 3.15, with the single-blade-passage configuration highlighted in blue and the quasi-periodic sector composed by the blue and red regions.

A detailed description of each configuration, covering geometry, mesh characteristics, time step, and boundary conditions, including inlet maps, is provided in the following sections.

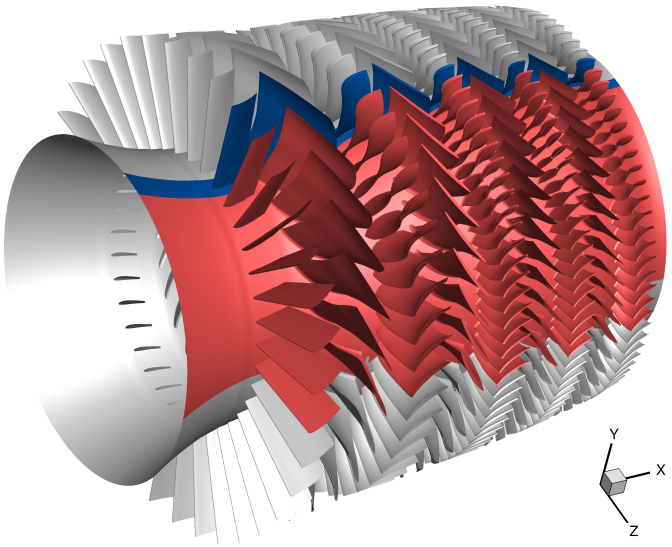

Figure 3.15: Full-annulus computational domain of the IHPC compressor.

3.2.1.1 Single Blade Passage Configuration

Geometry The single-blade-passage (SBP) configuration of the IHPC compressor replicates the complete experimental geometry, including all nine blade rows from the inlet guide vane (IGV) to the fourth stator (S4). All technological effects, except the fillets and tip gaps, are neglected. The three-dimensional computational domain used in this configuration is highlighted in blue in Figure 3.15.

Mesh The mesh employed in this simulation follows the guidelines detailed in Section 2.2.3, which are specifically designed to ensure adequate resolution of rotor-stator interactions, boundary layer development, and wake transport. The final mesh accounts for 19.7×10^6 mesh cells.

Boundary Conditions Boundary conditions are applied according to the methodology described in Section 2.2.3. A steady mixing-plane approach is used at each rotor-stator interface, enabling steady-state simulations while capturing the averaged effects of inter-row interactions.

Inflow Conditions The inlet conditions are defined using experimental data acquired at the peak-efficiency operating point under clean inflow conditions. As in the CREATE configuration, an axisymmetric inlet map is constructed by azimuthally averaging the measured radial profiles. The experimental map is discretised using six radial points and includes all seven required inlet quantities: total pressure, total temperature, the three velocity components, turbulent kinetic energy k, and turbulence length scale l. The resulting two-dimensional field is shown in Figure 3.16 for the total pressure and total enthalpy quantities.

This inlet map defines a uniform, undistorted inflow condition and is adopted as the reference boundary condition in all IHPC simulations performed under clean inflow conditions.

Initialisation Field The single-blade-passage calculations are initialised via a meridional field.

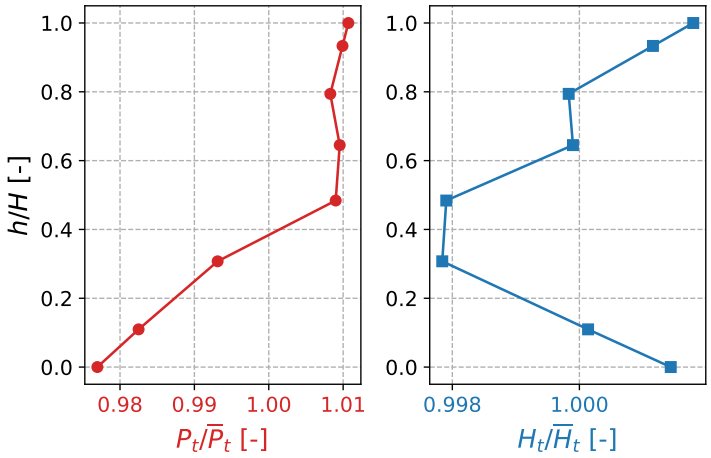

Figure 3.16: Inlet boundary condition characterization for the IHPC single-blade-passage case: radial proles of total pressure (red) and enthalpy (dark red), normalised by their respective mean values.

3.2.1.2 Quasi-Periodic Sector Configuration

Geometry The quasi-periodic sector configuration is a reduced case, compared to the full-annulus configuration, that enables the simulation of a large azimuthal domain while maintaining manageable computational cost. This configuration consists of a sector of around 90° of the compressor, as it represents the smallest sub-portion of the full annulus that remains as close as possible to satisfying periodicity for the majority of blade rows. The number of blades in each row for the quasi-periodic sector is reported in Table 3.1. The full-annulus values, introduced earlier in Section 2.1.2, are also recalled for comparison. The three-dimensional domain for this configuration is defined by the combined red and blue regions shown in Figure 3.15.

Table 3.1: Number of blades per row in the IHPC compressor: full annulus (2π) and quasi-periodic sector.

Sector	IGV	R1	S1	R2	S2	R3	S3	R4	S4
Full-annulus	36	28	49	40	84	52	90	56	78
Quasi-periodic	9	7	12	10	21	13	22	14	19

Mesh The computational mesh for the quasi-periodic sector is constructed by azimuthally replicating the single-blade-passage (SBP) mesh described previously. Each row is duplicated so that its number matches the blade passages indicated in Table 3.1. The resulting mesh contains approximately 261×10^6 cells.

Time Step For this case, the value of D_m, defined in Equation 2.1, is not equal to the ideal value of four, due to the non-perfect periodicity of the domain. The specific value computed for the IHPC quasi-periodic sector is $D_m \simeq 4.031$.

With 60 iterations per blade passage, corresponding to 5400 iterations per revolution, and taking into account the value of D_m, the resulting time step is 5.86×10^{-7} s.

Boundary Conditions The approach enabling the simulation of a quasi-periodic sector, for which a perfect spatial periodicity is not present across all bladed rows, is the Profile Transformation Approach presented in Section 2.2.1. As shown in Table 3.1, most blade rows are periodic within the selected 90° sector. However, some rows, specifically S1, S3, and S4, do not exhibit exact periodicity. For these rows, the PTA is used to impose modified circumferential boundary conditions at the rotor-stator interfaces. All remaining boundary conditions are consistent with the methodology presented in Section 2.2.3.

Inflow Conditions The inflow condition applied in this case corresponds to the clean, undistorted inlet map defined for the single-blade-passage configuration. All other boundary conditions follow the same methodology outlined earlier in Section 2.2.3.

Initialisation Field The quasi-periodic sector calculations are initialised with the converged solution of the single-blade-passage case at the peak efficiency point.

3.2.1.3 Full-Annulus Configuration

Geometry The full-annulus (360°) configuration of the IHPC compressor is constructed by azimuthal replication of the blade sectors defined in the single-blade-passage case. The baseline geometry remains unchanged and includes all nine bladed rows, from the inlet guide vane (IGV) to the fourth stator (S4). The complete three-dimensional numerical domain is shown in Figure 3.15, where the single-blade-passage is highlighted in blue, and the quasi-periodic sector is represented by the combined blue and red regions.

Mesh The mesh used in this configuration follows the discretisation criteria outlined in Section 2.2.3, consistently with the previous configurations. Owing to the complete circumferential extension, the resulting mesh is significantly larger and more computationally demanding, containing 1.05×10^9 mesh cells.

Time Step The time discretization criteria described in Section 2.2.2, which require at least 60 iterations per blade passage, correspond to 5400 iterations per revolution for the IHPC compressor. This translates to a physical time step of 5.91×10^{-7} s.

Boundary Conditions Unlike the quasi-periodic sector configuration, the full-annulus setup does not require the Profile Transformation Approach. A sliding mesh condition is applied at all rotor-stator interfaces, allowing for fully unsteady interactions between blade rows throughout the entire annulus. This enables high-fidelity resolution of azimuthally non-uniform and transient flow phenomena, including those induced by upstream distortions.

Inflow Conditions The inlet boundary condition for the clean, undistorted case is the same as the one used in the single-blade-passage and quasi-periodic configurations. It corresponds to the axisymmetric inlet map derived from azimuthally averaged experimental measurements at the peak-efficiency operating point.

To investigate the compressor's sensitivity to azimuthal inflow non-uniformity, an additional distorted inlet map is implemented. The distorted condition is designed to replicate the non-uniform inflow measured experimentally, as described in Section 2.3.1. Specifically, a 105° azimuthal sector at the inlet is subjected to a total pressure deficit corresponding to a corrected distortion coefficient of $k_{j=5,\text{new}} = -3.5\%$, as defined in Equation (2.15). The resulting inlet map for the distorted case is a combination of the inlet radial profiles of the clean inlet case and this newly introduced azimuthally distorted sector, and is illustrated in Figure 3.17. In particular, Figure 3.17a depicts the radial and azimuthal profiles of total pressure for a clean and a distorted sector, while Figure 3.17b shows the resulting inlet map.

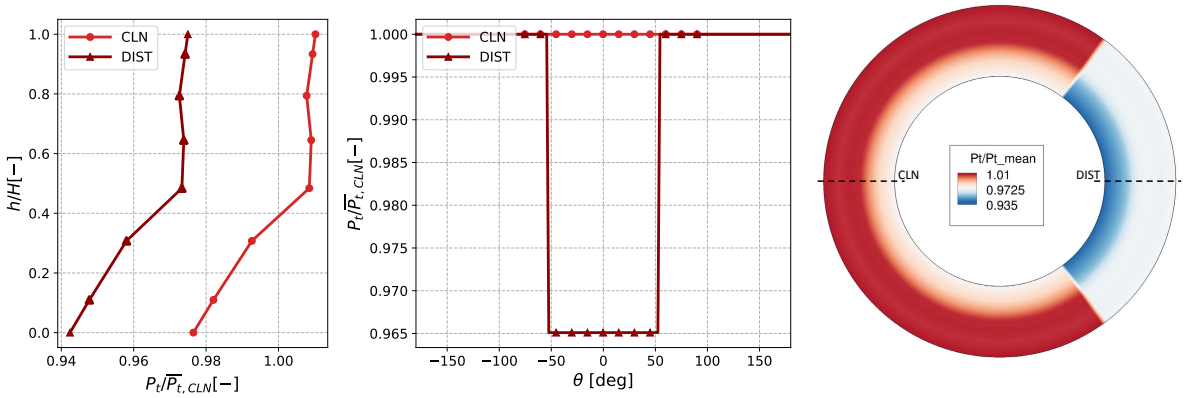

(a) Radial and azimuthal profiles of total pressure. **(b)** 2D inlet map of P_t.

Figure 3.17: Azimuthal total pressure distortion features for the full-annulus IHPC simulations.

Initialisation Field The full-annulus calculations are initialised with the converged solution of the quasi-periodic sector case at the peak efficiency point. To do so, the solution of a single channel is isolated from the $2\pi/4$ domain, and it is multiplied for the number of blade passages in the full-annulus configuration.

3.2.2 Validation against Experimental Data

The experimental data of the IHPC compressor are compared against the various available numerical configurations and modelling approaches for validation purposes.

Global Performance As with the CREATE compressor, the integral one-dimensional performance of the IHPC compressor is first analysed. Figure 3.18 presents the total-to-total pressure ratio as a function of the corrected mass flow rate, both for the complete 4.5-stage configuration and for each individual pseudo-stage (PSn). Each pseudo-stage PSn is defined as the combination of stator $n-1$ and rotor n. This definition is adopted to match the experimental measurement layout of the IHPC compressor, where flow quantities are available only at the leading edges of the stators. Accordingly, the experimental data for a given pseudo-stage PSn are taken at the leading edge of stator $n-1$, representing the upstream boundary, and at the leading edge of stator n, representing the downstream boundary.

In Figure 3.18, the presented data include: experimental results (red circles), mixing-plane single-blade-passage simulations (green crosses), PTA $2\pi/4$ sector simulations (blue diamonds),

and full-annulus 2π simulations (white triangles). All results are normalised with respect to the peak-efficiency operating point under clean inflow conditions from the experimental campaign.

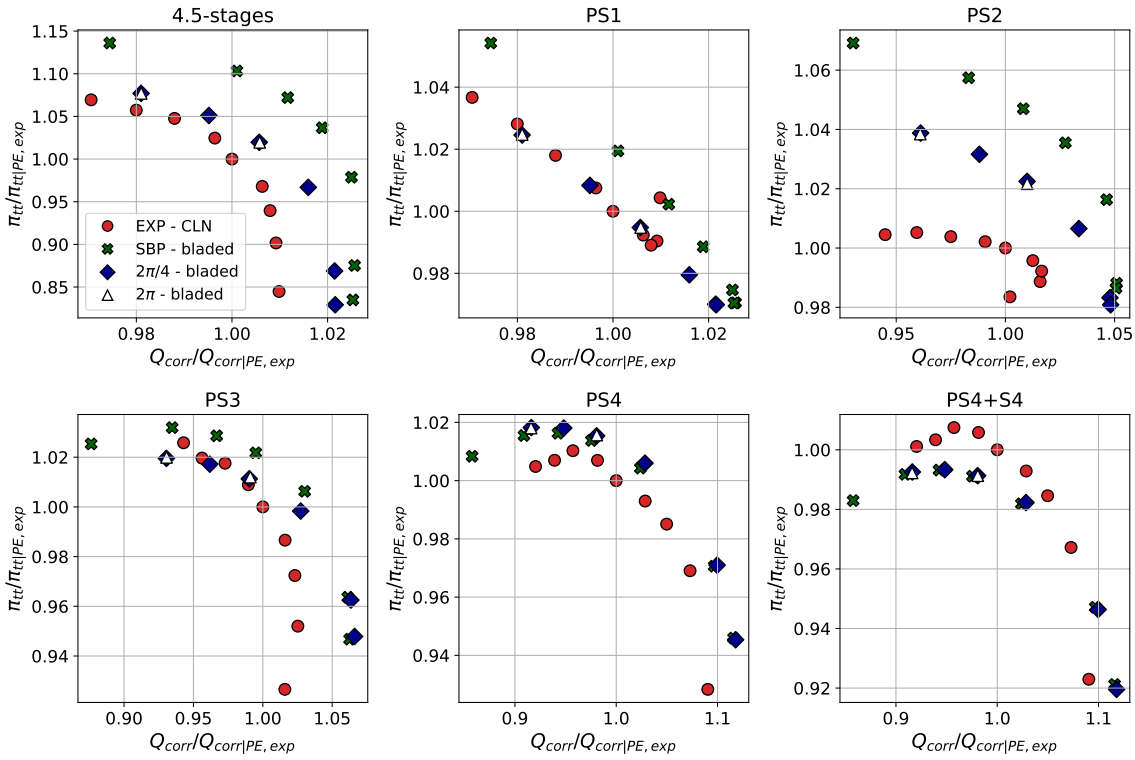

Figure 3.18: Compressor map of total-to-total pressure ratio vs. corrected mass flow with experimental data (red circles), single-blade-passage simulations (green crosses), $2\pi/4$ sector simulations (blue diamonds), full-annulus 2π simulations (white triangles).

As anticipated, the mixing-plane case shows significant discrepancies with respect to the experimental results. These are primarily due to artificial shock reflections at the mixing planes, particularly upstream of the leading edges of the first and second rotors, which introduce inaccuracies in the compressor map at pseudo-stages one and two. The PTA configuration significantly reduces these errors. The overall 4.5-stage performance closely matches the experimental data, with only a 1% difference in mass flow rate at the choke point. The performance of pseudo-stages one, three, and four is also well captured. Pseudo-stage two, however, continues to exhibit notable deviations, with an underprediction of the total pressure ratio by approximately 2% at the peak efficiency point and nearly 4% at near-stall. This discrepancy is not attributed to modelling or numerical setup errors, but rather to the inherent difficulty in capturing accurate stage matching numerically, compounded by the unusually flat characteristic observed experimentally for this stage.Nonetheless, the PTA approach substantially improves the accuracy compared to the mixing-plane approach. Additionally, the PTA results closely matche the full-annulus simulation, reinforcing confidence in the PTA methodology and confirming its reliability for the present compressor configuration.

Overall, the numerical results provide an accurate representation of the IHPC compressor's performance and are considered sufficiently representative of the real machine to support the subsequent analyses conducted in this thesis.

Local Flow Behaviour A second validation step is carried out by analyzing the radial evolution of total pressure and total temperature along the channel height at various axial stations throughout the compressor.

Figure 3.19 presents these profiles for the different simulation cases. Experimental data are shown in red. Due to the limited number of exploitable measurements, all valid experimental points are reported in the plots. The single-blade-passage (SBP) results are shown in green, while the quasi-periodic sector ($2\pi/4$) and full-annulus (2π) simulations are shown with a dashed blue line and a dotted light blue line, respectively.

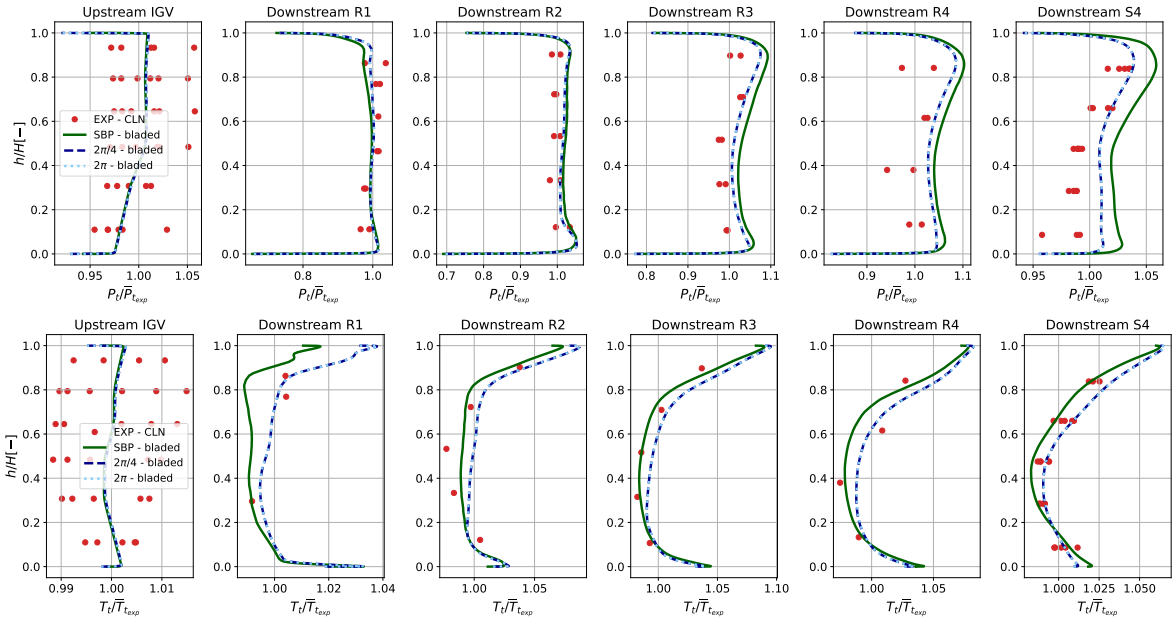

Figure 3.19: Mass flow-averaged radial profiles of total pressure and total temperature along the compressor channel. Experimental data are shown as red dots. Results from single-blade-passage, $2\pi/4$, and full-annulus 2π simulations are compared at multiple axial stations.

The top row of plots illustrates the total pressure distributions. Overall, good agreement is observed between the numerical predictions and the experimental data. A slight discrepancy exists between the single-blade-passage case and the quasi-periodic sector and full-annulus cases, with the latter two exhibiting consistently better alignment with the measurements. In particular, the $2\pi/4$ and 2π results remain within 2% of the experimental values across all stations.

The bottom row shows the total temperature profiles, where a similar trend is observed. The single-blade-passage case performs less accurately, especially in capturing the total temperature rise at the first rotor tip. In this region, the SBP case fails to adequately reproduce the effects associated with the strong shock present in the upper half of the rotor blade. Conversely, the quasi-periodic sector and full-annulus cases show good agreement with the experimental data, with their radial profiles intersecting the measured values throughout the compressor.

These results provide further validation of the unsteady simulations, demonstrating their ability to accurately capture the physical behavior of the IHPC compressor. The consistency between these numerical approaches and the experimental data justifies their continued use in the subsequent analyses presented in this thesis.

3.2.3 Characterization of the Flow Field in the IHPC Compressor

This section presents a detailed characterization of the flow field within the IHPC compressor, based on blade-resolved URANS simulations conducted at peak efficiency operating conditions under clean, uniform inflow.

Mid-Span Flow A first characterization of the mid-span flow field is provided for the IHPC compressor, following an analogous approach to the one used for the CREATE compressor. Figure 3.20 presents the entropy distribution at 50% of the blade channel height for the entire compressor, where the 4.5 stages over a full 360° azimuthal domain are visible.

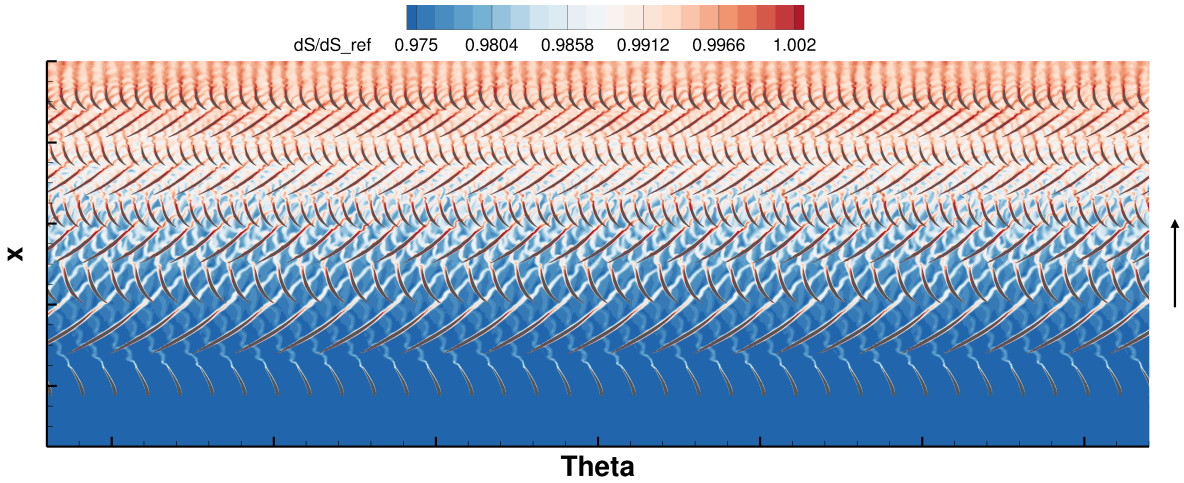

Figure 3.20: Entropy flow field at 50% h/H for the IHPC compressor.

The flow field appears uniform and exhibits clear azimuthal periodicity, with regions of high entropy, indicative of increased losses, located near the blade surfaces due to skin friction, as well as in the wake regions downstream of the blades. The mixing of blade wakes from each stage with those of subsequent stages results in a gradual increase in entropy along the axial direction of the compressor.

Further details regarding the behavior of different stages within the compressor are provided in Figures 3.21a and 3.21b, which display the relative Mach number and static pressure distributions at the first rotor row. Similarly, Figures 3.21c and 3.21d show the corresponding distributions for the fourth rotor. In both cases, the iso-$M_{rel} = 1$ contour is indicated in black.

The analysis reveals that the first rotor operates in a strongly transonic regime, with a normal shock developing on its suction side as the flow undergoes significant acceleration. Notably, since the left boundary of the plot corresponds to the rotor-stator interface, it can be inferred that the strong normal shock in the first rotor domain, when simulated using the mixing-plane approach, is reflected and leads to prediction errors, as discussed in Section 2.2.1. In contrast, the fourth rotor exhibits a limited supersonic region, still indicative of strong flow acceleration. This phenomenon is also present in the second and third rotors, though not shown here. Static pressure plots reveal low-pressure regions associated with shock formation, followed by a noticeable pressure recovery downstream, attributed to the expansion of the inter-blade region between the leading and trailing edges, resulting in a pressure rise as the flow decelerates through the blade passage.

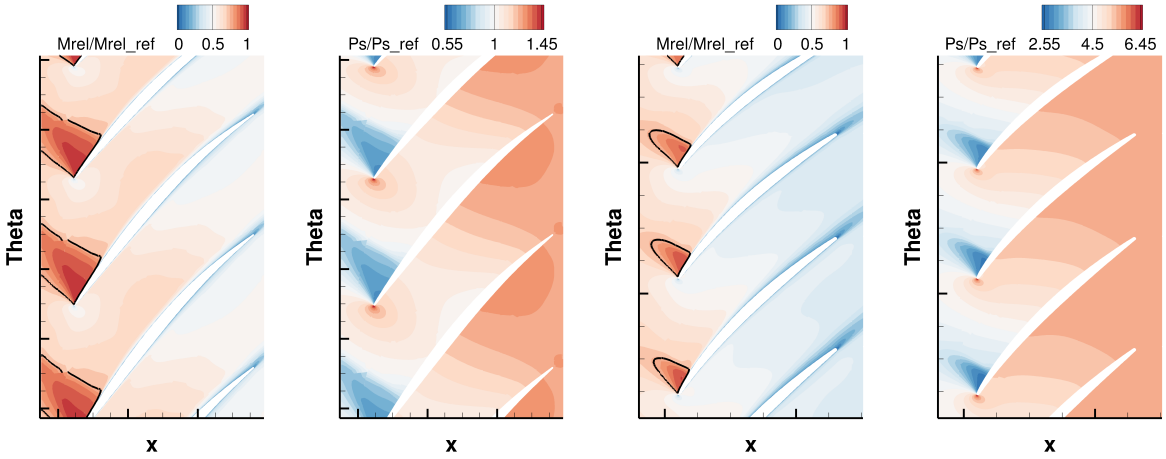

(a) M_{rel} at R1. **(b)** P_s at R1. **(c)** M_{rel} at R4. **(d)** P_s at R4.

Figure 3.21: Flow field characteristics at the first and fourth rotors of the IHPC compressor at 50% h/H. Contours of iso-$M_{rel} = 1$ line in black.

Secondary Flows To explore near-wall phenomena, Figure 3.22 presents a blade-to-blade entropy cut at 97% of channel height for each rotor. As observed in the CREATE compressor, rotor clearance generates a tip leakage vortex (TLV), which detaches from the rotor blade and impinges on the adjacent blade's pressure side, approximately on the second half of the chord. The intensity of the losses associated with the TLV increases with the relative gap-to-chord ratio, consistent with findings in the literature [122, 135]. This trend is evident in the IHPC compressor, with increasing intensity from the first to the fourth rotor. Additionally, the overall entropy level increases axially, contributing to the observed trend.

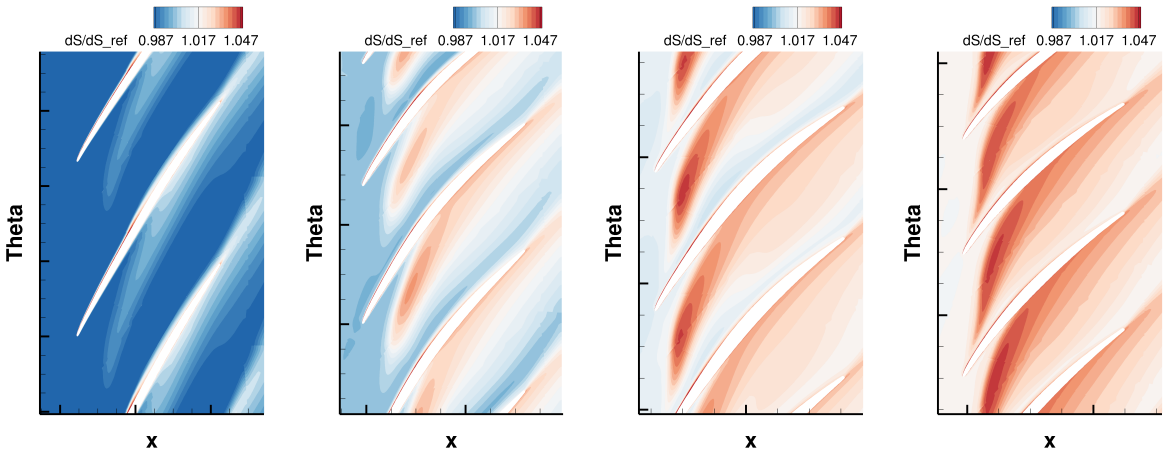

(a) ΔS at R1. **(b)** ΔS at R2. **(c)** ΔS at R3. **(d)** ΔS at R4.

Figure 3.22: Entropy distribution at the blade-to-blade cut at 97% h/H, for the first to the fourth rotor blades in the IHPC compressor.

Figure 3.23 shows the skin friction lines on the first rotor of the IHPC compressor, providing further insights into the secondary flow phenomena affecting the blade surface. Figure 3.23a presents the suction side of the blade. Near the hub, the impact of the passage

vortex is visible, as observed in the CREATE compressor. A separation line, indicating corner separation, is present near the lower third of the blade span. In the upper part of the blade, another separation line, followed by a reattachment line, is formed, delineating a separation bubble, corresponding to the shock location, which significantly alters the flow topology. The other rotors exhibit a similar behavior in terms of flow characteristics. In contrast, the stator rows display a simpler flow topology, as there are no tip leakage vortices impacting their pressure side, nor do shock waves form on these blades. However, the IGV shows a region of flow separation on its pressure side, caused by the shockwave emanating from the first rotor row, which impinges upon the IGV pressure surface.

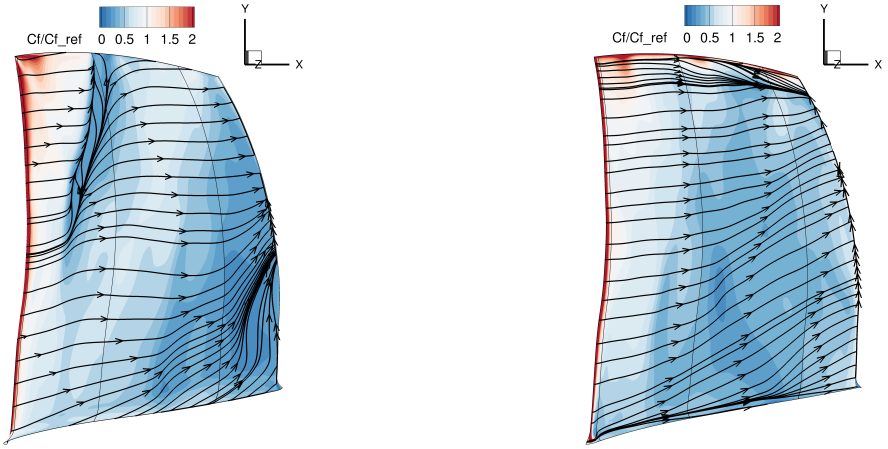

(a) Suction side. **(b)** Pressure side.

Figure 3.23: Skin friction lines on the first rotor blade of the IHPC compressor.

The detailed analysis of the flow field in the IHPC compressor underscores the critical role of complex flow interactions throughout the entire compressor. The combined effects of tip leakage vortices, shock waves, rotor wakes, and hub vortices contribute to a highly intricate flow topology that significantly affects rotor performance. These phenomena result in strong interactions, particularly within the transonic flow regions of the rotor blades, leading to considerable entropy generation and aerodynamic losses. Consequently, the IHPC compressor test case serves as an excellent benchmark for validating and analyzing the developed methods in a highly realistic high-pressure compressor environment.

Conclusion

This chapter presented the full set of blade-resolved configurations developed to serve as reference cases for the remainder of this work. A broad range of numerical simulations has been explored, spanning from computationally efficient single-blade-passage setups to highly demanding full-annulus calculations under inlet distortion conditions. Each configuration has been described in terms of its three-dimensional computational domain, mesh characteristics, and boundary conditions, as appropriate.

For both compressors investigated, a preliminary validation of the blade-resolved simulations against available experimental data has been carried out under clean inflow conditions. While minor discrepancies were observed, the results demonstrate that the simulations capture the overall behaviour of the experimental machines with good fidelity, despite the sim-

plifications required during model setup. A brief characterisation of the flow fields was also provided. These analyses reveal the presence of complex flow phenomena, including passage vortices, corner separations, tip leakage vortices, and shock structures.

The next chapter details the first application of the Hall-Thollet Body-Force model to the investigated compressors, using the high-fidelity reference data established in this chapter as the basis for its assessment. This evaluation forms the foundation for identifying the modifications required to ensure the reliable use of this reduced-order model in the detailed analysis of flow distortions in the multi-stage high-pressure compressors under investigation. These modifications will be presented and will serve as the basis for the modified model adopted in the subsequent chapters.

CHAPTER 4

DEVELOPMENT OF AN ENHANCED BODY-FORCE MODEL FOR MULTI-STAGE HIGH-PRESSURE COMPRESSOR MODELLING

This chapter provides a critical evaluation and methodological enhancement of the Hall-Thollet Body-Force model selected in this study. Specifically, it identifies the key challenges and limitations of the model when applied to high-pressure compressors and presents a strategy to address them. The chapter focuses on developing a robust calibration methodology independent of operating point, shaft speed, and inlet conditions; introducing near-wall corrections to enhance accuracy near the hub and shroud and mitigate flow instabilities at low mass flow rates; and incorporating secondary loss correlations to better capture complex flow phenomena. These enhancements aim to improve the model's predictive accuracy and reliability in high-pressure compressors, which is essential for assessing inlet distortion effects.

Contents

4.1 Body-Force Numerical Configurations **92**
4.1.1 Body-Force CREATE Configurations 92
4.1.2 Body-Force IHPC Configurations 92
4.2 Assessment of the Hall-Thollet Model for High-Pressure Compressors **93**
4.3 Modifications to the Hall-Thollet Model for High-Pressure Compressors . . . **99**
4.3.1 Calibration Strategy Development 99
4.3.2 Near-Wall Clipping Technique 106
4.3.3 Integration of Secondary Losses 109
4.3.4 Final Modified Model 113
Conclusion **115**

4.1 Body-Force Numerical Configurations

An overview of the Body-Force numerical configurations for both the CREATE and IHPC compressors is presented here. This section complements the previous chapter's description of the blade-resolved domains to provide a unified presentation of all numerical cases.

4.1.1 Body-Force CREATE Configurations

Multiple configurations of the CREATE compressor have been developed for the Body-Force (BF) modelling approach, to enable a direct comparison with the blade-resolved configurations. A 2° azimuthal sector is simulated and compared to both the single-blade-passage (SBP) and the $2\pi/16$ blade-resolved configurations, for the clean inflow and radial distortion studies respectively. Additionally, a Body-Force version of the P2D setup has been constructed and analysed to evaluate the model's capability to capture azimuthal distortion effects relative to its blade-resolved counterpart. In all cases, the geometry, mesh topology, inlet maps, and boundary conditions used in the BF simulations are consistent with those employed in the corresponding blade-resolved cases. At the same time, the simulations retain the methodological characteristics of the Body-Force approach, as described in Section 2.2.4.

Table 4.1 summarises the mesh sizes for each configuration. A significant decrease in mesh density is observed for the Body-Force setups, with, for example, a reduction of approximately 20 times in the P2D case, underscoring their computational efficiency. This advantage arises from the absence of explicitly modeled blades and the associated mesh complexity in the Body-Force method.

4.1.2 Body-Force IHPC Configurations

Similarly to the previous compressor, and to support comparison with the blade-resolved configurations, corresponding IHPC compressor numerical domain were produced for the Body-Force (BF) modelling approach. A 2° azimuthal sector is simulated and directly compared to both the single-blade-passage (SBP) and the $2\pi/4$ blade-resolved configurations, under clean inflow. In addition, a full-annulus Body-Force case has been constructed and evaluated in direct comparison with its blade-resolved counterpart, to investigate circumferential distortion.

Table 4.1: Mesh size for each configuration of the CREATE compressor.

Approach	Sector	Domain	Mesh size $[\times 10^6]$
Blade-resolved	SBP	3D	8.82
	$2\pi/16$	3D	64.27
	2π	P2D	53.99
Body-Force	2°	3D	0.38
	2π	P2D	2.76

The geometry, mesh structure, inlet maps, and boundary conditions used in the Body-Force simulations are consistent with those employed in the corresponding blade-resolved cases, while retaining the model-specific features and simplifications of the Body-Force approach, as described in Section 2.2.4.

Table 4.2 provides a summary of the mesh sizes for each configuration, encompassing both blade-resolved and body-force approaches. A substantial reduction in mesh size is observed when adopting the body-force method, with, for instance, a 13-fold decrease in mesh size for the full-annulus simulations.

Table 4.2: Mesh size for each configuration of the IHPC compressor.

Approach	Sector	Domain	Mesh size $[\times 10^6]$
Blade-resolved	SBP	3D	19.2
	$2\pi/4$	3D	261
	2π	3D	1050
Body-Force	2°	3D	0.59
	2π	3D	79.2

4.2 Assessment of the Hall-Thollet Model for High-Pressure Compressors

The Hall-Thollet model, introduced in Section 1.3.3.2, provides the starting point for the reduced-order approach developed in this thesis, which aims to predict flow behaviour with reliability comparable to that of (U)RANS calculations. The fundamental equations of the Hall-Thollet model, expressing the normal and parallel components of the blade forces, are rewritten for reference in Equation (4.1).

$$\begin{cases} f_n = \dfrac{W^2}{2sb|n_\theta|} 2\pi\delta K_{\text{mach}} \\ f_p = \dfrac{W^2}{2sb|n_\theta|} \left[2C_f + 2\pi K_{\text{mach}}(\delta - \delta^{\eta_{\max}})^2\right] \end{cases} \tag{4.1}$$

As previously discussed, this model has been applied in the literature to investigate various configurations; however, these studies did not feature the unique characteristics of multi-stage high-pressure compressors. The objective of this section is, therefore, to evaluate the performance of the original Hall-Thollet model against the available reference high-fidelity data for the two high-pressure compressor test cases, presented in Chapter 3, and to identify potential areas for model improvement.

The first investigated test case is the CREATE compressor, selected for its simpler characteristics compared to the second, more complex, transonic, and industrial configuration.

Figure 4.1 illustrates the performance characteristics of the 3-stage CREATE configuration, including the total-to-total pressure ratio, total-to-static pressure ratio, total-to-total temperature ratio, and isentropic efficiency, all plotted against the corrected mass flow rate. Each characteristic includes results from both the single-blade-passage (SBP) blade-resolved calculations and the Body-Force (BF) calculations using the original Hall-Thollet model (HT). The data are normalised to the values of the SBP blade-resolved case at the peak efficiency operating point. Since no established strategy exists in the literature for determining the appropriate operating point to extract the value of $\delta^{\eta_{\max}}$ in multi-stage compressors, the baseline Hall-Thollet model presented here adopts the peak efficiency point of the entire configuration as the reference.

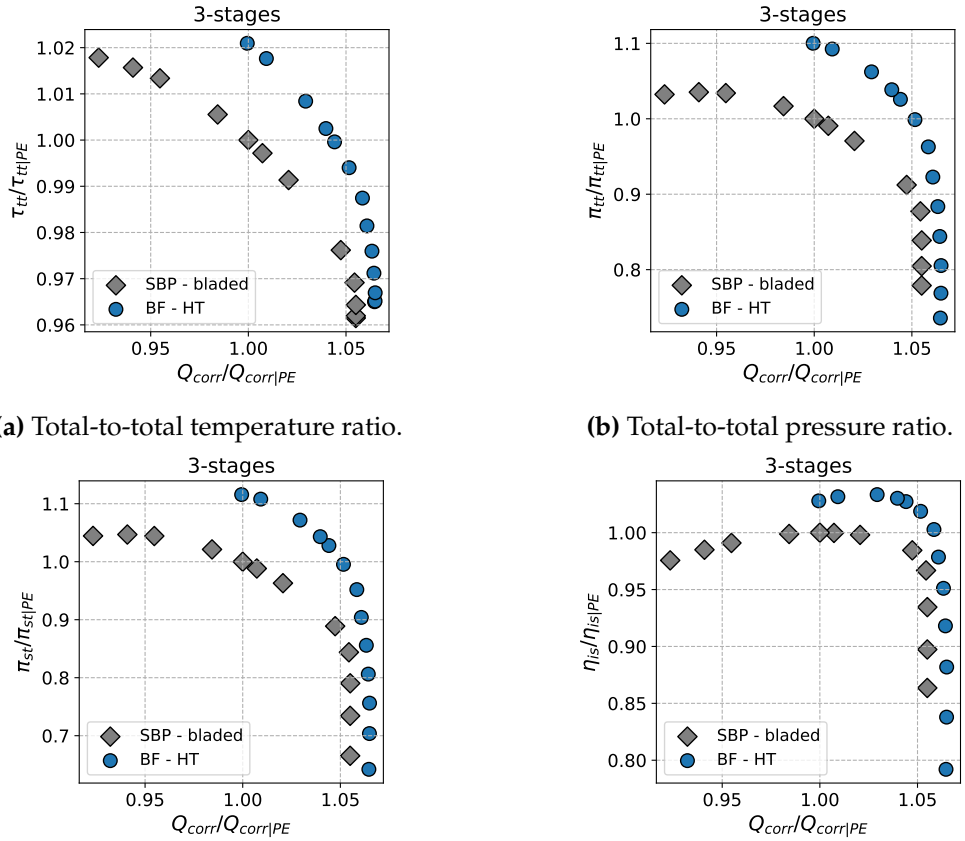

(a) Total-to-total temperature ratio.

(b) Total-to-total pressure ratio.

(c) Total-to-static pressure ratio.

(d) Isentropic efficiency.

Figure 4.1: Performance characteristics of the 3-stages CREATE compressor.

Two key observations can be made from these results. First, the total-to-total temperature ratio is overestimated, indicating that the flow deviation is underestimated and that the model imparts excessive work to the fluid. This suggests that the normal force component, which governs the blade turning, requires recalibration. Similarly, the total-to-total pressure ratio is higher than in the blade-resolved reference, by approximately 10% at the peak-efficiency operating point ($Q_{\text{corr}}/Q_{\text{corr}\,|\,\text{PE}} = 1$). While this overprediction is partly a consequence of the excessive work input, it is also amplified by an underestimation of losses: the maximal isen-

tropic efficiency predicted by the Body-Force model exceeds the reference value by approximately 3%, indicating that dissipation mechanisms are not fully captured. These discrepancies highlight the need to refine the parallel force formulation, particularly the term responsible for modelling nominal losses. Furthermore, the peak-efficiency operating point is not accurately reproduced, suggesting that the off-design term of the parallel force component requires further adjustment to ensure correct prediction across the operating range. It should be noted that the discrepancies identified above do not indicate fundamental deficiencies of the model, but rather highlight the need for targeted recalibration of specific force components to ensure accurate prediction of both work transfer and operating stability in multi-stage high-pressure compressors. In fact, these machines exhibit a complex aerodynamic environment characterised by strong adverse pressure gradients, significant secondary phenomena, high inter-row interactions, and low-aspect-ratio blades that accentuate three-dimensional effects, aspects that were not central in the original formulation of the model.

The second key observation concerns the reduced stability of the Body-Force simulations at lower mass flow rates. No stable operating point was obtained for $Q_{\text{corr}}/Q_{\text{corr|PE}} < 1$, effectively halving the stable operating envelope. In particular, instabilities emerged in the simulations at lower mass flow rates, which hindered convergence and limited the predictive capability of the model in off-design operation.

The row-by-row total-to-total pressure ratio predicted by the original Hall-Thollet model, compared with the blade-resolved SBP case, is shown in Figure 4.2.

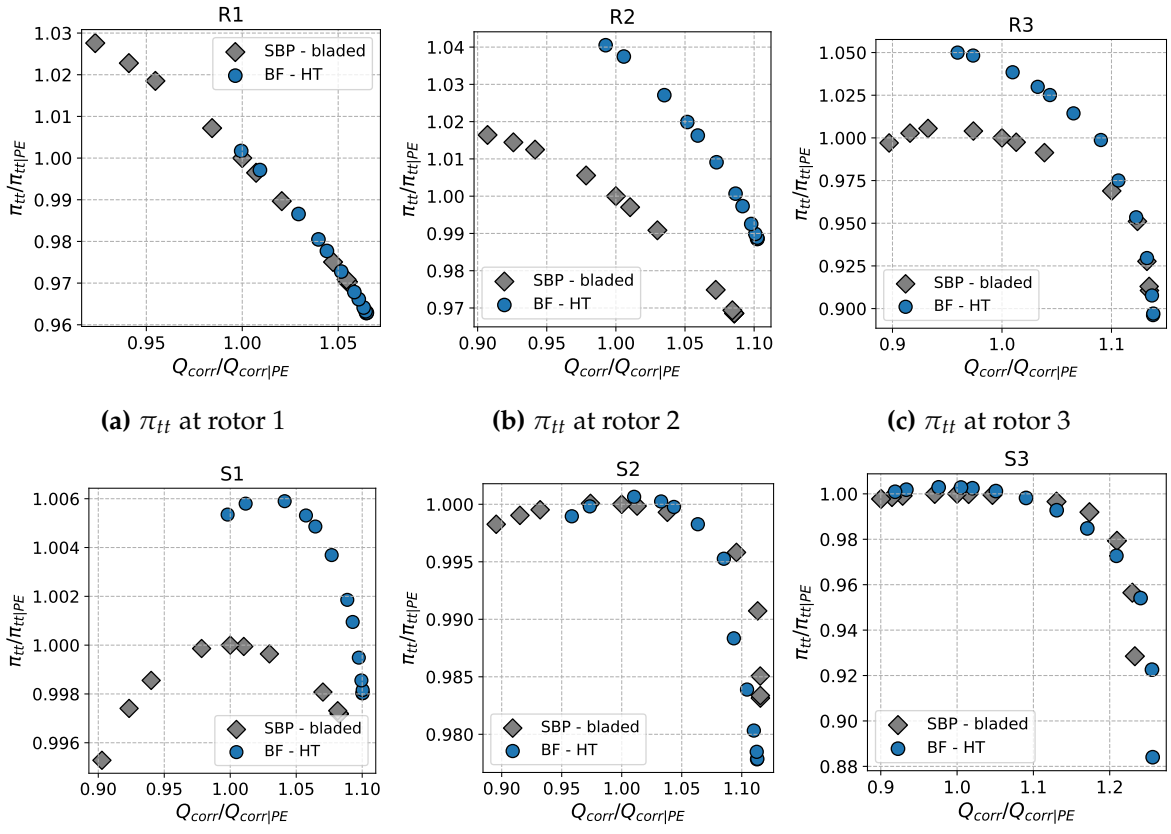

(a) π_{tt} at rotor 1 **(b)** π_{tt} at rotor 2 **(c)** π_{tt} at rotor 3

(d) π_{tt} at stator 1 **(e)** π_{tt} at stator 2 **(f)** π_{tt} at stator 3

Figure 4.2: Total-to-total pressure ratio of the CREATE compressor rows.

It can be seen that the error of around 10%, previously found in the 3-stage compressor map, is distributed across the individual rows, leading to poor predictions. For the CREATE compressor, the errors are primarily localised in the second and third rotor rows, as well as the first stator row, with prediction errors of approximately 4%, 5%, and 1%, respectively. Since matching is crucial in multi-stage turbomachinery, errors in a single row can significantly affect the performance predictions of subsequent rows. This interdependence means that, even if one single row is mismatched, all stages are impacted by the prediction errors of the baseline model, and errors can accumulate across the stages.

These observations on the performance predictions emphasise the need for a simple, general, and transferable calibration strategy that enhances the predictive capability of the model, while avoiding the need for additional corrections at different operating points, shaft speeds, or inlet conditions, thereby preserving its versatility. They also underline the importance of identifying and addressing the root causes of the instabilities observed at low mass flow rates. The calibration strategy developed for this purpose is presented in Section 4.3.1.

The predictions of the Hall-Thollet model are further analysed through the radial evolution of total pressure and total temperature across the compressor annulus. The blade-resolved, single-blade passage results are once again compared to the Hall-Thollet baseline model predictions. The results are presented downstream of each rotor row and at the compressor outlet, at the peak efficiency point, where $Q_{corr}/Q_{corr|PE} = 1$. These data are shown in Figure 4.3.

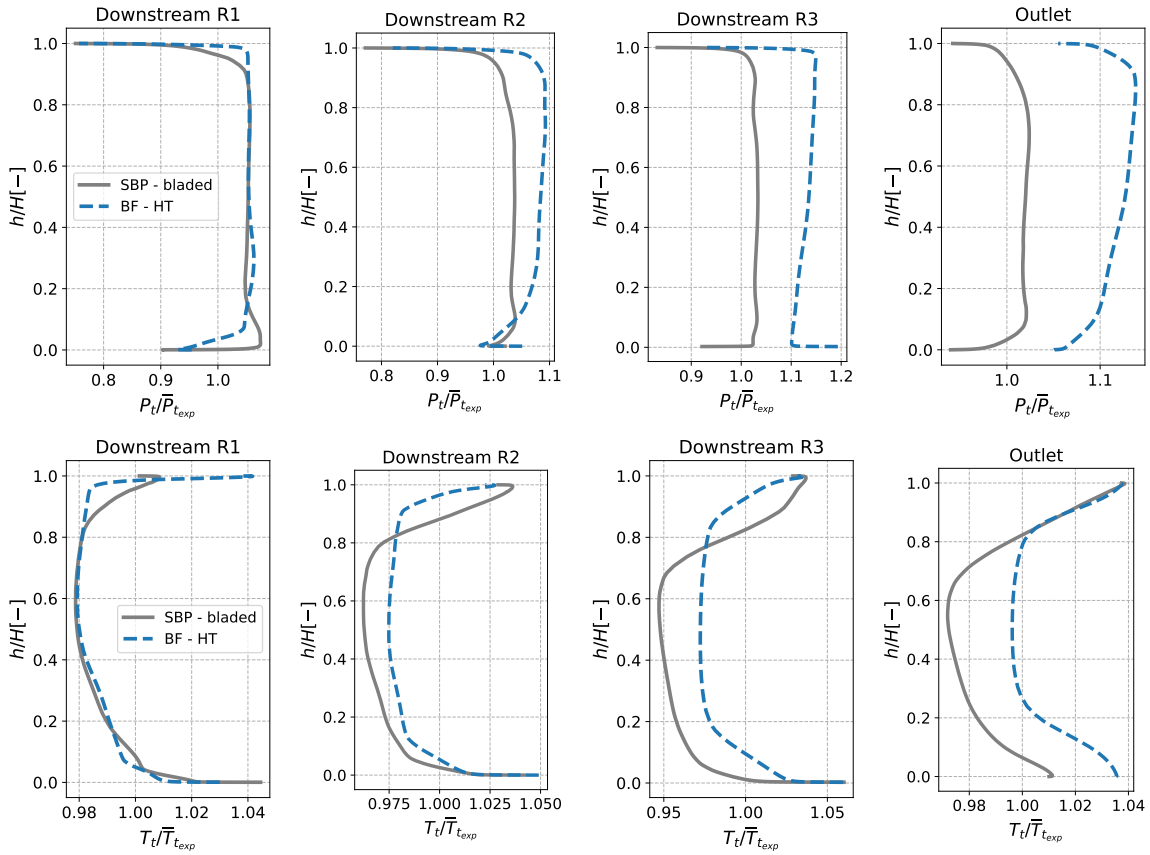

Figure 4.3: Radial profiles of total pressure and total temperature for the CREATE compressor.

The analysis of the radial profiles can be divided into mid-span behaviour and near-wall behaviour. At mid-span, the predictions differ noticeably between the two approaches, with the Hall-Thollet model yielding higher total pressure and total temperature values than those obtained from the reference calculations. A cumulative deviation is observed along the compressor, with the outlet showing discrepancies of nearly 10% in total pressure and approximately 3% in total temperature relative to the reference case.

At the endwalls, the Hall-Thollet model exhibits a consistent offset with respect to the blade-resolved profiles, with the largest deviations occurring near the compressor shroud. The total temperature distributions clearly indicate the absence of a local correction at the blade tips, as the reference profiles display a distinct shape that suggests the presence of strong secondary flow structures. Furthermore, while the flow near the hub agrees well with the reference solution across the first stages, it progressively deviates toward the compressor exit, showing higher total temperatures and steeper temperature gradients than those predicted by the blade-resolved calculations.

This analysis highlights the importance of incorporating local corrections at the endwalls to enhance the Hall-Thollet model's ability to capture near-wall flow behaviour and to enlarge the operating envelope by mitigating excessive near-wall losses or deviations that may contribute to instabilities at low mass flow rates. The approach developed to address this requirement is presented in Section 4.3.2. It also confirms the presence of a significant mismatch in the predictions at mid-span, which can be addressed through the calibration process discussed above.

Similar observations can be made for the industrial IHPC compressor. Figure 4.4 shows the performance characteristics of the 4.5-stage IHPC compressor. The performance parameters presented include the total-to-total pressure ratio, total-to-static pressure ratio, total-to-total temperature ratio, and isentropic efficiency, all plotted against the corrected mass flow rate. The reference data used for comparison are the time-averaged blade-resolved calculations of the $2\pi/4$ quasi-periodic sector, which also serves as the basis for normalizing the values in the plot. The Hall-Thollet model is analysed in its baseline formulation; however, in this case, the off-design term for the losses in f_p has been deactivated. This adjustment was made because the losses predicted by that term were too high, causing convergence issues and preventing the visualization of a comprehensive compressor map.

Once again, it is evident that all four performance quantities are over-predicted. For the industrial IHPC compressor, these errors are even more pronounced than those observed for the CREATE compressor. The total-to-total and total-to-static pressure ratios show deviations of 25% to 29% relative to the blade-resolved case. The total-to-total temperature ratio exhibits an error of 4%, while the isentropic efficiency is overestimated by just under 7%. In addition, the stable operating range predicted by the Body-Force model is approximately half that of the blade-resolved case, as was also observed for the CREATE compressor. These substantial discrepancies reinforce the need for a calibration strategy. As the machine increases in complexity, with additional stages, more intricate flow phenomena, and more varied geometries, the predictive accuracy of the modelling approach degrades, leading to less precise performance estimates.

Figure 4.5 illustrates the evolution of the total temperature radial profiles across the IHPC compressor. The $2\pi/4$ blade-resolved reference data and the Hall-Thollet model predictions are shown at the measurement planes located upstream of the four stator rows of the machine. Both the mid-span and near-wall regions exhibit notable discrepancies with respect to

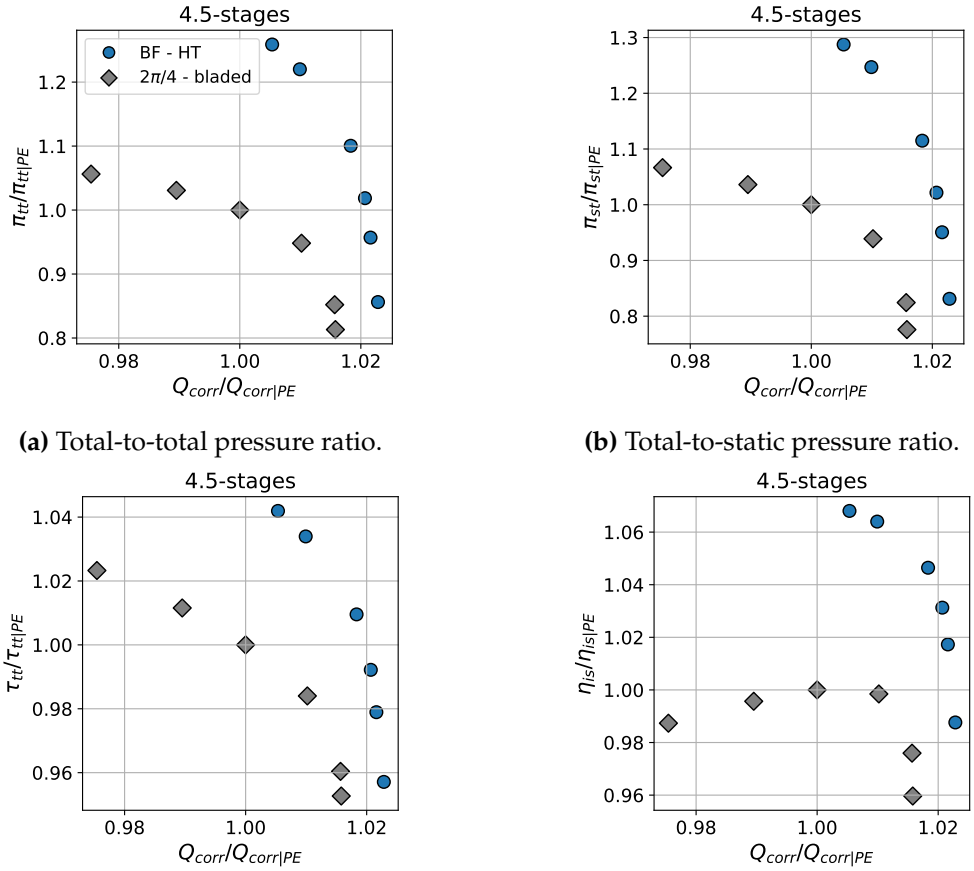

(a) Total-to-total pressure ratio.

(b) Total-to-static pressure ratio.

(c) Total-to-total temperature ratio.

(d) Isentropic efficiency.

Figure 4.4: Performance characteristics of the 4.5-stages IHPC compressor.

the reference case, and no radial location shows full agreement with the blade-resolved data. The largest deviations occur near the endwalls: a 4-5% error is observed in the tip region (95% h/H) downstream of the first rotor, and a 5% error appears at the hub downstream of the fourth stator. The error observed at the hub can be primarily attributed to the fact that, although the comparison is made at the same corrected mass flow, the operating conditions predicted by the model differ from those of the reference case due to model inaccuracies. As shown in the following chapters (see Sections 5.1 and 6.1), improving the model predictions naturally shifts the spanwise profiles, bringing the hub values closer to the reference data and revealing that the main discrepancy originates near the casing.

These findings, consistent with those obtained for the CREATE compressor, are particularly significant in revealing larger discrepancies at the blade tips. Consequently, they motivated the development of a model modification specifically aimed at capturing secondary flow phenomena in the tip region. The details of this new development are presented in Section 4.3.3.

In summary, the assessment of the baseline Hall-Thollet model against the CREATE and IHPC compressors revealed significant discrepancies in the predicted performance characteristics. While the model provides reasonable estimates at certain operating points, it consistently overestimates key parameters such as pressure ratios, temperature ratios, and isen-

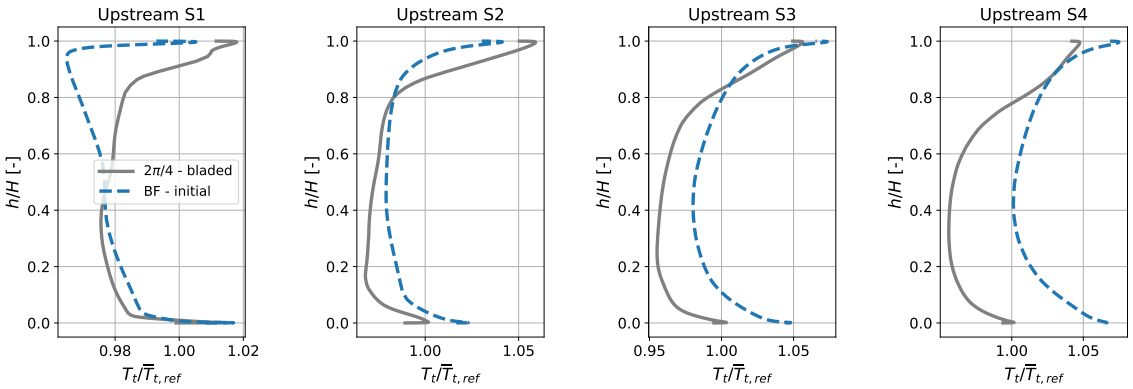

Figure 4.5: Radial profiles of total temperature for the IHPC compressor.

tropic efficiency. Additionally, the observed instability at low mass flow rates highlights the model's limitations in accurately capturing the flow dynamics under off-design conditions. Radial profiles, particularly near the endwalls, further emphasise mismatches between the model and reference data, indicating that important secondary flow phenomena are not adequately represented. These findings underscore the need for a more refined, adaptable modelling approach capable of addressing both global performance errors and localised discrepancies.

In response to these observations, several corrections were developed to enhance the Hall-Thollet model's predictive capability. These corrections target both global performance issues and localised flow phenomena, especially near the endwalls. A general calibration strategy was developed based on the study of the CREATE compressor to correct global performance characteristics (Section 4.3.1). This was complemented by a clipping technique to mitigate low mass flow rate instability and improve near-wall predictions (Section 4.3.2). For the IHPC compressor, the same calibration and clipping approaches were applied. However, the evaluation of this compressor revealed more pronounced secondary flow effects near the blade tips, necessitating an additional correction (Section 4.3.3).

The modifications introduced in response to these findings are described in detail in the following sections.

4.3 Modifications to the Hall-Thollet Model for High-Pressure Compressors

In this section, the key developments introduced to enhance the Hall-Thollet model are presented. It should be noted that the order of presentation does not correspond to the sequence in which they are applied in practice; the correct implementation sequence is provided in Section 4.3.4.

4.3.1 Calibration Strategy Development

The need for a calibration strategy emerged from the significant deviations observed between the blade-resolved and the baseline Hall-Thollet model solutions, as previously explained.

Looking at Equation (4.1) and referring to the detailed analysis of the force components in Section 1.3.3.2, it becomes clear that the prediction errors outlined above stem primarily

from the simplifying assumptions inherent in the aerodynamic coefficients used in the model. These coefficients, such as the lift coefficient from thin airfoil theory in incompressible flow, the skin friction coefficient for a 2D airfoil in turbulent flow, and the empirical quadratic drag coefficient law for an airfoil, are based on simplified assumptions, such as no interaction between blade rows. Additionally, they were originally formulated for low-loading blades. High-pressure compressor blades, however, operate under significantly different conditions. Their close spacing leads to interactions not only between adjacent blades but also with the wakes of upstream blades and the shocks generated by downstream or neighboring blades. The blades are highly loaded and have low aspect ratios, which often amplifies secondary flow effects and reduces the reliability of simplified aerodynamic coefficients. These factors therefore strongly challenge the assumptions central to the Hall-Thollet model when applied to such complex configurations.

In the literature, several studies have explored the need for calibration coefficients for both the normal and parallel force components in analogous models. However, the proposed calibration coefficients are often complex, varying with the operating point, shaft speed, and even across the blade span [56, 74, 75, 121].

A key objective of this section is to explore the development of a calibration strategy that simplifies this process. Specifically, the aim is to create a strategy that relies solely on scalar coefficients, which remain constant across different operating points, shaft speeds, and across the height of the compressor annulus. This approach could offer a significant advancement in simplifying the calibration process while improving model accuracy. The primary aim of this strategy is to accurately predict compressor performance across the entire machine.

The calibration strategy developed in this work relies on reference data. Specifically, blade-resolved, single-blade-passage data are used to determine the appropriate calibration coefficients. However, when sufficiently comprehensive, experimental data could also serve as a valuable alternative.

Calibration of work input and nominal losses The first step in determining a suitable calibration strategy is to assess the impact of modifying the various model coefficients on the performance predictions. Two correction coefficients are first introduced to assess the sensitivity of the model performance predictions to variations in the underlying aerodynamic assumptions. These coefficients act on the nominal work and losses. Specifically, the lift coefficient in the normal force component is modified such that C_L becomes $K_n C_L$, and the skin friction coefficient in the first term of the parallel force, which accounts for nominal losses, becomes $K_f C_f$.

Regarding the normal force coefficient, intuitively, if $K_n > 1$, the effective lift produced by the blade increases, thereby enhancing the work input to the flow. This results in a higher total-to-total temperature ratio and an increased total-to-static pressure ratio. Conversely, if $K_n < 1$, a reduction in these performance indicators is expected.

In the literature, several attempts have been made to develop corrected expressions for the lift coefficient of airfoils under realistic operating conditions. While the simplified expression $C_L = 2\pi\alpha$ often provides a reasonable first-order estimate for isolated profiles, it is generally acknowledged that empirical corrections are necessary for more accurate predictions in practical applications. For three-dimensional, non-isolated blades, the lift coefficient is influenced by several geometric and flow parameters, including blade thickness, aspect ratio, solidity, camber angle, Reynolds number, and others. Among these, the most significant are typically

solidity, aspect ratio, and camber angle. Generally speaking, these factors influence the lift coefficient in distinct ways: increasing solidity and camber generally lead to higher values of C_L, while increasing aspect ratio tends to reduce it [33, 37, 117]. These combined effects can cause the overall correction factor to be either above or below unity.

However, while these trends offer useful guidelines, they do not fully capture the complexity of aerodynamic behavior, particularly in more realistic operating conditions and industrial geometries. For instance, certain parameters can influence the lift coefficient in a complex and non-monotonic manner. Dixon [38] shows that the lift correction factor varies non-monotonically with space-to-chord ratio (the reciprocal of solidity) and stagger angle in cascades of thin flat plates. Fan blades, for which the Hall-Thollet model is typically successful, have high space-to-chord ratios, around 2-2.5, so that using a corrective coefficient close to unity provides a reasonable approximation, as the graph converges near that value. In contrast, high-pressure compressor blades have much lower space-to-chord ratios, generally between 0.8 and 1.3, placing them in the region of the graph where the corrective coefficient exhibits both the largest variation and a pronounced non-monotonic behavior. For example, a blade with a 70° stagger angle may require a correction factor as high as 1.6, while blades with lower stagger angles may need values as low as 0.4.

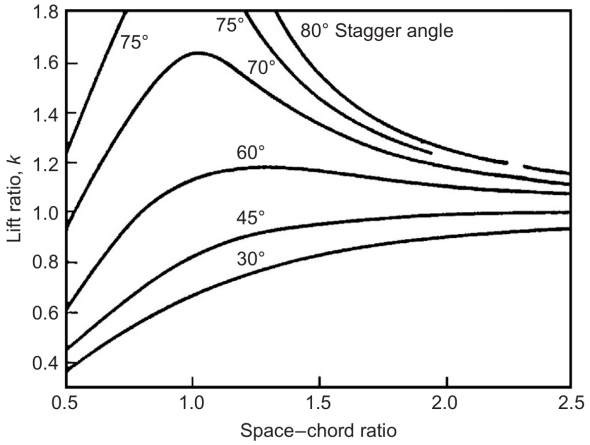

Figure 4.6: Lift ratio of a cascade of thin flat plates, illustrating its dependence on stagger angle and space-to-chord ratio [38].

While these considerations provide useful insight into the expected C_L behavior in less-idealised cases, it is important to note that, being derived from low-speed, low-Reynolds-number thin flat plates, they remain far from the conditions of an annular multi-stage industrial compressor and cannot be directly applied to high-pressure compressor blades due to substantial differences in flow conditions and blade geometry.

In summary, no universally applicable analytical or empirical correction is currently available in the literature for high-pressure compressor blades, due to the complexity and interdependence of the influencing parameters. The value of K_n is expected to vary both above and below unity, and the behavior of each blade row may differ due to variations in their operating conditions and geometric characteristics.

With respect to the corrective term K_f, it affects the friction coefficient on the blade surfaces, thereby influencing boundary layer development and viscous losses. These losses, in

turn, impact performance metrics such as the total-to-total pressure ratio and isentropic efficiency. An increase in K_f above unity leads to a reduction in these performance indicators, while a decrease in K_f has the opposite effect.

Similar to the lift coefficient, numerous analytical and empirical formulations have been proposed for the turbulent skin friction coefficient of a flat plate [112, 161]. However, these values are typically approximate and may vary under different conditions. Since the goal is to determine an accurate value of K_f specific to the compressor under investigation, relying solely on empirical coefficients from the literature may provide improved initial estimates but is unlikely to offer a fully suitable correction for this particular machine.

A preliminary study on the variation of these two terms is thus carried out. To this end, the isolated first-stage reduced configuration of the CREATE compressor has been generated and analysed. Specifically, the first stage of the machine is isolated while retaining the mesh and boundary conditions of the SBP configuration, with adjustments made to the outflow conditions to enable correct throttling of the operating points. A modified model, presented in Equation 4.2, in which the off-design loss term is deactivated and the correction coefficients K_n and K_f are incorporated, is used to investigate their impact on the compressor's performance characteristics.

$$\begin{cases} f_n = \dfrac{W^2}{2sb|n_\theta|} 2\pi\delta K_n K_{\text{mach}} \\ f_p = \dfrac{W^2}{2sb|n_\theta|} 2K_f C_f \end{cases} \tag{4.2}$$

Figure 4.7 shows the performance characteristics of the first rotor row in the reduced one-stage, single-blade-passage configuration of CREATE, with varying values of K_n and K_f.

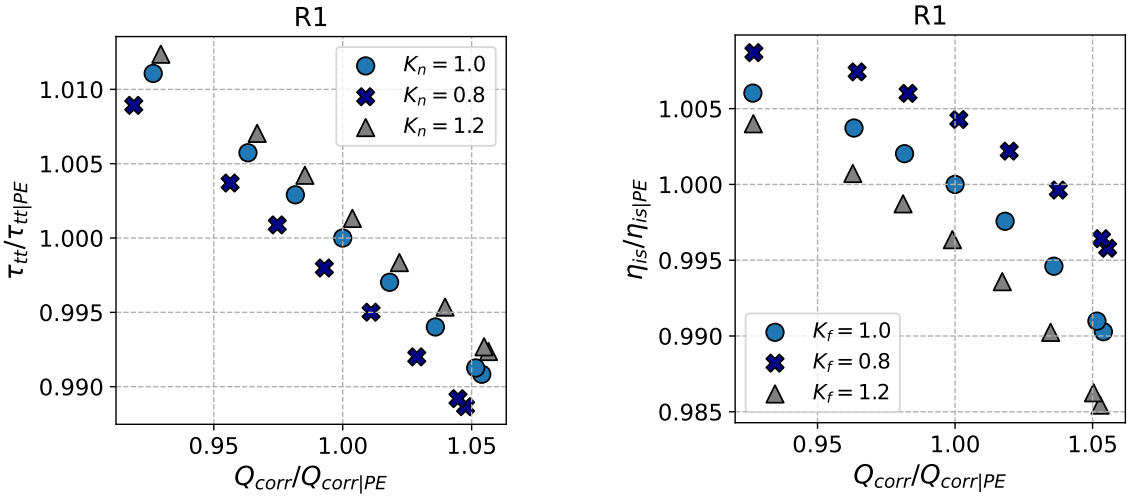

(a) Influence of K_n on the τ_{tt} map.

(b) Influence of K_f on the η_{is} map.

Figure 4.7: Influences of K_n and K_f on the performance maps of the first rotor of the isolated first-stage CREATE configuration.

Figure 4.7a depicts the total-to-total temperature ratio τ_{tt} map for K_n values of 0.8, 1.2, and the reference case at 1.0. As expected, lower values of K_n correspond to reduced work

input and thus lower τ_{tt}. Conversely, higher K_n values lead to increased τ_{tt} ratios. Therefore, the relationship between K_n and τ_{tt} is direct. On the other hand, Figure 4.7b illustrates the effect of varying K_f on the isentropic efficiency (η_{is}) map of the first rotor row. The maps correspond to K_f values of 0.8, 1.2, and the reference case at 1.0. Here, the coefficient multiplying the nominal loss term shows an inverse proportionality with the row isentropic efficiency. As anticipated, increased losses correspond to lower isentropic efficiency, which explains the inverse influence of this parameter on performance. Both parameters cause a translation of the performance map without altering its overall shape, unless critical operating conditions are reached. This behaviour is exploited in the present calibration approach, where such shifts are used to align the Body-Force model characteristics with those predicted by the reference data.

The maps presented illustrate the influence of each calibration coefficient on the compressor's performance metrics. Table 4.3 lists, for each coefficient, the performance parameter that serves as the reference for its calibration, distinguishing between rotor and stator as appropriate.

Table 4.3: Target performance parameters for each calibration coefficient.

Coefficient	Rotor	Stator
K_n	τ_{tt}	π_{st}
K_f	π_{tt} and η_{is}	π_{tt}

When K_n and K_f are varied simultaneously, the combined effect is largely governed by the parameter identified as dominant in Table 4.3, while the contribution of the other parameter remains minor. This is illustrated in Figure 4.8, which presents the relevant performance metrics for different combinations of K_n and K_f in the rotor.

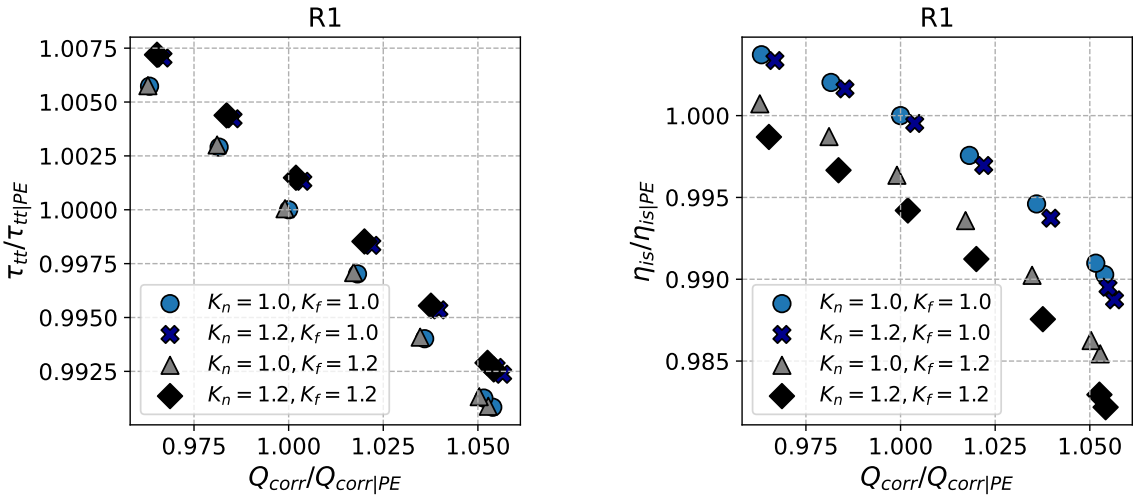

(a) Influence of K_n and K_f on the τ_{tt} map.

(b) Influence of K_n and K_f on the η_{is} map.

Figure 4.8: Influence of K_n and K_f on the performance maps of the first rotor of the isolated first-stage CREATE configuration.

The left panel shows the total-to-total temperature ratio, which is primarily influenced by the parameter K_n. This behavior is clearly observed: the two cases with $K_n = 1$ (circle and

triangle) overlap, as do the two cases with $K_n = 1.2$ (cross and diamond). A similar trend can be observed in the isentropic-efficiency plot, where the parameter K_f plays the dominant role. The two cases with $K_f = 1$ (circle and cross) coincide, while the cases with $K_f = 1.2$ (triangle and diamond) remain very close but exhibit a small interaction.

Calibration of off-design losses A key open question that arises in employing the Hall-Thollet model on multi-stage high-pressure compressors is the appropriate application of the off-design losses term. In the Hall-Thollet model, the off-design term is activated for all operating points where $\delta \neq \delta^{\eta_{\max}}$, with the $\eta_{\max}$ operating point identified as the point of maximum isentropic efficiency for the entire configuration, usually a fan rotor. In multi-stage machines, it is not immediately clear whether $\eta_{\max}$ should correspond to the maximum efficiency of the complete configuration, the maximum efficiency of each individual stage, or even each blade row.

The first option, selecting the operating point of maximum efficiency for the entire compressor, is quickly dismissed because this point corresponds to significantly differing operating conditions across individual stages. Applying off-design losses based on this criterion would lead to inaccurate loss adjustments for each row, either by targeting inappropriate operating conditions or by applying incorrect loss intensities. This can be visualised in the detailed row-by-row performance data in Appendix B, where, for the original Body-Force model, the application point of the off-design term is based on this criterion. It is evident that each row's maximum-efficiency point differs and does not necessarily align with that of the full compressor, as expected in a multi-stage compressor.

This work investigates the second and third options, studying the application of off-design losses on a stage-by-stage basis as well as on a row-by-row basis. A notable observation is that the quadratic term used in the parallel force formulation causes a deflection of the compressor characteristic relative to the characteristic without off-design losses, with the pivot point of this deflection located at $\delta = \delta^{\eta_{\max}}$. This behaviour is coherent for a single-stage machine, where performance characteristics typically exhibit a curved shape with a sharp choke limit on the right side of the compressor map, a slight inflection on the left side as stall is approached at low mass flow rates, and the $\eta_{\max}$ as the center of this inflection. However, multi-stage compressors can exhibit stage-by-stage and row-by-row characteristics that deviate significantly from this pattern, as upstream rows are often constrained by choking and surge in downstream rows, as explained in Section 1.1.3.1.

For this reason, in this work, the pivot point for applying off-design losses is proposed to be selected as the point of tangency between the compressor characteristics derived from the Body-Force and blade-resolved approaches. At this point, $\delta = \delta^{pivot}$. This point of tangency is identified by systematically varying K_n and K_f, which induce a translation of the compressor maps, as demonstrated above. Applying off-design losses at this operating point enables the correct inflection of the characteristic curve, thereby preventing a premature drop into choking or stall conditions. Finally, modifying the exponent of the quadratic term allows for adjusting the intensity of the off-design losses, with the coefficient K_D, which multiplies the quadratic exponent, controlling the inflection of the characteristic. To ensure robustness, the off-design term is reformulated as $2\pi K_{Mach}|\delta - \delta^{pivot}|^{2K_D}$, with the absolute value introduced to maintain real positive values when the exponent is non-integer.

A visual representation of the influence of the K_D parameter is provided in Figure 4.9, which shows the isentropic efficiency map of the first rotor row in the isolated first-stage,

single-blade-passage CREATE configuration.

The pivot point in this example has been chosen as the operating point at $Q_{\text{corr}}/Q_{\text{corr|PE}} = 1$. The value δ^{pivot} is extracted during pre-processing from a calculation with off-design losses deactivated, and then applied within the co-processing Body-Force module, where off-design losses are activated. Since $|\delta - \delta^{pivot}|$ is expressed in radians and usually ranges between 0 and 1, reducing the exponent $2K_D$ increases the off-design loss term. Consequently, reducing K_D increases the associated losses, indicating an inverse proportionality between the coefficient and efficiency. This effect is particularly pronounced for $K_D < 1$, where losses increase rapidly and can cause instabilities at lower mass flow rates. Conversely, for $K_D > 1$, the behavior is asymptotic and does not lead to such issues.

Regarding the choice between calibrating stage-by-stage or row-by-row, it has been found that, although good results can be achieved with a stage-by-stage approach, the row-by-row method offers greater flexibility and, consequently, improves the model's accuracy. The stage-by-stage approach, however, may be preferred if the goal is to reduce the overall calibration time, as it typically involves fewer iterations.

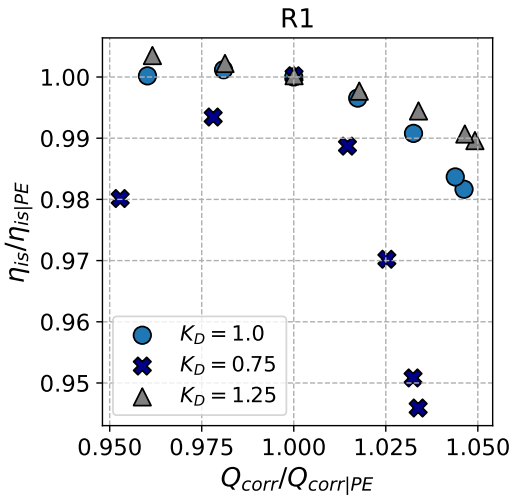

Figure 4.9: Influences of K_D on the isentropic efficiency maps of the first rotor of the single-stage CREATE configuration.

Final Calibration Strategy The calibration process, which incorporates all the presented coefficients, was first validated using the isolated first-stage, single-blade-passage CREATE configuration and then extended to a three-stage setup. The results show that the method is robust and accurate across different compressor architectures, as detailed in Sections 5.1 and 6.1 of the following chapters.

The formulation of the normal and parallel forces, incorporating the relevant calibration coefficients, is expressed in Equation (4.3).

$$\begin{cases} f_n = \dfrac{W^2}{2sb|n_\theta|} 2\pi\delta K_n K_{Mach} \\ f_p = \dfrac{W^2}{2sb|n_\theta|} \left[2K_f C_f + 2\pi K_{Mach}|\delta - \delta^{pivot}|^{2K_D}\right] \end{cases} \tag{4.3}$$

The overall calibration workflow, which is schematically outlined in Figure 4.10, illustrates the key steps involved in the calibration process.

Initially, the calibration coefficients K_n and K_f are determined for the first row of the configuration, with the off-design loss term inactive. These coefficients adjust the compressor characteristic of the considered row such that it becomes tangent to the characteristic curve obtained from the reference data. As previously discussed, each performance parameter is tuned using a distinct coefficient, with cross-influences between coefficients neglected. Once the tangent point, also referred to as the pivot point, is identified, the local 3D flow deviation angle, δ, is extracted at that specific operating point for the corresponding row. This value is then imposed as δ^{pivot} for all subsequent steps, ensuring consistency throughout the process. Finally, the coefficient K_D is calibrated to best reproduce the overall trend of the reference data. This calibration procedure is then repeated for each row of the compressor, proceeding sequentially from upstream to downstream, until all rows are calibrated and the workflow is complete.

As intended, the calibration strategy exclusively employs scalar coefficients. These coefficients remain fixed and require no adjustment for different operating points, inlet conditions, or shaft speeds. This invariance is a key aspect of the method's predictive capability and is demonstrated in the studies presented in Chapters 5, 6, and 7.

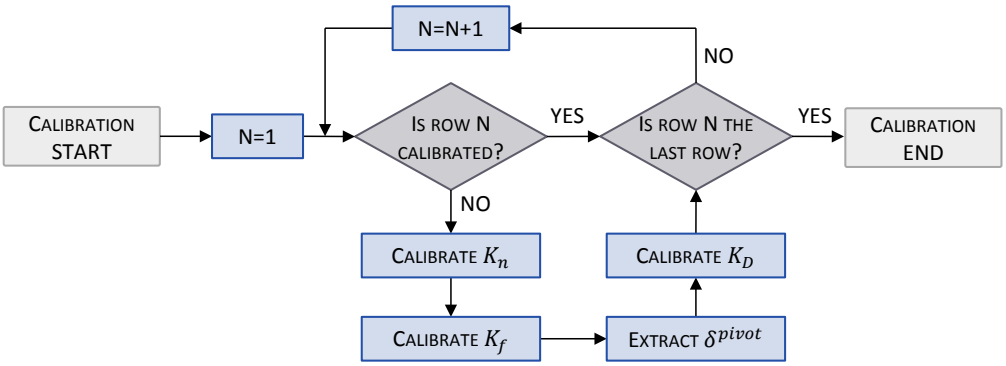

Figure 4.10: Workflow of the calibration strategy.

4.3.2 Near-Wall Clipping Technique

The necessity for near-wall corrections has been highlighted by multiple authors [49, 145, 155] and manifested in the present study in the analysis of the radial profiles in Figure 4.3. This challenge primarily arises from the formulation of the normal force component in the Hall model, which scales with the square of the relative flow velocity ($f_n \propto W^2$). When coupled with a viscous solver, this term decreases rapidly near the walls due to the no-slip condition, resulting in incorrect flow turning and often inducing non-physical flow separation caused by insufficient work input within the boundary layer.

Gallimore [49] and Simon [145] proposed and validated an alternative solution based on the assumption that static pressure within the boundary layer remains approximately constant. This assumption allows the normal force component in the near-wall region to be treated as constant. In Thollet's study [155], the impact of this issue and the related modification was deemed negligible for high aspect-ratio fan blades, where the near-endwall flow

had minimal effect on overall performance. However, to prevent unphysical separation at the hub, the pressure gradient within the boundary layer was artificially removed.

Building on these findings, the present work introduces a modification to the normal force. Unlike fan blades, low aspect-ratio blades operating in demanding conditions, characterized by strong adverse pressure gradients and significant secondary flow effects, are expected to be more strongly affected by this issue. These blades are more sensitive to near-wall effects due to the increased relative scale of boundary layer phenomena compared to channel height. Additionally, they experience strong adverse pressure gradients within the compressor annulus. Consequently, in this study, the solution proposed by Gallimore and Simon is adopted [49, 145]. The magnitude of the normal component of the blade force is held constant over a specified spanwise extent from the endwalls. This procedure, referred to as "clipping", mitigates the impact of near-wall effects on low aspect-ratio blades. Moreover, at the rotor tip, the blade force is set to zero within the tip gap to prevent the modelling of work input where it does not occur.

The determination of the appropriate height over which the clipping is applied requires careful consideration. The objective is to ensure that the clipping region adequately encompasses the boundary layer volume. A robust approach found in this work consists in estimating the boundary layer thickness from a single Body-Force simulation at the domain inlet, both at the hub and the shroud. This thickness is then expressed as a percentage of the total channel height. The resulting percentage is subsequently held constant for all downstream stages, providing a consistent, practical and easy to implement criterion for defining the clipping height across the compressor.

Figure 4.11 presents the normalised normal force component flow field for the 2° Body-Force sector of the CREATE compressor. Specifically, Figures 4.11a and 4.11b illustrate the flow field across all six rows before and after applying the clipping correction, respectively. It is evident from Figure 4.11a that near the walls, particularly at the leading edges of the different rows, the original formulation predicts high magnitudes of f_n, both positive and negative. Additionally, the stators exhibit zero normal force at the shroud due to the proportionality $f_n \propto W^2$, whereas the rotors show non-zero f_n values caused by tip flow velocity in the gaps and the relative shroud movement. Conversely, the modified formulation depicted in Figure 4.11b maintains a constant normal force value from the edge of the boundary layer to the blade walls. The rotor tip gaps have zero normal force, preventing non-physical flow turning. A detailed comparison of the clipping effect near the hub of the first stator is presented in Figures 4.11c and 4.11d, illustrating the original and modified formulations, respectively. This comparison clearly highlights the correction of the singularity at the leading edge and is expected to contribute to the mitigation of non-physical deviation and losses, which have been identified as a source of convergence difficulties at low mass flow rates, as discussed at the beginning of this chapter.

The final formulation for the normal force component with near-wall clipping is given by Equation (4.4), where $f_n(h/H)$ denotes the original normal force formulation dependent on the normalised radial position h/H across the annulus, and B is the blade height at the inlet, where the boundary layer thickness is extracted. The expression for f_n is recalled in Equation (4.5) for reference.

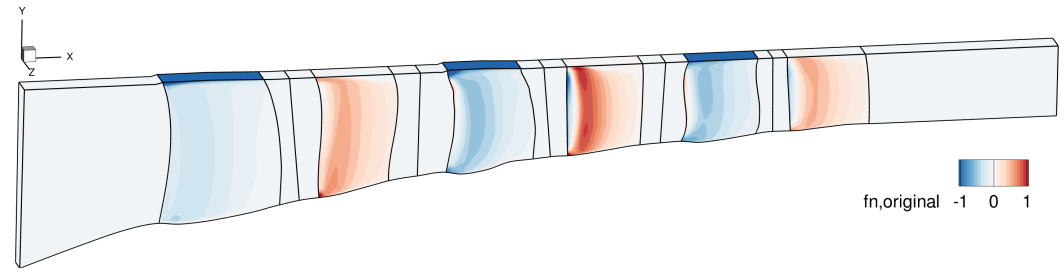

(a) Original normal force distribution across all rows.

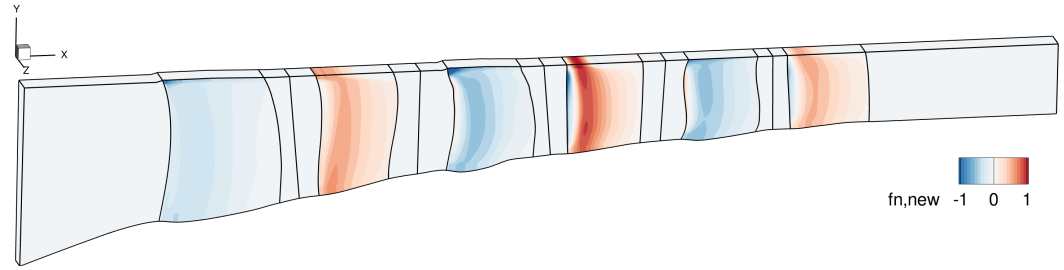

(b) Normal force distribution after clipping correction across all rows.

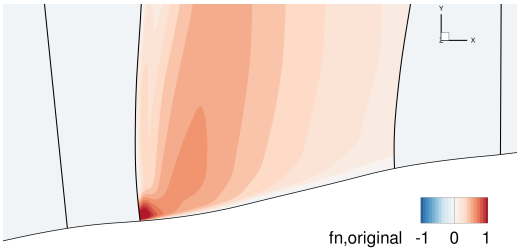

(c) Original normal force at first stator hub.

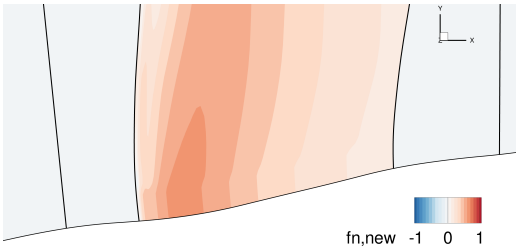

(d) Clipped normal force at first stator hub.

Figure 4.11: View of the normal force component for the 2° Body-Force sector of CREATE.

$$f_{n,clipped} = \begin{cases} f_n\left(\dfrac{\delta_{1,hb}}{B}\right) & \text{if} \quad \dfrac{h}{H} \leq \dfrac{\delta_{1,hb}}{B} \\ f_n\left(\dfrac{h}{H}\right) & \text{if} \quad \dfrac{\delta_{1,hb}}{B} \leq \dfrac{h}{H} \leq 1 - \dfrac{\delta_{1,sh}}{B} \\ f_n\left(1 - \dfrac{\delta_{1,sh}}{B}\right) & \text{if} \quad 1 - \dfrac{\delta_{1,sh}}{B} \leq \dfrac{h}{H} < \dfrac{h}{H}\Big|_{\text{gap}} \\ 0 & \text{if} \quad \dfrac{h}{H} \geq \dfrac{h}{H}\Big|_{\text{gap}} \end{cases} \tag{4.4}$$

$$f_n = \frac{W^2}{2sb|n_\theta|} 2\pi\delta K_n K_{Mach} \tag{4.5}$$

In Equation (4.5), the relative velocity W, the geometrical parameters s, b, and n_θ, the flow deviation δ, and the correction factor K_{Mach}, depend on the channel height (h/H) corresponding to the argument of $f_n(\cdot)$.

4.3.3 Integration of Secondary Losses

The integration of secondary losses has been developed for the IHPC compressor, which exhibited significant deviations from reference data at the endwalls. While this approach was specifically applied to this configuration, it is widely applicable and offers potential benefits for a range of compressor architectures.

The integration of secondary losses involves two main steps. First, a suitable correction term must be identified from the empirical, analytical, and hybrid expressions available for use within the Body-Force framework. Since Body-Force calculations do not include detailed blade geometries or near-blade flow information, the selected correlation must rely on simplified representations of secondary flow phenomena compatible with the model's available data. The second step consists of incorporating the chosen correction term into the Body-Force equations, typically expressed as a total pressure loss coefficient or an entropy loss. Both aspects are addressed in the following.

Secondary loss correlation The correlation employed to address the identified significant errors near the blade tips of the IHPC compressor is Roberts' total pressure loss coefficient for rotor tip losses, associated with the tip leakage vortex generated in the rotor gaps [135].

This correlation is an empirical expression based on the displacement thickness at the rotor inlet, $\overline{\delta_1^*}$, and the tip clearance, $\overline{tc}$, both normalised by the blade span B. Notably, the chosen correlation does not require the pressure difference between the pressure and suction sides of the blade, which is unavailable in Body-Force calculations. The displacement thickness δ_1^* can be computed using the empirical formula given in Equation (4.6), as reported by [16].

$$\delta_1^* = 0.048 \frac{x}{Re_x^{1/5}} \tag{4.6}$$

Roberts' correlation is composed of different elements, described in the following.

1. The maximum loss at the rotor tip region $(\overline{\omega}_{3D})_{max,rt}$ is a function of $\overline{\delta_1^*}$ and $\overline{tc}$, as in Equation (4.7).

$$(\overline{\omega}_{3D})_{max,rt}(\theta) = 0.25 \tanh \sqrt{\overline{\delta_1^*}(\theta) \cdot \overline{tc} \times 10^3} \tag{4.7}$$

2. The location of the maximum loss $(\overline{S}_{3D})_{max,rt}$, expressed as a percentage of the blade-span from the tip endwall, is also a function of those quantities, as in Equation (4.8).

$$(\overline{S}_{3D})_{max,rt}(\theta) \simeq 0.125 \tanh \sqrt{\overline{\delta_1^*}(\theta) \cdot \overline{tc} \times 10^3} \tag{4.8}$$

3. The radial position of the maximum loss is thus expressed as a percentage of the blade span, as in Equation (4.9).

$$h_{(\overline{\omega}_{3D})_{max,rt}}(\theta) = 1 - (\overline{S}_{3D})_{max,rt}(\theta) \tag{4.9}$$

4. The extent of the loss region is given in Equation (4.10).

$$(\overline{S}_{3D})_{rt}(\theta) \simeq 2.5(\overline{S}_{3D})_{max,rt}(\theta) \tag{4.10}$$

5. Finally, the distribution of total pressure loss $\overline{\omega}_{rt}$ is represented by the Gaussian distribution in Equation (4.11).
(4.11)

$$\overline{\omega}_{rt}(\theta) = (\overline{\omega}_{3D})_{max,rt}(\theta) \cdot exp\left(-\frac{(h - h_{(\overline{\omega}_{3D})_{max,rt}}(\theta))^2}{2\sigma^2(\theta)}\right) \quad \text{where} \quad \sigma^2(\theta) = \frac{(\overline{S}_{3D})^2_{rt}(\theta)}{-4\ln 0.01}$$

Figure 4.12 depicts the Gaussian distribution of Roberts losses [135]. The correlation presented here corresponds to the distribution on the right, at the blade tip, where all the presented parameters are visible: the maximum loss $(\overline{\omega}_{3D})_{max,rt}$ corresponding to the distribution peak, the location of this maximum, $(\overline{S}_{3D})_{max,rt}$, establishing the position with respect to the shroud, and the extent of the loss distribution region $(\overline{S}_{3D})_{rt}$.

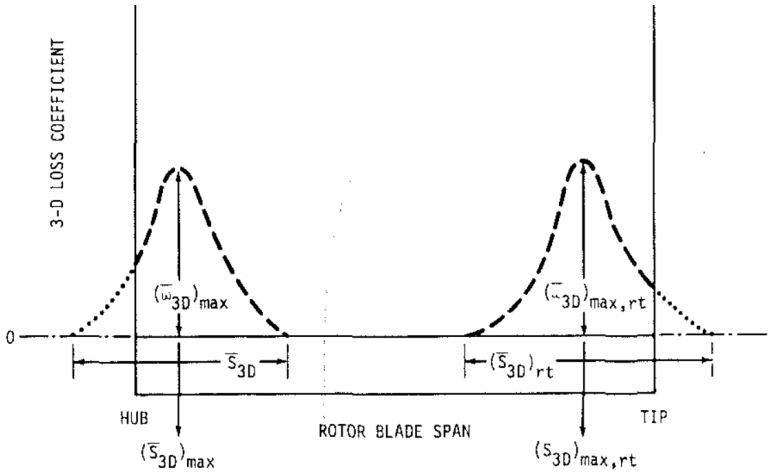

Figure 4.12: Schematic of the total pressure loss distribution [135].

Certain limitations must be acknowledged when employing this correlation. Firstly, as noted by Roberts et al. [135], the correlation was developed based on a limited dataset. Additionally, the original study focused exclusively on subsonic flow conditions. Lastly, the correlation's accuracy may diminish in the presence of flow distortions, since it was derived from configurations evaluated only at their design operating points, and therefore lacks validation for off-design scenarios.

For the investigated case, to improve the accuracy of the loss distribution, the radial position of the rotor tip vortex is limited such that the peak of the Gaussian loss distribution does not exceed approximately 5% of the channel height measured from the shroud wall. This adjustment is supported by multiple studies in the literature [91, 147, 163] that highlight the influence of the tip gap on the loss distribution and consistently locate the region of maximum losses near this 5% threshold.

Loss distribution integration in the Body-Force model To incorporate a total pressure loss coefficient $\overline{\omega}$ within the Body-Force equations, an additional term for the parallel force component is introduced. Based on Marble's relation [105], which links the parallel force f_p to the entropy gradient, and assuming a linear entropy variation along the meridional streamline, this additional parallel force component for modelling losses can be expressed as shown in Equation (4.12).

$$f_p(x,r,\theta) = -\frac{T_s V_m}{W}(x,r,\theta)\frac{\Delta s(r,\theta)}{c_m(r)} \tag{4.12}$$

Here, the subscript m denotes the quantities related to the meridional streamline; T_s is the static temperature; V and W represent the absolute and relative flow velocity magnitudes, respectively; and c is the blade chord length.

When the loss correlation is expressed in terms of entropy loss, it can be directly substituted into Marble's Equation (4.12). However, if the correlation is provided as a total pressure loss coefficient, additional steps are required.

The subsequent step consists of expressing the total pressure loss distribution in terms of an equivalent entropy loss. The total pressure loss coefficient between an inlet (1) and an outlet (2) station, typically obtained from empirical correlations, is defined as:

$$\overline{\omega} = \frac{p_{t1} - p_{t2}}{p_{t1} - p_1}. \tag{4.13}$$

Following the approach proposed by Aungier [2], the absolute pressure loss coefficient of the cascade is transformed into a relative pressure loss applicable to the rotor, expressed by Equation (4.14).

$$p^w_{t2}(r,\theta_2) = p^w_{t2,is}(r,\theta_2) - \overline{\omega}(\theta)\left(p^w_{t1}(r,\theta_2) - p_1(r,\theta_2)\right), \tag{4.14}$$

where the superscript $\cdot^w$ denotes quantities evaluated in the relative reference frame.

From this expression, the equivalence given in Equation (4.15) can be demonstrated:

$$\frac{p^w_{t2}(r,\theta_2)}{p^w_{t2,is}(r,\theta_2)} = 1 - \overline{\omega}(\theta)\frac{p^w_{t1}(r,\theta_2)\left[1 - \left(1 + \frac{\gamma-1}{2}M^2_{w1}(r,\theta_1)\right)^{-\frac{\gamma}{\gamma-1}}\right]}{p^w_{t2,is}(r,\theta_2)}, \tag{4.15}$$

where γ is the ratio of specific heats and M_{w1} denotes the relative Mach number at inlet.

Applying conservation of rothalpy to account for radial variations along the streamline from inlet to outlet, the isentropic outlet total pressure relates to the inlet quantities via the relation $p^w_{t2,is} = p^w_{t1}\left(\frac{T^w_{t2}}{T^w_{t1}}\right)^{\frac{\gamma}{\gamma-1}}$, such that Equation (4.15) is rewritten as:

$$\frac{p^w_{t2}(r,\theta_2)}{p^w_{t2,is}(r,\theta_2)} = 1 - \overline{\omega}(\theta)\left[1 - \left(1 + \frac{\gamma-1}{2}M^2_{w1}(r,\theta_1)\right)^{-\frac{\gamma}{\gamma-1}}\right]\left(\frac{T^w_{t2}(r,\theta_2)}{T^w_{t1}(r,\theta_1)}\right)^{-\frac{\gamma}{\gamma-1}} \tag{4.16}$$

Finally, by applying Gibbs' fundamental relation for the relative total quantities [53], the entropy loss associated with the pressure loss coefficient $\overline{\omega}$ can be expressed, consistent with the formulation of Guo et al. [63], as $\Delta s(r,\theta) = -R_{gas}\ln\left(\frac{p^w_{t2}(r,\theta_2)}{p^w_{t2,is}(r,\theta_2)}\right)$, which translates as shown in Equation (4.17).

$$\Delta s(r,\theta) = -R_{gas}\ln\left\{1 - \overline{\omega}(\theta)\left[1 - \left(1 + \frac{\gamma-1}{2}M^2_{w1}(r,\theta_1)\right)^{-\frac{\gamma}{\gamma-1}}\right]\left(\frac{T^w_{t2}(r,\theta_2)}{T^w_{t1}(r,\theta_1)}\right)^{-\frac{\gamma}{\gamma-1}}\right\} \tag{4.17}$$

To enable an accurate comparison of flow properties between stations 1 and 2 and to obtain reliable loss estimations within the model, it is necessary to identify the flow path linking these two stations. As the flow traverses the rotor blade row, it experiences an azimuthal displacement, denoted by $\Delta\theta(r,\theta)$, resulting from two distinct phenomena: the relative motion of the rotating reference frame, and the aerodynamic turning imparted by the blades in the relative frame. This azimuthal shift occurs independently of the inflow conditions. In the case of axisymmetric inflow, the flow field exhibits invariance along the azimuthal direction; therefore, comparisons performed at fixed azimuthal positions (iso-θ) between stations are valid and effectively correspond to imposing $\Delta\theta(r,\theta) = 0$. Conversely, when non-axisymmetric inflow distortions are present, flow properties vary with azimuthal position, and neglecting the azimuthal displacement $\Delta\theta(r,\theta)$ would lead to comparisons between flow regions that are not physically connected. To maintain consistency, flow quantities must be evaluated along the true flow path defined by $\Delta\theta(r,\theta)$. This azimuthal shift is decomposed into two components, as formalised in Equation (4.18).

$$\Delta\theta(r,\theta) = \Delta\theta_s(r) + \Delta\theta_r(r,\theta) \tag{4.18}$$

1. **Stagger Component** $\Delta\theta_s$
   The component $\Delta\theta_s$ quantifies the azimuthal shift introduced by blade stagger, capturing the deviation of the streamline resulting from the prescribed blade metal angles. By approximating the flow deflection as a circular arc, the effective stagger angle β_s can be determined based on the inlet and outlet blade angles:

   $$\beta_s = \frac{1}{2}\left[\beta_1(r) + \beta_2(r)\right]. \tag{4.19}$$

   For a blade section at radius r, the corresponding azimuthal shift relates to the blade chord length $c(r)$ as expressed in Equation (4.20).

   $$r\Delta\theta_s = c(r)\sin(\beta_s). \tag{4.20}$$

   Rearranging yields the stagger component of the azimuthal shift as given in Equation (4.21).

   $$\Delta\theta_s(r) = \sin\left(\frac{1}{2}\left[\beta_1(r) + \beta_2(r)\right]\right)\frac{c(r)}{r}. \tag{4.21}$$

   It is worth noting that for positive rotation speed, the flow angles β_1 and β_2 are negative in a compressor rotor, and consequently, the value of θ_s is also negative.

2. **Rotation Component** $\Delta\theta_r$
   The rotation component $\Delta\theta_r$ captures the azimuthal shift resulting from the blade motion. It is evaluated by multiplying the angular velocity ω by the transit time $\Delta t(r,\theta)$, which represents the time taken by the flow to cross the blade chord at the local mean relative velocity, as defined in Equation (4.22).

   $$\Delta\theta_r(r,\theta) = \omega\Delta t(r,\theta) = \omega\frac{c(r)}{\frac{1}{2}\left[W_1(r,\theta) + W_2(r,\theta)\right]}. \tag{4.22}$$

   In this formulation, $W_1(r,\theta)$ and $W_2(r,\theta)$ represent the relative velocities at the blade's leading and trailing edges, respectively. To maintain numerical stability, particularly

near the endwalls where the relative velocity approaches zero, the computed $\Delta t(r, \theta)$ is constrained within the bounds of the minimum and maximum values observed in the central span region ($0.05 \leq h \leq 0.95$). This clipping procedure prevents unrealistic values and avoids division by near-zero quantities. Additionally, as a first-order approximation, W_1 and W_2 are used without adjusting for the azimuthal displacement $\Delta\theta$, thereby eliminating the need for iterative correction.

The computed $\Delta\theta(r, \theta)$ is employed to execute a smooth, two-dimensional interpolation of flow field data across both radial and azimuthal directions. This is done at the level of individual mesh cells, allowing for a spatially varying rotation that adapts locally to the mesh structure. To preserve numerical accuracy, cubic interpolation is employed.

As previously outlined, $\Delta\theta(r, \theta)$ represents the azimuthal displacement experienced by the flow between station 1 and station 2. In order to enable a consistent comparison between the two datasets, the field at station 1 is shifted by the interpolated $\Delta\theta(r, \theta)$, while the field at station 2 remains unchanged. This results in $\theta_2 = \theta$ and $\theta_1 = \theta_2 - \Delta\theta$ in Equation (4.17). The method provides an analytical approximation of the flow path without explicitly tracking streamlines, offering a computationally efficient approach that ensures accurate spatial alignment of flow features between stations.

Final formulation of the rotor tip losses The final expression for the entropy increase Δs associated with Roberts' total pressure loss distribution at the rotor tips, $\overline{\omega}_{rt}$, is given in Equation (4.23). This corresponds to Equation (4.17) with $\overline{\omega} = \overline{\omega}_{rt}$ and $\theta_1 = \theta_2 - \Delta\theta$.

(4.23)
$$\Delta s_{rt}(r, \theta) = -R_{\text{gas}} \ln \left\{ 1 - \overline{\omega}_{rt}(\theta) \left[1 - \left(1 + \frac{\gamma - 1}{2} M^2_{w1}(r, \theta_2 - \Delta\theta) \right)^{-\frac{\gamma}{\gamma-1}} \right] \left(\frac{T^w_{t2}(r, \theta_2)}{T^w_{t1}(r, \theta_2 - \Delta\theta)} \right)^{-\frac{\gamma}{\gamma-1}} \right\}$$

The component of the parallel force associated with rotor tip losses is obtained by introducing Δs_{rt} into Equation (4.12), yielding Equation 4.24.

(4.24)
$$f_{p,rt} = -\frac{T_s V_m}{W} \frac{\Delta s_{rt}}{c_m}$$

The total parallel force is then composed of the viscous term from the Hall-Thollet model, $f_{p,HT}$, and the additional contribution from secondary loss integration. Thus:

(4.25)
$$f_p = f_{p,HT} + f_{p,rt}$$

4.3.4 Final Modified Model

The final formulation of the normal and parallel force components, including all implemented modifications, is given in Equation (4.26). In the normal force, the terms W, s, b, n_θ, δ, and K_{Mach} explicitly vary with the spanwise coordinate h/H. This set of equations includes the calibration coefficients, K_n, K_f and K_D; the additional term in the parallel force component resulting from the integration of rotor tip losses $f_{p,rt}$; and the piecewise definition of the normal force derived from the clipping technique.

$$
\begin{cases}
f_{n,clipped} = \begin{cases}
f_n\left(\dfrac{\delta_{1,hb}}{B}\right) & \text{if} \quad \dfrac{h}{H} \leq \dfrac{\delta_{1,hb}}{B} \\
f_n\left(\dfrac{h}{H}\right) = \dfrac{W^2}{2sb|n_\theta|} 2\pi\delta K_n K_{Mach} & \text{if} \quad \dfrac{\delta_{1,hb}}{B} \leq \dfrac{h}{H} \leq 1 - \dfrac{\delta_{1,sh}}{B} \\
f_n\left(1 - \dfrac{\delta_{1,sh}}{B}\right) & \text{if} \quad 1 - \dfrac{\delta_{1,sh}}{B} \leq \dfrac{h}{H} < \dfrac{h}{H}\Big|_{\text{gap}} \\
0 & \text{if} \quad \dfrac{h}{H} \geq \dfrac{h}{H}\Big|_{\text{gap}}
\end{cases} \\
f_p = \dfrac{W^2}{2sb|n_\theta|}\left[2K_f C_f + 2\pi K_{Mach}|\delta - \delta^{pivot}|^{2K_D}\right] - \dfrac{T_s V_m}{W}\dfrac{\Delta s_{rt}}{c_m}
\end{cases}
\tag{4.26}
$$

The complete workflow for applying the proposed modifications is illustrated in Figure 4.13. Initially, local corrections are applied. If the walls are modeled as viscous, the clipping mechanism is activated, extracting the reference boundary layer from a previous Body-Force calculation. Simultaneously, if rotors are present, tip losses are activated. Finally, once all local corrections have been applied, the calibration process begins. This order is crucial, as the local corrections directly influence the final values of the calibration coefficients, making it necessary to apply them first.

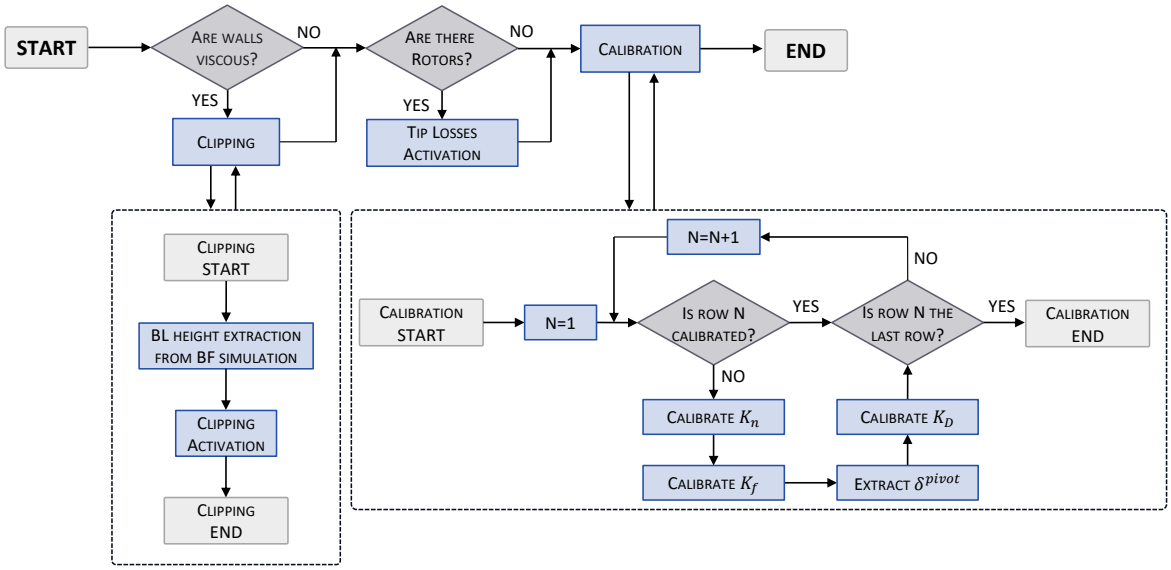

Figure 4.13: Workflow of the modified Body-Force Model.

This modified model has been applied individually to each compressor, taking into account their specific characteristics. Further details regarding the calibration and clipping parameters for each case are provided in Section 5.1 for the CREATE test case and in Section 6.1 for the IHPC compressor.

Conclusion

This chapter builds upon the reference numerical data developed in Chapter 3 to define and characterise key modifications to the baseline Hall-Thollet model aimed at improving its reliability for high-pressure compressors and to achieve prediction accuracy comparable to (U)RANS calculations. These enhancements form the basis for the analyses presented in Chapters 5, 6, and 7.

The chapter begins by identifying the prediction errors of the original Hall-Thollet model when applied to high-pressure compressors, whose aerodynamic conditions challenge its foundational assumptions. To address these limitations, three main improvements were introduced: a robust calibration methodology to enhance accuracy across operating conditions; near-wall corrections to improve model behavior near the hub and shroud as well as at low mass flow rates; and the incorporation of secondary loss correlations within the Body-Force model framework.

A calibration strategy independent of operating point, shaft speed, and inlet conditions was then proposed. This approach relies solely on scalar coefficients derived from a detailed sensitivity analysis that clarified the influence of each parameter on model performance. The near-wall correction, referred to as clipping, draws inspiration from prior studies highlighting accuracy issues near casing walls and flow instabilities at reduced mass flow rates, and was integrated to specifically mitigate these challenges. Furthermore, a general formulation for incorporating loss correlations was developed, expressed in terms of entropy losses or total pressure loss coefficients. A specific correlation addressing rotor tip losses due to leakage flow was presented and implemented, with adjustments made to reflect the characteristics of modern compressor blades. It was found that applying local corrections, including near-wall and secondary loss adjustments, prior to the global calibration is necessary, as these corrections directly affect the final values of the calibration coefficients. Following these modifications, the accuracy of the model is inherently limited by that of the reference data, here the (U)RANS calculations used in the calibration process, as well as by that of the employed correlations, in this case those of Roberts [135].

Although these correction strategies are applied to specific test cases, their applicability extends beyond the compressors considered in this study. The proposed Body-Force model and methodology provide a flexible framework adaptable to a range of high-pressure compressor configurations. While calibration parameters may vary between configurations, the underlying approach, which combines systematic calibration, clipping corrections near walls, and integration of secondary loss correlations, offers a robust foundation for improving predictive accuracy across diverse turbomachinery applications.

In summary, this chapter presents a comprehensive and enhanced Body-Force model that overcomes key limitations of the original formulation in high-pressure compressor applications. The model's performance and validation are examined in detail in subsequent chapters, starting with Chapter 5, which focuses on the CREATE compressor study.

CHAPTER 5

Investigation of Inlet Distortion Effects on the CREATE Compressor via Body Force Methodology

This chapter focuses on investigating the effects of inlet distortion on compressor performance and stability through the application of the enhanced Body-Force model. Beginning with clean inflow conditions, the analysis progressively introduces radial and circumferential distortion patterns to examine their influence on the compressor's aerodynamic behavior. The study covers multiple operating points to capture a wide range of performance regimes, including near-stall conditions. Emphasis is placed on evaluating the model's capability to accurately predict local and global flow variations induced by distortion while highlighting its computational advantages over traditional blade-resolved simulations. Through this approach, the chapter aims to validate the Body-Force model as a reliable and efficient tool for analyzing complex distortion phenomena in compressors.

Contents

5.1 Validation of the Modified Body Force Model on the CREATE Compressor . **118**
5.1.1 Global Performance Analysis . . . 119
5.1.2 Local Flow Analysis . . . 123
5.2 Impact of Radial Distortion on the CREATE Compressor . . . **128**
5.2.1 Impact on the Flow Field . . . 128
5.3 Impact of Circumferential Distortion on the CREATE Compressor . . . **131**
5.3.1 Impact on the Flow Field . . . 131
5.3.2 Impact on Stability Parameters . . . 134
5.4 Considerations on CPU Time Gain . . . **138**
Conclusion . . . **139**

5.1 Validation of the Modified Body Force Model on the CREATE Compressor

This section analyses the CREATE compressor, presented in Chapter 2, using the Body-Force approach developed in Chapter 4. As outlined previously, the adaptations made to the original Hall-Thollet model for this compressor comprise a calibration strategy to enhance global performance prediction and the application of normal-force clipping to improve near-wall flow representation.

The calibration procedure was carried out following the methodology described in Section 4.3.1. Two separate calibration processes were required due to fundamental differences in the configurations under consideration: one corresponding to the original full-height CREATE case, based on the SBP results and exploited for both the SBP and the $2\pi/16$ sector domains, and another specific to the pseudo-2D (P2D) configuration. The latter, characterized by the absence of viscous hub and shroud walls, does not necessitate near-wall corrections, and since these local corrections have been shown to influence the coefficient values, which justifies their required application first in the modification workflow presented in Chapter 4, it therefore requires different calibration values. Consequently, the calibration coefficients for the P2D case were recalculated, as their values are sensitive to local correction factors, in accordance with the approach detailed in Section 4.3.1.

The calibrated coefficients corresponding to the full-height CREATE configuration are summarized in Table 5.1, while those associated with the P2D configuration are reported in Table 5.2. As suggested in the previous chapter, the coefficient values do not exhibit a regular trend and may lie either above or below unity, a behaviour that strongly depends on the geometric and aerodynamic properties of each blade.

Table 5.1: Calibration coefficients for each blade of the full-height CREATE compressor configuration.

	R1	**S1**	**R2**	**S2**	**R3**	**S3**
K_n	1.10	0.75	0.85	1.25	0.70	0.75
K_f	0.80	1.15	1.05	0.70	1.20	1.00
K_d	1.21	1.30	1.17	1.15	1.12	1.03

Table 5.2: Calibration coefficients for each blade of the CREATE compressor in the P2D configuration.

	R1	**S1**	**R2**	**S2**	**R3**	**S3**
K_n	1.10	0.75	0.95	0.67	1.15	0.65
K_f	0.80	1.06	0.82	1.05	0.60	1.15
K_d	1.20	1.40	1.33	1.52	1.30	1.08

The clipping of the normal force was applied in accordance with the guidelines detailed in Section 4.3.2. The clipping heights were set to 2% channel height at the hub and 6% at the shroud, corresponding to the inlet boundary layer thickness, as illustrated in Section 4.3.2.

The remainder of this section is dedicated to the validation of the enhanced Body-Force model on the CREATE configuration. This validation is carried out through both global and local flow field analyses of the Body-Force predictions, with comparisons made against the reference data.

In particular, as outlined in Chapter 3, the model validation for the CREATE case involves a comparison between the reference blade-resolved, mixing-plane, single-blade-passage simulations and the Body-Force predictions obtained from the 2° sector configuration, under clean inflow conditions. These configurations were presented in Sections 3.1.1.1 and 4.1.1, respectively.

5.1.1 Global Performance Analysis

The analysis begins with the validation of the compressor's global performance predictions. Figure 5.1 presents key performance metrics for the complete three-stage compressor, including the reference blade-resolved data (SBP - bladed), which is also used to non-dimensionalise data, the Body-Force predictions using the original Hall-Thollet model (BF - HT), and the enhanced model predictions (BF - new). Specifically, Figure 5.1a shows the total-to-total pressure ratio, Figure 5.1b the total-to-static pressure ratio, Figure 5.1c the total-to-total temperature ratio, and Figure 5.1d the isentropic efficiency. These results were partially introduced in Chapter 4, In Figures 4.1 and 4.2, to highlight the limitations of the original model when applied to multi-stage high-pressure compressors. Here, the plots are supplemented with data from the enhanced model.

It can be observed that the applied corrections substantially reduce the prediction errors, identified in Chapter 4, across all performance metrics. Notably, the choke mass flow rate is now accurately reproduced, and the enhanced model achieves convergence at lower mass flow rates. In contrast, the original model failed to converge near the peak-efficiency flow rate, corresponding to $Q_{corr}/Q_{corr|PE} = 1$, as indicated in the plots.

An estimate of the prediction errors relative to the blade-resolved reference data is provided in Table 5.3. For each performance metric, the peak efficiency (PE) point, defined at $Q_{corr}/Q_{corr|PE} = 1$, and the near-stall (NS) point are analysed. The NS point is selected as follows: for the single-blade-passage case, it corresponds to the experimentally identified stable near-stall condition, whereas for the Body-Force calculation it is defined as the operating point exhibiting the same outlet pivot pressure as the single-blade-passage NS point. For each operating point, the prediction error for a metric X is computed as $(X_{BF} - X_{BR})/X_{BR}$, where BR denotes the blade-resolved reference calculations.

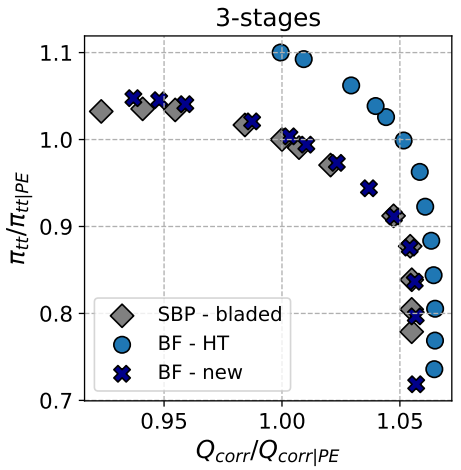

(a) Total-to-total pressure ratio π_{tt}.

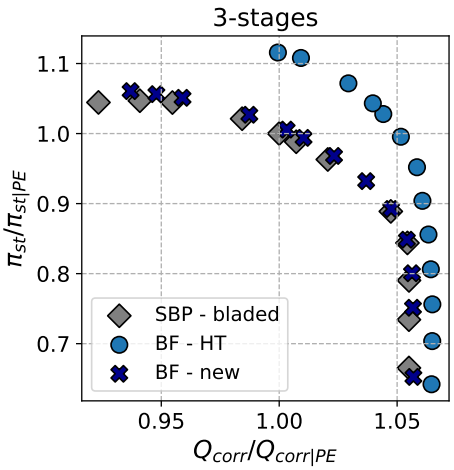

(b) Total-to-static pressure ratio π_{st}.

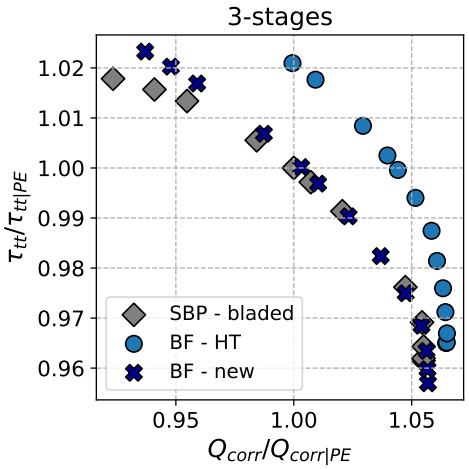

(c) Total-to-total temperature ratio τ_{tt}.

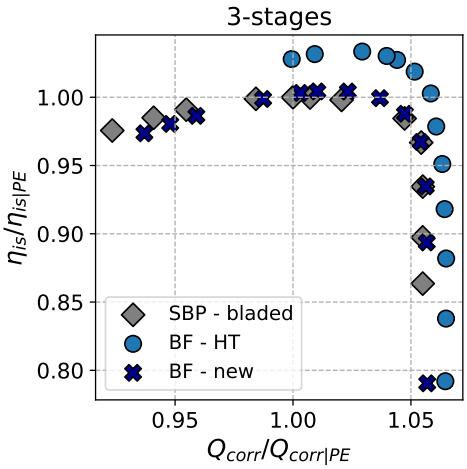

(d) Isentropic efficiency η_{is}.

Figure 5.1: Comparison of global performance metrics for the 3-stage CREATE compressor: blade-resolved reference (SBP - bladed), Body-Force with original Hall-Thollet model (BF - HT), and Body-Force with the enhanced model (BF - new).

Table 5.3 shows that at the peak efficiency point, the original model's errors in pressure ratios are approximately 10-11%, which are reduced to 0.5-0.7% by the modified model. Similarly, the isentropic efficiency error decreases from 2.86% to 0.16%, and the temperature ratio error is reduced from 2.08% to 0.01%. At the near-stall operating point, the original model fails to converge, whereas the enhanced model successfully converges, producing prediction errors between 0.6-1.1%. This significant reduction in errors is consistent across the compressor map's operating range.

It is important to recall that the improved global performance of the complete compressor results from a sequential calibration process applied to each row individually. To further illustrate the impact of the modifications, Figure 5.2 shows the performance metrics for the second rotor row, which was previously identified in Section 4.2 as one of the rows exhibiting the largest discrepancies with respect to the reference data.

Table 5.3: Relative prediction errors of global performance metrics for the unmodified and modified Body-Force models compared to blade-resolved RANS simulations, at peak efficiency (PE) and near-stall (NS) operating points.

Operating Point	Model	π_{tt}	π_{st}	η_{is}	τ_{tt}
PE	BF - HT	10.00%	11.16%	2.86%	2.08%
	BF - new	0.50%	0.70%	0.16%	0.01%
NS	BF - HT	–	–	–	–
	BF - new	1.05%	1.12%	-0.86%	0.60%

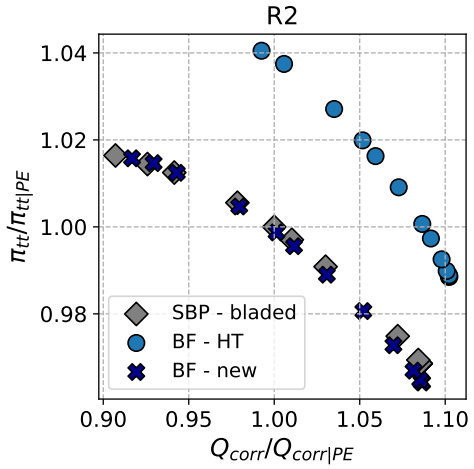

(a) Total-to-total pressure ratio π_{tt}.

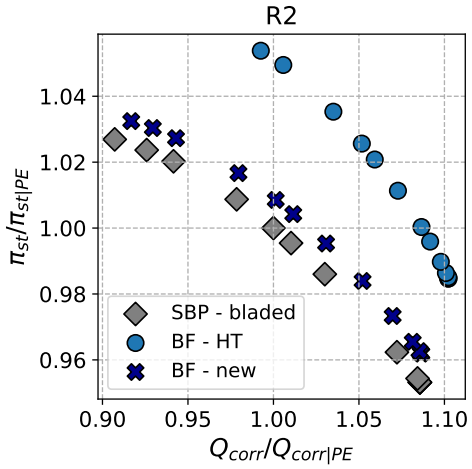

(b) Total-to-static pressure ratio π_{st}.

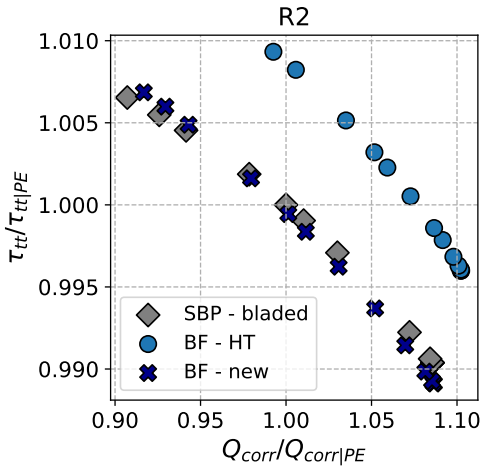

(c) Total-to-total temperature ratio τ_{tt}.

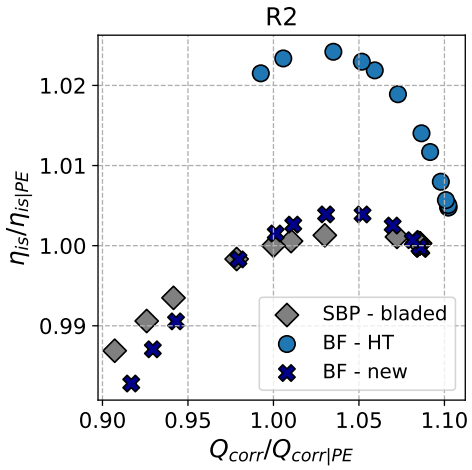

(d) Isentropic efficiency η_{is}.

Figure 5.2: Comparison of performance metrics for the second rotor row of the CREATE compressor: blade-resolved reference (SBP - bladed), Body-Force with original Hall-Thollet model (BF - HT), and Body-Force with the enhanced model (BF - new).

As shown in the figure, all key performance metrics for this row are significantly improved following the model updates. This confirms that the proposed sequential calibration strategy, calibrating rows from upstream to downstream, effectively produces accurate predictions both at the individual row level and at the global compressor level in a multi-stage configuration. For completeness, Appendix B includes the performance plots for each individual blade row, with the original and modified model.

Finally, an insight into the relative roles of the local and global modifications on performance predictions is provided. Figure 5.3 presents the total-to-total pressure-ratio characteristic of the complete compressor and of the first three blade rows. Data are shown for the blade-resolved reference data, the baseline Body-Force model, the modified Body-Force model, and an intermediate version in which only the clipping modification is applied, without calibrated coefficients.

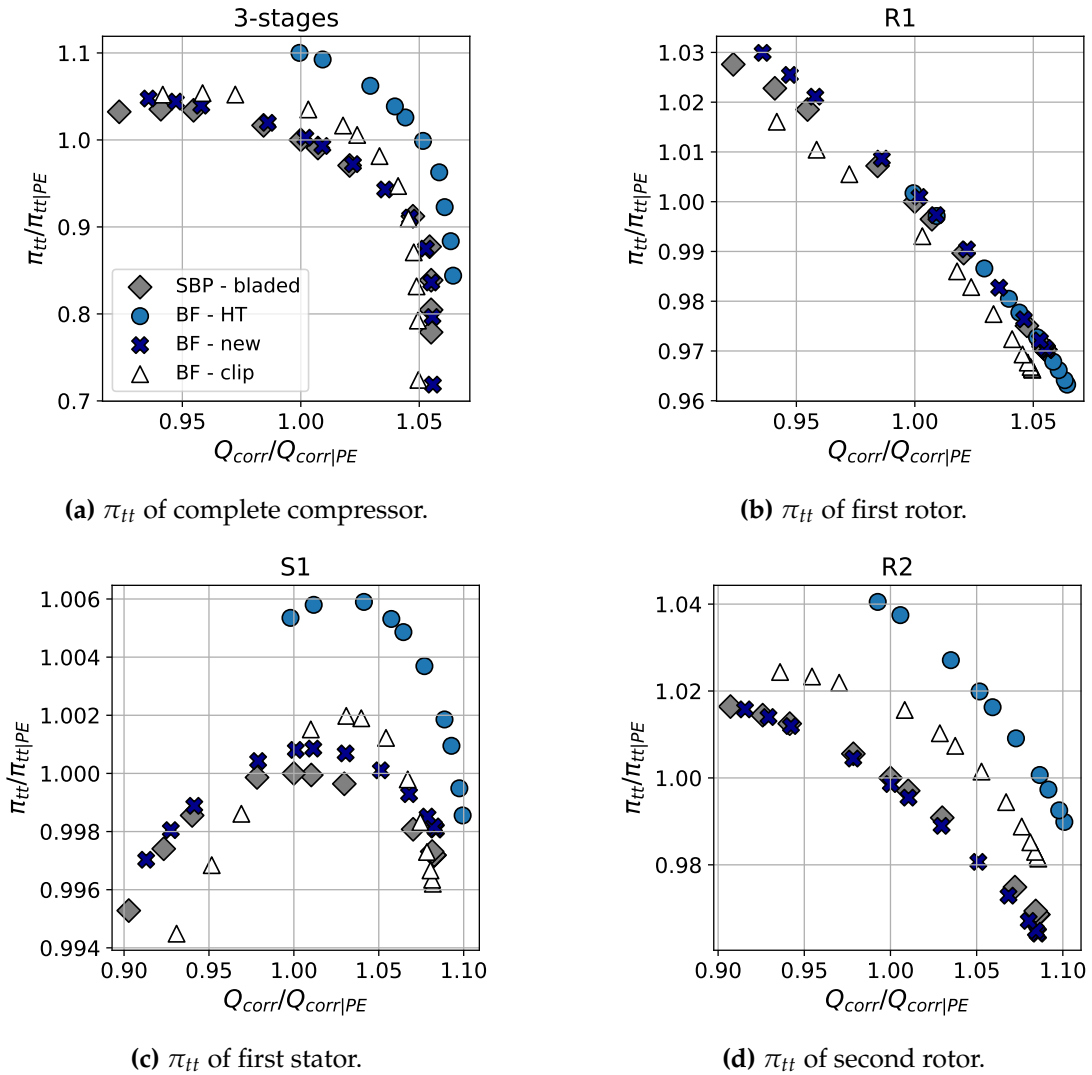

(a) π_{tt} of complete compressor.

(b) π_{tt} of first rotor.

(c) π_{tt} of first stator.

(d) π_{tt} of second rotor.

Figure 5.3: Comparison of π_{tt} characteristics of the CREATE compressor: blade-resolved reference (SBP - bladed), Body-Force with original Hall-Thollet model (BF - HT), Body-Force with the enhanced model (BF - new) and Body-Force with the clipping only (BF - clip).

These data show first that the clipping technique enlarges the stable operating range, allowing to converge at lower mass flow rates than the baseline model, and second that clipping alone cannot provide a coherent representation of the compressor performance. The complete-compressor characteristic appears in good agreement with the reference data, even without calibration, but this is the result of compensating errors. In fact, at the row level, the clipping-only case exhibits large prediction errors. Losses are over-predicted at the first rotor and under-predicted at the second rotor. The shape of the characteristic is also incorrect, particularly for the first stator, which could lead to premature stall or choke. The combination of both local and global corrections is therefore essential for accurate row-by-row predictions, which are required to correctly capture distortion response and its transmission through the compressor.

5.1.2 Local Flow Analysis

The previous section demonstrated the enhanced model's ability to accurately predict integral performance metrics. However, it is equally important to verify whether these overall performance improvements correspond to realistic local flow behavior. This section addresses this aspect by focusing on a detailed local flow analysis. Two operating points are considered for this purpose: the peak efficiency (PE) point and the near-stall (NS) point, defined as in the previous section. Spanwise profiles are normalized by the mean of the single-blade-passage, blade-resolved data, as described in Section 2.3.2, whereas meridional fields are normalized to the range between 0 and 1.

Peak Efficiency Operating Point The initial investigation of the local flow field focuses on spanwise profiles of total pressure and total temperature at various axial stations throughout the compressor. Total pressure profiles provide insight into aerodynamic losses and compression effectiveness, while total temperature profiles reflect the work input to the flow. Together, these quantities offer a preliminary assessment of the local flow behavior and enable comparison with blade-resolved predictions.

Figure 5.4 shows these profiles at stations downstream of each rotor and at the compressor outlet. The data include the blade-resolved reference calculations (SBP - bladed), the Body-Force approach with the original Hall-Thollet model (BF - HT), and the enhanced model (BF - new). A first observation concerns the mean values of the profiles. It is evident that the modified model provides much more accurate predictions at the iso-$Q_{corr}/Q_{corr|PE}$ operating point. A clear shift of the radial profiles is observed, which directly results from the applied calibration coefficients that translate the profiles effectively. Significant improvements are visible in both the total pressure and total temperature profiles. A second observation regards the near-wall flow behavior. Both at the hub and the shroud, the clipping applied to the normal force in the Body-Force model improves flow predictions in those regions. In particular, at the shroud, the total temperature values show notable improvement, with better agreement over the upper part of the blade span.

A better understanding of the contribution of the near-wall correction is gained by examining the spanwise profiles of absolute flow angle and entropy rise in Figure 5.5. The top row of Figure 5.5, showing the absolute flow angles, demonstrates that the work done by the blades on the fluid is increased near the walls, as desired, resulting in improved flow alignment. This effect is particularly evident near the shroud, where the original model failed to produce sufficient flow turning downstream of the rotor rows. The correction remains effective even

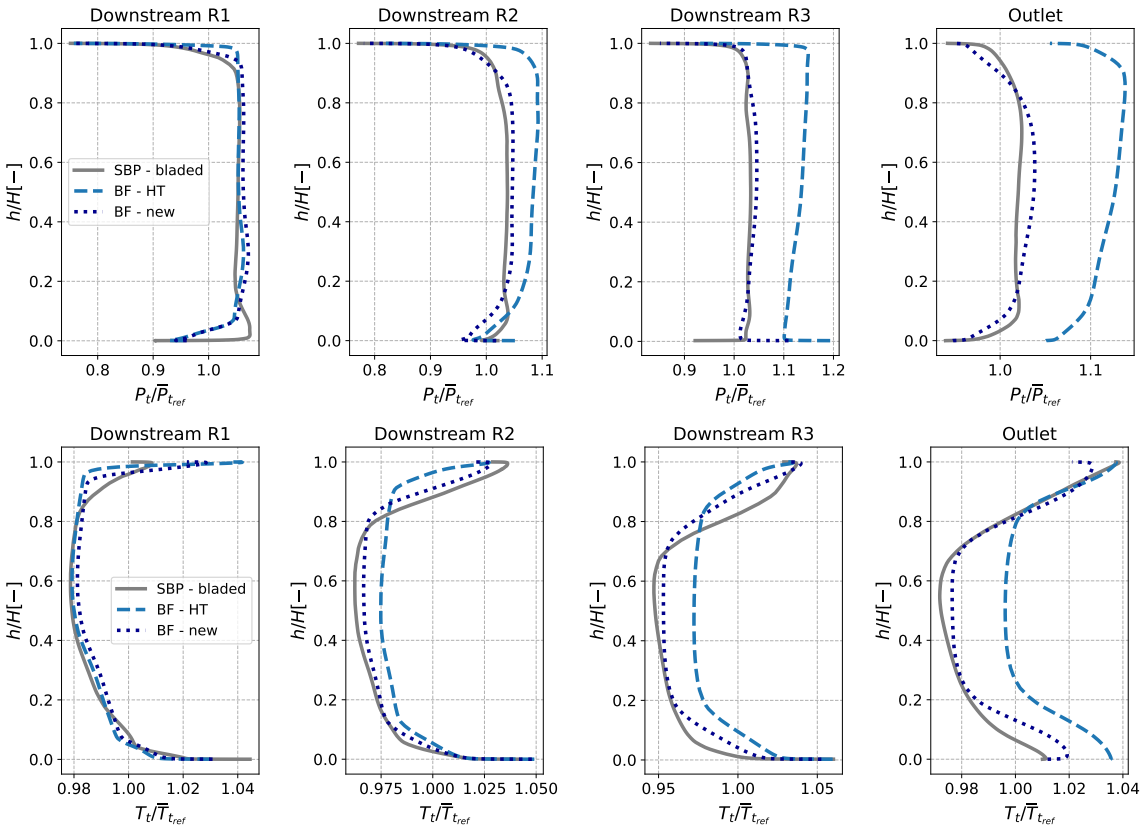

Figure 5.4: Spanwise profiles of total pressure (top row) and total temperature (bottom row) at stations downstream of each rotor and at the compressor outlet for the CREATE compressor at peak efficiency.

in the rear stages, where secondary flow effects become significant and strongly influence the spanwise flow angle profile. The bottom row presents the entropy rise profiles, which indicate that the modification of the parallel force leads to a direct modification of losses. Therefore, the enhanced model's predictions closely match the reference data, unlike the unmodified model.

A more qualitative representation of these results, which highlights the reliability of the Body-Force model's predictions across the full computational domain, is provided by the meridional views. These views show mass flow rate-weighted azimuthal averages of various flow field quantities on a meridional plane, through the post-processing procedure explained in Section 2.3.2.

Figure 5.6 depicts the absolute flow angle for both the blade-resolved reference data and the modified Body-Force model. This visualization confirms the trends observed in the radial profiles: the Body-Force model predicts the flow field with good accuracy compared to the reference. The only notable discrepancies occur near the hub downstream of the rotor rows, where the Body-Force model partially fails to realign the near-wall flow, resulting in slightly higher flow angles, and at the compressor outlet, where it predicts a smooth absolute flow-angle distribution, in contrast to the more uneven spanwise trend observed in the blade-resolved data, as shown in Figure 5.5, and likely attributed to the two counter-rotating structures generated by the hub and shroud coin separations at the suction side of the last stator row. However, the predictions show a general good agreement and an improvement

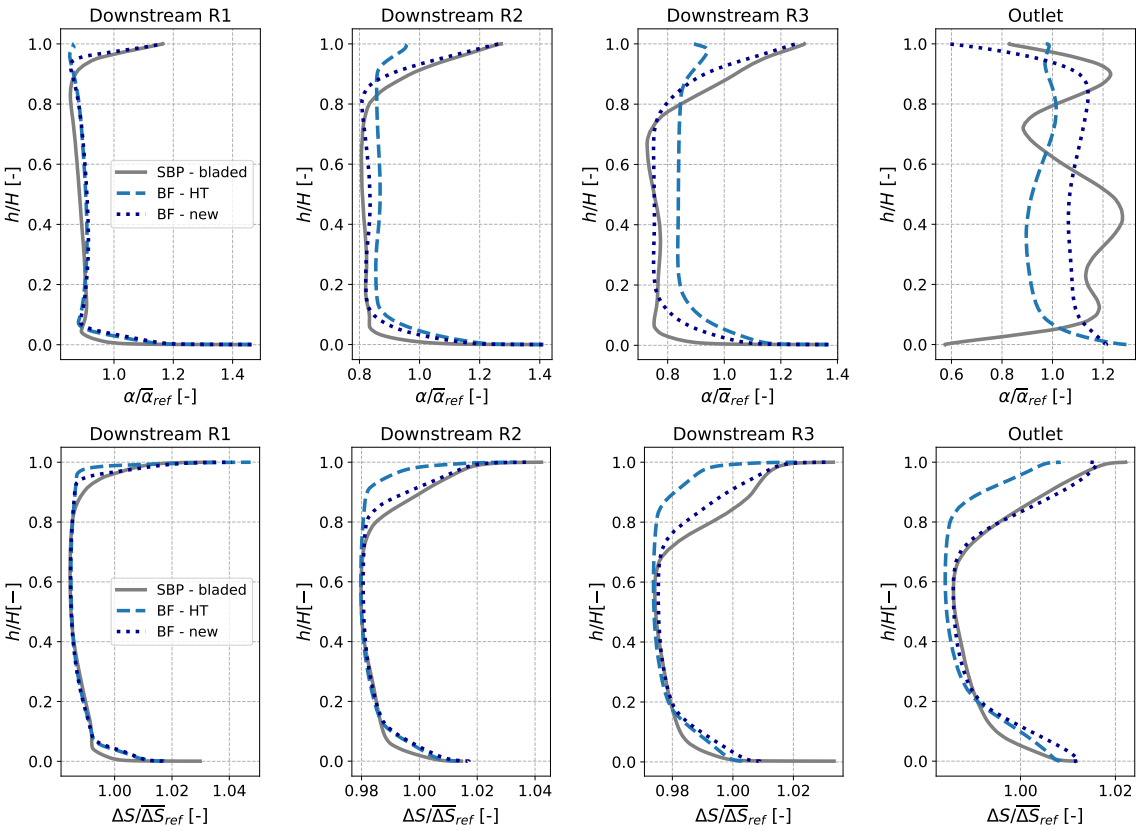

Figure 5.5: Spanwise profiles of absolute flow angle (top row) and entropy rise (bottom row) at stations downstream of each rotor and at the compressor outlet for the CREATE compressor at peak efficiency.

compared to the original model, as was showed in Figure 5.5, and show great agreement with respect to the reference data.

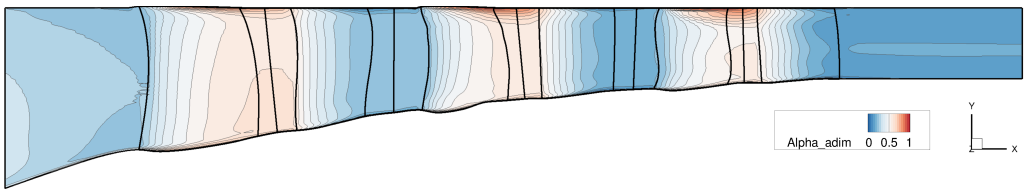

(a) Blade-resolved calculation.

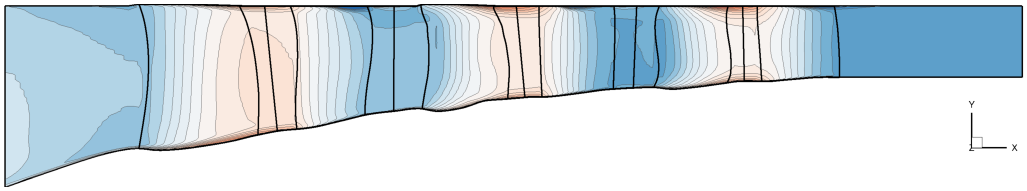

(b) Body-Force calculation.

Figure 5.6: Meridional views of absolute flow angle at the peak efficiency point for CREATE.

The meridional distributions of total pressure and total temperature are shown in Fig-

ures 5.7 and 5.8, respectively. As anticipated from the radial profiles, the Body-Force model reproduces the reference results well, particularly at mid-span. Minor deviations occur near the endwalls: sligthly lower total pressure at both the hub and shroud of the annulus; and a high-temperature region at the tip of the third rotor, linked to an intense tip-leakage vortex caused by the relatively large tip-gap height, is slightly underpredicted. This difference arises because the model does not explicitly account for tip-leakage losses in the CREATE compressor, although the clipping correction partially mitigates this effect. Overall, the meridional fields show very good agreement with the reference, confirming the modified model's capability to capture the key aerodynamic features of the flow.

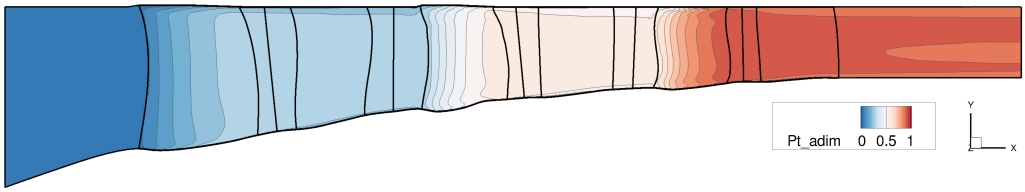

(a) Blade-resolved calculation.

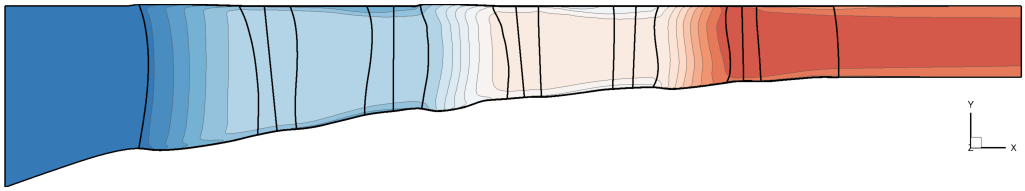

(b) Body-Force calculation.

Figure 5.7: Meridional views of total pressure at the peak efficiency point for CREATE.

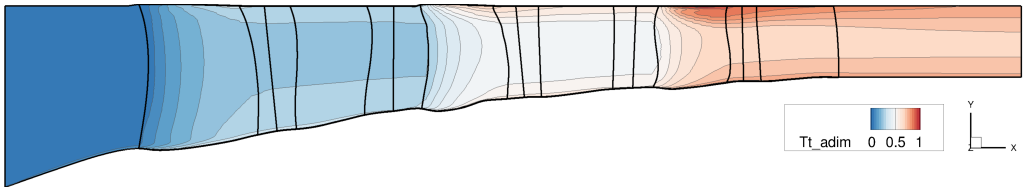

(a) Blade-resolved calculation.

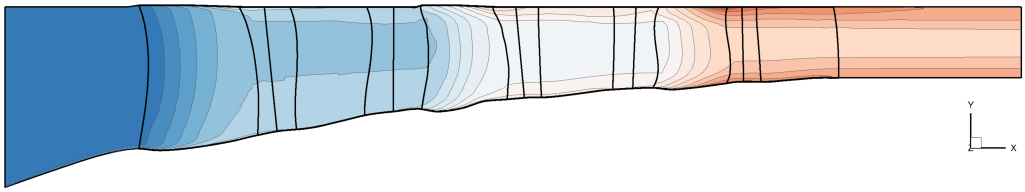

(b) Body-Force calculation.

Figure 5.8: Meridional views of total temperature at the peak efficiency point for CREATE.

This detailed flow-field analysis further reinforces confidence in the global performance results previously presented. Key quantities such as pressure rise, temperature increase, flow turning, and losses across the bladed rows are accurately captured both in an integral sense and locally. Regions of differing aerodynamic loading are clearly identifiable, and the overall magnitudes of these variations across the compressor are well reproduced, demonstrating the

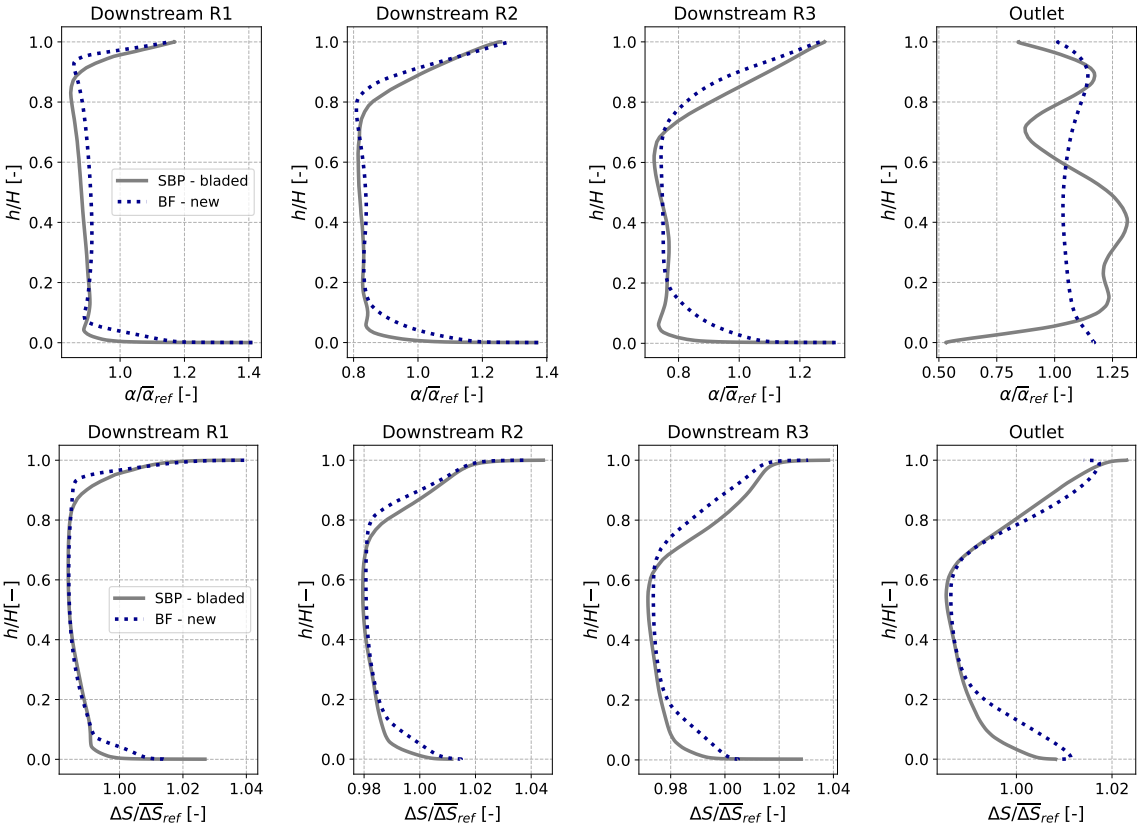

Figure 5.9: Radial profiles of total pressure and total temperature for the CREATE compressor at NS.

model's ability to represent the main flow features and performance trends.

Near-Stall Operating Point At the near-stall operating point, which corresponds to a stable condition close to the surge point at low mass flow rates, comparisons are made only between the blade-resolved reference data and the modified Body-Force model, since the unmodified model did not converge.

Figure 5.9 shows spanwise profiles of absolute flow angle and entropy rise at multiple axial stations within the compressor, including downstream of each rotor row and at the outlet. The results demonstrate that the modified Body-Force model accurately captures both midspan and near-wall flow characteristics, closely matching the blade-resolved reference data and correctly predicting the associated work and loss distributions. Minor discrepancies appear near the hub region, where the model underestimates the flow turning under elevated adverse pressure gradients. This limitation results in less accurate prediction of the aerodynamic work input near the hub, highlighting the challenges faced by the Body-Force model in capturing complex near-wall flow phenomena under demanding off-design conditions.

In summary, the comprehensive validation of the enhanced Body-Force model demonstrates its robustness and reliability in predicting both global performance metrics and detailed local flow characteristics across the multi-stage compressor. The sequential calibration approach, combined with near-wall corrections, enables accurate reproduction of integral quantities such as pressure and temperature ratios, as well as isentropic efficiency. Moreover, local flow field assessments, spanning spanwise profiles and meridional views of flow angle,

total pressure, total temperature, and entropy rise, confirm that the model closely matches blade-resolved reference data throughout the compressor, particularly at mid-span and near the shroud. While some discrepancies persist near the hub region under challenging off-design conditions, the overall fidelity of the model is very high and provides a solid foundation for extending its application to more complex flow scenarios, such as inlet distortion analyses. Importantly, this approach is particularly attractive for distortion studies, where the compressors baseline operation is already characterised and reference data are available. In this context, the Body-Force model can then be applied to a wide range of distortion scenarios, effectively replacing computationally expensive full-annulus URANS simulations.

5.2 Impact of Radial Distortion on the CREATE Compressor

The CREATE compressor is first investigated under conditions of radial inlet distortion. As discussed in Chapter 2, this compressor was not tested under different inflow conditions during the experimental campaign. Therefore, the distortion cases developed in this and the following sections are academic in nature and are designed to approximate realistic operational scenarios.

Section 3.1.1.2 introduced a radial distortion profile, depicted in Figure 3.3, intended to replicate the spanwise total pressure distribution downstream of an industrial S-duct, which is the focus of investigation in this section. The imposed distortion is particularly severe near the walls, with a 4% pressure deficit at the shroud relative to the mean total pressure of the clean inflow case, and a 2% deficit at the hub. Additionally, a maximum increase of approximately 3% in total pressure is observed at 40% of the blade span. The configurations considered in this investigation consist of the $2\pi/16$ periodic sector for the blade-resolved unsteady simulations and the 2° sector for the Body-Force simulations, at the peak efficiency operating point.

It is important to note that the clean inflow case already exhibits spanwise variations in total pressure and total enthalpy. While the radial-distorted case introduces a different radial variation, the underlying nature of the distortion remains similar. Therefore, a detailed flow-field analysis is not conducted here. This study primarily serves as a preliminary assessment of the Body-Force model's performance under inflow conditions that differ from those used during its calibration. Specifically, this analysis aims to investigate two key aspects: first, whether the Body-Force model accurately predicts flow behaviour under inflow conditions different from those in which it has been validated; and second, whether it provides reliable predictions when compared to unsteady simulations, which inherently account for rotor-stator interactions, an effect not explicitly represented in the model.

5.2.1 Impact on the Flow Field

To answer the first question, the effects of the imposed radial distortion at the compressor's peak-efficiency operating point are illustrated in Figure 5.10, which shows the spanwise variation of flow quantities between the clean and radial-distorted cases, in terms of total pressure and total temperature spanwise profiles. In particular, the variation of a quantity X is defined as $1 - X_{DIST}/X_{CLN}$ [%]. The profiles are shown at different axial stations: downstream of each rotor and at the outlet, to highlight the distortion evolution across the compressor.

It can be observed that the initially prescribed spanwise total pressure variation, characterised by two negative peaks near the walls, maintains a coherent trend as the flow passes

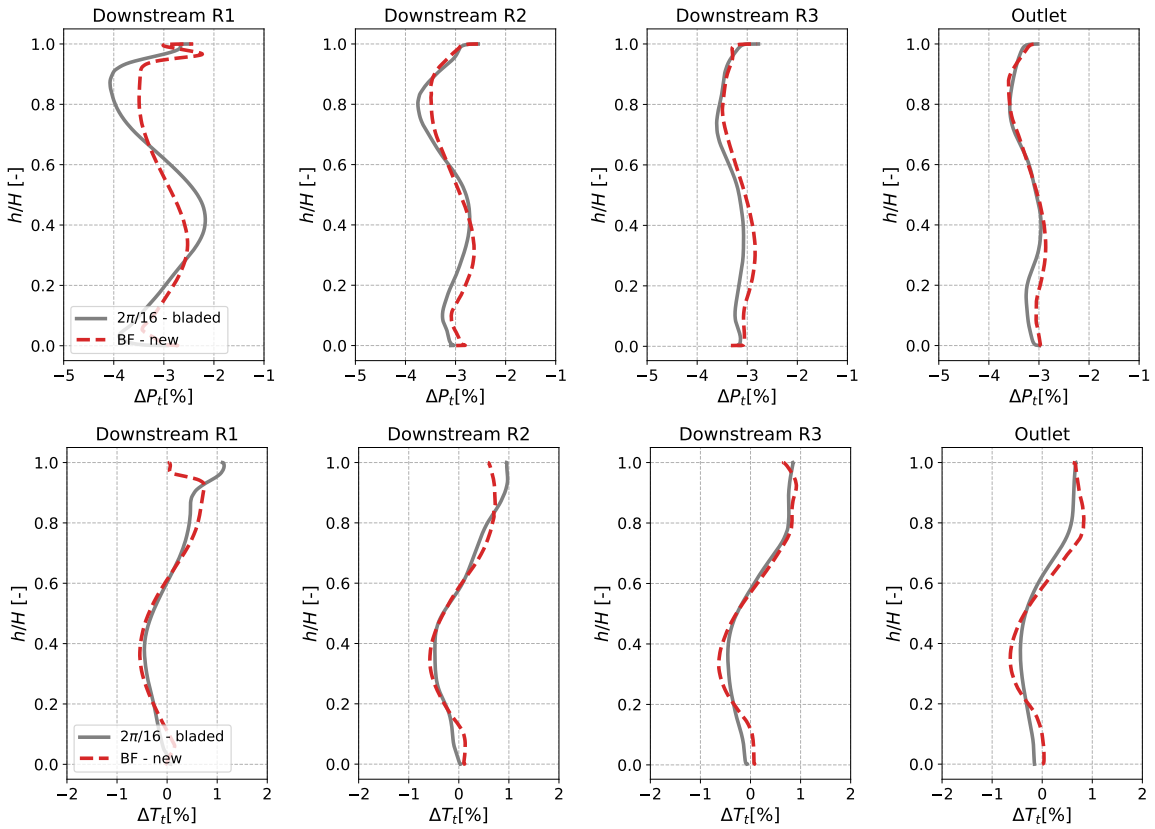

Figure 5.10: Radial profiles of total pressure and total temperature for the CREATE compressor under radial distortion. Relative variations with respect to the clean inflow case.

through successive blade rows but is progressively attenuated. Both the blade-resolved and Body-Force simulations show a reduction of the total pressure deficit of approximately 2% peak-to-peak immediately downstream of the first rotor. By the compressor outlet, the spanwise variation has decreased further, with the difference between the minimum and maximum deficit values reducing to within 1%, around an average total pressure deficit of approximately 3%. Both approaches consistently predict this attenuation of total pressure deficit.

In contrast, the total temperature distortion remains relatively constant throughout the compressor, with deviations confined to a narrow range of about -1% to $+1\%$ relative to the clean inflow case. These temperature variations directly reflect the radial distribution of total pressure. Regions of pressure deficit correspond to locally reduced flow coefficients and higher incidence angles, which increase aerodynamic loading and the associated work input, resulting in local temperature rises. This effect is strongest near the shroud, where radial flow migration amplifies the local energy exchange. Conversely, areas with a pressure surplus, such as near mid-span, exhibit lower total temperatures. The Body-Force method reproduces these trends well, although it slightly underpredicts the temperature rise near the tip of the first rotor row by about one percentage point.

The trends observed in the total temperature profiles can be further supported by analysis of the meridional flow field. Figure 5.11 shows the meridional distribution of mass-pondered azimuthal average of total temperature under radial distortion, as predicted by the blade-resolved (Figure 5.11a) and Body-Force (Figure 5.11b) approaches. The two flow fields are in

close agreement, consistent with observations from the clean inflow case. A difference in the intensity of the total temperature rise is observed near the tip region of the third rotor. This discrepancy is consistent with the differences already identified under clean inflow conditions, as showed in Figure 5.8, and does not indicate an error in predicting the effect of the inlet distortion. This is confirmed by the radial profiles downstream of this row in Figure 5.10, which show that the differences are in fact minimal and there is a very good agreement between the blade-resolved and Body-Force approaches.

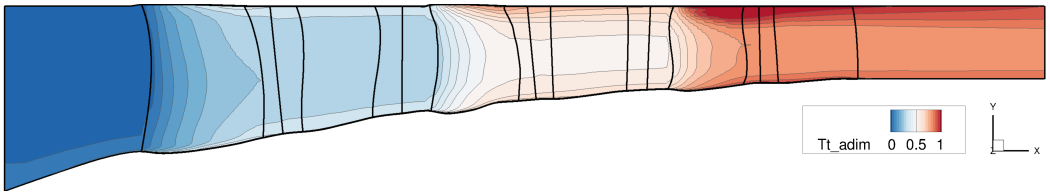

(a) Blade-resolved calculation.

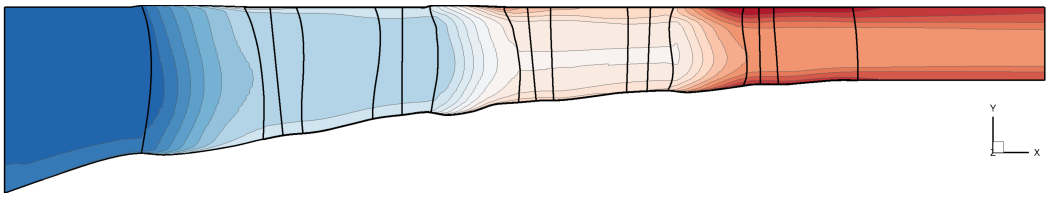

(b) Body-Force calculation.

Figure 5.11: Meridional views of total temperature at the peak efficiency operating point for the CREATE compressor in presence of radial distortion.

To address the second point of investigation, whether the Body-Force model's predictions remain reliable when compared to unsteady simulations, Figure 5.12 is presented. The figure shows the relative error in total temperature between the blade-resolved and Body-Force approaches for both the clean and distorted inflow cases. In the clean inflow case, the blade-resolved simulations employ a mixing-plane condition, while in the distorted inflow case, an unsteady-interface condition is used for the blade-resolved simulations. The error is expressed as: $1 - X_{BF}/X_{BR}$ [%]. The figure illustrates that, when transitioning to a more detailed unsteady representation, the errors introduced by the Body-Force model remain not only small but also consistent with those observed in the steady-state simulations, displaying similar patterns in the same regions for both inflow cases. In particular, larger errors, around 2%, are observed near the endwalls, while the error at mid-span remains close to zero.

Overall, the results presented in this section confirm that the modified Body-Force approach remains valid under varying inlet conditions, particularly in the presence of radial distortion, and when compared to an unsteady blade-resolved approach, without requiring any further model modification. The method accurately captures local flow variations, reproducing both the qualitative trends and the quantitative behaviour of key flow quantities such as total pressure and total temperature. Importantly, the model retains a high level of accuracy even in critical regions near the endwalls, where radial gradients and secondary flows are strongest. These findings demonstrate the robustness of the modified Body-Force method in predicting the effects of radial inlet distortion in multi-stage axial compressors.

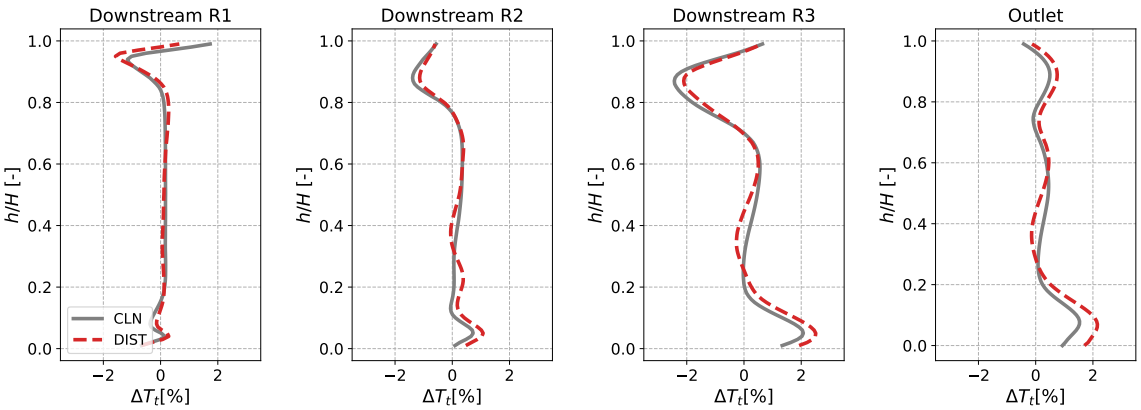

Figure 5.12: Radial profiles of total temperature for the CREATE compressor under clean and distorted inflow. Relative variations with respect to the blade-resolved approach.

5.3 Impact of Circumferential Distortion on the CREATE Compressor

The second part of the investigation of the CREATE compressor under inlet distortion focuses on circumferential distortion, aiming to assess whether the model continues to perform correctly under an inflow condition that differs significantly from the clean and radial distortion case, which shared similarities in nature, and to address a distortion pattern of particular interest due to its strong impact on compressor stability.

The circumferential distortion case has been introduced in Section 3.1.1.3, and is, as explained, academic in nature due to the lack of experimental data under distorted inflow conditions. The inlet distortion map, shown in Figure 3.6, consists of a purely circumferential pressure deficit spanning 120° in the azimuthal direction. Two levels of distortion intensity are considered, corresponding to pressure deficits of 4% and 10%.

The analysis is conducted on the 360° P2D configuration using both blade-resolved and Body-Force simulations. Due to the nature of this configuration, results are reported at mid-span (50% h/H), where radial variations are assumed negligible. The reduced computational cost of the P2D setup allows systematic support from blade-resolved reference simulations, including validation of the Body-Force model under distortion, evaluation of distortion effects on the flow field, and assessment of aerodynamic stability.

5.3.1 Impact on the Flow Field

An initial assessment of the impact of circumferential distortion on the flow field is conducted by analysing the azimuthal variation of several flow quantities at the compressor outlet, at mid-span (50% h/H), for three inflow conditions: clean (CLN), 4% total pressure deficit, and 10% total pressure deficit. All flow quantities are normalised by their corresponding values in the clean inflow case.

Figure 5.13 presents the azimuthal profiles of total pressure, total temperature, and entropy rise. The blade-resolved URANS simulation results are shown in grey, their low-pass filtered representation in black, and the Body-Force model results in red. This visualisation allows simultaneous evaluation of the Body-Force model's accuracy against the blade-resolved

reference data, as well as the effects of circumferential distortion on the flow field at the compressor outlet.

Regarding the total pressure profiles in Figure 5.13a, a close agreement is observed between the two simulation approaches. The 4% total pressure deficit results in a mean total pressure distortion of less than 2% at the outlet, while the 10% deficit leads to a distortion of less than 6%, indicating a clear attenuation of the inlet distortion through the compressor. The total temperature profiles in Figure 5.13b reveal a distinct temperature surplus within the distorted region. Since no total temperature variation was imposed at the inlet, the observed distortion develops downstream as a consequence of the inlet pressure deficit. Outside the distorted region, a total temperature deficit occurs, yielding an overall peak-to-peak variation of slightly less than 2% for the 4% distortion case and approximately 3-4% for the 10% case. A similar trend is observed in the entropy rise profile in Figure 5.13c, where elevated entropy generation corresponds to the distorted region, indicating increased aerodynamic losses associated with the distortion. No additional losses occur outside this region.

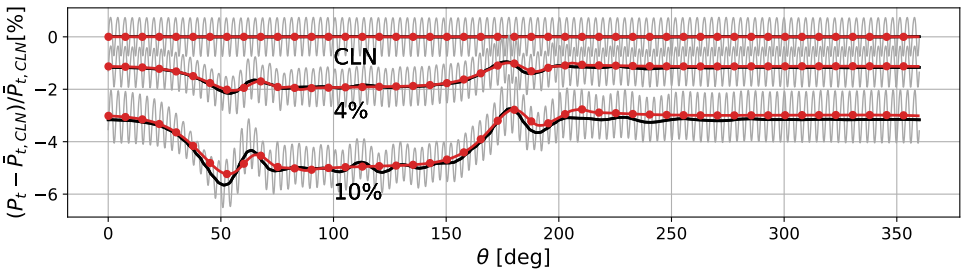

(a) Azimuthal distribution of stagnation pressure.

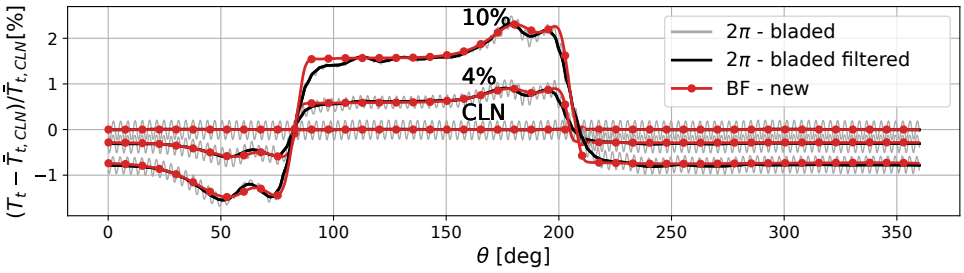

(b) Azimuthal distribution of stagnation temperature.

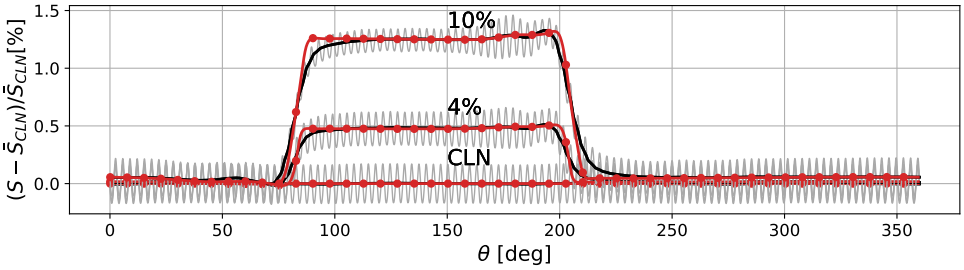

(c) Azimuthal distribution of entropy.

Figure 5.13: Azimuthal profiles of stagnation pressure, stagnation temperature, and entropy at the compressor outlet, at 50% h/H, for clean inflow, 4% and 10% total pressure deficit. Results from blade-resolved simulations (grey), filtered data (black), and Body-Force model (red) are compared.

The maximum relative errors of these quantities between the Body-Force and blade-resolved simulations, directly issued from the normalised azimuthal profiles in Figure 5.13, are summarised in Table 5.4. Even under the more severe 10% inlet distortion, the maximum absolute relative errors remain below 0.5% for stagnation pressure and temperature, and below 0.2% for entropy. These low error margins demonstrate that the Body-Force model effectively reproduces both aerodynamic and thermodynamic effects of inlet distortion, with slight increases at higher distortion levels consistent with the expected rise in nonlinear flow phenomena. The errors remain well within acceptable limits for engineering applications. Importantly, these results confirm the versatility of the modified Body-Force model, applicable to both radial and azimuthal variations in inflow conditions.

Table 5.4: Maximum absolute relative errors of the Body-Force model with respect to blade-resolved URANS simulations for stagnation pressure, stagnation temperature, and entropy at the compressor outlet, for varying inlet distortion intensities.

Total pressure deficit	$\mathbf{P_{t,err}}$	$\mathbf{T_{t,err}}$	$\mathbf{\Delta S_{err}}$
4%	0.31%	0.29%	0.12%
10%	0.47%	0.50%	0.20%

Figure 5.14 expands on the previous analysis, illustrating the evolution of P_t and T_t azimuthal profiles across the compressor, from the inlet to downstream of each stator Sn. Results from both the Body-Force model and the blade-resolved filtered case are shown for the 10% distortion scenario, where the features are most pronounced.

As anticipated, the stagnation pressure deficit attenuates as the flow progresses through the compressor, and the boundaries of the distorted sector become progressively less defined downstream, as shown in Figure 5.14a. The stagnation temperature profiles in Figure 5.14b confirm that no temperature distortion is present at the inlet, while a clear distortion develops downstream as a result of the imposed pressure deficit. This behaviour mirrors the radial distortion case and is linked to the redistribution of the flow within the distorted sector. Additionally, the distorted region shifts along the rotation direction of the compressor blades, as visible in the total temperature plot.

Figure 5.15 illustrates the redistribution mechanism. In regions of reduced inlet pressure, the local flow coefficient decreases, as shown in Figure 5.15b, leading to higher incidence angles on the blades, visible in Figure 5.15c. These altered inlet conditions drive circumferential migration of the flow toward the low-pressure region, producing non-uniform inlet angles and swirl that manifest downstream as elevated total temperatures within the distorted sector, as seen in Figure 5.14b. The mechanism described is well established in the literature, as discussed in Chapter 1 and in previous studies [63, 64].

A slight discrepancy in the prediction of the relative flow angle appears downstream of the third stator (Figure 5.15c) due to limitations in the calibration of the Body-Force model at each blade row. This leads to a modest increase in error further downstream. Nevertheless, the relative flow angle error at the downstream station of the last stator remains below 1.5% compared to the URANS reference. Among the flow quantities presented, the relative flow angle is the most sensitive, while other quantities maintain very close agreement with the reference data, even at the compressor outlet.

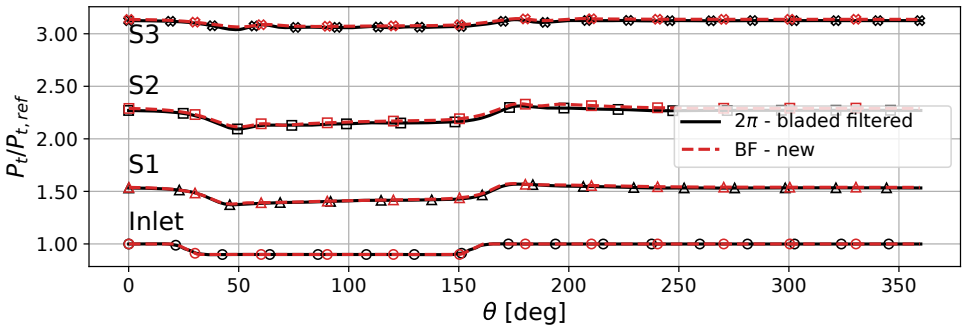

(a) Azimuthal distribution of stagnation pressure.

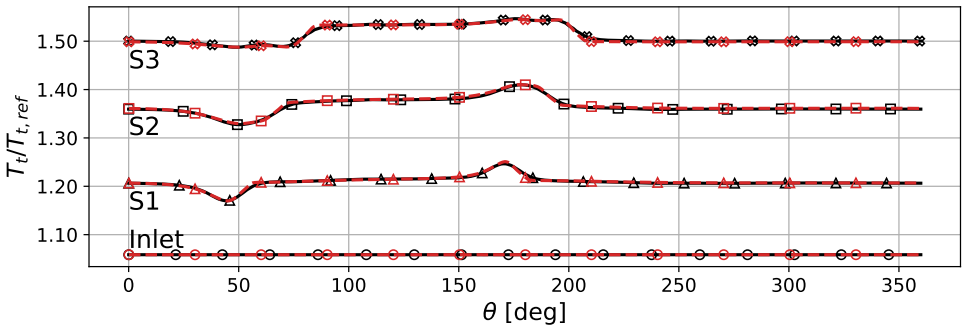

(b) Azimuthal distribution of stagnation temperature.

Figure 5.14: Evolution of stagnation pressure and temperature across the axial stations of the compressor under 10% circumferential distortion.

Figure 5.16 provides further visualisation of the circumferential shift of the distorted region along the rotation direction. It shows the distribution of the entropy field on the iso-50% h/H cut of the flow field and illustrates how the distortion window moves through the compressor. The figure also highlights the comparable order of magnitude of entropy levels predicted by both the blade-resolved and the Body-Force approaches inside and outside the distorted region.

The results confirm the reliability of the modified Body-Force approach in predicting the aerodynamic response of the CREATE compressor under circumferential inlet distortion. Despite the complexity introduced by azimuthal non-uniformities, the model consistently captures the main flow features, including distortion attenuation, flow redistribution, and the development of secondary thermodynamic effects. Key local quantities, such as stagnation pressure, stagnation temperature, and entropy, are accurately reproduced, with relative errors remaining below 0.5% even at higher distortion levels. These findings demonstrate the model's capability to resolve flow non-uniformities not only in the radial direction but also across the azimuth.

5.3.2 Impact on Stability Parameters

It is of particular interest to assess the impact of circumferential distortion on the aerodynamic stability of the compressor. To this end, two stability parameters introduced in Section 1.1.3.1 are employed: the De Haller number, $DH = W_2/W_1$, traditionally used to indicate the risk

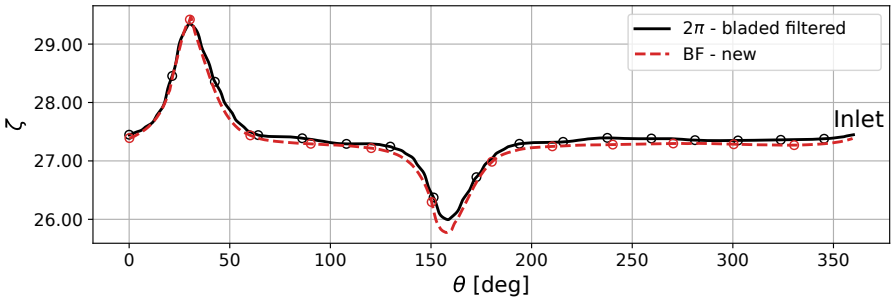

(a) Azimuthal distribution of swirl angle $\zeta = \tan^{-1}(V_\theta / V_x)$ at the compressor inlet.

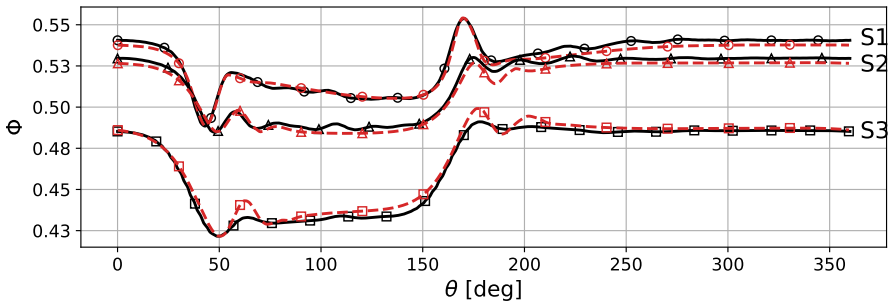

(b) Azimuthal distribution of the flow coefficient $\Phi = V_x/(\omega r)$, at each stator outlet.

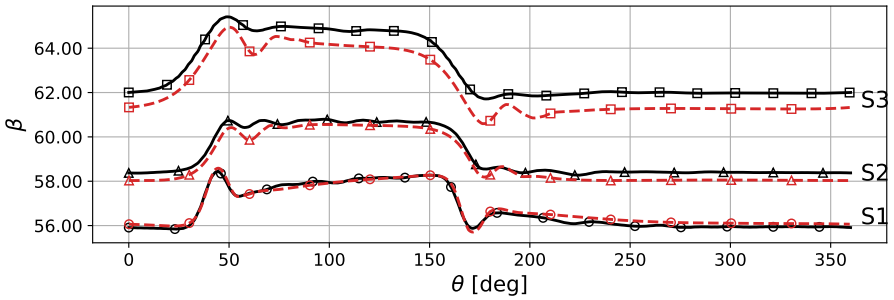

(c) Azimuthal distribution of the relative flow angle β, at each stator outlet.

Figure 5.15: Azimuthal profiles of swirl angle, flow coefficient and relative flow angle across different axial stations, for the 10% distortion case.

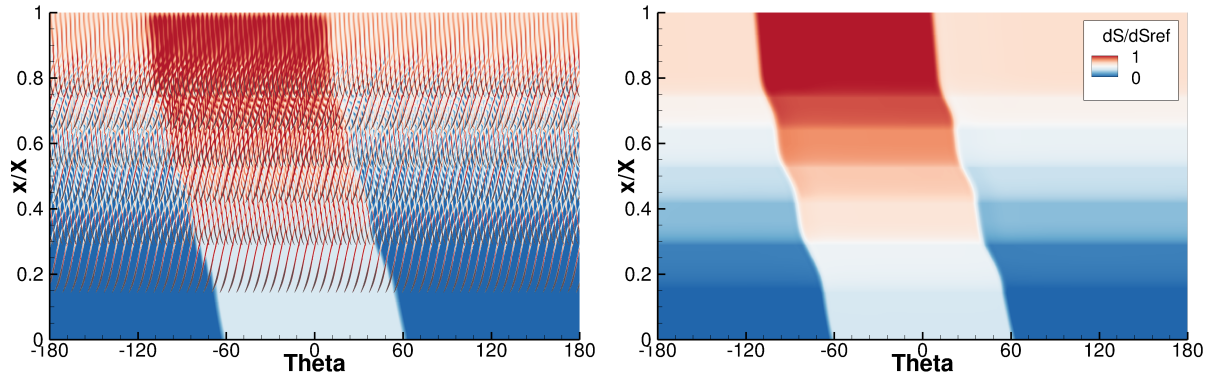

Figure 5.16: Entropy field of the blade-resolved (left) and Body-Force (right) P2D cases at 4% distortion.

of flow separation within a blade row; and the Lieblein diffusion factor, $DLI = 1 - W_2/W_1 + \Delta W_\theta/(2\sigma W_1)$, which provides a measure of aerodynamic loading.

Since the configuration under investigation is a P2D domain without near-wall effects, and given that the acceptable thresholds for DH and DLI can be case-dependent [94], suitable reference limits are derived from the full-span single-blade passage (SBP) simulation at the near-stall operating point with clean inflow. This approach ensures that, when the P2D results exceed these thresholds, analogous full 3D configurations would likely encounter stability issues.

The threshold values are extracted from the most critical row, which was found to be stator S3, considering the mid-span region in order to exclude boundary-layer effects. The resulting limits are $DH_{lim} = 0.52$ and $DLI_{lim} = 0.64$. For the present P2D study, local values falling below DH_{lim} or exceeding DLI_{lim} are therefore interpreted as indicators of potential stability degradation.

The identification of stator S3 as the most critical row from a stability perspective is supported by the data presented in Figure 5.17. This figure displays the De Haller number (DH) and the Lieblein diffusion factor (DLI) for each blade row under the 10% distortion at the near stall operating point, with rotors shown in the left column and stators in the right. The results are drawn exclusively from the Body-Force simulations, as the model has demonstrated a high level of reliability in all previous analyses. Additionally, omitting the blade-resolved data ensures improved readability of the figure without compromising the validity of the discussion. For reference, the critical thresholds derived from the SBP near-stall configuration are shown as horizontal green lines.

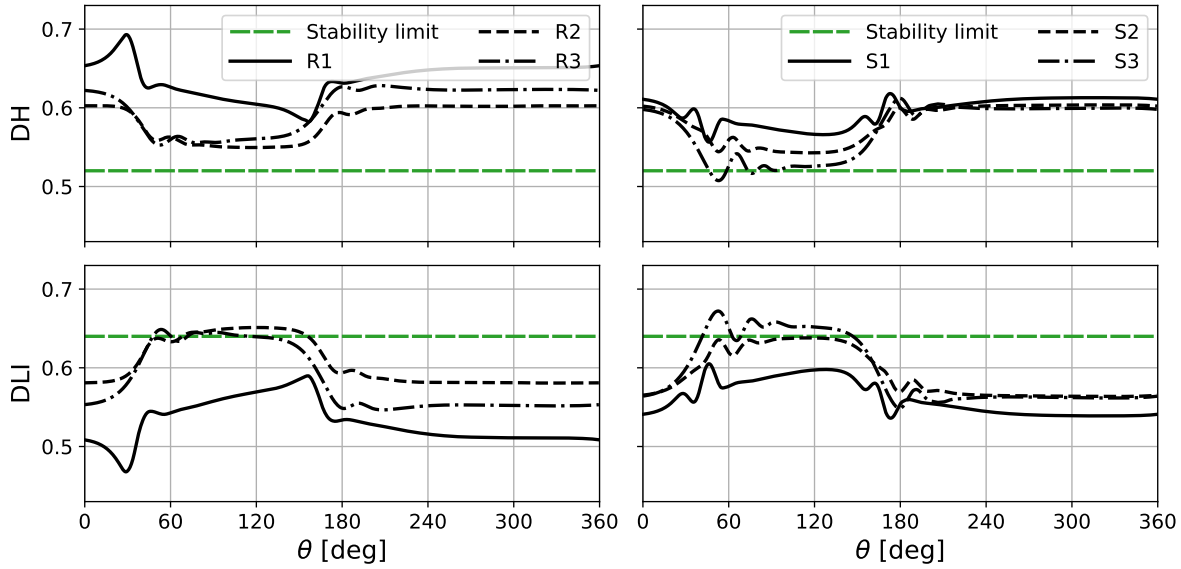

Figure 5.17: Azimuthal profiles of stability parameters DH and DLI for all blade rows under 10% inlet total pressure distortion, predicted by the Body-Force model.

It is evident from the figure that stator S3 exhibits both the lowest DH and the highest DLI across all rows, clearly identifying it as the most critically loaded section of the compressor. This indicates that in S3, the combined effect of pronounced flow deceleration and strong tangential deflection reaches a maximum, resulting in the highest aerodynamic diffusion. As

such, this row is the most susceptible to local instability phenomena, including separations and stall onset.

The figure further reveals that rotor R2 is the most loaded among the rotors, whereas the stators display a progressively increasing level of aerodynamic loading from stator S1 to stator S3. Both the first rotor and stator rows remain well within the stability margins, suggesting that the first stage operates under relatively safe conditions. This also implies potential design flexibility in this stage, which could be exploited to mitigate the impact of inlet distortion through targeted modifications.

Once the most critical row has been identified, a more detailed analysis is carried out for stator S3. Figure 5.18 presents the values of DH and DLI predicted by both the blade-resolved (BR) and Body-Force (BF) approaches for this row, under inlet total pressure distortions of 4% and 10%. The established stability thresholds are again indicated by horizontal green lines for reference. Results are shown for the peak efficiency operating point in the left column, and for the near-stall condition in the right column. These two operating points are defined by using the same reference pivot pressure for the valve law as in the peak-efficiency and near-stall operating points of the single-blade-passage case, which were themselves established through comparison with experimental data.

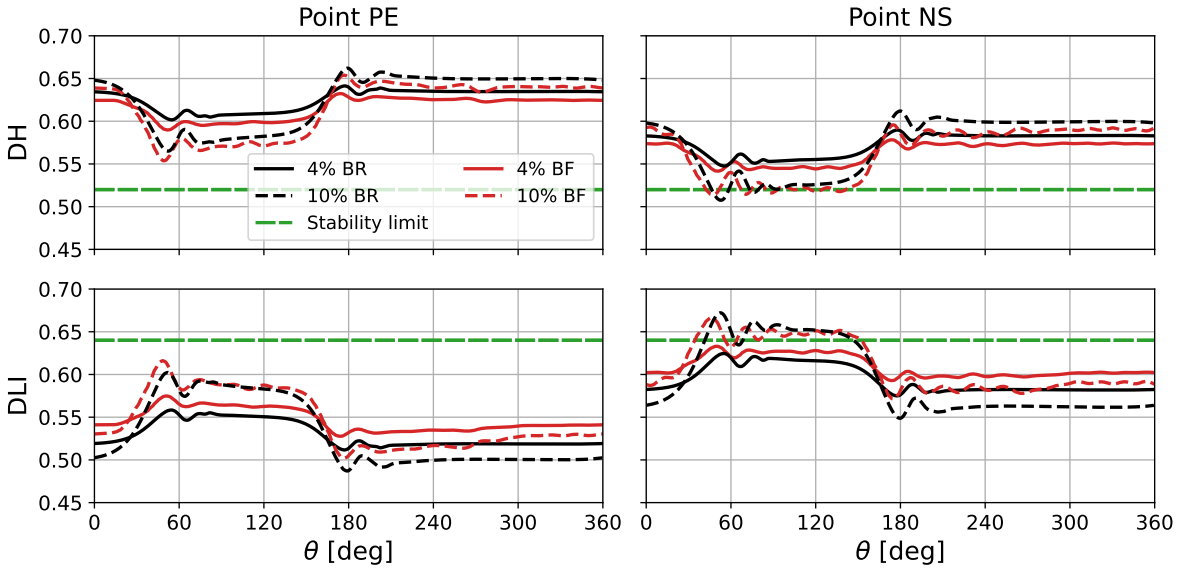

Figure 5.18: Azimuthal profiles of stability parameters DH and DLI for stator S3 under 4% and 10% total pressure distortions, at peak efficiency (PE) and near-stall (NS) operating points, with the blade-resolved (BR) and Body-Force (BF) approaches.

At the peak efficiency point, the azimuthal profiles of the stability parameters remain safely within the admissible range, with DH values above and DLI values below their respective limits. This confirms a stable operating condition for both the P2D configuration and its potential three-dimensional counterpart.

Conversely, near the stall condition, both distortion cases approach or exceed the stability thresholds. In particular, the 10% distortion case, as predicted by both blade-resolved and Body-Force simulations, violates the critical limits for both DH and DLI, indicating that this operating condition is more prone to instability than the near-stall SBP reference case. If extrapolated to a full 3D configuration, this could imply that near-wall phenomena, absent in

the P2D model, may further compromise stability and potentially trigger flow separation or stall. However, given the two-dimensional nature of the present configuration, such effects cannot be captured directly. A more comprehensive assessment of near-wall phenomena and their impact on compressor stability is provided in Chapter 6, where the industrial compressor with inflow distortion is analysed in its full three-dimensional geometry.

In both distortion cases, and for both operating conditions, a good agreement is observed between the blade-resolved and Body-Force approaches. As anticipated, since stator S3 is the final row in the compressor, cumulative modelling discrepancies across upstream rows result in a small deviation in the predicted values. Nonetheless, the local differences remain within 2% at all azimuthal locations. More importantly, the impact on stability is accurately reproduced, and both methods lead to consistent conclusions regarding the row's susceptibility to critical behaviour.

5.4 Considerations on CPU Time Gain

For each configuration considered, the computational time required to reach convergence at the peak-efficiency operating point is summarised in Table 5.5.

The first four columns of Table 5.5 identify each configuration in terms of the modelling method employed, either blade-resolved or Body-Force, the temporal approach, steady or unsteady, as well as the corresponding geometric setup in terms of azimuthal sector and 3D or P2D domain.

The fifth column of Table 5.5 presents the CPU time per core per job, given by the relation $T_{\mathrm{CPU}}/(N_{\mathrm{cores}}N_{\mathrm{jobs}})$, normalised by the value obtained for the single-blade-passage blade-resolved case. This metric reflects the elapsed wall-clock time from the start of the simulation to the output of the final solution, and is primarily governed by the number of cells allocated per core and the efficiency of the load balancing, which in turn depends on the mesh block structure. As all cases were executed with a comparable computational load of approximately 200 000 cells per core, this value remains relatively consistent across configurations. However, some variation persists, largely due to differences in numerical setup, most notably between steady and unsteady calculations. For instance, the unsteady URANS simulations used in the distortion studies require second-order temporal integration and impose unsteady inter-row boundary conditions, both of which significantly increase computational cost even when the core load remains equivalent.

The subsequent columns provide the number of cores used, which is based on the mesh size, the number of jobs required to achieve convergence, stricly linked to the number of iterations or time steps, and finally the total CPU time obtained as the product of these three quantities.

The table highlights two key advantages of the Body-Force modelling approach. First, the number of cores needed is significantly lower compared to blade-resolved simulations, as the mesh size is drastically reduced when individual blades are not explicitly meshed. While this reduction contributes to a lower overall CPU time, its impact on elapsed time is less pronounced due to the benefits of parallel computing. Second, and more importantly, the number of jobs required for convergence is substantially reduced in Body-Force simulations. This is particularly evident when comparing steady Body-Force simulations with unsteady blade-resolved URANS calculations used for inlet distortion analyses. For instance, in both radial and circumferential distortion studies, the number of jobs, and consequently the computa-

tional time, required by the Body-Force model is one tenth of that needed by the corresponding URANS simulations.

In terms of total CPU time, the Body-Force model exhibits significant computational efficiency while maintaining a high degree of accuracy. For the calibration and validation case, the Body-Force approach requires approximately 65 times less CPU time than the blade-resolved single-blade-passage simulation. In the more complex and unsteady circumferential and radial distortion cases, the reduction in computational cost reaches factors of approximately 235 and 3300, respectively. These results underscore the substantial efficiency gains made possible through the use of reduced-order modelling in complex compressor simulations.

An influential factor not explicitly accounted for in the present comparison, for the sake of simplicity, is the initialisation strategy employed for the blade-resolved simulations. All such cases, at increasing levels of geometric complexity, were initialised from pre-converged solutions. For example, the $2\pi/16$ unsteady computation was started from the corresponding steady simulation, which itself had been initialised via duplication of the converged single-blade-passage solution. Similarly, when throttling the operating point, each new calculation was initialised from a previously converged point at nearby conditions. While this staged initialisation procedure facilitates convergence, it introduces a non-negligible cumulative computational cost that is not reflected in the reported metrics. In contrast, all Body-Force simulations were initialised from a uniform flow field, without any preparatory calculations. Accounting for this distinction would further reinforce the computational advantages of the Body-Force approach, particularly for large-scale unsteady configurations.

Table 5.5: Computational cost at convergence for each case, normalised by SBP case.

Method	Approach	Sector	Domain	$\left.\frac{\mathbf{T_{CPU}}}{\mathbf{N_{cores}} \mathbf{N_{jobs}}}\right\|_{\text{norm}}$	$\mathbf{N_{cores}}$	$\mathbf{N_{jobs}}$	$\left.\mathbf{T_{CPU}}\right\|_{\text{norm}}$
Blade-resolved	Steady	SBP	3D	1.00	48	2	9.60×10^1
	Unsteady	$2\pi/16$	3D	1.73	288	10	4.98×10^3
	Unsteady	2π	P2D	1.17	240	10	2.81×10^3
Body-Force	Steady	2°	3D	0.75	2	1	1.50×10^0
	Steady	2π	P2D	1.19	10	1	1.19×10^1

Conclusion

This chapter presented a comprehensive assessment of the capabilities of the developed Body-Force model and of the behavior of the CREATE compressor under a range of inlet distortion conditions.

The first part focused on validation under clean inflow conditions, comparing the model against blade-resolved reference simulations. The predictions, both in terms of overall compressor performance and local flow field quantities, proved to be highly accurate. Across the entire compressor map, performance estimates remained within approximately 1% of the reference results. This agreement held not only at the system level, but also row-by-row, particularly where correction terms had been applied.

Further, at both peak efficiency and near-stall operating points, the model accurately reproduced spanwise and axial flow distributions. Only minor discrepancies were observed

near the endwalls, and these did not significantly affect the global analysis of the flow.

With confidence established under nominal undistorted conditions, the model was then applied to two distortion scenarios: a radial distortion and a circumferential distortion.

The radial distortion case served as an important test of the model's generalisability, showing that its predictive capability remains robust even under inlet conditions different from those used in its formulation. The results highlighted the near-wall regions as the most sensitive, offering physically consistent insights without requiring any model re-tuning.

The P2D case of circumferential distortion study further reinforced the model's reliability. Predictions of outlet quantities, such as total pressure, total temperature, and pressure rise, were within 1% of the blade-resolved reference values. Beyond accuracy, the analysis revealed how the model captures key physical mechanisms: total pressure distortion dissipation, swirl-induced flow redistribution, and variations in work input. Stability was also investigated, identifying the last stator as the most critical blade row, and highlighting the combinations of distortion and operating point most prone to instability. The Body-Force model's predictions were consistent with those of the blade-resolved simulations.

A particularly important outcome is that all of these results were obtained without modifying the calibrated coefficients or normal force clipping values. This robustness and validity across multiple operating and inlet conditions highlights the model's generalisability and practical applicability in predictive contexts.

The chapter concluded with an evaluation of computational performance. For instance, in the P2D circumferential distortion case, the Body-Force approach required up to two hundred times less CPU time than the equivalent blade-resolved simulation. Significant gains were observed across all cases, particularly in unsteady simulations, highlighting the substantial computational advantage of the reduced-order model.

It is thus evident that the Body-Force model offers a powerful, efficient, and reliable tool for predicting compressor flow behavior under complex and non-uniform inflow conditions.

In the following chapter, Chapter 6, a different, industrial, transonic compressor will be studied under both clean inflow and azimuthal distortion conditions. This investigation will further evaluate the model's robustness in the context of a more complex geometry and challenging flow regime, while analysing a realistic distorted inflow condition derived from experimental data, in contrast to the academic cases developed in the current chapter, across multiple operating points. Particular attention will be given to the mechanisms of distortion propagation and stability degradation within a fully three-dimensional framework.

CHAPTER 6

Investigation of Inlet Distortion Effects on Aerodynamics and Stability of the IHPC Compressor via Body Force Methodology

This chapter focuses on the analysis of a high-speed multistage compressor subjected to circumferential inlet distortion, with particular emphasis on the resulting three-dimensional flow effects and associated aerodynamic complexity. The investigation employs the developed Body-Force methodology, aiming to characterise the propagation of inlet distortions through the compressor and to understand their influence on local and global flow behaviour. A key objective is to evaluate the reliability of the Body-Force model in capturing essential flow features, distortion transmission, and mechanisms related to stability and stall inception under off-design and distorted inflow conditions. Furthermore, the chapter addresses the computational efficiency of the approach, demonstrating its suitability for full-annulus simulations and extensive parametric studies that would be otherwise impractical with high-fidelity methods.

Contents

6.1 Validation of the Modified Body Force Model on the IHPC Compressor . . . **142**
6.1.1 Global Performance Analysis . . . 142
6.1.2 Local Flow Analysis . . . 145
6.2 Impact of Circumferential Inlet Distortion on the IHPC Compressor . . . **151**
6.2.1 Impact on the Flow Field . . . 152
6.2.2 Impact on the Stability of the IHPC Compressor . . . 157
6.3 Considerations on CPU Time Gain . . . **165**
Conclusion . . . **167**

6.1 Validation of the Modified Body Force Model on the IHPC Compressor

This section investigates the industrial, transonic IHPC compressor described in Chapter 2, using the Body-Force methodology developed in Chapter 4. The application of the enhanced Body-Force model to the IHPC compressor incorporates all the features developed in Chapter 4, including the calibration strategy, the normal force clipping, and the integration of rotor tip gap losses.

Specifically, the normal force clipping is applied as per the methodology in Section 4.3.2, with clipping heights set to 2%, the boundary mayer thickness at the inlet, at both the hub and the shroud of the stators, and at the hub of the rotors. The clipping is deactivated at the rotor tip region, where secondary losses have been incorporated.

The calibration process followed the procedure outlined in Section 4.3.1, and the resulting calibrated coefficients for this compressor configuration are provided in Table 6.1.

Table 6.1: Calibration coefficients for each blade row of the IHPC compressor configuration.

	IGV	**R1**	**S1**	**R2**	**S2**	**R3**	**S3**	**R4**	**S4**
K_n	1.00	1.32	0.70	1.25	1.00	1.00	1.00	0.80	0.80
K_f	2.00	1.55	1.25	0.70	1.15	1.00	0.45	1.00	1.20
K_d	1.00	0.85	1.17	1.00	1.20	0.95	1.00	1.15	1.50

The remainder of this section is dedicated to validating the modified Body-Force model against reference blade-resolved data for the IHPC configuration. This validation is divided into two parts: the first assesses the integral performance of the compressor, while the second focuses on the local flow field analysis. For this comparison, the blade-resolved configuration is the $2\pi/4$ sector case, as detailed in Section 3.2.1.2, while the Body-Force configuration is a 2° sector, as described in Section 4.1.2.

6.1.1 Global Performance Analysis

The performance predictions of the different modelling approaches for the 4.5-stage IHPC compressor are examined in this section. Figure 6.1 presents the main performance parameters of the compressor: the total-to-total pressure ratio (Figure 6.1a), the total-to-static pressure ratio (Figure 6.1b), the total-to-total temperature ratio (Figure 6.1c), and the isentropic

efficiency (Figure 6.1d). The figure compares results from the reference blade-resolved simulation ($2\pi/4$ bladed case), the original Hall-Thollet Body-Force model (BF - HT), and the modified Body-Force model (BF - new). For the case with the original Hall-Thollet formulation, the off-design loss term was deactivated, as its inclusion prevented convergence for a significant number of operating points.

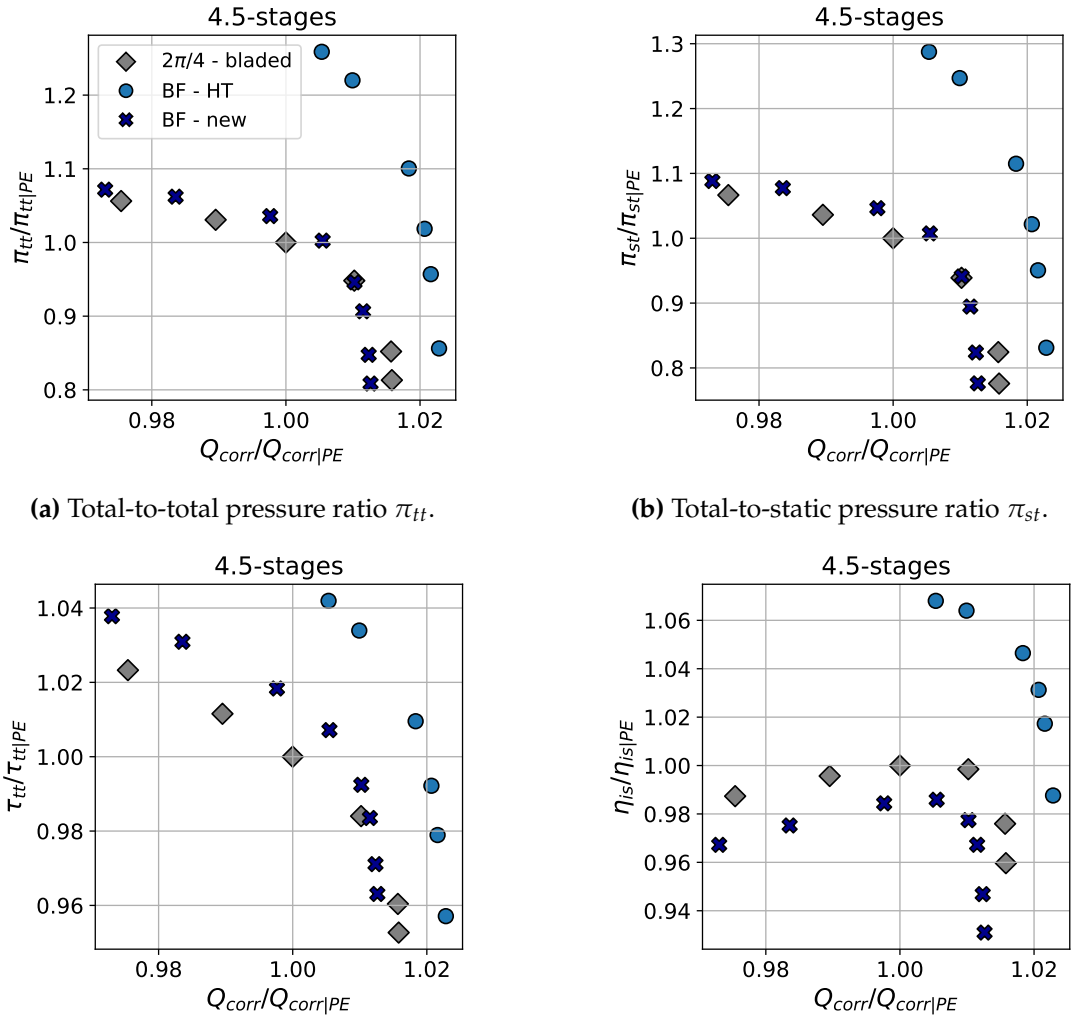

(a) Total-to-total pressure ratio π_{tt}.

(b) Total-to-static pressure ratio π_{st}.

(c) Total-to-total temperature ratio τ_{tt}.

(d) Isentropic efficiency η_{is}.

Figure 6.1: Comparison of global performance metrics for the 4.5-stage IHPC compressor: blade-resolved reference ($2\pi/4$ - bladed), Body-Force with original Hall-Thollet model (BF - HT), and Body-Force with the enhanced model (BF - new) at PE.

As demonstrated in Section 4.2, the unmodified Hall-Thollet model exhibited substantial discrepancies relative to the reference data. The proposed modifications markedly improve the agreement with the blade-resolved results across all performance parameters. Different improvements can be identified with the new Body-Force approach: the mass flow rate at choke is predicted with greater accuracy, the model allows for convergence towards lower mass flow rates, and the characteristics exhibit the correct shape, with the characteristic inflection occurring at the point of maximal efficiency.

A quantitative summary of the prediction errors for both Body-Force models, relative to the reference case, is reported in Table 6.2. The operating points selected for error evaluation correspond to the conditions closest to $Q_{corr}/Q_{corr|PE} = 1$ (peak-efficiency point) and $Q_{corr}/Q_{corr|PE} = 0.975$ (near-stall point). For the modified Body-Force model, since two operating points are close to the $Q_{corr}/Q_{corr|PE} = 1$ condition, the mean performance metrics at these two points is considered.

Table 6.2: Relative prediction errors of global performance metrics for the unmodified and modified Body-Force models compared to blade-resolved RANS simulations, at peak efficiency (PE) and near-stall (NS) operating points.

Operating Point	**Model**	π_{tt}	π_{st}	τ_{tt}	η_{is}
PE	BF - HT	25.85%	28.72%	4.19%	6.78%
	BF - new	1.83%	1.96%	1.28%	-1.51%
NS	BF - HT	–	–	–	–
	BF - new	1.47%	2.05%	1.45%	-2.06%

The results in Table 6.2 demonstrate that the original Hall-Thollet Body-Force model (BF - HT) exhibits substantial prediction errors at the peak-efficiency point, with deviations exceeding 25% for both total-to-total and total-to-static pressure ratios. These discrepancies highlight the model's limited capability to capture compressor performance accurately. In contrast, the modified Body-Force model (BF - new) markedly improves the predictions, reducing the errors to below 2% for all performance parameters at peak efficiency. At the near-stall operating point, results from the original model were not available due to convergence issues. Conversely, the modified model manages to converge and maintains a consistent level of accuracy, with relative errors below 2.1% across all quantities. The slightly negative values of isentropic efficiency error indicate a small overestimation of the losses compared with the reference data. It can be observed that the prediction errors of the unmodified model on the IHPC compressor are considerably larger than those obtained for the CREATE compressor, where deviations did not exceed approximately 10%. This difference highlights the greater aerodynamic complexity of the IHPC, which more strongly challenges the underlying assumptions of the original model.

As for the previous compressor configuration, a detailed analysis is provided for the row exhibiting the largest local prediction discrepancies, which is here the second rotor row, whose performance plots are shown in Figure 6.2. For this rotor, the pressure ratio and isentropic efficiency errors, originally around 5-6%, are reduced to below 1% following the model modifications, confirming the effectiveness of the proposed improvements at the row level. It is also worth noting that, as observed for the CREATE compressor, the global performance errors of the IHPC reflect the cumulative effect of discrepancies at individual rows. This underscores the effectiveness of the implemented modifications and the calibration procedure, which, although currently performed manually, requires only a few iterations to achieve accurate predictions across multiple subsequent rows.

Overall, these results demonstrate that the implemented modifications enable reliable and robust prediction of compressor performance across the operating range, from peak efficiency to near-stall conditions.

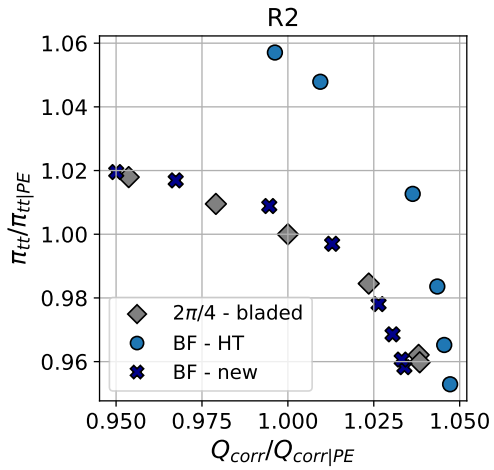

(a) Total-to-total pressure ratio π_{tt} of R2.

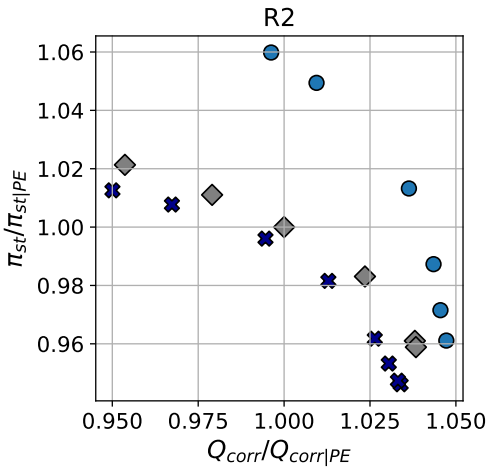

(b) Total-to-static pressure ratio π_{st} of R2.

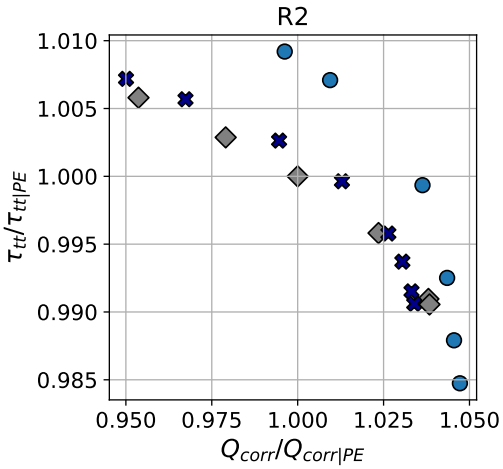

(c) Total-to-total temperature ratio τ_{tt} of R2.

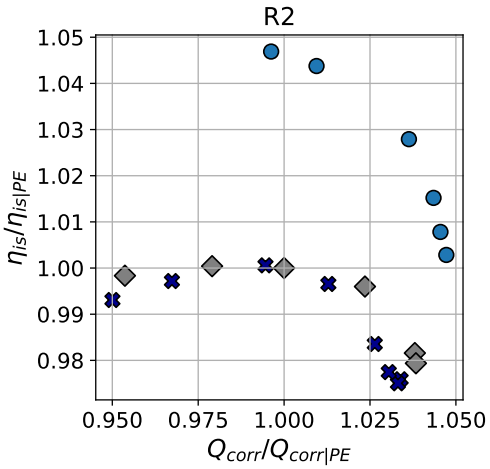

(d) Isentropic efficiency η_{is} of R2.

Figure 6.2: Comparison of global performance metrics for the second rotor of the IHPC compressor: blade-resolved reference ($2\pi/4$ - bladed), Body-Force with original Hall-Thollet model (BF - HT), and Body-Force with the enhanced model (BF - new) at PE.

6.1.2 Local Flow Analysis

A fundamental step in the validation of the modified model on the IHPC compressor is the local flow analysis, with particular focus on the effects of the secondary loss term added in the rotor tip region. To do so, similarly to the previous chapter, spanwise flow profiles and meridional flow fields are analysed at both the peak efficiency and near stall operating points under clean inflow conditions.

Peak Efficiency Operating Point At the peak-efficiency operating point, the points closest to $Q_{corr}/Q_{corr|PE} = 1$ are considered. Figure 6.3 shows the spanwise distribution of entropy rise across the entire compressor, from the inlet to the outlet, including the planes upstream of each stator. The results correspond to the reference blade-resolved simulation ($2\pi/4$ bladed case), the original Hall-Thollet Body-Force model (BF - HT), and the modified Body-Force

model (BF - new). The entropy profiles provide a direct mean of assessing the impact of the injected rotor tip losses. Each measurement plane located upstream of a stator also represents the downstream plane of the preceding rotor, allowing the local entropy increase associated with the added losses to be clearly identified.

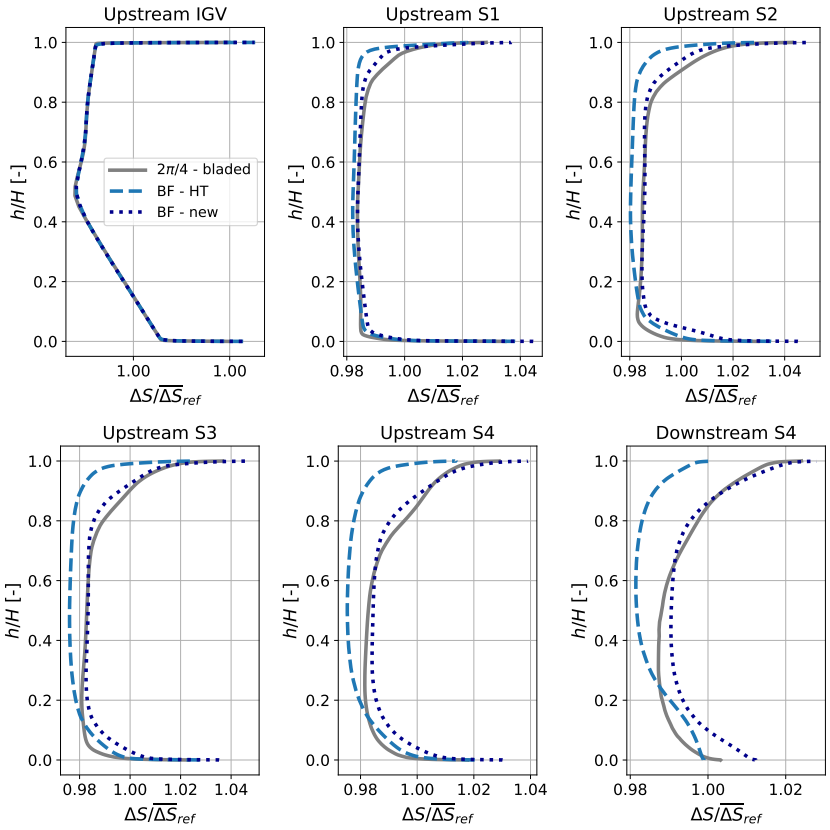

Figure 6.3: Mass flow-averaged radial distribution of entropy loss at PE. Bladed-resolved ($2\pi/4$ - bladed), and Body Force data using the original (BF - HT) and the modified model (BF - new) at PE.

In the figure, a distinct inflection in the radial profiles can thus be observed at the shroud. The modified Body-Force model reproduces the reference entropy distribution near the shroud at all stations, confirming that the injected losses effectively improve the model predictions in the affected region and reduce the discrepancy with the blade-resolved data. Beyond the near-shroud correction, the overall mean level of the radial entropy profiles is significantly better aligned with the reference data. This improvement results from the calibrated loss coefficients, as discussed in the previous chapter. Some local discrepancies persist near the hub, consistent with the behaviour previously observed on the CREATE compressor, indicating that further refinement of the modelling is required in this region. It should also be noted that the blade-resolved simulations include hub fillets, which are not present in the Body-Force computational domains. This choice was made because, without a model to account for the effect of fillets on flow turning, including them in the Body-Force geometry would only increase metallic blockage, without offering any benefit to compressor performance. As such, this approach has been deliberately avoided, although it remains a potential source of error at the compressor hub.

To isolate the impact of the rotor tip correction, Figure 6.4 is presented. This figure complements the previous one by showing the profiles from the Body-Force model, which includes only the rotor tip losses (BF - ω_{rt}). It allows the decomposition of the impact of the rotor tip losses from the other model modifications, specifically highlighting their effect in the near shroud region downstream of the rotor. As observed, the introduced losses cause a significant inflection in the entropy spanwise profiles at the shroud compared to the baseline model, providing the required and expected variation. Additionally, it is evident that an additional correction step is still necessary to accurately match the reference profiles. This is achieved through the supplementary corrections (clipping and calibration), whose impact was isolated in the previous chapter and remains consistent in the case of the IHPC compressor.

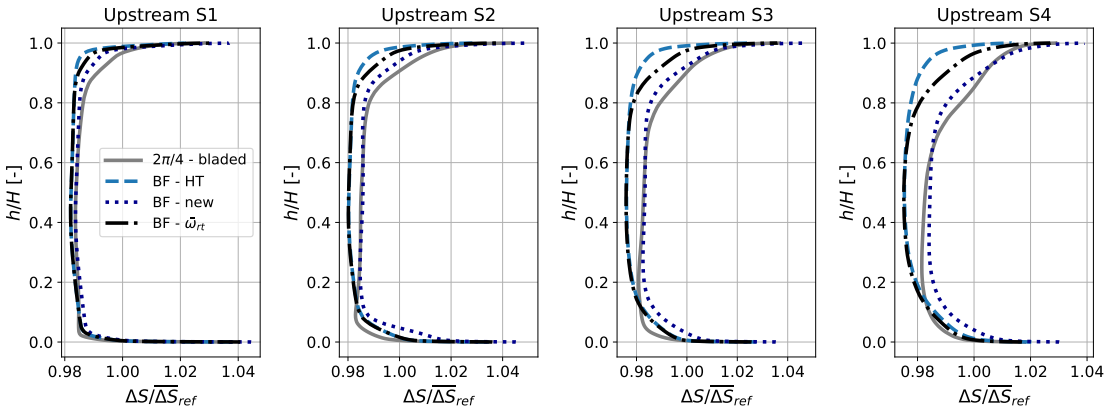

Figure 6.4: Mass flow-averaged radial distribution of entropy loss at PE. Bladed-resolved ($2\pi/4$ - bladed), and Body Force data using the original (BF - HT), the modified model (BF - new), and the model with rotor tip losses only (BF - ω_{rt}) at PE.

Apart from the entropy spanwise profiles, which are useful for verifying the impact of the loss model, it is also important to assess whether the applied rotor tip loss correction positively influences other flow quantities. To this end, Figure 6.5 presents the spanwise distributions of total pressure and total temperature at two representative locations. Figure 6.5a focuses on the region downstream of the first rotor. It is evident that, for this row, the applied corrections do not lead to a significant improvement in model predictions. Only a slight enhancement is observed near the tip region of the total temperature profile. This limited effect can be attributed to the constraints of the correlation used to model rotor tip losses. As discussed in Section 4.3.3, the adopted calibration was derived from a small number of subsonic rotor cases, which limits its applicability to the first rotor, which operates in a strongly transonic regime in the present configuration. A study in the literature also demonstrated the possibility of locally correcting the total temperature ratio by introducing a model in the Body-Force framework to account for shock losses [121] via the Denton entropy correlation [35]. This approach has not been adopted here, as detecting the transonic regions where the correction should be applied requires detailed CFD results or other data-driven methods, the computational effort for which was not deemed justified, given that the maximum error is approximately 2.3% at around 90% h/H, which remains within an acceptable range. The underprediction of total temperature in the upper half-span downstream of the first rotor will therefore be considered in the following analyses, with its limited error taken into account. In

contrast, Figure 6.5b shows the same quantities downstream of the third rotor and exhibits behavior consistent with that observed downstream of rotors two and four. At this location, both total pressure and total temperature profiles are accurately predicted, indicating that the applied corrections are effective for these rows.

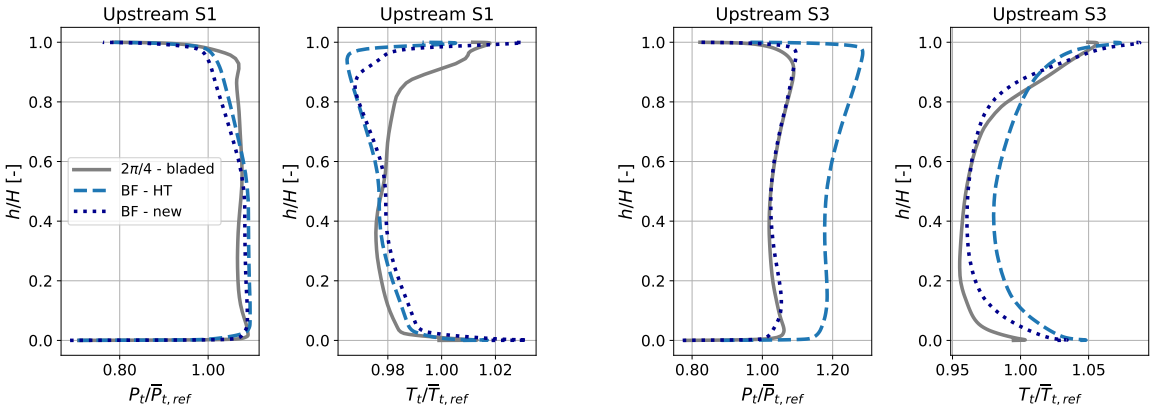

(a) Plane upstream of S1. **(b)** Plane upstream of S3.

Figure 6.5: Mass flow-averaged radial distribution of total pressure and temperature at PE. Bladed-resolved ($2\pi/4$ - bladed) , and Body Force data using the original (BF - HT) and the modified model (BF - new) at PE.

Further evidence of the model's predictive capability is provided by qualitative comparisons of the meridional flow fields obtained from the reference blade-resolved simulation and the modified Body-Force computation. Figure 6.6 presents the total temperature distribution. A noticeable discrepancy appears at the first rotor, where the compressor is known to develop a normal shock extending significantly upstream. Because the Body-Force formulation resolves only the azimuthally averaged flow within each blade passage, it does not fully capture the local supersonic regions, leading to some localized deviations from the reference solution.

The entropy field, shown in Figure 6.7, highlights the direct influence of rotor tip losses on entropy generation along the shroud. The predicted magnitude of the entropy rise and the radial extent of the high-loss region at the casing are in close agreement between the two approaches. A slightly elevated entropy level is observed near the hub at the compressor exit; this behaviour has already been discussed through the analysis of radial profiles. Overall, the predictions at the inlet and outlet of each blade row, and consequently the integral performance metrics and the radial distributions within the annular domain, remain accurate, confirming the reliability of the modified Body-Force model for its intended application. Across the remainder of the compressor, the agreement with the reference simulation is consistently good, further demonstrating the robustness of the approach.

Overall, the modified Body-Force model proves highly effective in representing both the global performance and the local flow behaviour of this complex compressor, while the original model exhibited considerable limitations. Only a few specific regions, such as the tip of the first rotor, show minor discrepancies, which remain within an acceptable range.

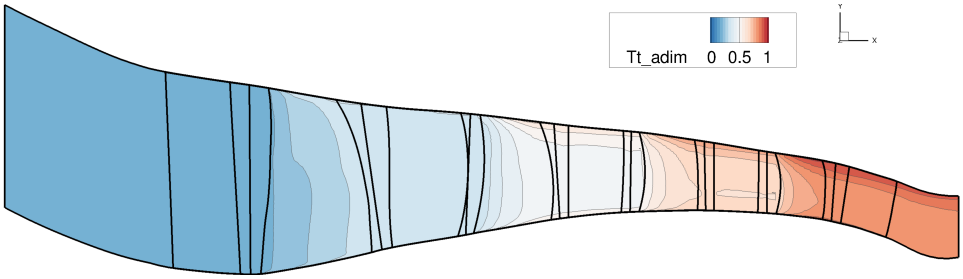

(a) Blade-resolved calculation.

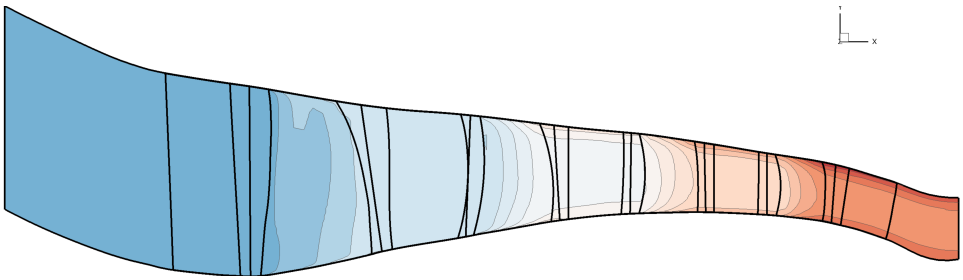

(b) Body-Force calculation.

Figure 6.6: Meridional views of total temperature at the peak efficiency operating point for the IHPC compressor.

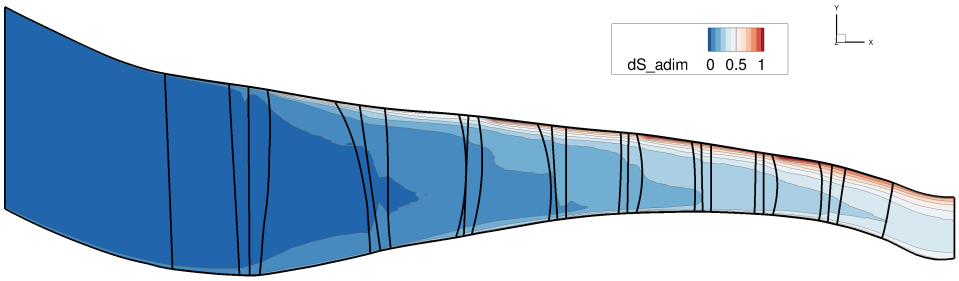

(a) Blade-resolved calculation.

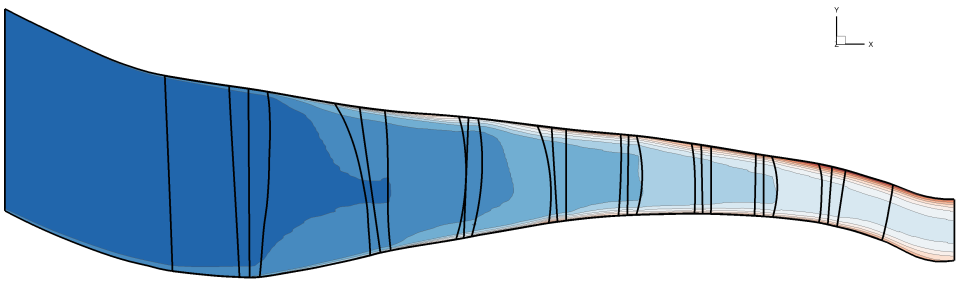

(b) Body-Force calculation.

Figure 6.7: Meridional views of entropy rise at the peak efficiency operating point for the IHPC compressor.

Near Stall Operating Point Figure 6.8 presents the spanwise entropy profiles at the near-stall operating point, similar to those shown at peak efficiency. The data include results only from the blade-resolved reference simulation and the modified Body-Force model, as the unmodified model failed to converge at these lower mass flow rates, as did the model that includes rotor tip losses only.

The entropy distributions near stall confirm the trends observed at peak efficiency: excellent agreement at mid-span, attributable to the calibration procedure, as shown in Figure 6.4 for the peak-efficiency point; good correspondence at the shroud, primarily due to the rotor tip loss integration, again seen in Figure 6.4; and only minor discrepancies at the compressor hub, as previously discussed, which consistently remain within 1-2%. These results indicate that the modifications introduced into the Body-Force model continue to yield a coherent and accurate representation of the flow behaviour, even under demanding off-design conditions. This consistency further highlights the robustness of the proposed loss modelling across the compressor operating range, despite the rotor tip loss correlation having been validated mainly at design conditions [135].

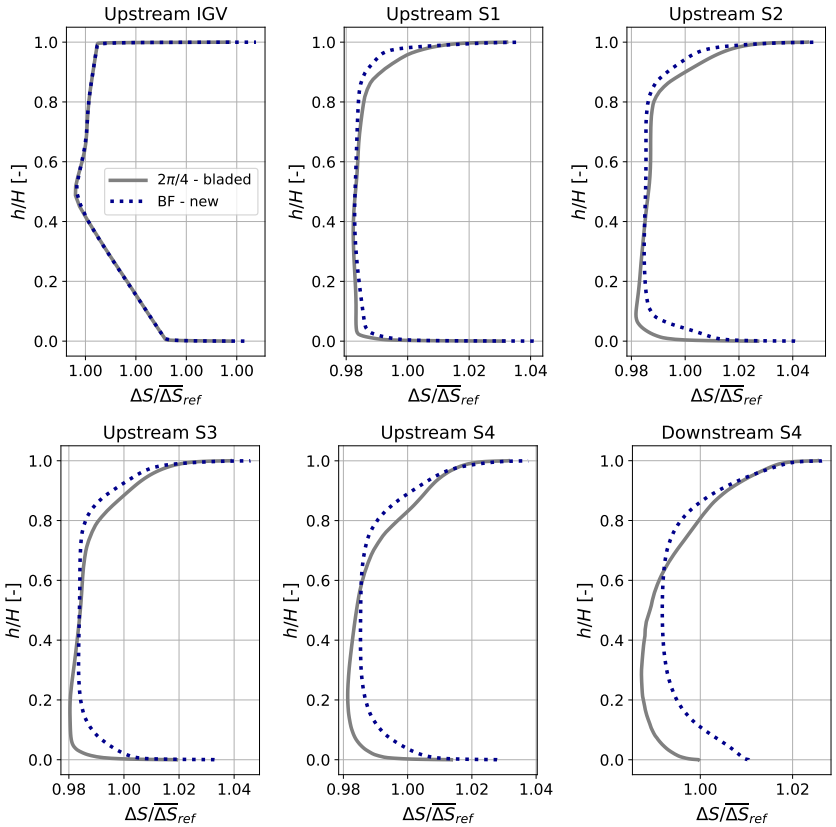

Figure 6.8: Mass flow-averaged radial distribution of entropy loss at PE. Bladed-resolved ($2\pi/4$ - bladed) , and Body Force data using the original (BF - HT) and the modified model (BF - new) at NS.

Concluding Remarks on the Body-Force reliability under Clean Inflow The comprehensive validation of the modified Body-Force model under clean operating conditions, across multiple operating points, demonstrates its capability to accurately predict both global per-

formance metrics and local flow characteristics. The model consistently reproduces key parameters such as pressure ratio, temperature ratio, and isentropic efficiency within a few percentage points of the blade-resolved reference data. In addition, detailed comparisons of spanwise entropy profiles and total pressure and temperature distributions show good agreement throughout the compressor, confirming the model's ability to capture critical aerodynamic phenomena. Overall, these results validate the effectiveness of the proposed modifications in enhancing the fidelity of the reduced-order model, thereby providing confidence in its use for performance assessment and flow analysis in complex multistage compressor configurations across a wide range of operating conditions.

6.2 Impact of Circumferential Inlet Distortion on the IHPC Compressor

The IHPC compressor is now studied under the effect of a circumferential inlet distortion, characterised by a region of reduced total pressure spanning an azimuthal extent of 105° with an intensity of −3.5% relative to the clean inlet total pressure. This purely azimuthal distortion is superimposed on the radial map characterising the clean inflow condition, as was presented in Figure 3.16. Consequently, the compressor inlet exhibits a combined radial and circumferential variation in total pressure, as shown in Figure 3.17. The characterisation of this circumferential distortion is presented again for reference in Figure 6.9. The magnitude of the imposed deficit is derived directly from experimental measurements, as detailed in Section 2.3.1. In addition, a more severe distortion intensity of −7.5% relative to the clean inlet total pressure will be introduced in subsequent analyses to assess compressor stability under increasingly challenging conditions.

The simulations under circumferential distortion are performed using the full-annulus, full-height computational domain of the compressor for both the blade-resolved and Body-Force approaches. The blade-resolved reference simulations, counting over one billion mesh cells, required substantial external computational resources provided through a grant of twenty million CPU hours on the GENCI IRENE supercomputer [52], enabling the simulation of both peak-efficiency and near-stall operating points under undistorted conditions and −3.5% azimuthal distortion, covering four operating points.

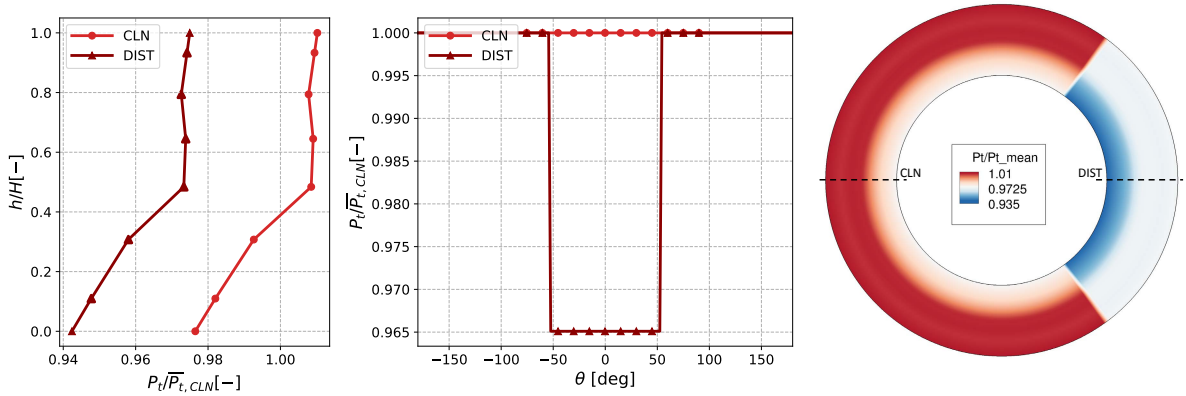

(a) Radial and azimuthal profiles of total pressure. **(b)** 2D inlet map of P_t.

Figure 6.9: Azimuthal total pressure distortion features for the full-annulus IHPC simulations.

6.2.1 Impact on the Flow Field

The impact of distortion on the flow field at the peak efficiency operating point is evaluated in this section. As for the CREATE compressor, it is first instructive to examine the flow quantities at the compressor outlet, as these provide insight into both the transmission of distortion through the machine and the reliability of the Body-Force predictions. To do so, Figure 6.10 presents the azimuthal profiles of total pressure, total temperature, and entropy rise at the compressor outlet plane at 50% span.

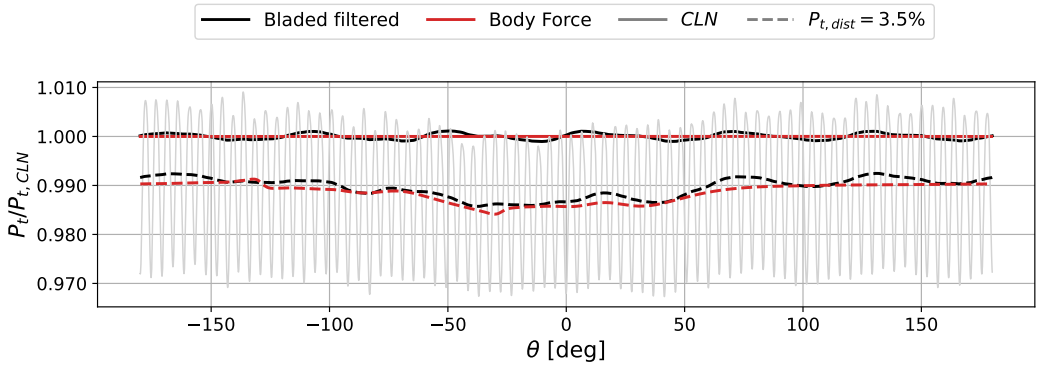

(a) Azimuthal profile of total pressure.

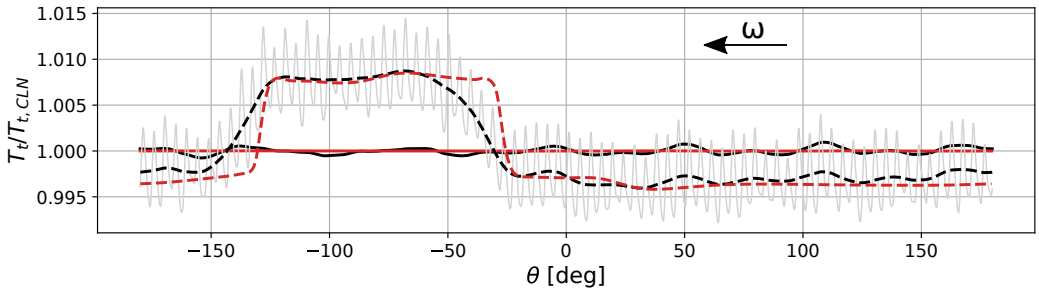

(b) Azimuthal profile of total temperature.

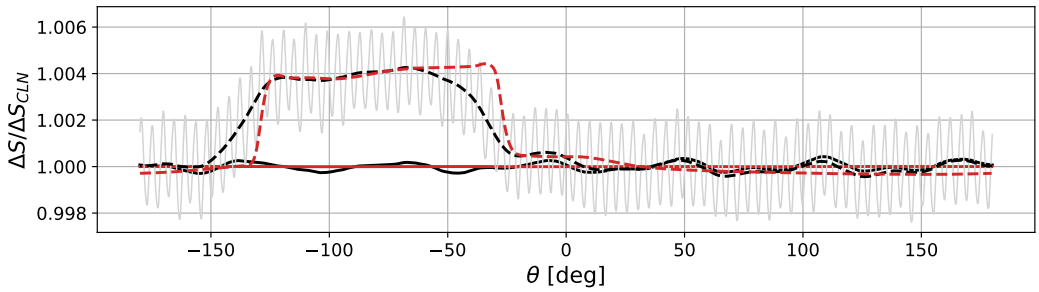

(c) Azimuthal profile of entropy increase.

Figure 6.10: Compressor outlet flow quantities at 50% channel height. Body Force (red), filtered bladed data (black), and unfiltered bladed data (gray) shown for distortion case only et PE.

In Figure 6.10, solid lines correspond to the clean inflow case, while dashed lines represent the circumferentially distorted inflow. Results from the Body-Force model are shown in red, and those from the blade-resolved simulations in black. The blade-resolved data are filtered using a low-pass filter to smooth wake signatures; for clarity, only the distorted inflow case

is presented in unfiltered form in gray. The cutoff frequency of the filter varies between the plots in this section to highlight specific peaks or variations. As a result, the signal may appear noisy in some regions but remains physically meaningful.

Figure 6.10 shows that the Body-Force method accurately reproduces the deficit and surplus of each flow quantity relative to the clean reference case. The good agreement with the blade-resolved data confirms that the modified Body-Force formulation effectively represents the flow behavior at the compressor outlet, where mixing and secondary flow effects dominate. This highlights its suitability for complex multistage configurations. Another important observation is that the total pressure decreases across the entire compressor annulus, stabilizing at approximately a 1-1.5% deficit at the outlet, compared to the initial 3.5% deficit imposed at the inlet. This indicates that the distortion is progressively attenuated across the stages. Similar to the previous compressor, the total pressure profiles reveal a temperature distortion region, which was not directly imposed but arises from the flow redistribution mechanism triggered by the pressure deficit. Increased losses are also observed in this region, as shown in the entropy plot. Finally, discrepancies appear in the total temperature and entropy distributions, particularly in areas where the curve slope changes abruptly, marking the transition to the distorted sector. In these regions, the blade-resolved computations show smoother boundaries compared to the Body-Force predictions. This behavior, not observed in the P2D CREATE configuration, suggests that these differences arise from intensified local phenomena, such as shock interactions and strong wake mixing, which are not directly modeled in the current Body-Force model but are prominent in the flow field of this 4.5-stage transonic compressor.

As for the CREATE compressor, these observations are further supported by the azimuthal distributions of total pressure and total temperature at several axial locations within the compressor, shown in Figure 6.11. The figure presents data at the inlet plane and at the outlet of each stator row at mid-span. Results for the 3.5% total pressure deficit case are shown for the Body-Force method (in red) and the blade-resolved simulations (in black). The y-axis labels have been omitted for confidentiality, and were normalised by an identical reference value for each axial station.

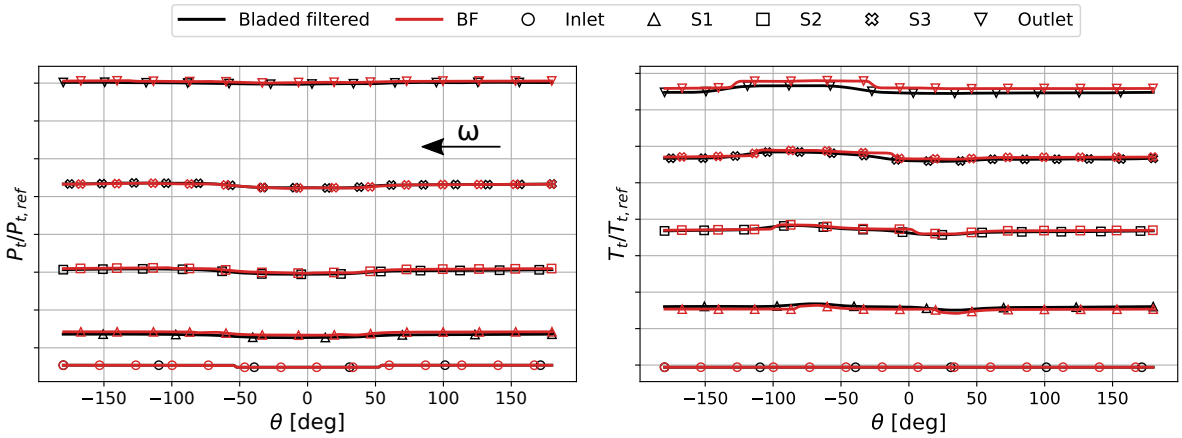

(a) Azimuthal distribution of total pressure. **(b)** Azimuthal distribution of total temperature.

Figure 6.11: Azimuthal profiles of total pressure (left) and total temperature (right) at 50% h/H, comparing bladed URANS and Body Force results for distorted inflow at different stations at PE.

A preliminary consideration concerns the accuracy of the Body-Force predictions. As anticipated, minor differences appear near the boundaries of the distorted sector; however, the overall magnitude and spatial evolution of the quantities are well reproduced throughout the whole compressor. Figure 6.11a illustrates the evolution of total pressure. The initial distortion slot progressively dissipates along the compressor stages, with the deficit decreasing to the 1-1.5% range observed in the previous figure. Similarly, Figure 6.11b shows the development of a corresponding slot in the total temperature field, which intensifies toward the compressor outlet. In addition, the distorted region shifts in the direction of rotation, moving from right to left in the figure. The distorted slot is centered at $\theta = 0°$ at the inlet and around $\theta = -90°$ at the outlet, indicating a significant shift across the four stages of the machine. The azimuthal extent of the region also varies: it is 105° at the inlet and increases towards the compressor exit. The Body-Force approach predicts an amplitude of 110°, while the blade-resolved calculation shows around 120° of amplitude.

To understand these observations, the underlying mechanism induced by the circumferential distortion has to be explained. As precedently done for the CREATE configuration, the flow coefficient and relative flow angle distributions are presented in Figure 6.12 to complement the total pressure and total temperature observations. These profiles are evaluated at the compressor inlet for both the clean inflow and the 3.5% distortion cases, at mid-span. This plot is one of the cases in which the cut-off frequency has been deliberately kept high, to avoid the smoothing of the plot peaks of the black line.

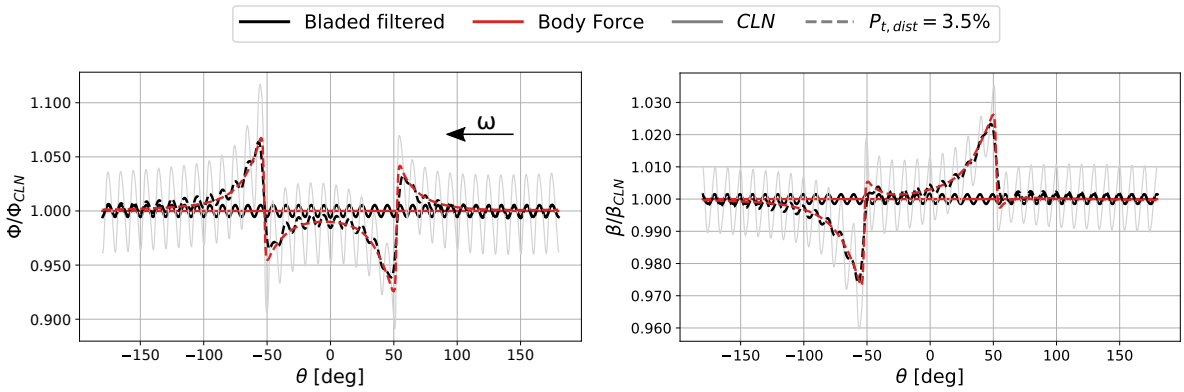

(a) Azimuthal profile of flow coefficient (Φ). **(b)** Azimuthal profile of relative flow angle (β).

Figure 6.12: Azimuthal profiles of flow coefficient (Φ) and relative flow angle (β) at the compressor inlet, at 50% h/H and at PE.

The figure indicates that the imposed total pressure deficit modifies the flow coefficient (Figure 6.12a), which appear lower in the distorted region with respect to its value in clean conditions, thereby altering the flow redistribution across the annulus. The flow is redistributed towards areas of lower static pressure, corresponding to the distorted region, which results in an increased incidence angle, as evidenced by the relative flow angle distribution (Figure 6.12b). In particular, although the mean β angle is slighlty larger within the distorted zone, two opposite peaks are observed at its boundaries. Upon entering the distorted region (around 60°), the relative flow angle rises sharply, implying a higher blade incidence and strong aerodynamic loading gradients. At the exit of the distorted region (around $-60°$), the

angle decreases correspondingly. These characteristics identify the inlet boundary of the distortion as the most critical area with respect to blade loading and overall compressor stability.

Beyond their physical interpretation, these results further corroborate the reliability of the Body-Force methodology, as it consistently and accurately reproduces the trends observed in the reference blade-resolved simulations.

The propagation of distortion through the compressor can be further examined using two-dimensional contour plots, which provide information across the entire blade span rather than at a single channel height, as considered previously. Figure 6.13 presents the total temperature field in the azimuthal-radial plane downstream of each rotor row. The left column shows the blade-resolved results, which include fluctuations from blade wakes and their mixing, while the right column shows the corresponding Body-Force predictions.

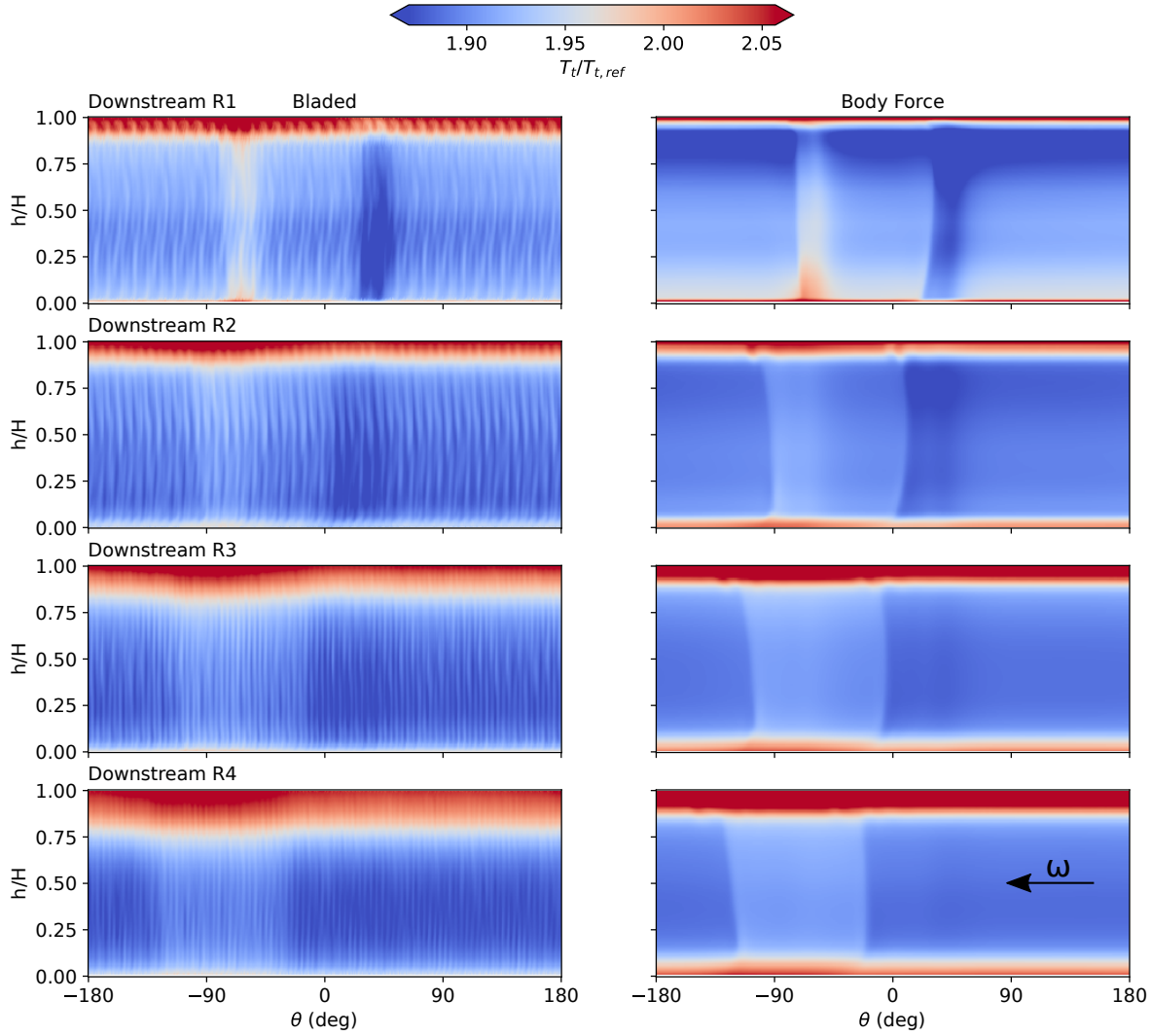

Figure 6.13: 2D contour of total temperature showing azimuthal and radial variation downstream of each rotor, comparing the Body Force (right) and Bladed (left) results at PE.

Consistent with the mid-span observations, the main features of the distorted region are well reproduced, including its magnitude, azimuthal displacement, and boundary position across the domain. Some differences are evident, particularly a lower total temperature near the tip of the first rotor and a higher total temperature in a thin layer near the hub. These discrepancies correspond to those noted in the clean inflow analysis, previously reported to be limited to around 2%, and are inherent to the modelling approach, which appears to require further improvement in the hub region. Similarly to the azimuthal smoothing of the distortion boundaries, the radial transition between higher and lower temperature regions is smoother in the blade-resolved simulations than in the Body-Force results, likely due to comparable dissipation and mixing mechanisms. Nevertheless, these differences do not compromise the model's ability to accurately capture and propagate distortion effects through the compressor stages, as quantitatively confirmed by the spanwise profiles.

Another two-dimensional representation, which overcomes the limitation of analyzing discrete axial locations but requires a fixed spanwise position, is the entropy field in the blade-to-blade plane at 50% channel height, shown in Figure 6.14, where the inlet is at the bottom of the figure, and the outlet at the top. Results are presented for both modelling approaches: the blade-resolved simulation in the upper panel and the Body-Force prediction in the lower panel.

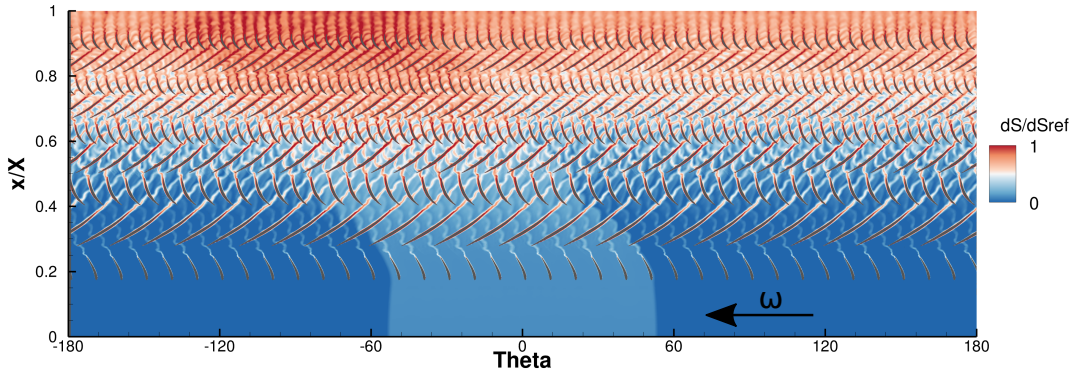

(a) Bladed URANS approach

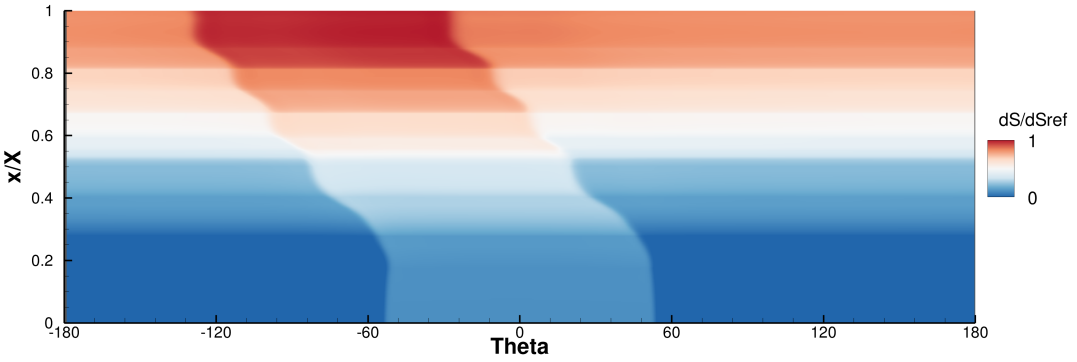

(b) Body Force approach

Figure 6.14: Blade-to-blade entropy field at 50%h/H for the 3.5% distortion case at PE.

The same flow characteristics previously discussed are clearly visible, including the intensity of the losses associated with the distorted region and its azimuthal displacement in the direction of rotation, from right to left of the figure. A progressive attenuation of the sharp boundaries of the distorted region is evident in the blade-resolved results, whereas this behavior is less pronounced in the Body-Force case. This observation is consistent with the trends reported in Figure 6.10, confirming that mixing plays a dominant role in the dissipation of distortion boundaries, a mechanism not explicitly modeled in the Body-Force model.

Concluding Remarks on Distortion Propagation and Body-Force Model Validation Overall, the analysis demonstrates that the imposed total pressure distortion gradually attenuates as it propagates through the compressor stages, accompanied by a redistribution of the flow field affecting both total pressure and total temperature. The distortion induces local variations in flow incidence and loading, particularly at the boundaries of the distorted region. Specifically, the leading boundary of the distortion experiences positive increments in both incidence and loading. As a result, the leading boundary is identified as the most critical zone for stability considerations. Comparison of the blade-resolved and Body-Force simulations confirms that the latter successfully captures the principal distortion features, including its transmission, azimuthal shift, and intensity decay. Although some discrepancies arise, mainly related to local dissipation effects and mixing mechanisms not explicitly modeled, the overall agreement remains strong, with errors around 2%, whereas other similar models applied to simpler configurations typically exhibit errors exceeding 5% under peak-efficiency conditions and even higher at off-design or distorted conditions [155]. These results validate the modified Body-Force approach's capability to reproduce the essential aerodynamic response of the compressor under off-design and fully realistic three-dimensional distorted conditions, extending its validation beyond the 2.5D circumferential distortion case of CREATE.

6.2.2 Impact on the Stability of the IHPC Compressor

This section focuses on the analysis of near-stall conditions to assess the influence of circumferential inlet distortion on compressor stability. To this end, a second distortion case is introduced, following the same pattern as the previous case but with a total pressure deficit of -7.5% relative to the clean inflow, which is compared with the original -3.5% distortion case. Only the Body-Force simulations are considered in this investigation. This choice is justified by the confidence established in the model's reliability throughout Chapters 5 and 6, as well as by the prohibitive computational cost of performing multiple high-fidelity full-annulus simulations at the near stall condition for a parametric study of distortion intensity.

Flow Behaviour at Near-Stall Conditions The analysis first focuses on the azimuthal distributions of flow quantities at the outlet plane of the compressor, evaluated at mid-span (50% h/H), as shown in Figure 6.15. The figure reports Body-Force results for three inlet conditions: clean inflow, 3.5% distortion ($k_{3.5}$), and 7.5% distortion ($k_{7.5}$). Figure 6.15a corresponds to the peak-efficiency operating point, while Figure 6.15b represents the near-stall condition. The near-stall point for the 7.5% distortion has been defined as the operating condition corresponding to the same outlet back pressure (as imposed by the valve law) as the near-stall point of the 3.5% distortion case and the clean inflow case. As a result, although the outlet back pressure is identical for all curves in a given plot, the operating conditions themselves are not strictly equivalent, as will be discussed in the following analysis. Furthermore, whenever a

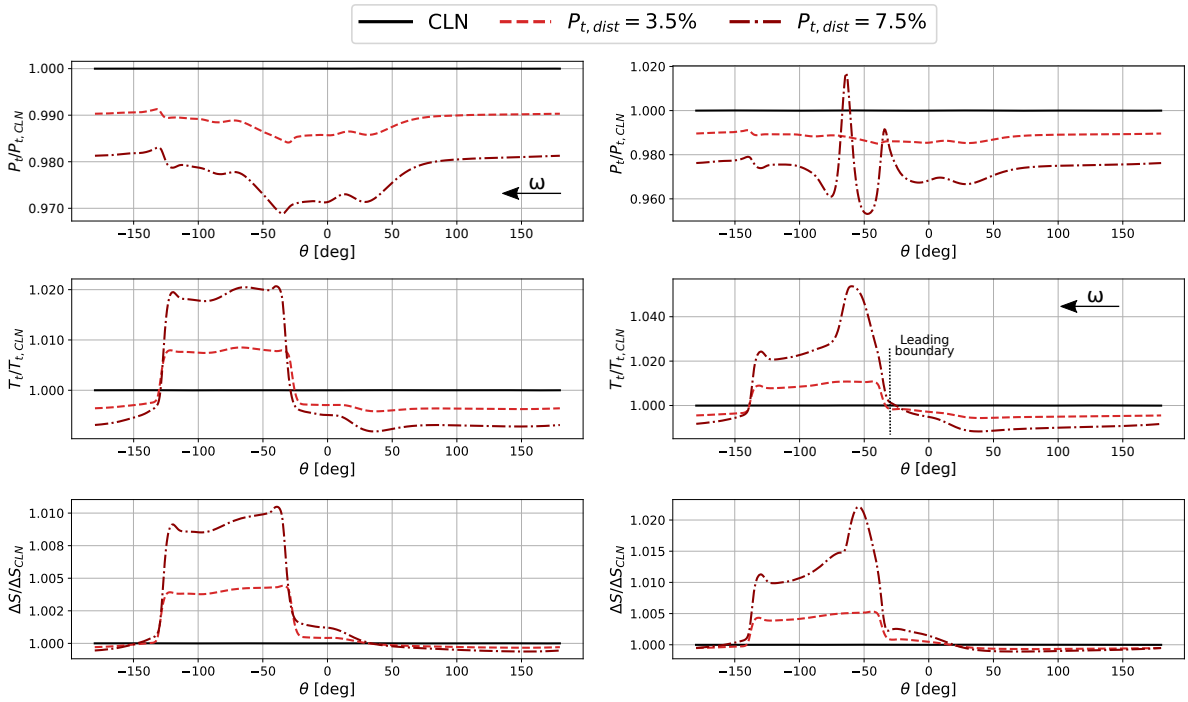

(a) Peak-efficiency operating point

(b) Near-stall operating point

Figure 6.15: Body-force azimuthal profiles of total pressure (top), total temperature (middle), and entropy rise (bottom) at 50% h/H at the compressor outlet, shown for the distortion cases $k_{3.5}$ and $k_{7.5}$ at the PE and NS points.

critical point is mentioned, it refers to a simulation that did not reach full convergence but was terminated after the same number of iterations required by the stable points to achieve convergence. Although the results at the critical operating points must be interpreted with caution, they remain informative for identifying trends in the flow properties.

At the peak-efficiency operating point (Figure 6.15a), the flow field exhibits coherent behavior as the distortion intensity increases: the distorted region remains unchanged in extent and shape, while the distortion intensity grows proportionally with the injected inlet deficit. While the first distortion case produced a maximum total pressure deficit of around 1.5% at the outlet, i.e. roughly 40% of the injected distortion of 3.5%, the second case induces a maximum deficit of 3%, also approximately 40% of the inlet distortion of 7.5%, indicating that the outlet deficit scales proportionally with the inlet distortion, with a factor of around 2.4. Similarly, the total temperature and entropy distributions increase within the distorted region, reflecting the additional work input and associated aerodynamic losses, while a slight reduction is observed in the undistorted region relative to the clean inflow case. This reduction is associated with the increased work in the distorted region and, given the close proximity of the operating points, can be interpreted under an assumption of approximately constant total work, resulting in a reduced work contribution in the undistorted region. Overall, the plots exhibit a predictable trend with increasing distortion intensity, provided the operating point remains stable.

For the near-stall condition, shown in Figure 6.15b, the behavior changes abruptly. The case with the highest distortion intensity becomes critical and exhibits pronounced peaks.

The total pressure distribution shows abrupt variations, both positive and negative, starting at around $-30°$ azimuth, corresponding to the leading boundary of the distorted region at the outlet plane. Similarly, the total temperature and entropy fields reveal a deformation of the previously nearly symmetric distortion pattern, with elevated temperatures and losses in the region where the blades first encounter the distortion, again at $-30°$ azimuth. As a reminder, the compressor rotation is such that the blades move from right to left in the plots. These observations indicate that the near-stall point for the more intense distortion exhibits critical behavior and confirm the conclusion drawn in the previous section, which identified the distortion entry region as the most critical for blade loading and overall compressor stability.

To investigate the origin of the anomalous peaks discussed above, Figure 6.16 presents the two-dimensional entropy flow field in the axial and azimuthal directions at 25% h/H, for the near stall operating point with the -7.5% distortion deficit. Two vertical lines are drawn to indicate the leading and trailing edges of the fourth stator row. The figure clearly identifies this row as the region exhibiting stability issues. A pronounced increase in entropy, indicative of strong localised aerodynamic losses, is observed. Furthermore, these losses appear to span multiple blade passages, approximately 7-8, highlighting the spatial extent of the critical region. Once again, the critical behaviour emerges at the leading boundary of the distortion, around $-20°$ in the azimuthal direction within the area bounded by the black lines.

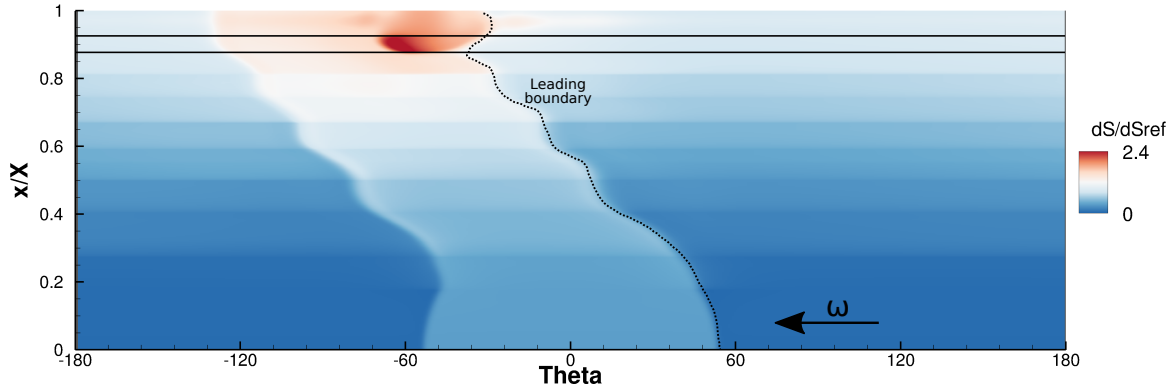

Figure 6.16: Entropy flow field at 25% channel height for the critical near-stall point with 7.5% distortion. Vertical black lines mark the leading and trailing edges of the fourth stator (S4).

Given that the fourth stator is identified as the location of the localised losses, a more detailed investigation of the flow downstream of this row is presented. In particular, Figure 6.17 shows the 2D distributions of the absolute flow angle (left), axial velocity (middle), and entropy (right) at this location. The rotation direction in this plot is clockwise.

The figure indicates that the localised losses, as revealed by the elevated entropy, are primarily concentrated near the hub and at the entrance of the distorted region. At the same location near the hub, the axial velocity exhibits negative values, indicating flow separation, while the flow angle increases significantly, reflecting a strong turning of the flow within the corresponding blade passages. This is followed by a pronounced reduction in flow angle in the adjacent passages, compensating the turning.

These observations demonstrate that the Body-Force model predicts a hub separation extending over approximately eight blade passages. The extent of this separation suggests that

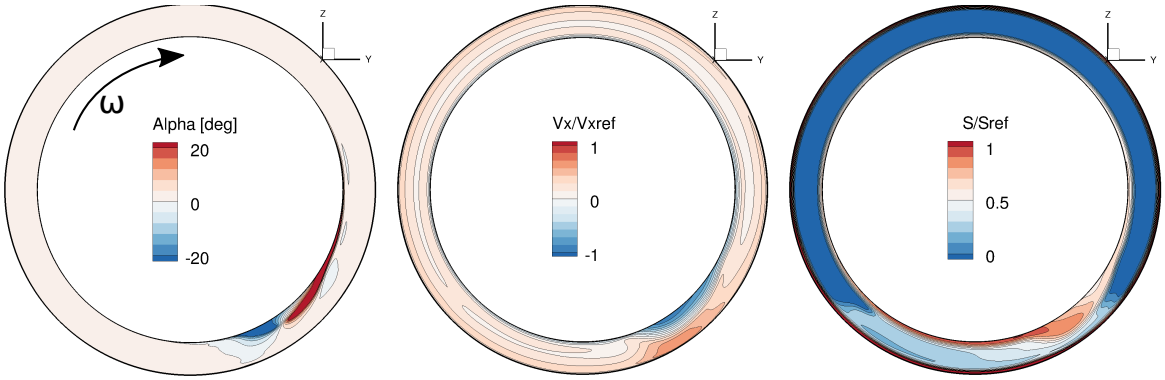

Figure 6.17: Map of absolute flow angle (left), axial velocity (middle), and entropy rise (right) at the outlet plane of stator S4, for the critical near-stall point with 7.5% distortion.

the simulated operating point may already correspond to stalled conditions, as multiple passages are affected. Although experimental or blade-resolved data are not available to directly validate this conclusion, several lines of evidence support the reliability of the Body-Force predictions. First, previous studies have demonstrated that Body-Force formulations similar to the one used here are capable of predicting flow separation and stall inception [3, 82, 84]. Second, hub separation has been identified in the literature as a primary mechanism of stall inception in high-speed axial compressors [39, 40, 95]. This typically occurs when strong radial hub distortion increases blade loading near the hub by locally accelerating the flow and steepening the adverse pressure gradient, thereby intensifying near-wall separation and promoting stall onset. Third, the inlet distortion distribution in the present study suggests a similar scenario: as shown in Figure 3.17, the radial distortion at the compressor inlet remains relatively uniform across the upper half of the blade span but decreases sharply in the lower half. This spanwise variation, combined with the azimuthal total pressure deficit at the inlet, indicates conditions favorable to hub separation, consistent with mechanisms reported in the literature. Fourth, analyses from the previous section, which included the reference blade-resolved simulations, indicate that the region where the blades first encounter the distortion is particularly critical for aerodynamic loading and loss generation, consistent with the location of the hub separation predicted by the Body-Force model at the critical operating point. Finally, during the experimental campaign, the distortion grid was intentionally designed not to extend into the first 5% of the blade span near the hub to avoid stability issues, further highlighting the sensitivity of this region.

Taken together, these points provide strong support for the conclusion that the hub region is particularly susceptible to separation and likely represents the critical zone for stall initiation in the present case.

Assessment of the Stall Margin Reduction The onset of instabilities observed in the simulations motivates a quantitative assessment of the reduction in stall margin caused by total pressure distortion at the compressor inlet. For this purpose, the results obtained from the Body-Force model are compared with experimental measurements, with particular emphasis on the case corresponding to 3.5% total pressure distortion, which matches the experimental condition. The last stable operating point was determined by incrementally reducing the outlet back pressure of the valve law along the compressor iso-speed line in steps of 0.2% until the

stability limit was reached, defined as the point at which the mass flow rate began to decrease, indicating the onset of instability. A smaller increment than 0.2% was judged unnecessary, as the current resolution provided sufficient accuracy while avoiding excessive computational demand.

Figure 6.18 presents the compressor performance maps, in terms of total-to-total pressure ratio against corrected mass flow rate, obtained from the Body-Force simulations under clean conditions (orange), 3.5% distortion (brown) and 7.5% distortion (black). Corresponding experimental data are also shown for the clean (red) and distorted (dark red) cases. The observed shift between the clean and distorted experimental characteristics is primarily attributed to differences in shaft speed and total temperature conditions between the two experimental setups, as they were not conducted under identical conditions. Consequently, this shift is not relevant for evaluating the impact of distortion on compressor behavior.

To assess this impact, the arrows are set to a slope that indicates the value of the performance ratio $PR = \pi_{tt}/Q_{corr}$ at the last stable operating point for each scenario. Table 6.3 summarises these values and reports the relative changes for the distorted cases with respect to the clean inflow, computed according to Equation (6.1).

$$\Delta PR = 1 - \frac{\left(\frac{\pi_{tt}}{Q_{\text{corr}}}\right)^{\text{stall}}_{\text{DIST}}}{\left(\frac{\pi_{tt}}{Q_{\text{corr}}}\right)^{\text{stall}}_{\text{CLN}}} \tag{6.1}$$

The experimental data indicate a reduction in the performance ratio of approximately -2.27%, while the Body-Force model predicts a comparable reduction of -1.78% for the 3.5% distortion case, demonstrating good agreement within 0.5 percentage points. The 7.5% distortion case results in a larger decrease of approximately -5.17%, suggesting a nonlinear amplification of performance degradation with increasing inlet distortion.

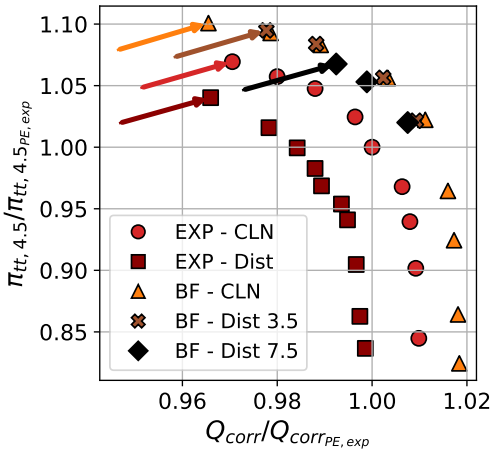

Figure 6.18: Compressor map from Body Force under clean and distorted inlet conditions (3.5% and 7.5%) compared with experimental data.

Analysis of Last Stable Operating Points The last stable operating points from each Body-Force simulation, shown in Figure 6.18, are examined to characterise the flow patterns associated with the near-wall instability identified earlier. For this purpose, flow quantities are

Table 6.3: Values of the performance ratio PR and their relative changes ΔPR for experimental and Body Force cases at the last stable operating point near stall.

Case	$PR = \frac{\pi_{tt}}{Q_{corr}}$	ΔPR
EXP - CLN	0.3742	-
EXP - Dist	0.3657	-2.27%
BF - CLN	0.3872	-
BF - Dist 3.5%	0.3803	-1.78%
BF - Dist 7.5%	0.3672	-5.17%

compared at 5% and 50% of the channel height (h/H), representing the near-wall region prone to instability and the core flow region, respectively.

Figure 6.19 presents the axial velocity (V_x) and absolute flow angle (α) at the compressor outlet. In particular, Figures 6.19a and 6.19b illustrate the azimuthal variation of these quantities at 50% and 5% of the channel height, respectively for the last stable operating points under clean conditions (grey line) and with 3.5% (red line) and 7.5% (dark red line) total pressure distortion. At 50% h/H, distortion causes moderate variations in both flow angle and axial velocity. In contrast, at 5% h/H, the flow angle exhibits local deviations exceeding 10° under the highest distortion, signalling considerably increased blade loading near the hub. Simultaneously, the axial velocity decreases to approximately half of its undistorted value, indicating strong flow deceleration in the near-wall region. While the flow remains globally stable at this stage, these features mark the onset of conditions that may lead to instability.

Figures 6.19c and 6.19d extend the analysis to include the first critical operating point for the 7.5% distortion case. At 50% h/H, the flow displays rapid azimuthal variations in both flow angle and axial velocity upon entering the distorted region, around $\theta = -30^\circ$. These variations are amplified at 5% h/H, where the flow angle spans from $+75^\circ$ to -75°, indicating flow separation across multiple blade passages, aprroximately 7-8, consistent with the patterns observed in Figure 6.17. Furthermore, the axial velocity reaches values close to zero, reflecting severe flow deceleration and the onset of near-hub flow reversal. Although the critical point itself should be interpreted with caution, as no stable convergence was achieved, the last stable operating points exhibit behaviour fully consistent with that observed at the critical point, providing confidence in the conclusions drawn.

These observations demonstrate that hub flow separation and rapid deceleration induced by inlet total pressure distortion can act as early indicators of stall inception. The concentration of these effects near the hub wall, coupled with the azimuthal extent of flow reversal, confirms that hub separation plays a primary role in compromising compressor stability under distorted inflow conditions.

Stability Parameters Analysis Finally, these operating points are used to evaluate compressor stability through the two stability parameters introduced in Section 1.1.3.1: the De Haller number, $DH = W_2/W_1$, traditionally used to indicate the risk of flow separation within a blade row; and the Lieblein diffusion factor, $DLI = 1 - W_2/W_1 + \Delta W_\theta/(2\sigma W_1)$, which provides a measure of aerodynamic loading. Typically, low DH values (< 0.5) correspond to strong flow deceleration and are indicative of increased susceptibility to flow separation and instability. And DLI values exceeding a certain threshold (> 0.7) are associated with elevated losses and an increased likelihood of flow separation. The threshold limits chosen here are

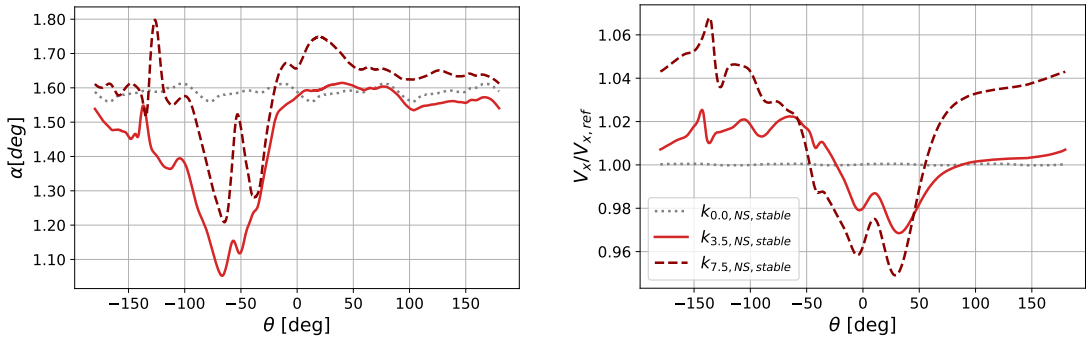

(a) h/H=50% - Last stable operating points near stall

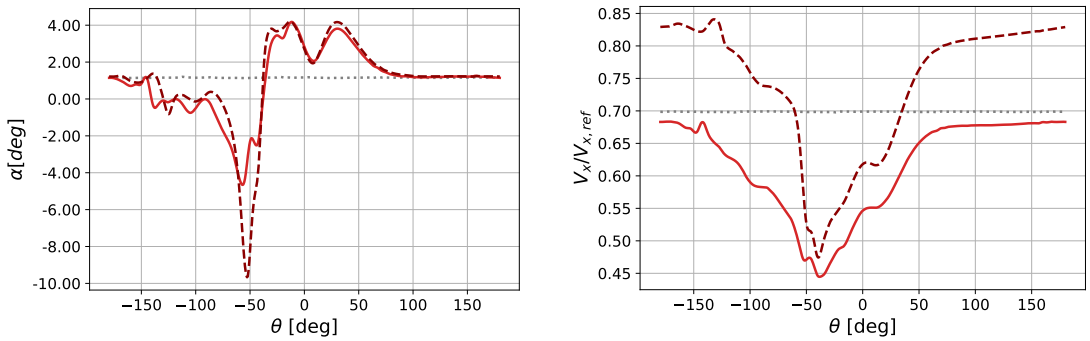

(b) h/H=5% - Last stable operating points near stall

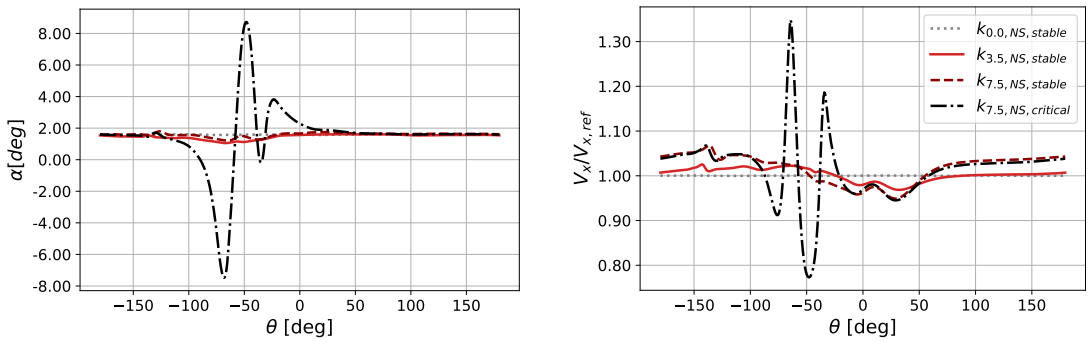

(c) h/H=50% - Stable and critical operating points near stall

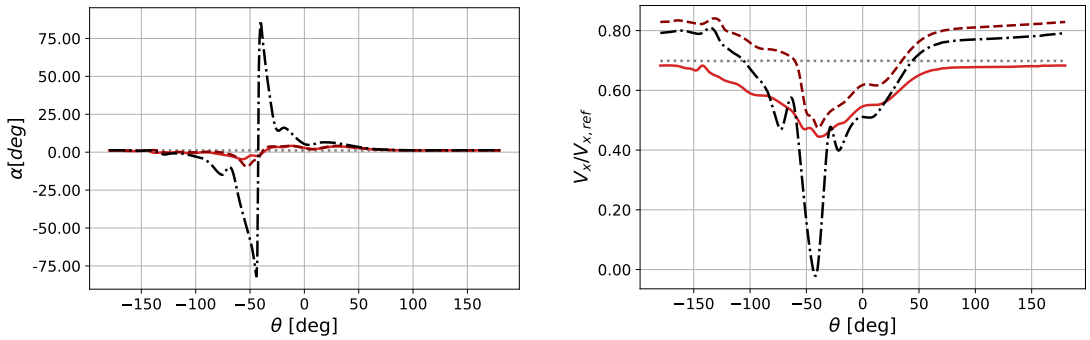

(d) h/H=5% - Stable and critical operating points near stall

Figure 6.19: Azimuthal distribution of flow angle α and axial velocity V_x at the outlet for last stable operating points at 0% (CLN), 3.5%, and 7.5% distortion, and the first critical point at 7.5% distortion.

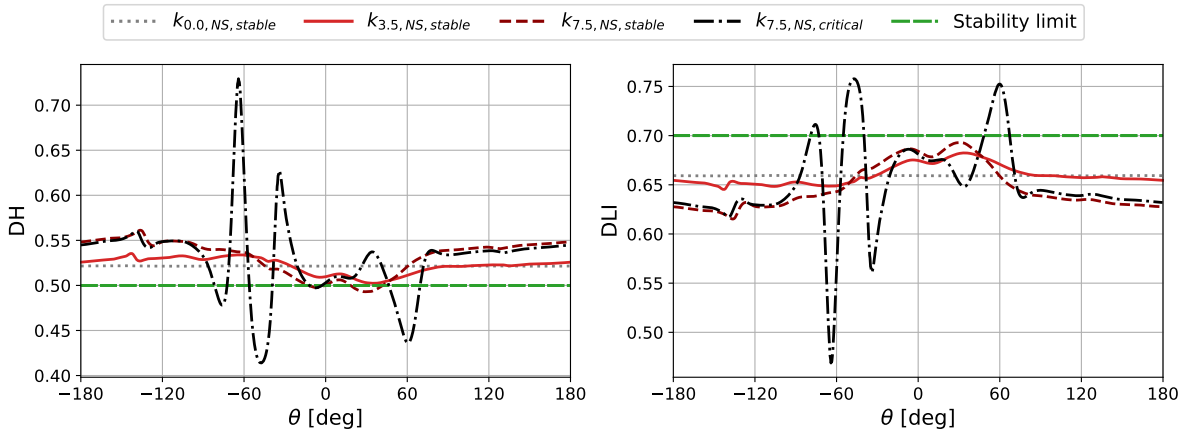

Figure 6.20: Azimuthal distribution of DH and DLI at the outlet of S4 at 50% h/H for the last stable operating points with 0%, 3.5%, and 7.5% distortion, and the first critical point at 7.5% distortion.

based on the values at the stable near-stall point for clean inflow at 50% channel height, with an additional 5% margin applied in the direction that increases risk: the DLI threshold is set to 105% of the clean inflow value, while the DH threshold is set to 95% of the clean inflow value. This ensures that the thresholds account for small deviations from the clean case in a manner consistent with the physical interpretation of each parameter.

Figure 6.20 shows the De Haller number (DH) and Lieblein diffusion factor (DLI) at 50% h/H for the cases considered: the last stable operating points under clean, 3.5%, and 7.5% distortion, as well as the first critical point at 7.5% distortion.

The results indicate that, although the stable operating points approach the stability thresholds, only the 7.5% distortion case locally exceeds these limits. Since this exceedance is confined to a limited azimuthal region, it is not deemed critical. By contrast, the critical point at 7.5% distortion surpasses the stability limits multiple times across distinct azimuthal locations. This behaviour highlights the presence of several regions where blade aerodynamic loading and flow deceleration become excessive, providing compelling evidence of instability onset.

Concluding Remarks on Stability Analysis with the Body-Force Model In summary, the Body-Force simulations provide a consistent and physically meaningful picture of compressor behaviour under inlet total pressure distortion at near-stall conditions. The analysis of the last stable operating points, together with the first critical point, demonstrates that the onset of instability is strongly localised near the hub, where flow separation and rapid deceleration occur. The evolution of entropy, flow angle, axial velocity, De Haller number, and Lieblein diffusion factor across azimuthal and spanwise locations confirms that these near-hub effects are precursors to stall inception. Despite the absence of blade-resolved validation data, the agreement with established stability criteria and trends reported in the literature reinforces the reliability of the Body-Force model in capturing the mechanisms leading to stall under distorted inlet conditions. Overall, the results indicate that hub separation plays a dominant role in destabilising the compressor, and that the Body-Force approach can be used to quantitatively assess the reduction in stall margin due to inlet distortion.

6.3 Considerations on CPU Time Gain

This section analyses the computational efficiency gained by performing Body-Force simulations compared to blade-resolved simulations for the IHPC compressor investigated in this chapter. A comprehensive comparison of the computational costs for each configuration is presented in Table 6.4. As for the CREATE compressor analysis, the first four columns of Table 5.5 identify each configuration in terms of the modelling method employed, either blade-resolved or Body-Force, the temporal approach, steady or unsteady, as well as the corresponding geometric setup in terms of azimuthal sector and domain type.

The following column shows the CPU time per core per job, normalised by the same value for the blade-resolved single-blade-passage (SBP) case ($|_{\text{norm}}$). It is important to note that this normalised CPU time depends significantly on load balancing across cores. Due to the multi-block meshing approach, where some blocks contain a larger number of cells and are not evenly divided, the computational workload may be unevenly distributed. Additionally, numerical settings, such as the treatment of the rotor-stator interface, and communication overhead between cores in large parallel runs also influence this value. Consequently, configurations using more cores tend to experience increased communication time, which can lengthen the overall CPU time. Another important difference arises from the use of a different computing facility for the blade-resolved unsteady full-annulus calculations, which results in a notably different value for this quantity in this specific case.

The sixth column, N_{cores}, indicates the number of cores employed for each simulation. This number scales approximately with the mesh size, assuming a roughly constant number of mesh cells allocated per core to optimise the load balancing and the communication time between cores. A notable difference is observed for the blade-resolved unsteady full-annulus calculations, which required twice the number of cores reported in the table (i.e., 3584×2) to prevent processor memory overload, thereby increasing the memory allocation without directly affecting the total CPU time. This extra allocation is not reflected in the total CPU time reported in the table, but should be noted, as the effective CPU time would be roughly twice as large if the full number of cores were considered or if an equivalent normalised CPU time were used.

The following column, N_{jobs}, denotes the number of simulation jobs required to reach convergence. As regards the unsteady calculations, a specific number of jobs correspond to one full revolution of the compressor: four jobs represent one revolution for the $2\pi/4$ blade-resolved case, while eight jobs correspond to one revolution for the 2π full-annulus case. The table thus shows that four revolutions were needed to reach convergence for teh full-annulus case, and three revolutions for the $2\pi/4$ case.

Finally, the last column reports the total CPU time to reach convergence, calculated as the product of the first three columns: the normalised CPU time per core per job, presented in the first column as $([T_{CPU}/(N_{cores}N_{jobs})]_{\text{norm}})$, the number of cores ($N_{cores}$), and the number of jobs (N_{jobs}). This provides a practical measure of the total computational effort required for each configuration.

Computational Cost Assessment The blade-resolved SBP case, with a relatively small mesh and domain, serves as the baseline with a normalised $T_{CPU}/(N_{cores}N_{jobs}) = 1$, using 72 cores and requiring only one job, resulting in a total CPU time of approximately 72 units. Scaling up to the $2\pi/4$ blade-resolved configuration, the normalised CPU time per core increases to 1.68, the number of cores rises significantly to 1632, and 12 jobs are needed for convergence.

This yields a total CPU time of approximately 3.29×10^4, illustrating the substantial increase in computational cost due to the larger domain and finer mesh. The full-annulus (2π) blade-resolved simulation presents the highest computational demand, with a normalised CPU time of 2.74 per core per job, utilisation of 3584 cores, and 32 jobs required for convergence. The total CPU time amounts to approximately 3.14×10^5 core-hours, highlighting the immense resources needed for fully resolved, full-annulus unsteady simulations.

In contrast, the Body-Force model offers significantly lower computational costs. The 2° sector simulation, using only 2 cores and a single job, achieves a normalised CPU time of 0.31, leading to a total CPU time of approximately 0.62 units. This corresponds to a reduction of approximately two orders of magnitude compared to the SBP blade-resolved case and more than four orders of magnitude with respect to the quasi-periodic sector case, demonstrating the efficiency of the reduced-order approach for sector simulations. The full-annulus Body-Force simulation, while employing more cores (248) to handle the larger domain, still requires only a single job and has a normalised CPU time of 2.51, resulting in a total CPU time of approximately 622 units. Although higher than the 2°-sector Body-Force case, it remains roughly 500 times lower than the corresponding blade-resolved full-annulus simulation, or about 1000 times lower if the additional cores used to avoid memory overload in the blade-resolved calculations are taken into account.

Finally, it should be noted that the more complex blade-resolved configurations are initialized using the converged flow fields of simpler, previously solved cases. Consequently, the actual cumulative computational cost is substantially higher than the values reported in Table 6.4, meaning that the computational savings offered by the Body-Force simulations are even more pronounced.

Table 6.4: Computational cost at convergence for each case, normalised by $T_{CPU}/(N_{cores}N_{jobs})$ of the blade-resolved SBP case.

Method	**Approach**	**Sector**	**Domain**	$\left.\frac{\mathbf{T_{CPU}}}{\mathbf{N_{cores}N_{jobs}}}\right\|_{\text{norm}}$	$\mathbf{N_{cores}}$	$\mathbf{N_{jobs}}$	$\left.\mathbf{T_{CPU}}\right\|_{\text{norm}}$
Blade-resolved	Steady	SBP	3D	1	72	1	7.20×10^1
	Unsteady	$2\pi/4$	3D	1.68	1632	12	3.29×10^4
	Unsteady	2π	3D	2.74	3584	32	3.14×10^5
Body-Force	Steady	2°	3D	0.31	2	1	6.2×10^{-1}
	Steady	2π	3D	2.51	248	1	6.22×10^2

Concluding Remarks on Computational Efficiency Overall, the Body-Force approach delivers remarkable predictive capabilities, capturing the essential flow physics of the IHPC compressor across various inflow and operating conditions, while enabling full-annulus simulations at a fraction of the computational cost compared to fully blade-resolved methods. This substantial reduction in resource requirements opens the door to extensive parametric studies and detailed investigations of unsteady phenomena that would be otherwise computationally prohibitive with traditional high-fidelity simulations in the design workflow. Consequently, the Body-Force model represents a powerful and efficient tool for compressor analysis, balancing accuracy and computational feasibility.

Conclusion

This chapter presented a comprehensive investigation of the behaviour of a high-speed multistage compressor under circumferential inlet distortion, encompassing fully three-dimensional flow effects and elevated aerodynamic complexity.

The study first validated the modified Body-Force methodology under clean inflow conditions across a range of operating points, from peak efficiency to near-stall. Comparisons with blade-resolved reference data demonstrated that the model accurately reproduces both global performance metrics and local flow characteristics, including pressure and temperature distributions, flow angles, and spanwise entropy profiles. This successful validation confirms the model's ability to capture essential aerodynamic phenomena, such as tip losses, secondary flows, and shock interactions, providing a robust foundation for subsequent analyses under distorted conditions. In particular, the analysis shows that the model remains reliable when applied to off-design operating points, demonstrating its predictive capability beyond the calibration conditions.

The propagation of the imposed circumferential total pressure distortion through the compressor was then examined. The distortion was observed to attenuate gradually while inducing a redistribution of the flow field, affecting both total pressure and temperature, as seen for the CREATE compressor in Chapter 5. The leading boundary of the distorted region emerged as the most critical zone for flow loading and stability considerations. Comparisons with blade-resolved simulations confirmed that the Body-Force model captures the main distortion features, including its azimuthal evolution, intensity decay, and associated flow deviations. Minor discrepancies, primarily linked to local dissipation and mixing effects not explicitly resolved by the model, did not compromise the overall predictive capability.

A detailed stability analysis under distorted inlet conditions identified the near-hub region as the critical zone for stall initiation. The evolution of axial velocity, flow angle, entropy, and stability indicators showed that flow separation and rapid deceleration near the hub act as precursors to instability. The Body-Force predictions align with literature trends, indicating that hub separation dominates the destabilisation, allowing quantitative evaluation of stall margin reduction due to distortion.

Finally, the chapter assessed the computational efficiency of the Body-Force approach. By enabling full-annulus simulations at a fraction of the cost of blade-resolved methods, the model facilitates extensive parametric studies and detailed investigations of unsteady effects that would otherwise be impractical. This combination of accuracy and computational feasibility underscores the model's value as a predictive tool for compressor analysis under both undistorted and distorted inflow conditions.

Overall, the findings of this chapter demonstrate that the modified Body-Force methodology is a robust and efficient approach for capturing the key aerodynamic responses and stability behaviour of a high-speed multistage compressor under off-design conditions and complex three-dimensional inlet distortions. The methodology provides a sound basis for further studies of off-design operation and unsteady phenomena, bridging the gap between high-fidelity simulations and computationally feasible approaches in the design process.

The following chapter, Chapter 7, will explore the applicability of the modified Body-Force model in supporting design decisions. In particular, the model will be tested for varying geometrical features and, where successful, used to assess the effects of these variations on the compressor's robustness to inlet distortion.

CHAPTER 7

IMPACT OF DESIGN PARAMETERS ON THE STABILITY OF THE IHPC COMPRESSOR UNDER INLET DISTORTION

This chapter investigates the use of the Body-Force modelling approach to assess the sensitivity of the IHPC compressor to specific geometric parameters. The study focuses on modifications of solidity and aspect ratio applied to the first rotor row, to isolate its effects and ensure a clear evaluation of the resulting influence on the aerodynamic behaviour of downstream blades. Analyses are conducted under both clean and circumferentially distorted inflow conditions, with particular attention to the hub and shroud regions. Furthermore, the chapter evaluates the applicability and limitations of the Body-Force model for design-influence studies across various flow regimes, operating points, and inflow conditions.

Contents

7.1 Scope and Hypotheses of the Design Study **170**
7.2 Analysis of the Impact of Solidity Variations **171**
7.2.1 Geometrical Modification Specifications 171
7.2.2 Evaluation under Clean Inflow 172
7.3 Analysis of the Impact of Aspect-Ratio Variations **180**
7.3.1 Geometrical Modification Specifications 180
7.3.2 Evaluation under Clean Inflow 180
7.3.3 Evaluation under Circumferential Distortion 185
7.4 Discussion on the Model Capability **190**
Conclusion **193**

7.1 Scope and Hypotheses of the Design Study

The objective of this chapter is to evaluate the capability of the developed model to predict the effects of geometrical variations in the IHPC multi-stage high-pressure compressor. The assessment is first conducted under clean inflow conditions; if the model demonstrates sufficient predictive accuracy, it is subsequently employed to investigate the impact of such design modifications on the compressor's robustness in the presence of inlet distortion.

To this end, the calibration coefficients of the baseline geometry are retained. Although the design variations are expected to affect the optimal values of these coefficients, this assumption is adopted for two main reasons. Firstly, it eliminates the need to recalibrate the model for each geometrical modification. Secondly, it allows for the verification of whether the modified model is able to capture the correct performance trends without recalibration, thereby reducing the overall computational effort.

A further simplification introduced in this study concerns the selection of the reference simulations. The reference data here employed are derived from blade-resolved single-blade-passage calculations. While previous investigations have shown that the absolute values obtained from such simulations are not entirely accurate due to shock reflections at the mixing plane, it is assumed here that the relative performance trends remain representative of the real physical behaviour. Moreover, performing unsteady calculations of the quasi-periodic sector and the full-annulus of the machine on multiple operating points for each geometrical parameter would entail a prohibitive computational cost.

In this work, geometric changes are limited to the first rotor row. Simulating the entire compressor ensures realistic flow conditions, while restricting the modifications to one row provides a controlled framework in which the influence of individual design variations can be clearly assessed.

This choice is also supported by two key factors. Firstly, the first stage typically has the largest stability margin, allowing for geometric changes without significantly affecting overall compressor stability. Secondly, as the aim of this study is to assess the compressor's robustness to inlet distortion, modifying the first rotor is an effective way to analyse how distortion propagates through the entire compressor. In contrast, altering downstream stages would

have a more limited effect on distortion transmission and could introduce undesirable instabilities in regions less robust to inlet distortion.

The geometrical investigation is divided into two parts. The first examines the effect of varying the solidity, while the second analyses the impact of modifying the aspect ratio, via a chord length modification. These parameters were chosen due to their significant influence on design, as discussed in Section 1.2.3. The methodology and results are presented in the following sections.

7.2 Analysis of the Impact of Solidity Variations

7.2.1 Geometrical Modification Specifications

This section examines a variation in solidity, defined as the blade chord-to-pitch ratio, by approximately 30%. The modification is achieved by keeping the chord length fixed while reducing the number of blades on the rotor from 28 to 22, with the blade geometry remaining unchanged. The original and modified geometry of the first rotor row are shown in Figure 7.1, where the base geometry is depicted in blue and the modified geometry in white.

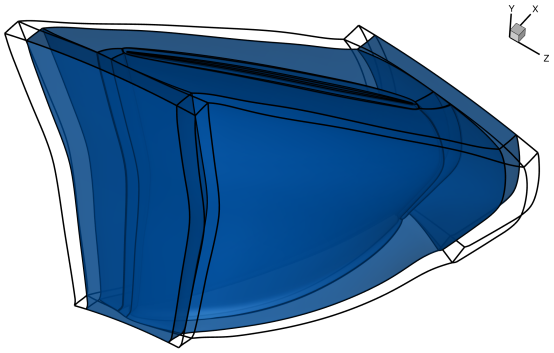

Figure 7.1: Solidity modification of the first rotor row: base geometry in blue, and modified geometry in white.

The reduction in solidity, the effects of which are discussed in Section 1.2.3, is often considered in the early stages of the design process. This is primarily because decreasing the number of blades reduces the compressor's mass, lowers production costs, simplifies integration, and can enhance performance. Low solidity is generally advantageous for performance, as high solidity can degrade it due to blade interactions. However, reducing solidity can also have detrimental effects, such as a reduction in stall margin due to increased blade loading, and an increase in flow deviation caused by more widely spaced blades, which result in less controlled flow and can promote flow separation. These issues are particularly significant in the presence of inlet distortion, which further exacerbates the reduction in stall margin.

To assess the impact of this variation, the effect of the reduced solidity is first analysed under clean inflow conditions. This allows for the evaluation of the Body-Force model's accuracy in the presence of design changes before considering more complex flow conditions.

7.2.2 Evaluation under Clean Inflow

Full IHPC Compressor Configuration at Design Speed As previously outlined, the first step in the analysis is to verify the predictions of the Body-Force approach against the reference data. Figure 7.2 presents the overall performance of the IHPC compressor, as characterised by the total-to-total pressure ratio, total-to-static pressure ratio, total-to-total temperature ratio, and isentropic efficiency. Both blade-resolved (BR) and Body-Force (BF) results are shown for the base geometry ($N_{R1} = 28$) and the modified geometry ($N_{R1} = 22$). It should be noted that the reference data are not precise in absolute terms, due to the choice outlined above, and only the relative differences between the curves for each approach are considered in the analysis.

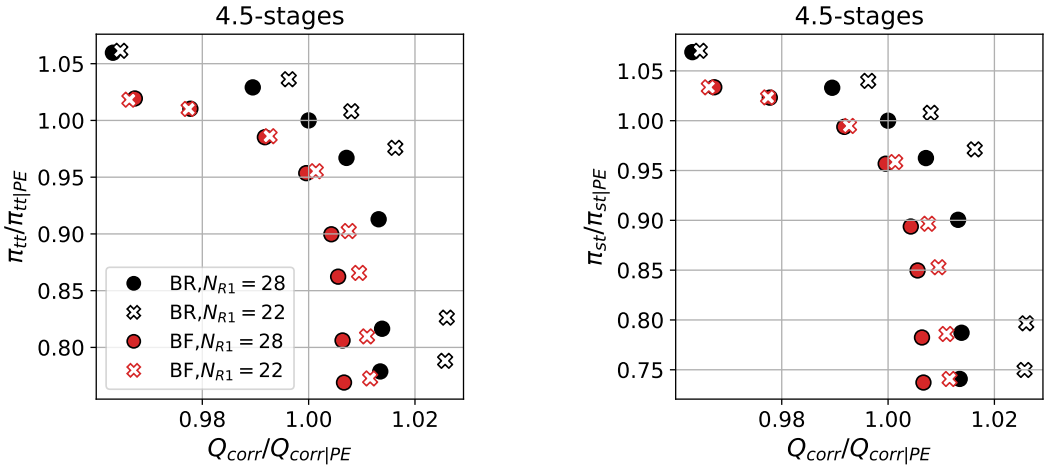

(a) Total-to-total pressure ratio.

(b) Total-to-static pressure ratio.

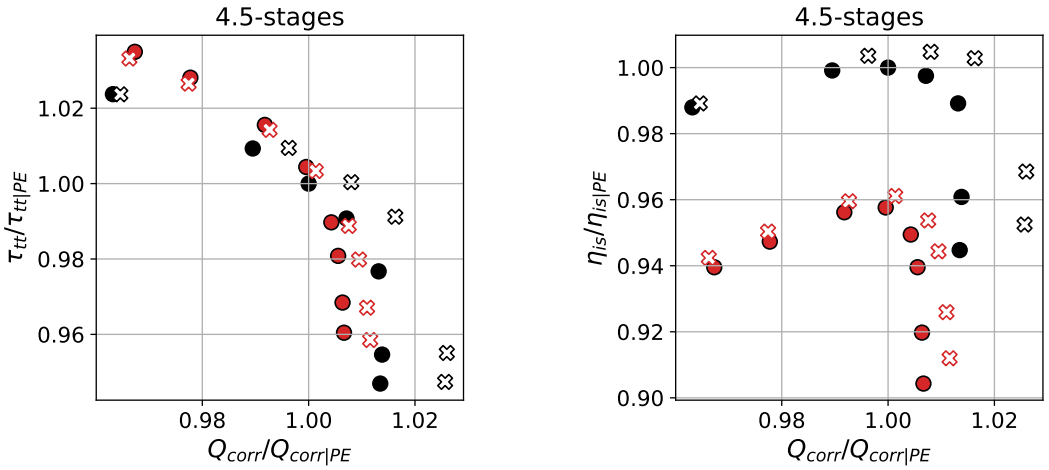

(c) Total-to-total temperature ratio.

(d) Isentropic efficiency.

Figure 7.2: Comparison of the 4.5-stage compressor performance for the solidity variation via the blade-resolved and Body-Force approaches.

The Body-Force approach demonstrates good agreement with the blade-resolved data, with both models indicating an increase in choke mass flow rate. For all operating points,

both approaches show an increase in pressure and temperature ratios at iso-mass flow rate, with the difference between the two geometries diminishing as the stall limit is approached. Despite the overall agreement, several discrepancies are observed. Notably, the Body-Force model predicts an increase in choke mass flow rate that is approximately half the value obtained from the blade-resolved simulations. Furthermore, the performance of the first rotor row, where the geometric modification was applied, is not accurately captured by the Body-Force model. To visualise this, Figure 7.3 presents the same performance metrics as before, but for the first rotor row.

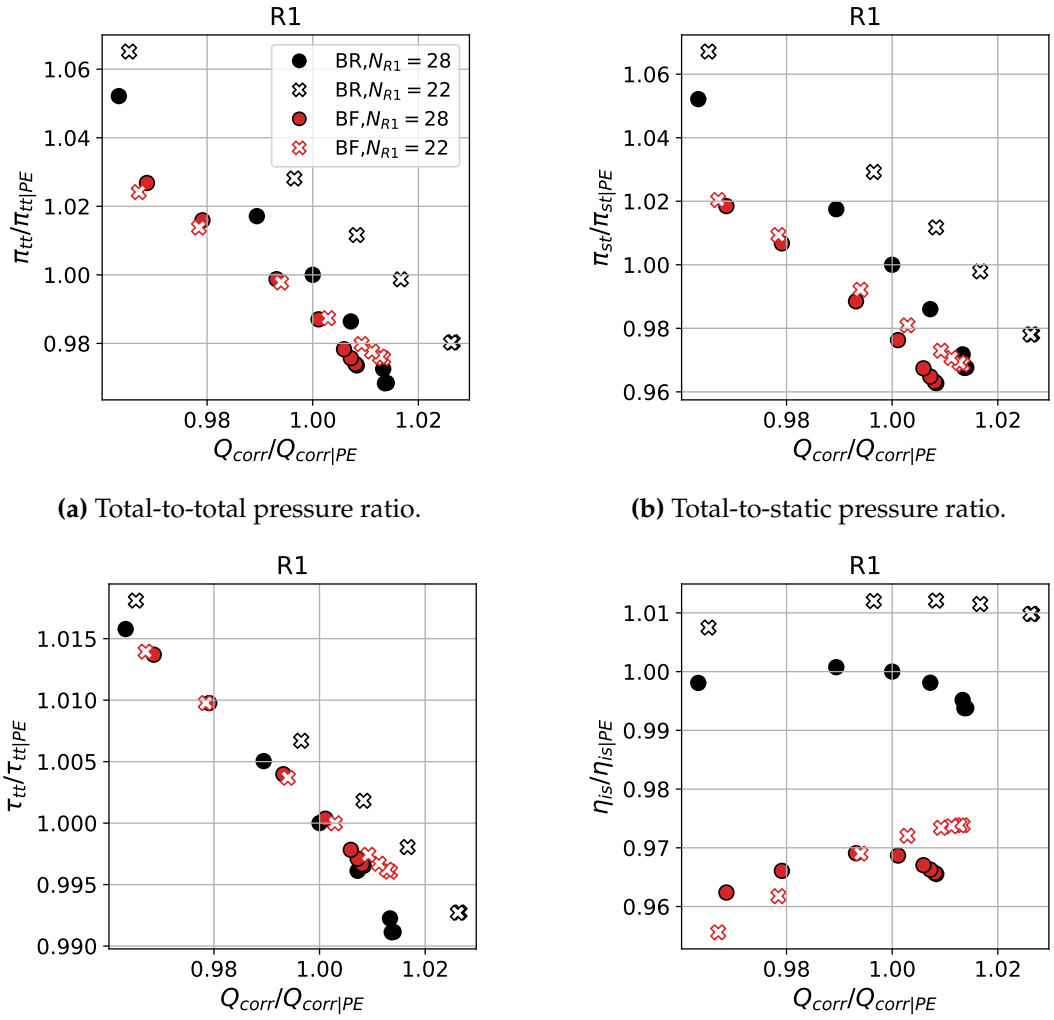

(a) Total-to-total pressure ratio.

(b) Total-to-static pressure ratio.

(c) Total-to-total temperature ratio.

(d) Isentropic efficiency.

Figure 7.3: Comparison of the first rotor row performance for the solidity variation via the blade-resolved and Body-Force approaches.

As shown in the figure, the blade-resolved simulations predict a nearly constant performance offset between the base and modified geometries. In contrast, the Body-Force model fails to reproduce this trend, showing a convergence of the two characteristics towards lower mass flow rates. This suggests that the overall agreement in performance is likely the result of error compensation, rather than a precise representation of the effect of the solidity mod-

ification on the first rotor. Furthermore, the same test case was evaluated using the original Hall-Thollet model to assess whether the discrepancies could be attributed to the model developments introduced in this study. However, it was found that both the original and modified models predicted identical trends, indicating that the discrepancies arise from some other underlying factor.

Full CREATE Compressor Configuration at Design Speed A first step is to determine whether the inability to accurately capture the effect of solidity arises from the modelling approach itself or from the investigated geometry. To this end, a similar analysis was conducted on the CREATE compressor, where the number of blades in the first rotor row was reduced from 64 to 48, matching the percentage reduction in blade number applied to the IHPC compressor.

Figure 7.4 shows the total-to-total pressure ratio and isentropic efficiency for the first rotor row of the CREATE compressor, based on calculations for the full three-stage configuration. This analysis directly evaluates the model's ability to capture local variations at the rotor, as was done for the IHPC compressor, where issues were identified.

The trends observed show good agreement between the two modelling approaches across varying solidity. Specifically, for both the Body-Force (BF) and blade-resolved (BR) models, the total-to-total pressure ratio (π_{tt}) characteristics are similar at choke but diverge as the operating conditions approach stall. Similarly, the isentropic efficiency curves follow a comparable trend for both approaches, with the curves crossing near the peak efficiency point of the base geometry ($Q_{corr}/Q_{corr|PE} = 1$). The $N_{R1} = 48$ case thus exhibits higher efficiency at high mass flow rates and lower efficiency at low mass flow rates, with respect to the baseline geometry. These observations suggest that the Body-Force model provides accurate predictions of the CREATE compressor's performance across varying solidity.

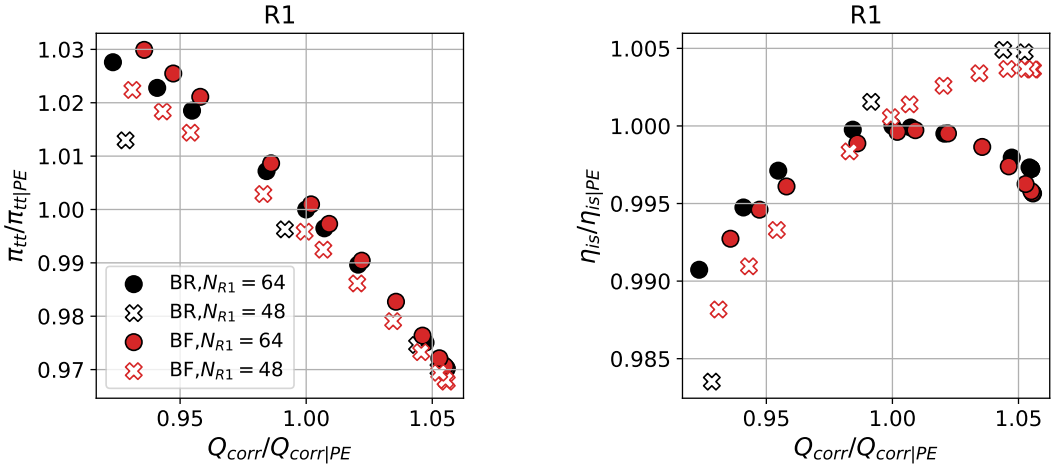

(a) Total-to-total pressure ratio.

(b) Isentropic efficiency.

Figure 7.4: Comparison of the 3-stage CREATE compressor performance for the solidity variation via the blade-resolved and Body-Force approaches.

These observations suggest that the difficulties in predicting performance trends due to changes in the solidity of a rotor row are not inherent to the modelling approach. Instead, they are likely linked to differences between the two compressors investigated. In particular,

it is hypothesised that the discrepancies may be related to the differing flow regimes of the CREATE and IHPC compressors, which are the primary distinction between the two cases.

IHPC Isolated First Rotor Configuration at Part Speed To investigate the hypothesis outlined above, the first rotor row of the IHPC compressor is simulated at 80% part-speed conditions. This enables the examination of the IHPC compressor in a high-subsonic flow regime, in contrast to the fully transonic conditions at design-speed, and matches the flow regime of the CREATE compressor, thereby providing a reliable confirmation of the hypothesis. Furthermore, by simulating only a single rotor row, computational costs are reduced, and the need for blade pitch adjustments in the IGV and first stator rows is avoided.

Figure 7.5 illustrates the operating regime of the first rotor row for the various investigated configurations, expressed in terms of relative Mach number at 95% of the channel height, within the region of higher peripheral speed where pronounced shock phenomena occur. The black contour line marks the condition corresponding to $M_{\text{rel}} = 1$.

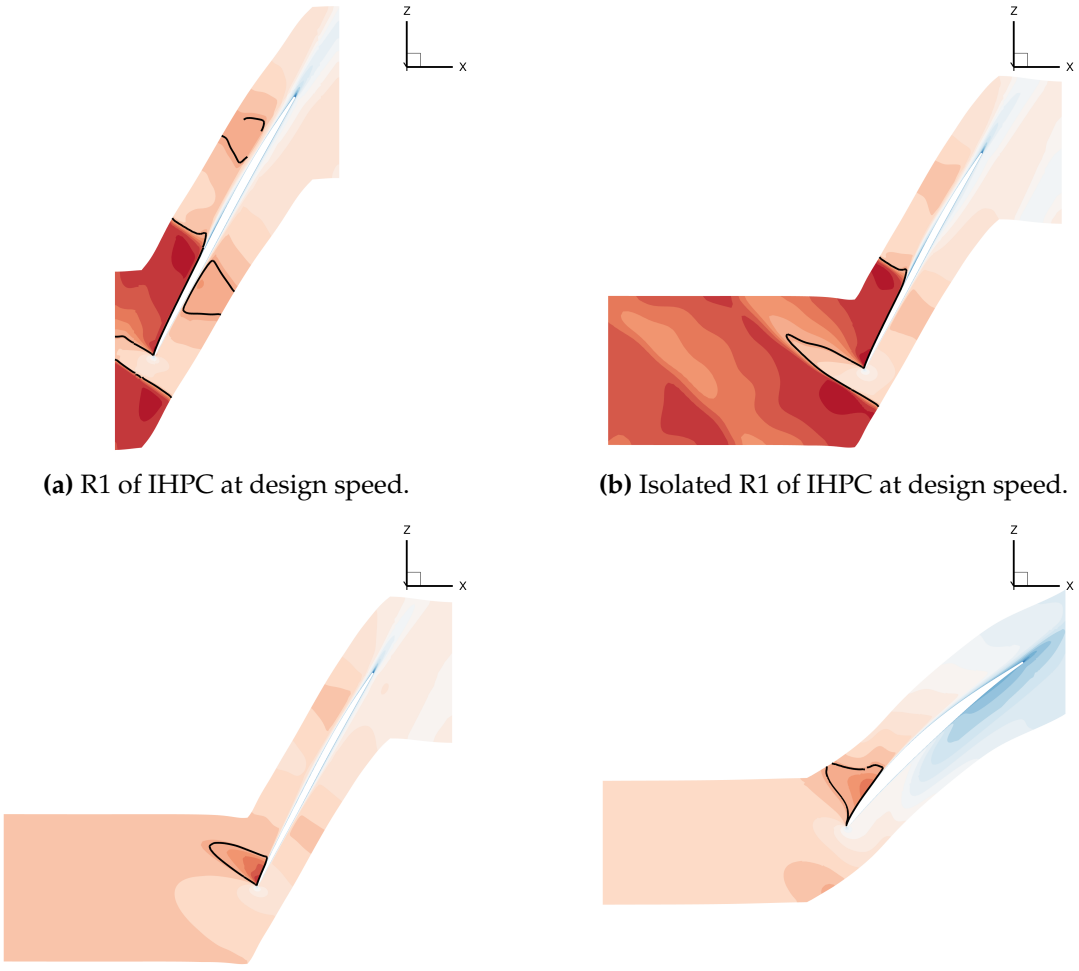

(a) R1 of IHPC at design speed.

(b) Isolated R1 of IHPC at design speed.

(c) Isolated R1 of IHPC at 80% speed.

(d) R1 of CREATE at design speed.

Figure 7.5: Comparison of the relative Mach number fields for the IHPC and CREATE first rotor rows at peak-efficiency conditions, at 95% h/H. Iso-$M_{rel} = 1$ contour line in black.

Figure 7.5a shows the first rotor row of the IHPC 4.5-stage configuration at design speed, exhibiting clear transonic behaviour characterised by a normal shock at the rotor leading edge. Figure 7.5b presents the isolated rotor row at design speed, confirming that its numerical behaviour is consistent with that observed for the same rotor within the full configuration. In contrast, Figure 7.5c displays the behaviour of the isolated rotor row at part-speed conditions, while Figure 7.5d shows the flow field for the CREATE first rotor, extracted from the full configuration at design speed. These two latter cases confirm that the IHPC rotor at part-speed exhibits a similar flow regime and shock topology to that of the CREATE configuration, with a small supersonic bubble near the leading edge on the suction side, rather than a strong detached shock traversing the blade passage.

It can now be verified whether, under the same flow regime as the CREATE compressor, the Body-Force model can accurately predict the performance of the isolated first rotor of the IHPC at varying solidity. Figure 7.6 presents the performance metrics of the rotor row at 80% part-speed. It presents the total-to-total pressure ratio, the total-to-static pressure ratio, the total-to-total temperature ratio and the isentropic efficiency of the isolated first rotor row, simulated at part-speed conditions (80% of ω), for both the base geometry ($N_{R1} = 28$) and the modified geometry ($N_{R1} = 22$).

Results are presented for both modeling approaches: blade-resolved (BR) and Body-Force (BF). As explained, the discrepancies observed between the two approaches for the base geometry stem solely from using the single-blade-passage dataset as reference, which was affected by errors caused by shock reflection at the mixing planes. To address this, the plot has been rescaled as follows: the corrected mass flow rate is normalized by the respective choke value for each modeling approach, and the performance parameter is normalized by the value at choke from the blade-resolved dataset. This rescaling ensures that the comparison reflects only the relative effects of solidity modifications, rather than inherent differences between the Body-Force and single-blade-passage simulations.

As a general observation, a very good agreement between the blade-resolved and Body-Force data is visible across varying solidity at reduced shaft speed. This observation confirms two key points: first, the Body-Force model is capable of predicting compressor performance at part-speed without recalibration, even under significant shaft deceleration (here, 80% of ω); second, it reliably captures the effects of solidity modifications at the rotor row level in a low-transonic regime.

Examining the results in more detail, for both approaches, the choke mass flow rate increases as the number of blades is reduced. The magnitude of this variation, of around 4%, is accurately captured by the Body-Force approach, unlike the case of the 4.5-stage configuration at design speed. Furthermore, the trends of all four performance metrics are well reproduced, with performance increasing across all operating points for the lower blade count. This increase gradually diminishes from the choke point towards the stall limit.

It is also evident that the operating points in the middle of the characteristic, which correspond to the viable operating points of the full 4.5-stage configuration, are minimally affected by the solidity modification. This limited effect may be difficult to capture in the complete multi-stage configuration, offering an additional explanation for the challenge in predicting the impact of solidity changes on the full compressor.

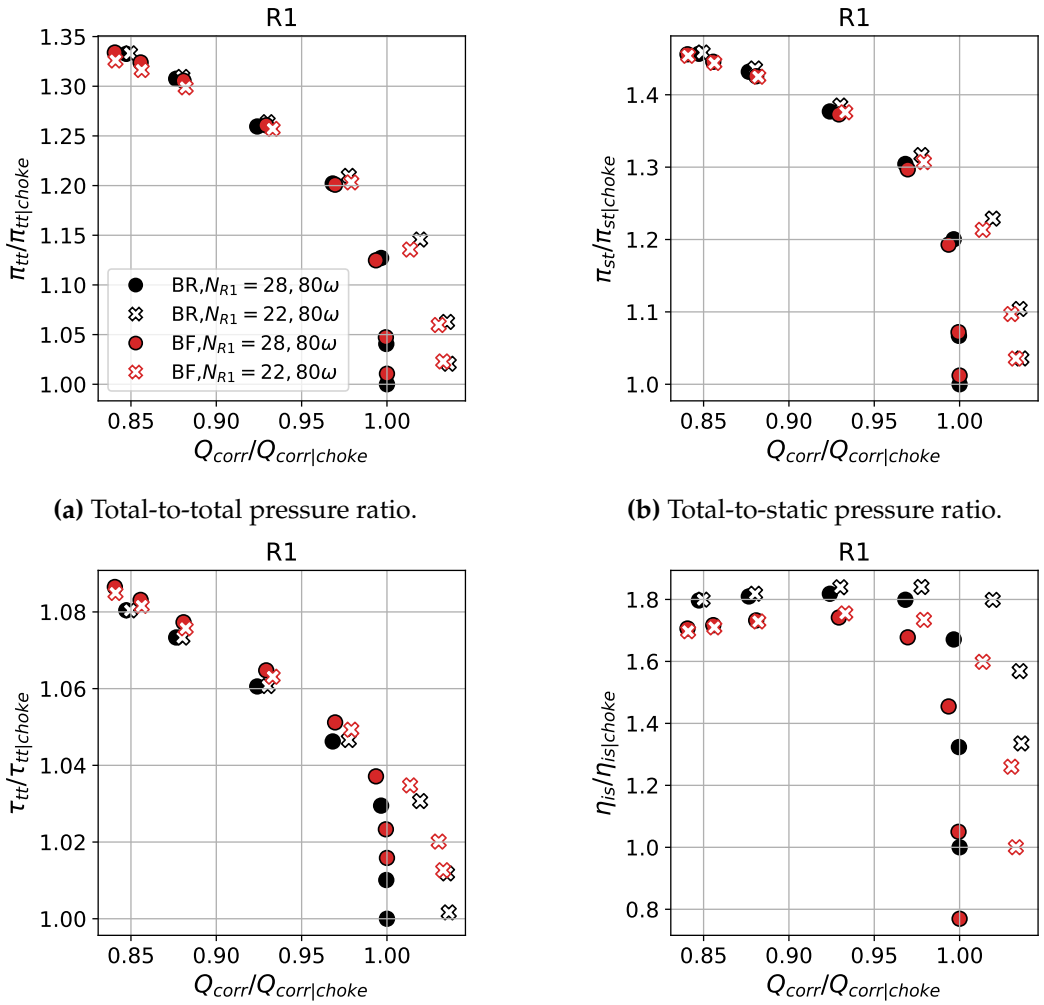

(a) Total-to-total pressure ratio.

(b) Total-to-static pressure ratio.

(c) Total-to-total temperature ratio.

(d) Isentropic efficiency.

Figure 7.6: Comparison of the isolated first rotor row performance at 80% speed for the solidity variation via the blade-resolved and Body-Force approaches. Plots rescaled to address errors in the reference dataset prediction.

Full IHPC Compressor Configuration at Part Speed Given the positive results obtained with the isolated rotor row at part-speed, the full configuration was subsequently tested at part-speed as well. Initially, a shaft speed of 80% ω, corresponding to the conditions of the isolated first row analysis at part-speed, was considered, with the corresponding adjustments to the IGV and first stator pitch. However, challenging aerodynamic conditions arose, notably a very strong and extensive recirculation over the second half of the first stator span. This prompted the search for a more stable operating regime at higher shaft speed, while avoiding the formation of a strong normal shock at the first rotor row, to remain in the high-subsonic regime. Ultimately, a shaft speed of 90% ω was selected, as it provided a less critical regime. As anticipated, a modification of the IGV and first stator pitch was required, and the mesh characteristics were maintained as close as possible to those of the base configuration, while accommodating the more pronounced stagger angles of the part-speed configuration. Despite

this case being less critical, significant flow separation persisted on both the IGV and first stator blades, accompanied by several supersonic regions in the downstream rotor rows, caused by the blockage induced by these separations.

An insight on the extensive flow separation occurring on the IGV row at 90% part speed is provided in Figure 7.7. A separation zone, extending over the entire blade span, is clearly visible at the leading edge on both the suction side and the pressure side. This phenomenon is attributed to the complex aerodynamic conditions associated with the part-speed regime, coupled with the inability to fully adapt the blade pitch to the flow incidence angle, due to mechanical constraints of the machine.

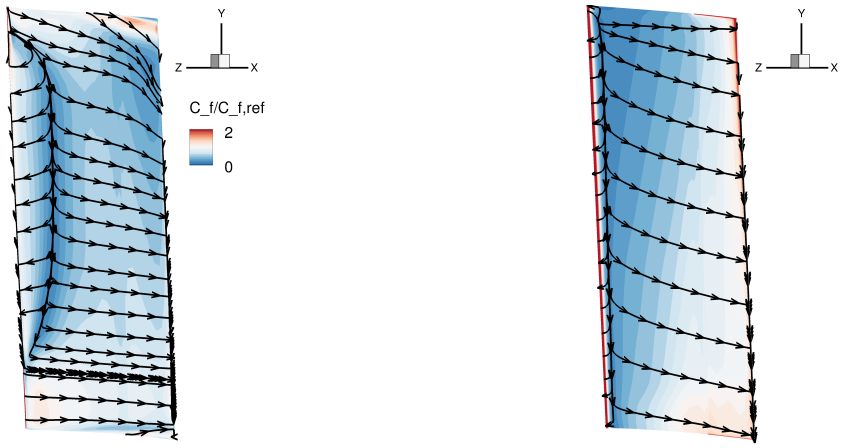

(a) Suction side. **(b)** Pressure side.

Figure 7.7: Skin friction lines and contour on the IGV blade at 90% part speed at PE.

The results for the complete configuration, obtained with both modelling approaches at 90% and 100% ω, are presented in Figure 7.8 for the full configuration and in Figure 7.9 for the first rotor row. The reported data correspond to the total-to-total pressure ratio and the isentropic efficiency, for the base geometry ($N_{R1} = 28$) and for both modelling approaches: blade-resolved (BR) and Body-Force (BF).

It is evident from these figures that the model does not accurately predict the performance of the compressor, either globally or on a row-by-row basis, for the full configuration at part-speed. The isentropic efficiency in both plots deviates by more than 10%, while the total-to-total pressure ratio differs by approximately 15%. Several factors may explain these discrepancies. The full part-speed configuration requires substantial pitch adjustments at the IGV and first stator, altering the geometry and aerodynamic response of these blades, which are implicitly represented through the calibration coefficients and the formulation of the model. In this part-speed configuration, the effects of the altered flow regime and the geometric pitch variation are intertwined, making it difficult to isolate the primary cause of the discrepancies. In addition, the same rows experience significant flow separation, placing the blades outside the operating envelope assumed by the model. Finally, variations in the aerodynamic response of these blades propagate downstream, inducing inter-stage mismatches that further affect overall compressor behaviour.

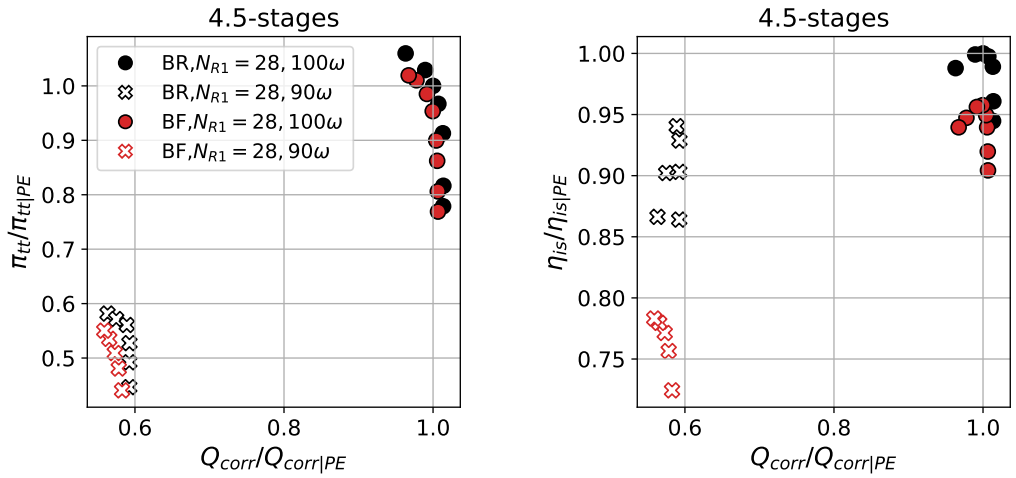

(a) Total-to-total pressure ratio. **(b)** Isentropic efficiency.

Figure 7.8: Comparison of the 4.5-stage compressor performance at 90% speed for the solidity variation via the blade-resolved and Body-Force approaches.

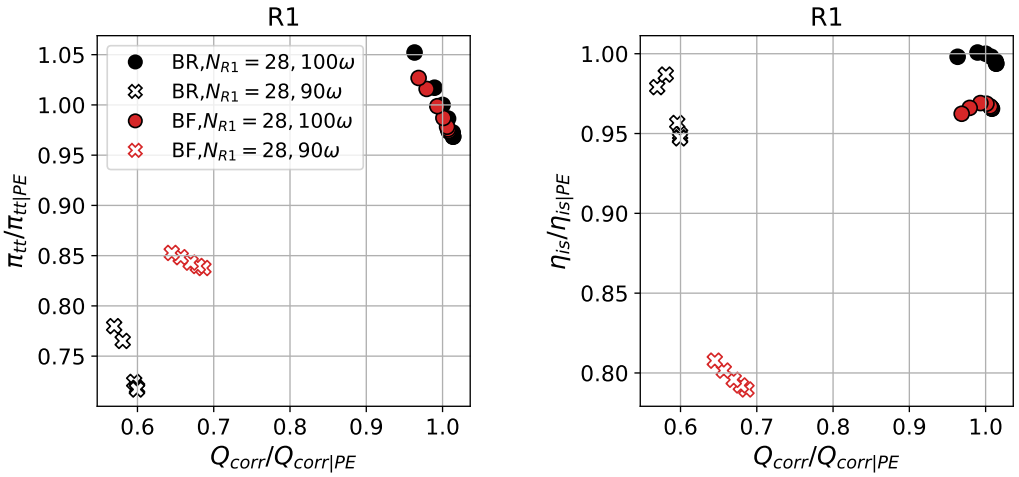

(a) Total-to-total pressure ratio. **(b)** Isentropic efficiency.

Figure 7.9: Comparison of the first rotor row performance at 90% speed for the solidity variation via the blade-resolved and Body-Force approaches.

Concluding Remarks on Model Capabilities for Solidity Variation In conclusion, the analysis of the Body-Force model's capability to reproduce the effects of solidity variation under clean inflow conditions has led to several key observations. The model does not accurately capture the influence of solidity changes when the flow field is dominated by strong detached shocks or pronounced flow separations, as these phenomena substantially alter the local aerodynamics beyond the assumptions embedded in the model formulation. However, when operating in subsonic to low-transonic regimes, the Body-Force model successfully reproduces the geometric effects with a high degree of fidelity.

In particular, the effects of solidity modification were accurately captured, without the need for recalibration, for the low-transonic CREATE configuration, as well as for the iso-

lated first rotor row of the IHPC compressor operating at part speed, which also exhibits low-transonic behaviour. These results validate the model's capability to not only predict geometric effects across a range of flow regimes, but also to maintain predictive accuracy across varying shaft speeds. This constitutes a significant finding, as it extends the demonstrated applicability of the Body-Force approach beyond its previous validation domain, which was previously restricted to the design-speed condition.

Nevertheless, since the solidity effect is not accurately captured in the full IHPC configuration, further investigations into its influence on distortion propagation and attenuation would not yield reliable results and are therefore avoided. Despite this limitation, the present study has clearly delineated the operating regimes in which the Body-Force approach can be applied with confidence, while also identifying the conditions that challenge its underlying assumptions. More details on this are given in Section 7.4.

7.3 Analysis of the Impact of Aspect-Ratio Variations

7.3.1 Geometrical Modification Specifications

The aspect-ratio (AR) variation analysed in this section consists of increasing the height-to-chord ratio of the first rotor blade while keeping the blade height, the thickness-to-chord ratio, and the pitch-to-chord ratio fixed. The aspect ratio, defined as $AR = B/c$, is therefore increased by reducing the blade chord by approximately 25%. To maintain the specified non-dimensional ratios, the chord reduction is accompanied by an increase in the number of blades from 28 to 36, as well as a proportional reduction in blade thickness matching the chord reduction. Finally, the annulus convergence across the blade is kept unchanged, resulting in a more rapid convergence of the annulus for shorter chord lengths and, consequently, a reduction in the overall axial length of the compressor.

Figure 7.10 compares the base geometry (in grey) with the modified geometry (in blue). In particular, Figures 7.10a and 7.10b provide detailed views of the leading and trailing edges of the first rotor blade, respectively.

The influence of aspect-ratio variations on compressor behaviour has been discussed in Section 1.2.3. Increasing the blade aspect ratio, achieved here by reducing the chord for a given height, allows a reduction in engine mass and overall axial length, thereby facilitating engine integration. Aerodynamically, it typically results in lower profile losses due to the reduced chord and thickness, and diminishes the relative significance of secondary flows owing to the comparatively higher blade span. However, higher aspect-ratio blades are also more susceptible to mechanical failure, flutter, and erosion because of their reduced thickness, and may induce local aerodynamic instabilities. These sensitivities can become particularly important under off-design conditions or in the presence of inlet distortion, where the reduced robustness of high-aspect-ratio blades may negatively impact compressor operability.

The specific response of the IHPC compressor to this aspect-ratio modification is investigated in the following sections, starting with an assessment under clean inflow conditions.

7.3.2 Evaluation under Clean Inflow

A preliminary analysis is carried out to assess the impact of the modified geometry on the compressor under clean operating conditions. Figure 7.11 presents the performance of the full compressor in terms of the total-to-total pressure ratio, total-to-static pressure ratio, total-to-

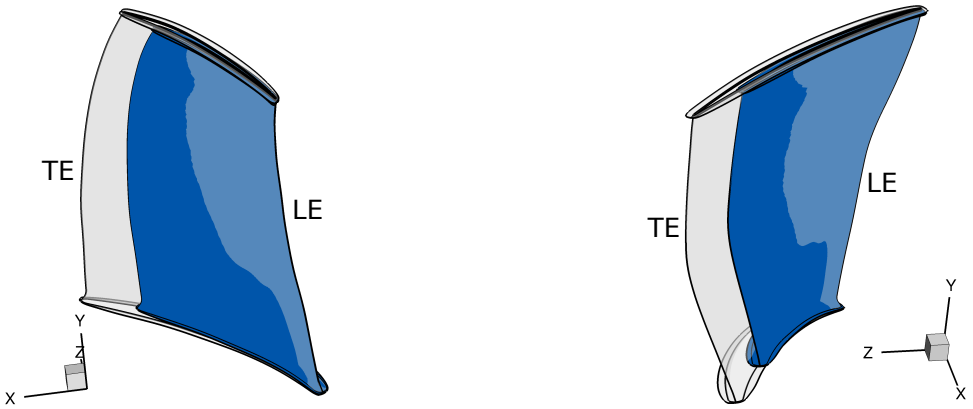

(a) First rotor row leading edge.

(b) First rotor row trailing edge.

Figure 7.10: Aspect-ratio modification of the first rotor row: base (grey) and modified (blue) geometry.

total temperature ratio, and isentropic efficiency. The results are reported for two modelling approaches: the blade-resolved (BR) method, using a single-blade-passage configuration, and the Body-Force (BF) method. In addition, both the baseline geometry (100% c) and the modified geometry (75% c) are considered. It should be noted, as previously explained, that for each modelling approach only the relative positions of the two characteristics at different geometries are compared, since the absolute values of the reference single-blade-passage data are not accurate.

The figure demonstrates a good agreement between the predictions obtained with the two modelling approaches. As discussed in the previous study, the discrepancies observed for the baseline geometry, and the corresponding offset for the modified geometry, arise from the fact that the blade-resolved reference simulations considered here employ the single-blade-passage (SBP) configuration, rather than the more accurate $2\pi/4$ sector case, whose computational cost was prohibitive for the present geometry study. Apart from this offset, the Body-Force (BF) model provides reliable predictions.

The choke mass flow rate is observed to increase slightly with the aspect ratio, with the BF model predicting a 0.44% increase and the SBP simulations a 0.63% increase, indicating good agreement between the two approaches. The first three performance metrics, excluding the isentropic efficiency, exhibit an increase across the entire operating range, with the difference in performance between the two geometries diminishing at lower mass flow rates. Concerning the isentropic efficiency, operating points with $Q_{corr} > Q_{corr|PE}$ display a higher efficiency for the increased aspect ratio, whereas points with $Q_{corr} < Q_{corr|PE}$ show a decrease in efficiency when the aspect ratio is raised. This remains true for both approaches.

In particular, it is important to verify whether, unlike in the solidity study, the predictions for the modified row are consistent with the reference calculations. Figure 7.12 presents the total-to-total and total-to-static pressure ratios of the first rotor row of the compressor, for the same data sets as discussed previously. It can be observed that the trends of both performance metrics are again well reproduced across the entire operating range by the modelling approach, as was the case for the full compressor. This behaviour contrasts with the observations from the solidity study, where the row-by-row performance metrics were not accurately captured, despite an acceptable overall prediction for the complete compressor.

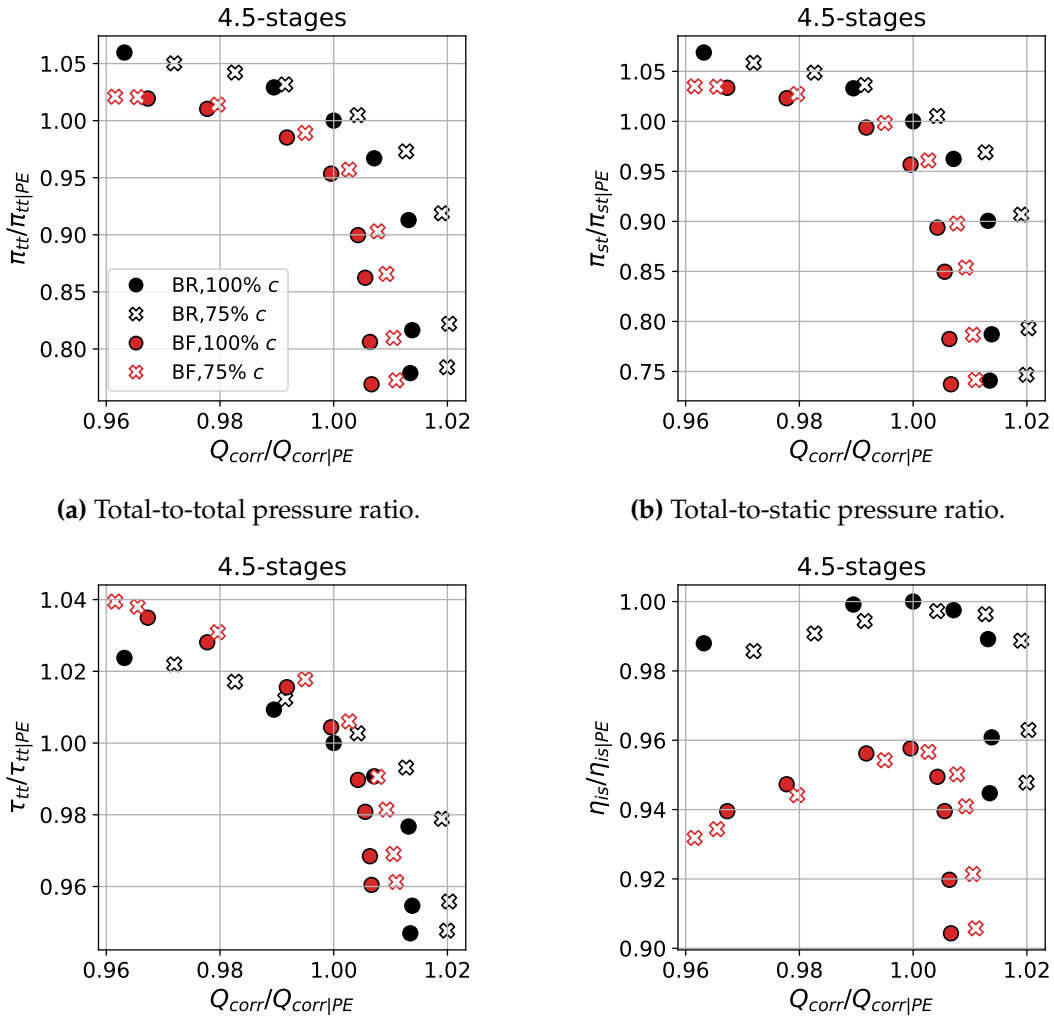

(a) Total-to-total pressure ratio.

(b) Total-to-static pressure ratio.

(c) Total-to-total temperature ratio.

(d) Isentropic efficiency.

Figure 7.11: Comparison of the 4.5-stage compressor performance for the aspect-ratio variation via the blade-resolved and Body-Force approaches.

Despite the valuable insights provided by the integral performance metrics, a deeper understanding of the compressor's behaviour at varying aspect ratios requires investigation of the local flow characteristics. For this purpose, Figures 7.13 and 7.14 present the radial profiles of different flow quantities downstream of the first rotor. The data shown correspond to both modelling approaches, blade-resolved (BR) and Body-Force (BF), for two geometries: the baseline configuration (100% c) and the modified configuration (75% c).

In Figure 7.13, the radial profiles of total pressure, total temperature, entropy, and absolute flow angle downstream of the first rotor are shown from left to right. First, it can be observed that, despite absolute differences between the profiles, both modelling approaches consistently capture the relative changes in these quantities across the blade span when the aspect ratio is varied. Near the hub, for instance at 10% of the blade height (h/H), both total pressure and total temperature values are slightly reduced with the chord modification. This trend is consistent for both modelling approaches. Near the shroud, however, these quantities

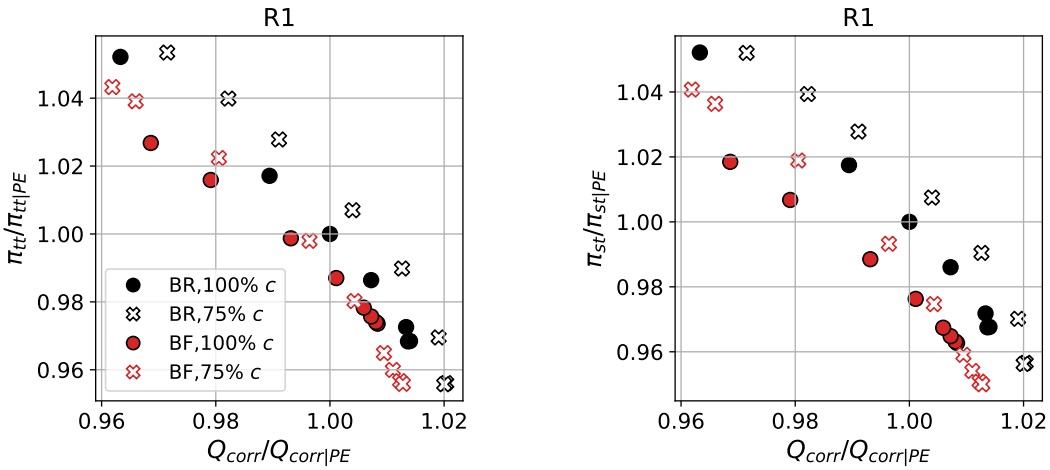

(a) Total-to-total pressure ratio.

(b) Total-to-static pressure ratio.

Figure 7.12: Comparison of the first rotor row performance for the aspect-ratio variation via the blade-resolved and Body-Force approaches.

do not show significant variation, indicating that losses and work are primarily affected near the hub. Additionally, the entropy level remains constant across the entire blade span, suggesting that the geometry modification does not significantly influence viscous losses. Finally, the absolute flow angle is mainly altered near the shroud, where it decreases, indicating improved flow alignment. No significant modification is observed in the remainder of the blade span. For this quantity, the two modelling approaches again yield similar results.

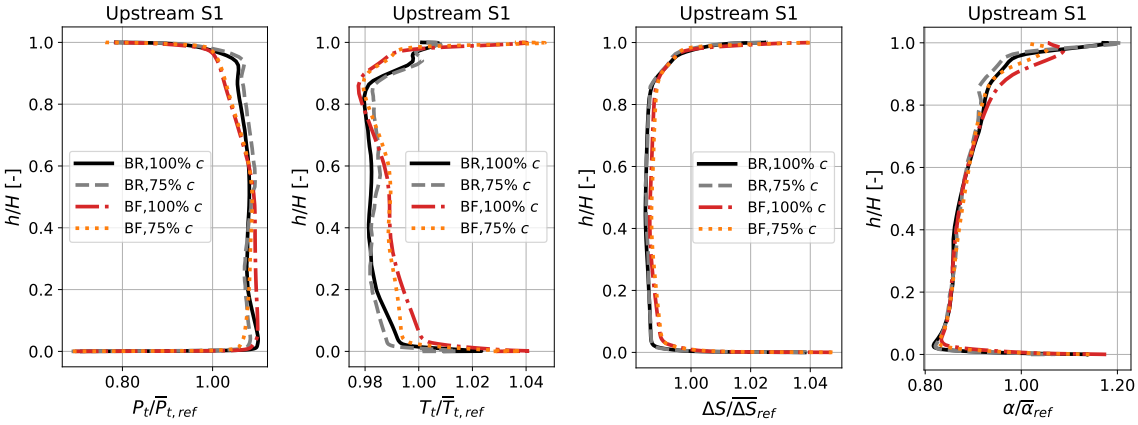

Figure 7.13: Comparison of radial profiles of total pressure, total temperature, entropy and absolute flow angle downstream of the first rotor at the peak efficiency point.

A useful means of evaluating the variation in the stability of the compressor due to the chord modification is to analyse how the velocity triangles change across the blade span. For this purpose, the analysis focuses on two relevant regions: near the hub (at approximately 10% h/H) and near the shroud (at 90% h/H). Figure 7.14 illustrates the variation of all velocity components in cylindrical coordinates, along with the velocity magnitude, downstream of the first rotor.

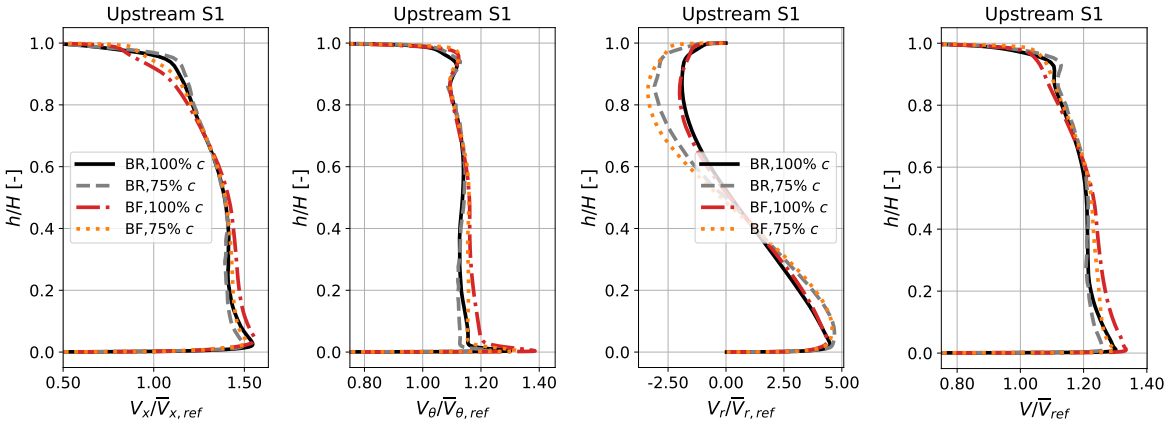

Figure 7.14: Comparison of radial profiles of axial, azimuthal, radial flow velocity and magnitude of flow velocity downstream the first rotor at the peak efficiency point.

Near the hub, the absolute flow angle remains nearly constant, while both the axial and azimuthal velocity components exhibit a slight reduction. These changes are accompanied by a decrease in the magnitude of the absolute velocity. When interpreted through the velocity-triangle relations at fixed blade speed, the observed absolute-flow trends correspond to an increase in the relative flow angle and a reduction in the relative velocity magnitude. According to the definition of the De Haller number adopted in previous chapters, and assuming unchanged upstream conditions, this implies a decrease in the W_2/W_1 ratio. The hub region can therefore be expected to exhibit an increased sensitivity to flow instabilities. Near the shroud, the absolute flow angle decreases, the axial velocity increases, and the azimuthal velocity remains approximately unchanged. For the same blade speed, this combination of absolute velocity components is consistent with a reduction in the relative flow angle and an increase in both the absolute and relative velocity magnitudes. As a result, the modified configuration is associated with a higher W_2/W_1 ratio than the baseline case without chord modification, suggesting a more stable behaviour in the shroud region. The redistribution of the radial velocity component is also captured by the Body-Force model, which indicates a stronger migration of the flow toward the midspan.

To verify whether these trends persist at different operating conditions, the radial distributions of the velocity components and absolute flow angle are also examined at the near-stall operating point (Figure 7.15). The overall behaviour remains qualitatively similar to that observed at the previous operating point, with two notable differences. First, a slight increase in the absolute flow angle is observed near the hub, whereas it remained nearly unchanged at peak efficiency. When interpreted within the velocity-triangle framework, this trend is consistent with a further increase in the relative outlet velocity, which may enhance the susceptibility to instability in the hub region. Second, a small increase in V_θ is observed near the shroud. Since the DLI is particularly sensitive to variations in azimuthal velocity, these changes affect its value near the shroud. While the azimuthal velocity at the shroud remains almost unchanged for the peak-efficiency condition, its increase at near-stall conditions is reflected, within the adopted DLI formulation, by a corresponding reduction in the robustness indicated by the DLI.

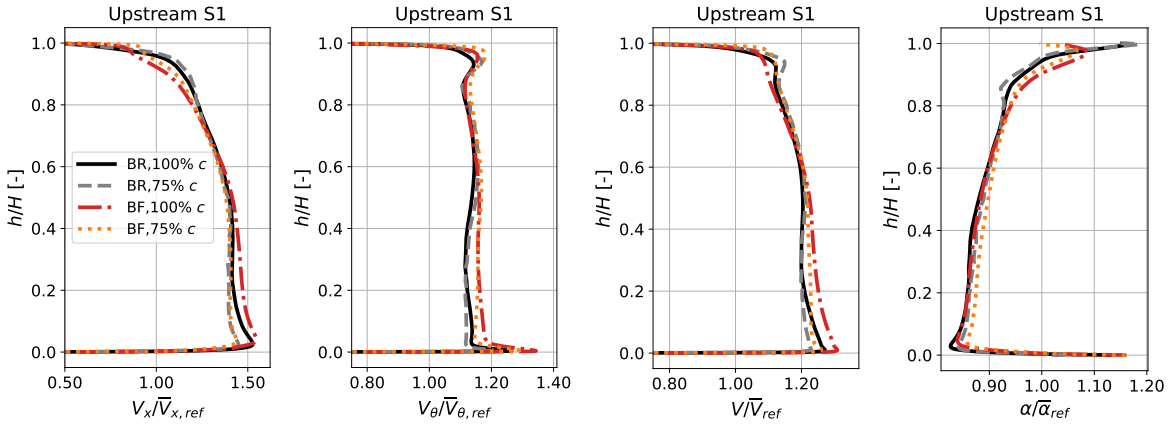

Figure 7.15: Comparison of radial profiles of axial, azimuthal, radial flow velocity and magnitude of flow velocity downstream the first rotor at the near stall point.

Concluding Remarks on Model Capabilities for Aspect-Ratio Variation It can be concluded that the Body-Force model is capable of predicting the effects of aspect-ratio variation both globally, in terms of performance, and locally, in terms of spanwise profiles of various flow quantities, under clean inflow conditions and across different operating points. An important observation is that this geometric effect is correctly captured even if the simulated case is transonic, a limitation highlighted in the previous study. One possible explanation for this difference in reliability is outlined in Section 7.4.

Regarding the impact of this modification on the compressor's behaviour, it is clear that the effect is strongly three-dimensional. It is not possible to directly correlate performance variations with local modifications of flow quantities, as these quantities vary significantly across the blade span. However, some insights can be drawn by examining specific critical regions of the compressor, such as the hub and shroud regions.

The hypotheses regarding the variation in stability of the investigated rotor row will be further analysed and validated in the following section, with consideration of the circumferential distortion discussed in Chapter 6.

7.3.3 Evaluation under Circumferential Distortion

The case presented in the previous section, involving a modification of the aspect ratio of the first rotor row, is here analysed in its full-annulus configuration under -3.5% total pressure circumferential distortion. The distortion characteristics are the same as those investigated in Chapter 6, and the analysis is exclusively performed through the Body-Force approach, as the full-annulus blade-resolved calculations exhibit a prohibitive cost.

To confirm the hypotheses formulated in the previous section, and based solely on the compressor behaviour under clean inflow conditions, the DH and DLI parameters are analysed. Figure 7.16 presents the De Haller number and the Lieblein diffusion factor of the compressor under distortion at the peak-efficiency operating point, for 10% h/H (Figure 7.16a) and 90% h/H (Figure 7.16b). The tresholds for both the DH and DLI parameters are chosen as in Section 6.2.2 of Chapter 6.

The profiles shown in the figure confirm the hypotheses outlined above. In particular, at 10% h/H, the De Haller number slightly decreases due to a reduction in W_2, bringing the

profile closer to the stability limit. On the other hand, the DLI parameter remains almost unchanged, as the decrease in W_2/W_1 is counteracted by a decrease in V_θ. This behaviour indicates that, at the peak-efficiency operating point, the DH parameter predicts that the compressor becomes slightly less stable near the hub when the blade aspect ratio is increased. Conversely, near the shroud, both the DH and DLI parameters indicate a greater stability margin, as anticipated, owing to the increased W_2 and the reduced V_θ. This results in a tip region that is more stable at the peak-efficiency operating point.

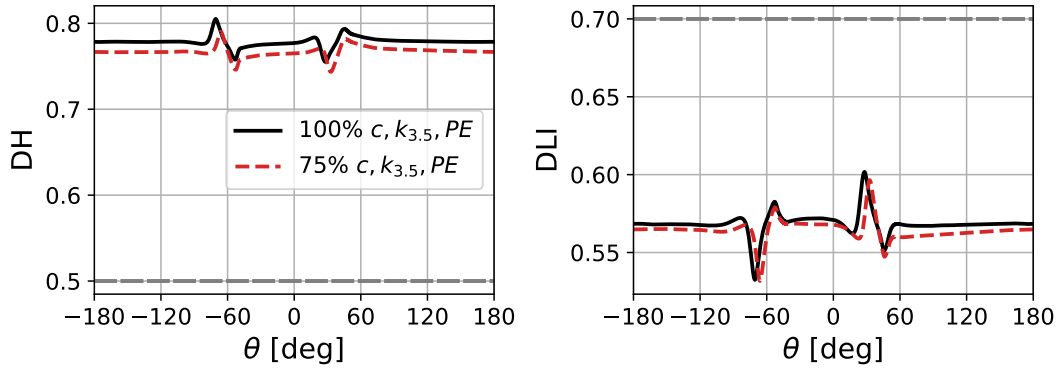

(a) 10% h/H.

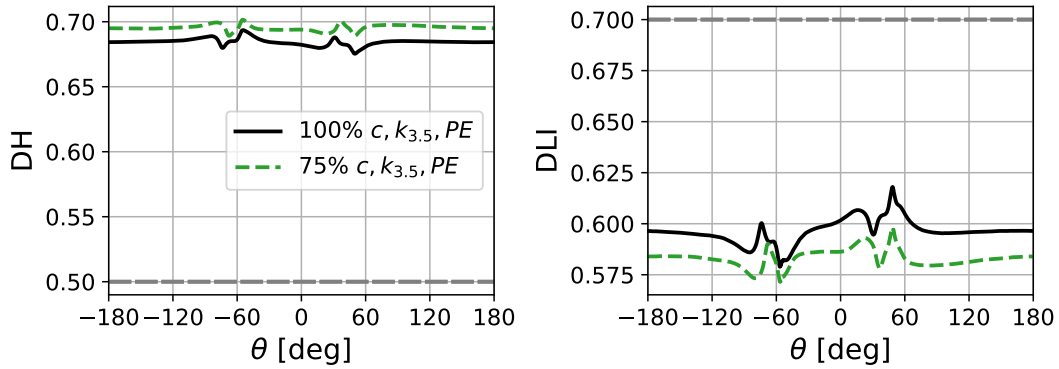

(b) 90% h/H.

Figure 7.16: Azimuthal profiles of DH (left) and DLI (right) of R1 at the peak efficiency point for both the baseline and modified geometries, obtained using the Body-Force approach.

Moving to the near-stall operating point, Figure 7.17 presents the same profiles as before, but for this more critical condition. It can be observed that the behaviour near the hub is consistent with that seen at the peak-efficiency point, with a reduced DH value and, in this case, also an increased DLI value. This is due to the non-negligible variations in azimuthal velocity and flow angle observed near the hub. Both parameters therefore suggest a reduction in stability. Near the shroud, the De Haller number is slightly reduced, while the Liblein diffusion factor is noticeably increased, once again as a consequence of the variation in azimuthal velocity discussed above.

The near-stall analysis highlights the critical impact of increasing the aspect ratio: in both near-wall regions, the flow exhibits a reduced stability compared with the baseline geometry. This behaviour is not optimal, since it has been demonstrated in Chapter 6 that the stall inception mechanism involves the hub region, whose stability is consistently degraded by the

geometrical modification.

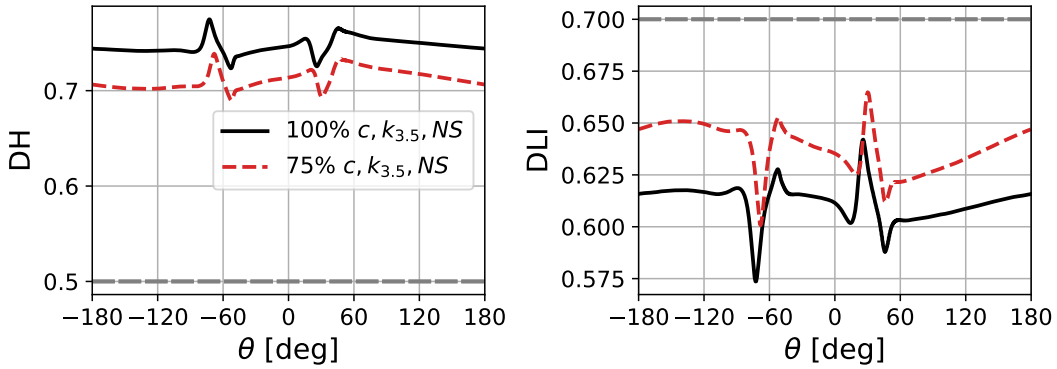

(a) 10% h/H.

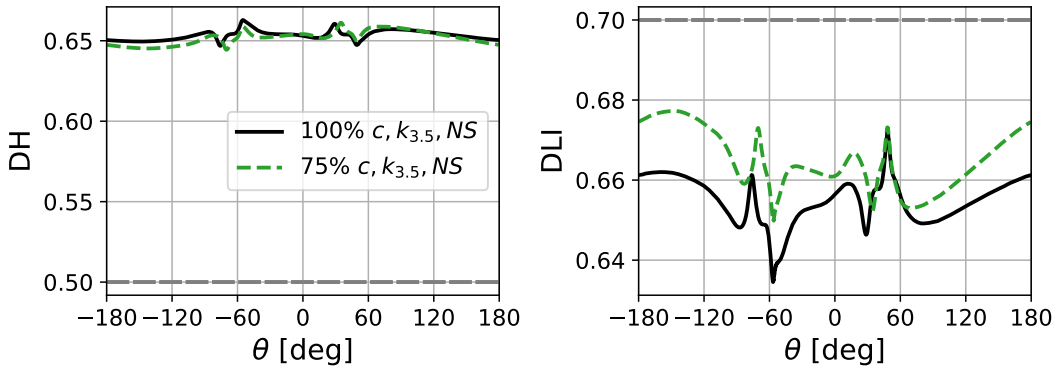

(b) 90% h/H.

Figure 7.17: Azimuthal profiles of DH (left) and DLI (right) of R1 at the stable near stall point for both the baseline and modified geometries, obtained using the Body-Force approach.

As discussed in Chapter 6, the last stator row was identified as the most susceptible to instabilities, at increasing total pressure deficit. Accordingly, the azimuthal profiles of De Haller numer and Liblein diffusion factor at both the peak-efficiency and near-stall operating points are presented in Figure 7.18, for the near-hub and near-shroud regions.

It is interesting to note that the modification of the aspect ratio at the first rotor row has a pronounced influence on the last row of the compressor, suggesting that a targeted geometrical variation of the upstream rows could effectively be used to modify, and potentially delay, the onset of instability.

Near the hub, at 10% h/H, the trend indicates a reduction in stability margins, signalled by both the DH and DLI indices, when increasing the aspect ratio and when approaching the near-stall operating point. In all cases, except for the baseline geometry at peak efficiency, the stability limits near the hub are critically exceeded. Furthermore, the severity of the stability degradation in the distorted region increases as the near-stall condition is approached, and again for the higher aspect-ratio configuration, resulting in extremely critical values of DH and DLI. Near the shroud, the impact remains significant but exhibits the opposite behaviour: the stability margin is effectively improved in the tip region of this critical blade.

These observations are closely related to the mechanism of distortion transmission across the compressor. The pronounced influence of the first rotor modification on the last stator row,

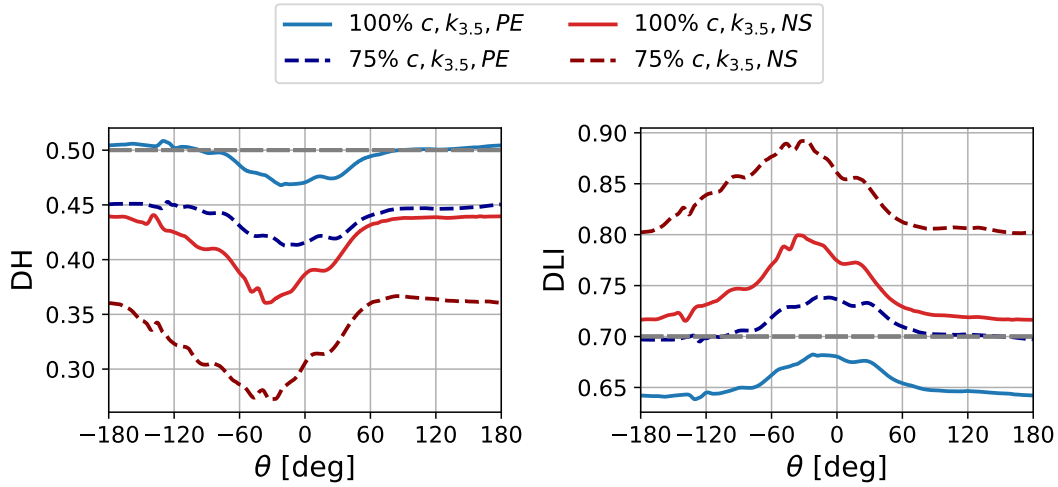

(a) 10% h/H.

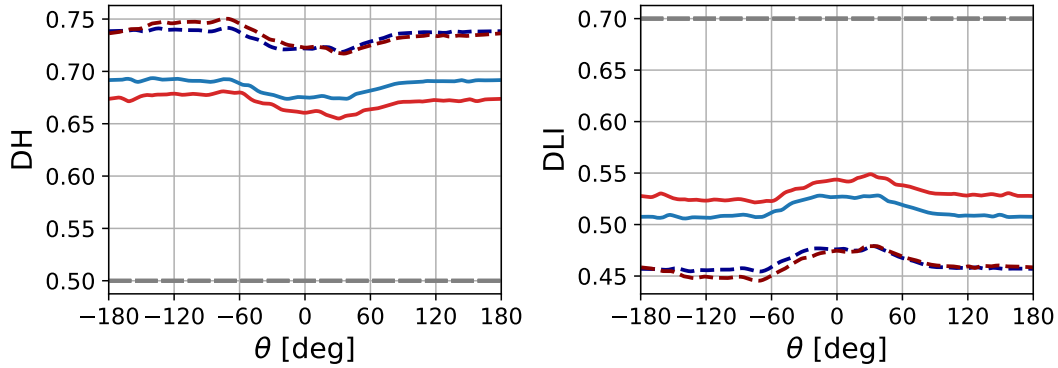

(b) 90% h/H.

Figure 7.18: Azimuthal profiles of DH (left) and DLI (right) of S4 at the peak efficiency and stable near stall point for both the baseline and modified geometries, obtained using the Body-Force approach.

which is even greater than the effect of the modification on the first rotor itself, indicates that a different transmission mechanism is taking place. To confirm this, Figure 7.19 presents the entropy contours on the outlet plane of the compressor, at the peak-efficiency operating point, for both geometries. The figure highlights a reduction in losses near the compressor shroud, which is consistent with the previously discussed improvement in the stability of this region. Conversely, the behaviour at the hub, although slightly degraded, remains very similar to that of the original geometry, showing only a minor increase in losses for the 75% c configuration. Finally, at approximately mid-span, and particularly at the leading boundary of the distorted region, the losses are noticeably higher compared with the baseline geometry. As this region operates within a relatively stable portion of the flow field, the increase does not lead to any significant stability issues, although it does contribute to the overall reduction in robustness. Another important observation is that, in the configuration with the modified geometry, the distorted region exhibits a smaller circumferential shift by approximately ten degrees. This behaviour could be attributed to the different flow turning produced by the two geometries, as previously demonstrated for the clean inflow case. The effect is evident both from the com-

parison of the leading boundary of the distortion region in Figure 7.19 and from the relative position of the peak values shown in Figure 7.18a.

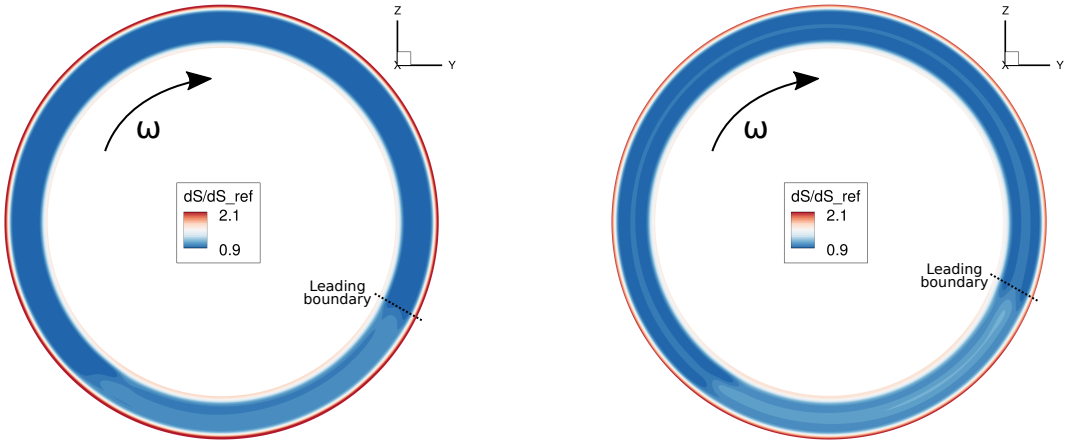

(a) 100% c. **(b)** 75% c.

Figure 7.19: Two-dimensional entropy contours at the compressor outlet for the geometries at varying aspect ratio at the peak-efficiency point for the $k_{3.5}$ distortion.

Similarly, Figure 7.20 provides a qualitative visualisation of the trends previously quantified through the spanwise and azimuthal profiles. The total pressure is higher near the compressor tip for the 75% c geometry and lower in the hub region, indicating increased stability at the shroud and a slight reduction at the hub. At mid-span, the injected total-pressure distortion is partially attenuated: the total pressure within the distorted region is higher than in the baseline geometry, implying a reduced pressure deficit.

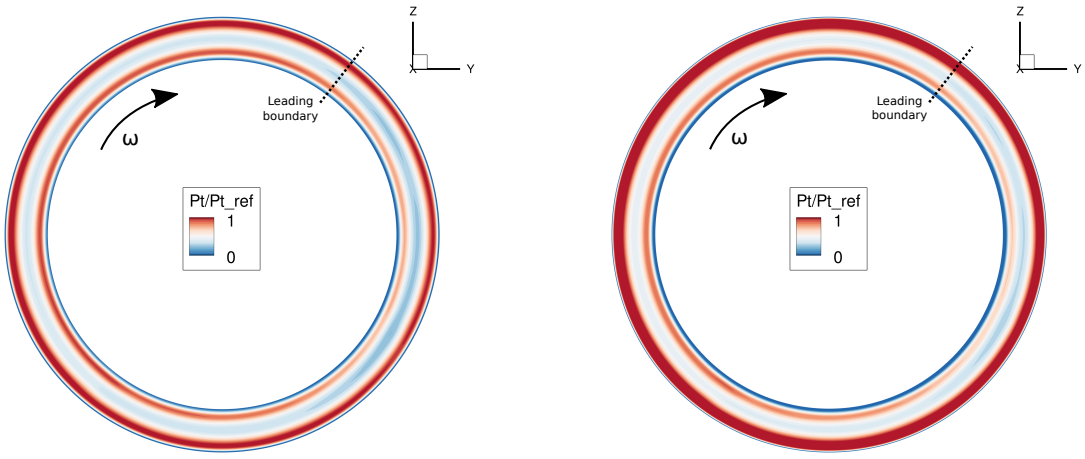

(a) 100% c. **(b)** 75% c.

Figure 7.20: Two-dimensional total pressure contours at the compressor outlet for the geometries at varying aspect ratio at the peak-efficiency point for the $k_{3.5}$ distortion.

As discussed earlier, the reduced robustness at the hub is not optimal for this configuration, as the most critical region of the S4 blade is located near the hub, where losses increase.

Nevertheless, these analyses suggest that modifying the aspect ratio may offer a means to selectively influence specific near-wall regions while also promoting attenuation of the injected distortion at mid-span, thereby enabling a delay in the onset of instability.

To assess the impact of the aspect-ratio modification on compressor stability, an analysis of the performance ratio, analogous to that presented in Section 6.2.2, is conducted for the configuration with the modified aspect ratio. Table 7.1 presents the performance ratio (PR) of the last stable point of this configuration under both clean and distorted inflow conditions, compared with the clean case of the baseline geometry with the Body-Force approach. In the table, a loss in stability is already observed under clean inflow, with $\Delta PR = -1.32\%$. This degradation becomes more pronounced under distortion: for $k = -3.5\%$, the loss in performance ratio increases to $\Delta PR = -3.20\%$, and for $k = -7.5\%$, it reaches $\Delta PR = -5.06\%$. The trend is clear: increasing the aspect ratio of the first rotor row results in a marked reduction in stability across all inflow conditions when compared with the baseline geometry. This finding is consistent with the analysis of the local flow field and of the stability indices, both of which highlighted a more critical response near stall.

Table 7.1: Values of the performance ratio PR and their relative changes ΔPR with respect to the base geometry case under clean inflow.

Case	Chord	$PR = \frac{\pi_{tt}}{Q_{\text{corr}}}$	ΔPR
BF - CLN	100% c	0.3872	-
BF - CLN	75% c	0.3821	-1.32%
BF - Dist 3.5%	100% c	0.3803	-1.78%
BF - Dist 3.5%	75% c	0.3748	-3.20%
BF - Dist 7.5%	75% c	0.3676	-5.06%

As could be expected, the region where losses increase most sharply, and from which instabilities may originate, is once again the hub region. This area was previously identified as the most critical one in the analysis of the baseline geometry, and its sensitivity to distortion has further increased with the modification of the aspect ratio of the first rotor row. The effect is illustrated in Figure 7.21, which presents the entropy contours on the cut at iso-$h/H = 5\%$ (Figure 7.21a), where the two vertical lines indicate the leading and trailing edges of the last stator row, and on the outlet plane (Figure 7.21b), both for the critical operating point near stall for the 75% c configuration. The contour at $h/H = 5\%$ shows that the highest losses are again concentrated in the downstream stage and appear to propagate both upstream and azimuthally from the distorted region, while the outlet-plane distribution confirms that the hub region exhibits the most pronounced increase in losses.

7.4 Discussion on the Model Capability

The objective of this section is to assess whether it is possible to identify the cause for which the solidity variation was not correctly captured by the Body-Force model, whereas the aspect ratio variation was, and consequently to propose a possible rationale and a generic guideline to determine whether a geometric study can be performed with confidence. To do so, a brief analysis of the differing influence of solidity and aspect ratio geometric modifications on the flow structure of the first rotor row is presented.

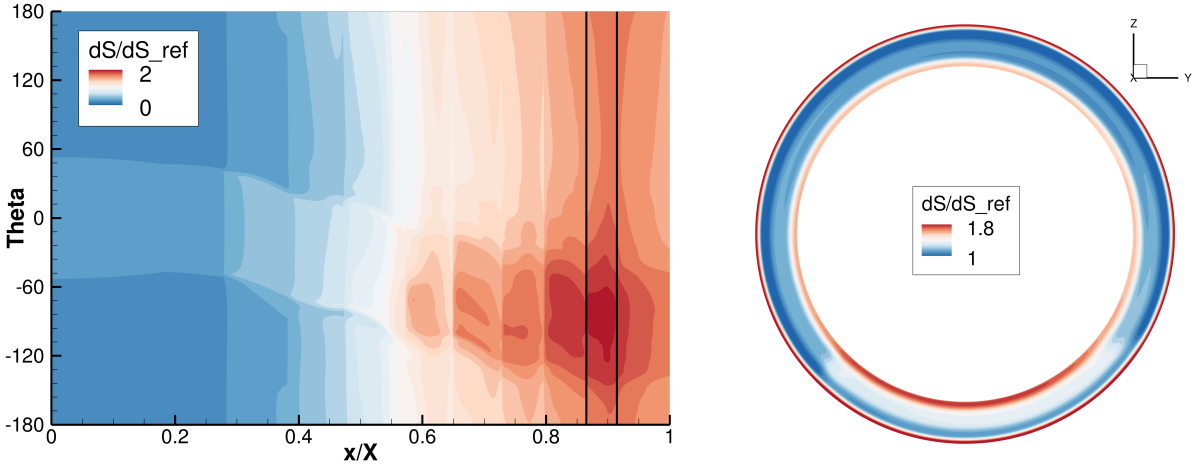

(a) Cut at iso-$h/H = 5\%$.

(b) Oulet plane.

Figure 7.21: 2D entropy contours at the critical operating point near stall for the 75% c case.

In Section 7.2, it was stated, based exclusively on the solidity investigations, that the origin of the unsuccessful capture of these geometric effects was probably associated to the flow regime, which was different in the IHPC compressor at full spedd than in the CREATE compressor. In particular, low-supersonic configurations, without a detached shock at the blade leading edge, allowed the solidity effects to be correctly captured, whereas cases characterised by a detached shock or strong flow separations were not successful. It was subsequently demonstrated that the aspect ratio study was successful even in the presence of a detached shock. This raised the question of how it is possible to determine a priori whether the Body-Force model is capable of predicting the influence of geometric variations.

To investigate this aspect, the relative Mach number field for the first rotor of the complete compressor configuration, obtained from blade-resolved calculations at peak efficiency and nominal speed, is presented. In particular, Figure 7.22a shows the baseline geometry, Figure 7.22b the solidity modification case, and Figure 7.22c the aspect ratio case. These figures show that the baseline geometry exhibits a detached shock, which impacts the suction side of the neighbouring blade at approximately 40% of the chord length. A similar behaviour is observed for the aspect ratio variation case. In the solidity-modified configuration, however, the shock structure within the passage has changed. It now impacts the neighbouring blade further downstream, at about 50% of the chord, and the flow appears to undergo a gradual deceleration before transitioning to subsonic conditions downstream of the shock.

This behaviour is further confirmed by the corresponding static pressure field shown in the bottom row of Figure 7.22. For the solidity case, it clearly highlights both the flow deceleration prior to returning to subsonic conditions and the more extended region involved in the shock phenomenon, while the other two cases exhibit sharper boundaries in the supersonic region. This may be attributed to the fact that, in the solidity-modified configuration, the shock extends into the decelerating region of the blade chord, which changes the pre-shock Mach number.

It therefore appears that the correct capture of chord effects and the incorrect capture of solidity effects may be linked to a modification of the fundamental aerodynamic properties of the investigated blade. Specifically, it may be the change in the shock structure at vary-

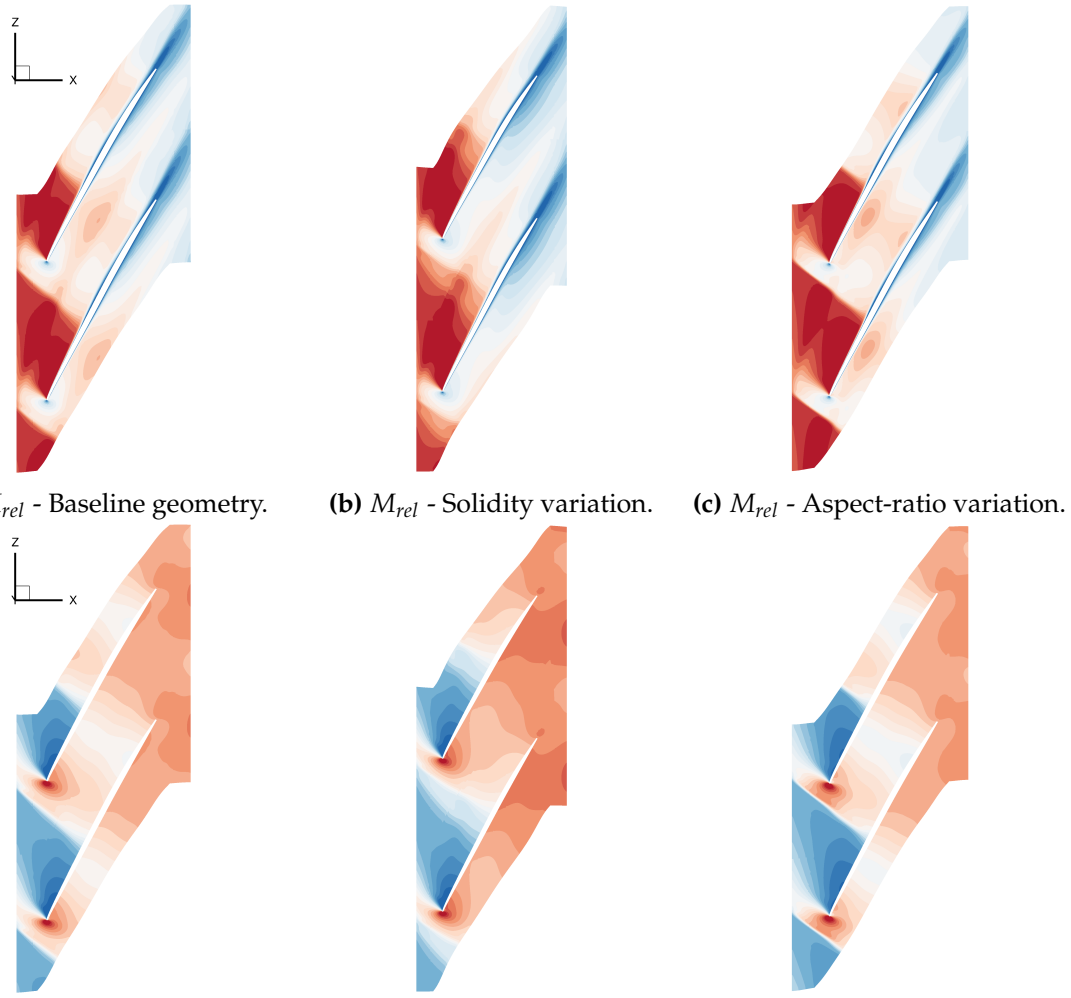

(a) M_{rel} - Baseline geometry. **(b)** M_{rel} - Solidity variation. **(c)** M_{rel} - Aspect-ratio variation.

(d) P_s - Baseline geometry. **(e)** P_s - Solidity variation. **(f)** P_s - Aspect-ratio variation.

Figure 7.22: Field of M_{rel} and P_s at the peak-efficiency operating point at 95%h/H.

ing solidity that alters the model predictions, noting that the chord study is performed at iso-solidity. In particular, since the same behaviour was observed when using both the original and the modified Body-Force models, the incorrect predictions do not originate from the implemented modifications, such as the calibration coefficients. Instead, they may stem from the application of an identical modelling approach to configurations exhibiting a substantial change in their fundamental aerodynamic characteristics, especially in transonic flow regions, which are well known to be challenging for Body-Force-based formulations to capture accurately. It can thus be deduced that geometric parametric studies using the Body-Force model can be performed with confidence provided that the associated geometric variations do not induce significant changes in the dominant shock structures. When such changes occur, particularly in transonic conditions, but also as observed for the part-speed case with extensive flow separation, the predictive capability of the model should be carefully reassessed.

The studies presented in this chapter on the capabilities of the model under geometrical variations for the clean inflow condition may therefore be considered in light of this interpretation, as follows:

- The blade solidity study at nominal speed was unsuccessful, consistent with the hypothesis that changes in the shock structure within the passage may be responsible, as shown in Figure 7.22.
- The chord study at nominal speed was successful, which is consistent with the proposed hypothesis, since it was conducted at iso-solidity and the shock structure in the passage was demonstrated to retain the same fundamental characteristics as the baseline geometry case.
- The solidity study on the CREATE compressor at nominal speed, with all stages included, was correctly predicted. This is again in agreement with the hypothesis, as this configuration does not exhibit strong detached shocks whose structure vary significantly with solidity.
- The isolated first rotor of the IHPC compressor at 80% part speed was specifically designed to reproduce the same flow regime as the CREATE compressor, and behaved in a manner similar to the CREATE compressor at nominal speed for the same reason, correctly predicting solidity effects. Figures 7.23a and 7.23b show the relative Mach number field for the baseline and solidity-modified cases of the isolated first rotor of the IHPC compressor. These figures indicate that the transonic region is limited, does not change significantly, and is not characterised by a detached shock.
- The IHPC compressor at 90% part speed, with all stages included, was not correctly predicted. This can be attributed to a significant change in aerodynamic behaviour, which is not linked to shock characteristics but rather to the strong and extensive flow separations occurring at both the IGV and S1. These separations also modify the behaviour of R1. Figure 7.23c shows the baseline geometry case at 90% part speed for the full IHPC compressor configuration. It clearly illustrates that the aerodynamics are substantially altered by the separations in both upstream and downstream rows, affecting not only the shock structure but also the flow angle and velocity.
- The same conclusions regarding modifications in shock behaviour were confirmed at near-stall operating conditions. Although the shock position varies slightly with operating point, its fundamental properties remain unchanged for the baseline geometry and the aspect-ratio variation, unlike in the case where the solidity is modified.

All these analyses confirm the hypothesis proposed earlier: the ability to correctly capture geometric effects appears to depend on changes in the fundamental aerodynamic properties of the blade, particularly the showk structure in the passage and flow separation.

Conclusion

This chapter focused on assessing the feasibility of design influence studies using the Body-Force modelling approach, applied to the IHPC compressor. Two design parameters were investigated: solidity and aspect ratio. Modifications were applied exclusively to the first rotor row of the compressor for two reasons: to evaluate the impact of the modification without interference from changes in other blades, and to assess how a change in an upstream blade influences the behaviour of downstream blades.

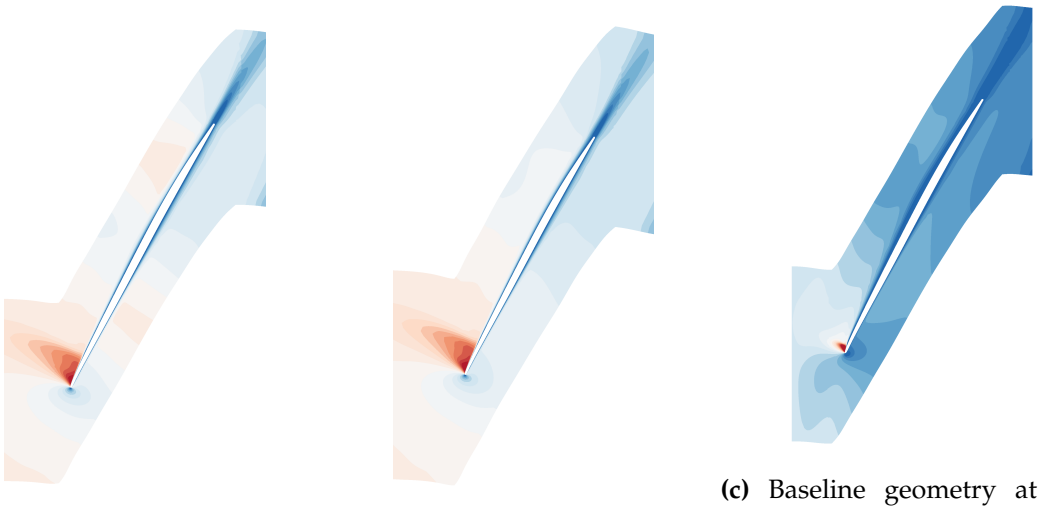

(a) Baseline geometry at 80% speed on isolated rotor.

(b) Solidity variation at 80% speed on isolated rotor.

(c) Baseline geometry at 90% speed on complete configuration.

Figure 7.23: Field of M_{rel} at the peak-efficiency operating point at 95%h/H, for the part-speed cases.

Regarding the solidity study, it was found that the model is unable to capture the effects of this parameter when the flow exhibits strong detached shocks or extended separations. Such conditions alter the aerodynamic response of the blade, challenging the assumptions of the model. Nevertheless, the model successfully predicted the effects of solidity for low-transonic configurations, such as the CREATE compressor and the isolated first rotor of the IHPC compressor at part speed, demonstrating its validity across different shaft speeds from the design condition.

The aspect-ratio study proved more fruitful, as the model was able to accurately predict its effects for the full transonic IHPC configuration. An initial analysis under clean inflow confirmed the reliability of the model and highlighted that the aerodynamic effects induced by aspect-ratio modifications are complex and highly three-dimensional. A detailed analysis of these effects was then performed under both clean and circumferentially distorted inflow, focusing on two critical regions: the hub and the shroud.

Modifying the aspect ratio of the first rotor row offers certain advantages, including a reduction in engine mass and length, as well as increased stability near the shroud for some operating points, particularly in the most critical row. However, this modification consistently leads to a severe reduction in stability near the hub, observed both at peak-efficiency and near-stall conditions, thereby compromising compressor robustness in the hub region, previously identified as the origin of instabilities.

Overall, the Body-Force model provides a reliable framework for assessing the effects of geometrical modifications in compressors operating within subsonic to low-transonic regimes. The application of the model to fully transonic flows with detached shocks, or to flows characterised by extensive flow separation, should be undertaken with caution, as such conditions undermine the fundamental assumptions of the model.

CONCLUSION

C

CONCLUSIONS AND PERSPECTIVES

Recalling Research Objectives and Methodology

This research aimed to investigate inlet distortion effects in the complex aerodynamic environment of multi-stage high-pressure compressors. A lower-order modelling framework was developed to combine computational efficiency with predictive accuracy and to achieve reliability comparable to (U)RANS calculations, serving as an alternative to the extensive 3D full-annulus simulations typically required for such studies.

Body-Force models were chosen as the methodological foundation because of their proven ability to reproduce three-dimensional flow effects and capture the compressor's aerodynamic response to distortion. Among existing Body-Force formulations, the Hall-Thollet model was adopted as the baseline for its suitability for turbomachinery applications. However, its applicability to highly challenging aerodynamic regimes, characterised by strong adverse pressure gradients, low blade aspect ratios, and high aerodynamic loading, remained largely unexplored. Addressing this gap constituted an essential component of the present study.

To support the analysis, enhancement, and validation of the proposed Body-Force model, high-fidel ity blade-resolved datasets were generated for two representative test cases: the CREATE compressor and the IHPC compressor. The CREATE compressor, a well-instrumented research rig with extensive experimental data, served as the primary validation case. By contrast, the IHPC compressor provided a more industrially representative, geometrically and aerodynamically complex configuration, enabling assessment of the model under realistic and demanding operating conditions, including a realistic circumferential distortion. Together, these test cases formed a validation matrix capable of probing the generalisability, robustness, and practical relevance of the model across a range of compressor configurations and operating conditions.

The enhanced Body-Force model was first validated under clean inflow conditions to demonstrate its ability to reproduce key flow features across the entire operating range. Subsequently, its performance was evaluated across a wide parametric space involving multiple distortion patterns, intensities, and geometric modifications. For the CREATE compressor, total-pressure radial distortion representative of S-duct inflow was examined, as well as circumferential distortion of varying intensity on a pseudo-2D configuration to reduce computational cost. The IHPC compressor was assessed under a realistic, experimentally-derived circumferential total-pressure distortion using a full-annulus configuration. Finally, a parametric design study was performed on the IHPC compressor.

The findings of this research can be grouped into two main categories: conclusions regarding the accuracy, robustness, and applications of the proposed Body-Force model, and conclusions concerning inlet distortion effects and related compressor design insights.

Conclusions on the Proposed Body-Force Model

An initial assessment of the baseline Hall-Thollet model highlighted its expected limitations in the complex aerodynamic environment of high-pressure compressors. Several key improvements were identified and implemented. First, a near-wall clipping technique was introduced to improve the flow behaviour near the wall and enhance numerical robustness. This addressed the issue of the model's force component producing turning and approaching zero within the boundary layer, which could generate non-physical separations. Then, a method to include secondary losses in the model was proposed, specifically integrating a rotor tip-gap loss coefficient to better capture the effects of the tip-leakage vortex. Finally, a simple and generalisable calibration procedure was developed, which modifies the aerodynamic coefficients of the model to improve predictive accuracy using single-blade-passage reference simulations as targets. Following these modifications, the accuracy of the model is inherently limited by that of the reference data, here the (U)RANS calculations used in the calibration process, as well as by that of the employed correlations, in this case those of Roberts [135].

Under clean inflow conditions, these modifications proved highly effective. The models deviation from reference values decreased from 10% and 25% for the two compressors, respectively, to around 2% for both across the entire operating range. Beyond global performance, local flow behaviour was well reproduced, showing excellent agreement with reference data. Minor local discrepancies were observed, mainly near the compressor hub, highlighting areas where the model could be improved to capture more specific effects.

After validation under clean inflow conditions, the model was tested under several distorted inflow conditions. For both compressors, encompassing different distortion patterns and intensities, the model accurately predicted distortion transmission mechanisms, flow quantity evolution across the annulus azimuthal direction and along the compressor axis, performance degradation, stall margin reduction, and non-uniform flow redistribution, closely matching high-fidelity simulations. For the industrially representative compressor, the model also identified the critical region undermining stability and elucidated the mechanism of instability onset.

Finally, parametric studies were carried out on the first rotor blade of the second compressor using the Body-Force model, with results compared to reference simulations. Two geometric parameters were varied: blade solidity and blade aspect ratio. The model accurately predicted the impact of solidity variations under high-subsonic regimes and at reduced shaft speeds, although limitations were observed in transonic conditions or when strong boundary layer separations occurred. Variations in blade aspect ratio were well captured even under transonic conditions, allowing the model to effectively support distortion studies across a range of geometric configurations.

The extensive test matrix demonstrates that the proposed model is reliable, accurate, robust, and versatile. It remains valid across a range of operating points, inflow conditions, distortion patterns and intensities, and shaft speeds, without the need to recalibrate aerodynamic coefficients. Limitations are mainly associated with the range of validity of the model itself, which can be significantly challenged in cases of extensive flow separation or strong secondary flow effects, as encountered for the geometrical studies. The framework also establishes a solid foundation for further developments, informed by the problems assessed and the solutions introduced in this study.

Furthermore, the model proved extremely computationally efficient. For every simulation, the Body-Force model was two to three orders of magnitude faster than its blade-resolved

counterpart, in terms of CPU time. Although additional time is required for the initial setup of the enhanced Body-Force model, this step is performed only once, and the resulting model can be reused for all subsequent parametric distortion and design studies, greatly improving workflow efficiency. The framework also establishes a solid basis for future investigations involving more severe distortion conditions and unsteady flow phenomena, which are further discussed in the Perspectives section.

Conclusions on the Impact of Inlet Distortion on Compressor Aerodynamics

From a physical standpoint, the distortion analyses provided valuable insights into compressor behaviour. For both compressors, circumferential distortion studies revealed how inlet distortions propagate through the machine. The injected total pressure distortion alters the local flow coefficient, redirecting flow toward regions of lower static pressure. This increases incidence and generates locally higher work input, which gradually raises the total temperature along the compressor annulus, creating a distorted region that is convected with shaft rotation. At the same time, the imposed total pressure deficit dissipates through flow redistribution and spatially varying work input, reducing the deficit at the compressor exit. Near-wall analyses of the IHPC compressor further quantified the resulting stall margin reduction, showing close agreement with experimental data.

In the CREATE compressor, studied in a pseudo-2D configuration, the last stages were particularly sensitive to distortion effects. The final stator was identified as the most critical, exhibiting extreme values of the stability indices. The IHPC compressor exhibited similar behaviour, with the fourth and last stators showing stability issues. Near-wall analyses enabled quantification of stall margin reduction, demonstrating close agreement with experimental data. These analyses also identified the leading boundary of the distorted region as the most critical zone, while hub separation was pinpointed as the source of instability, which rapidly propagated across several blade passages at the fourth stator, ultimately triggering instability.

A design study on the IHPC compressor, focusing on aspect-ratio variation under circumferential distortion, revealed that the effects of this parameter are strongly three-dimensional. It was observed that the hub and shroud regions exhibited opposite effects on robustness, and that this behaviour further changed at different operating points. Near stall, the stall margin of the critical row, the last stator, improved significantly at the rotor tip but degraded sharply at the hub, which was already a critical region. Notably, the onset of hub separation instability was predicted to appear earlier than in the base geometry case.

General Conclusion

As a general conclusion, this research shows that low-fidelity modelling can play a significant role in turbomachinery analysis and design. By offering a framework that is accurate, robust, and adaptable across a wide range of operating conditions, distortion patterns, and geometries, the enhanced Body-Force model complements high-fidelity tools and enables rapid parametric exploration, informed decision-making, and early-stage optimisation for distortion robustness. Its ability to predict distortion-induced behaviour and stability trends at orders-of-magnitude lower computational cost contributes to the development of more efficient, resilient, and sustainable compressor technologies. These findings highlight the current strengths of the model while also providing a foundation for its continued evolution and extension.

Perspectives

This work has highlighted several promising avenues for further development, building on the methodological and physical insights gained throughout the thesis.

Model Improvement The model has demonstrated overall good predictive capability for the investigated test cases; however, some limitations have been identified. A first source of deviation is the inaccurate capture of supersonic regions, as also highlighted by previous works [121, 131], which not only affects predictions in high-subsonic and transonic compressors, but consequently restricts the applicability of loss corrections, owing to the difficulty in reliably identifying the regions of interest. As suggested in previous work [121], supersonic regions could be identified from blade-resolved simulations or inferred from precomputed or data-driven databases, thereby enabling the appropriate application of loss corrections. Nevertheless, this approach requires extensive supplementary data and is therefore viable only when errors associated with supersonic flow predictions have a critical impact. A second limitation, specific to the investigated configurations, is the omission of hub and shroud fillets in the Body-Force calculations owing to the lack of dedicated modelling, which leads to endwall deviations relative to the blade-resolved reference simulations, as seen in Sections 5.1 and 6.1. The inclusion of simplified fillet effects, either through dedicated corrective source terms or modified endwall loss models, could substantially improve prediction accuracy in these regions.

A further improvement that would enhance the applicability of the model within a design context concerns the calibration procedure, which would greatly benefit from automation. An ideal approach would consist of expressing the calibration coefficients as functions of the aerodynamic and geometrical characteristics of each blade. Although comprehensive datasets are not currently publicly available, the results discussed suggest that these characteristics form a suitable basis for inferring coefficient values. In this regard, when available, calibration coefficients describing blade behaviour could also be inferred from correlations derived from extensive industrial datasets [131], providing guidance across different blade geometries and operating conditions. Such an approach would eliminate the need for iterative calibration, improve physical consistency, and ensure direct applicability to different machines. Significant challenges remain, as the formulation of aerodynamic coefficients for strongly interacting, highly loaded, low aspect-ratio blades with pronounced secondary effects is inherently complex. The systematic generation of multi-parameter charts could enable coefficient definitions of sufficient accuracy for pre-design applications. Finally, calibration coefficients could be derived within an optimisation framework, although coupling the Body-Force model with optimisation algorithms remains challenging, particularly with respect to the definition of an appropriate objective function. Machine learning techniques may also represent a promising avenue towards this objective.

Another major extension that would substantially broaden the applicability of the model is the development of an unsteady formulation. Such an extension would enable the investigation of transient phenomena, flow instabilities, and complex unsteady inflow conditions. Possible implementation strategies include the introduction of a relaxation or a time-lag term for updating the source-terms [3, 131] or the adoption of a panel-method formulation employing concentrated rather than distributed source terms [15]. An unsteady Body-Force model would allow the detailed characterisation of instability development, the tracking of transient flow features, and the identification of critical phenomena such as surge or rotating stall,

thereby providing valuable insight into dynamic flow behaviour and transient performance degradation.

Finally, the limitations identified in the geometrical sensitivity study warrant further investigation. The analysis of the model under variations in blade solidity revealed a reduced level of reliability when dominant aerodynamic phenomena, such as shock structures or flow separation, undergo significant changes in intensity or nature. In these cases, the model is unable to accurately predict the flow behaviour, as the blade aerodynamic coefficients exhibit abrupt variations that are not captured by the current formulation. Potential remedies include regime-dependent modelling strategies, in which different sets of coefficients or modelling assumptions are activated based on local flow indicators, or the coupling of the Body-Force model with simplified shock or separation detection criteria.

Model Exploitation The capabilities of the developed model, combined with its low computational cost, open opportunities for in-depth and systematic studies.

One avenue is to exploit the rapid turnaround of the Body-Force model for optimisation studies aimed at improving compressor design, operability, and robustness to inlet distortions, as well as integration within the airframe. The reduced cost enables exploration of large design spaces, which is generally prohibitive with blade-resolved simulations. Previous work has demonstrated the advantages of Body-Force approaches for aero-propulsive integration and optimisation in the presence of inlet distortion [42], highlighting their suitability for early-stage design and system-level studies. The model developed in the present work, being more comprehensive, could further enhance the fidelity of such optimisation frameworks. In addition to formal optimisation, parametric investigations or response surface studies could identify key sensitivities and performance trends, guiding subsequent high-fidelity design steps.

Another direction is the use of the model within a multi-fidelity coupling framework. For instance, zonal detached eddy simulations could be applied in the inlet duct or intake, where large-scale unsteady turbulence and distortion generation occur, while the Body-Force model represents the bladed components. This approach allows accurate representation of distortion transport and unsteady inflow structures, while maintaining computational tractability and capturing the overall compressor response. It is particularly relevant for studying distortion-compressor interactions, stability margins, and unsteady operability limits in realistic engine integration scenarios.

Distortion Study Finally, assessing the compressor under more complex inlet distortion patterns is of interest. A first extension concerns swirl distortion, which is common in practical applications and can significantly affect compressor performance, stability margin, and blade loading. Its investigation would provide a relevant benchmark to evaluate the robustness and predictive capability of the model.

A more advanced direction is the study of unsteady distortion, enabled by an unsteady formulation of the model. Time-varying distortions can induce transient performance degradation and significantly influence stability limits. Accounting for these effects enables analysis of distortion transfer and dynamic compressor response, contributing to a comprehensive assessment of operability under realistic inflow conditions.

APPENDIX A

MESH SENSITIVITY STUDY ON THE CREATE COMPRESSOR

A.1 Assessment of the Single-Blade-Passage Mesh

A grid sensitivity study was conducted on the single-blade-passage configuration of the CREATE compressor to identify an optimal balance between computational cost and solution fidelity. Three structured grids with an O4H topology were evaluated: COARSE, MEDIUM, and FINE. The main characteristics of these grids are presented in Table A.1. The N_x values in the table represent the number of cells in the axial direction of the O-grid. The N_θ values denote the number of azimuthal cells per blade passage, while N_r represents the number of radial mesh cells.

Notably, the FINE grid contains approximately $\sqrt[3]{2}$ times the number of mesh points in each blade-to-blade (B2B) direction relative to the COARSE grid, with a corresponding increase in radial resolution to maintain mesh quality. As a result, the total mesh size of the FINE grid is approximately twice that of the COARSE grid. The COARSE and MEDIUM grids have similar configurations, with the latter featuring a refinement of the first rotor and increased radial resolution. The FINE grid is more densely resolved in all directions. Additionally, the O-block contains 37 layers for the COARSE and MEDIUM grids, increasing to 47 layers for the FINE grid.

Table A.1: Characteristics of single-blade-passage mesh grids for the CREATE compressor.

Grid	**Cells** [$\times 10^6$]	$\mathbf{N}_r$	$\mathbf{N}_x$	$\mathbf{N}_\theta$
COARSE	6.96	85 (R) 85 (S)	81	59
MEDIUM	8.82	101 (R) 85 (S)	81 101 (R1)	59 79 (R1)
FINE	14.61	125 (R) 117 (S)	102	74

The grids were evaluated at the peak efficiency operating point. The performance differences relative to the FINE grid were quantified as $err_{grid} = (g_{FINE} - g_{grid})/g_{FINE}$, where g

represents the performance metric. Results are presented in Table A.2.

Table A.2: Grid sensitivity study results on CREATE compressor performance at peak efficiency.

Parameter	$\text{err}_{\text{COARSE}}$	$\text{err}_{\text{MEDIUM}}$
Q_{corr}	0.46%	−0.09%
π_{tt}	0.44%	−0.07%
η_{is}	0.38%	0.27%

The MEDIUM grid yields performance metrics in close agreement with the FINE grid, exhibiting errors below 0.1% for corrected mass flow rate (Q_{corr}) and total-to-total pressure ratio (π_{tt}), and errors under 0.3% for isentropic efficiency (η_{is}). The COARSE grid demonstrates more significant deviations. Accordingly, the MEDIUM grid was selected for subsequent analyses.

The chosen MEDIUM grid exhibits excellent mesh quality characterized by minimal skewness, with angles greater than 35°, a maximum local expansion ratio near 2, slightly elevated locally due to rotor tip gaps and blade fillet geometry, a span-wise angular deviation below 40°, and a first mesh cell at the wall such that $y^+ \approx 1$.

A.2 Mesh Modifications for Unsteady Simulations

The single-blade-passage mesh for the CREATE compressor was initially designed for steady-state simulations using mixing-plane boundary conditions. While this mesh ensured excellent performance under such conditions, it was found to be insufficient when applied to Unsteady Reynolds-Averaged Navier-Stokes (URANS) simulations.

Specifically, the original mesh lacked the resolution needed to accurately transport wakes across the rotor-stator (RS) interfaces, leading to numerical dissipation and a loss of fidelity in the unsteady solution.

To address this limitation, the mesh characteristics described in Section 2.2.3 were adopted for all subsequent configurations. The revised approach includes a transition from the original O4H topology to an O6H configuration, providing better alignment and refinement of the mesh cells at the rotor-stator interfaces.

Figure A.1 illustrates the effect of this refinement by comparing the normalised entropy field in the region where the wake of the first rotor crosses the rotor-stator interface and impinges on the first stator. Figure A.1a shows the original single-blade-passage mesh, where entropy structures become significantly diffused at the interface and even change direction due to the orientation of the mesh cells in the up and down mesh blocks. In contrast, Figure A.1b, corresponding to the refined mesh described in Section 2.2.3, demonstrates much better preservation of wake features, including their direction, intensity, and width. It can be concluded that the adoption of the O6H block structure improves cell alignment at the interface, while the increased azimuthal resolution enhances the transport of flow features with reduced numerical dissipation.

Overall, the revised mesh achieves high solution quality while maintaining a reasonable mesh size, thus remaining compatible with multi-sector URANS simulations.

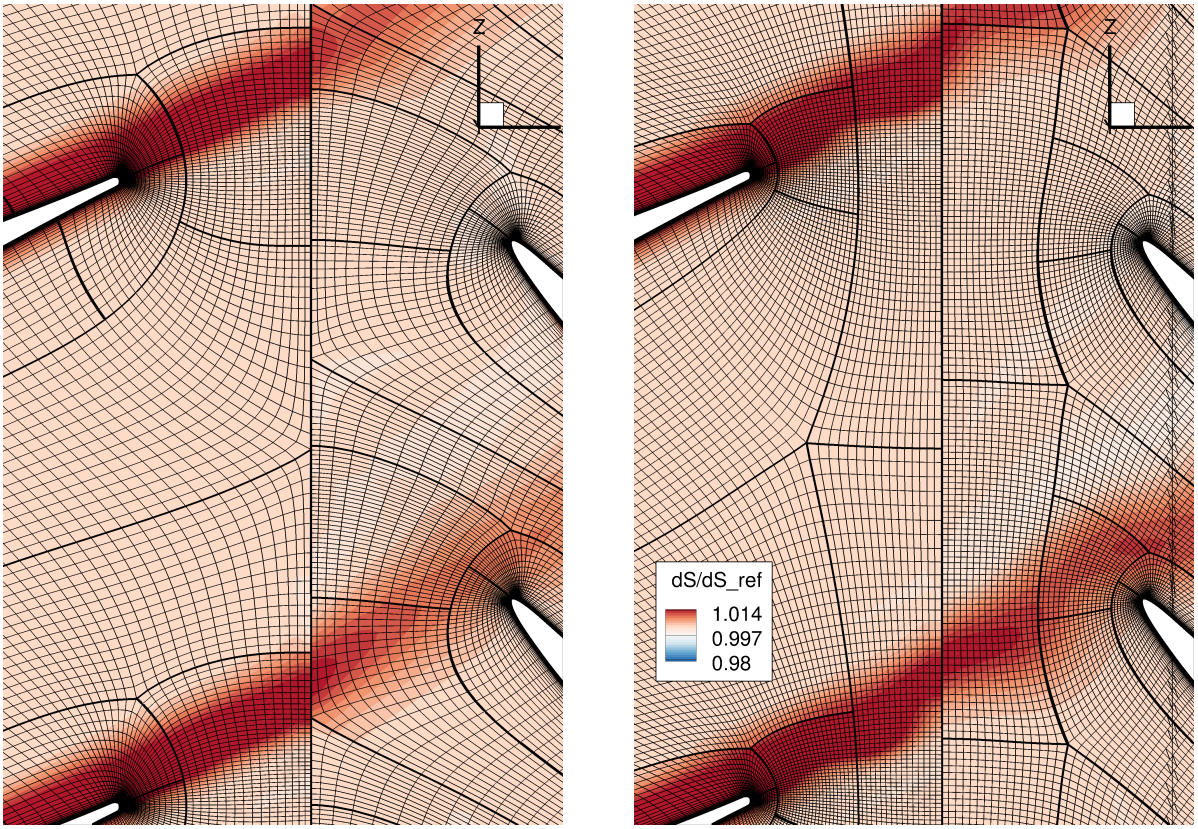

(a) Original single-blade-passage mesh. **(b)** Refined mesh with O6H topology.

Figure A.1: Normalised entropy field in the wake of the first rotor, across the rotor-stator interface.

A.3 Mesh Sensitivity Study for Body-Force Calculations

A brief sensitivity study was conducted to evaluate the impact of mesh resolution on Body-force calculations. Four different meshes were tested on the 2° sector of CREATE, differing in the number of points in three directions, as summarized in Table A.3. Notably, the upstream and downstream blocks share the same number of axial points in each mesh, but both values are reported for completeness.

Table A.3: Mesh details for Body-force calculations of CREATE.

Mesh	N_r	N_x – Row	N_x – Up	N_x – Down
MESH0	81	81	25	25
MESH1	101	101	25	25
MESH2	101	161	33	33
MESH3	121	181	33	33

Figure A.2 shows the total-to-total pressure ratio of the CREATE compressor, computed for the baseline Hall-Thollet model without off-design losses using each of the four meshes. The results reveal that significant differences appear only in the choke region of the compressor map at higher mass flow rates, where mass conservation issues, as discussed in Section 1.3.3.2, become more critical.

The mesh retained for subsequent studies, detailed in Section 2.2.4, corresponds to MESH1. This selection reflects a compromise between accuracy and computational cost. While MESH0 exhibited more pronounced deviations compared to the more refined meshes, MESH1 provided sufficient accuracy with manageable computational expense.

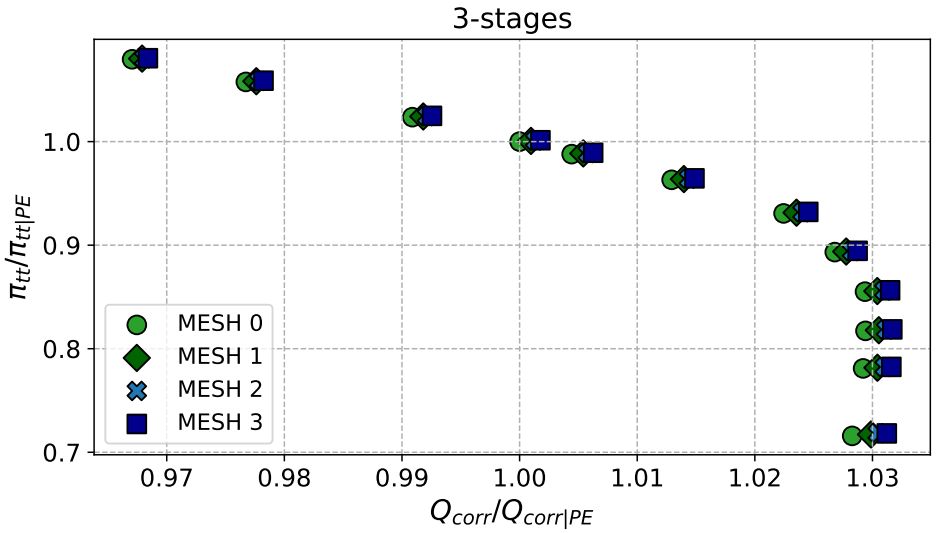

Figure A.2: Total-to-total pressure ratio of the CREATE compressor computed using four different Body-force meshes. Noticeable differences occur mainly in the choke region at high mass flow rates.

APPENDIX B

ROW-BY-ROW PERFORMANCE PREDICTIONS OF THE CREATE COMPRESSOR VIA BODY-FORCE METHODOLOGY

This appendix presents a detailed assessment of the modified Body-Force model performance prediction for each bladed row of the CREATE compressor. The figures included illustrate the main performance metrics: total-to-total pressure ratio (π_{tt}), total-to-static pressure ratio (π_{st}), total-to-total temperature ratio (τ_{tt}), and isentropic efficiency (η_{is}), all plotted as functions of the corrected mass flow rate. The data are normalised with respect to the values at the peak efficiency operating point.

Each plot compares the results from three modelling approaches: the reference blade-resolved simulations (SBP - bladed), the Body-Force method using the original Hall-Thollet model (BF - HT), and the Body-Force method incorporating the modified model (BF - new).

Results for the first rotor are shown in Figure B.1, followed by the first stator in Figure B.2, the second rotor in Figure B.3, the second stator in Figure B.4, the third rotor in Figure B.5, and finally the third stator in Figure B.6.

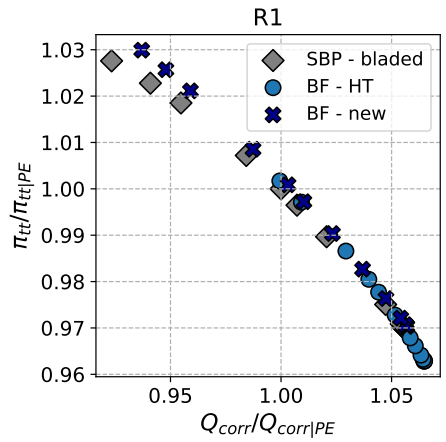

(a) Total-to-total pressure ratio π_{tt} of R1.

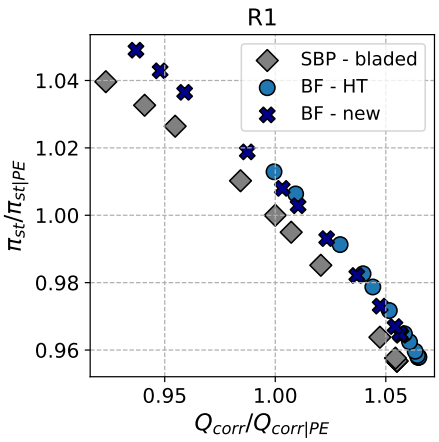

(b) Total-to-static pressure ratio π_{st} of R1.

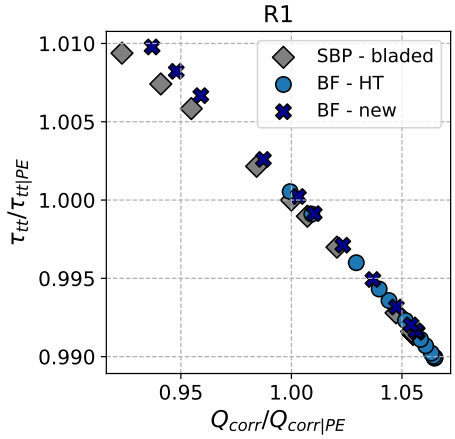

(c) Total-to-total temperature ratio Π_{tt} of R1.

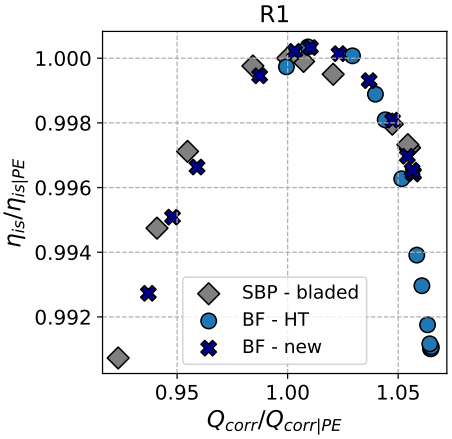

(d) Isentropic efficiency η_{is} of R1.

Figure B.1: Performance metrics for the first rotor row of the CREATE compressor.

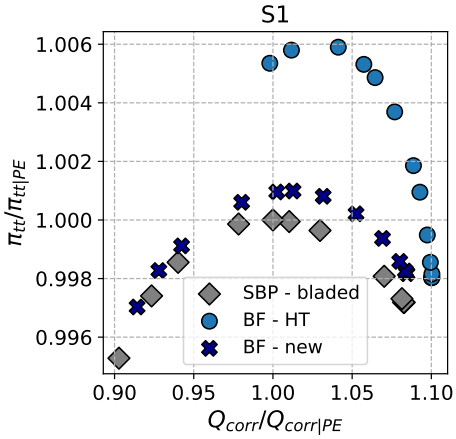

(a) Total-to-total pressure ratio π_{tt} of S1.

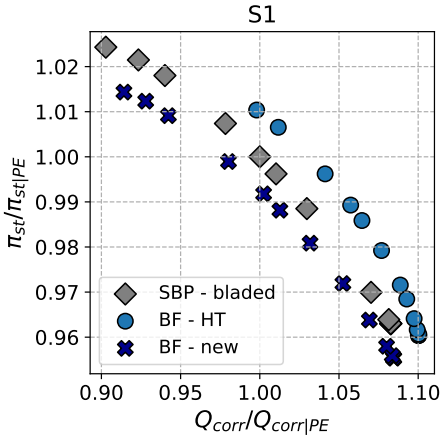

(b) Total-to-static pressure ratio π_{st} of S1.

Figure B.2: Performance metrics for the first stator row of the CREATE compressor.

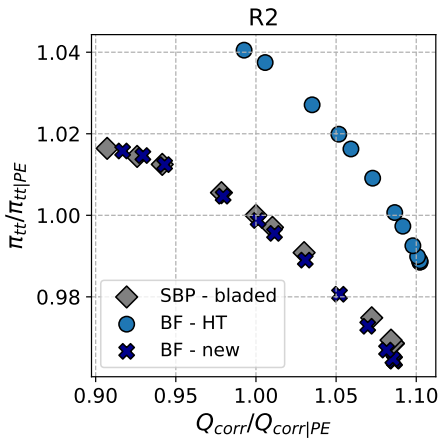

(a) Total-to-total pressure ratio π_{tt} of R2.

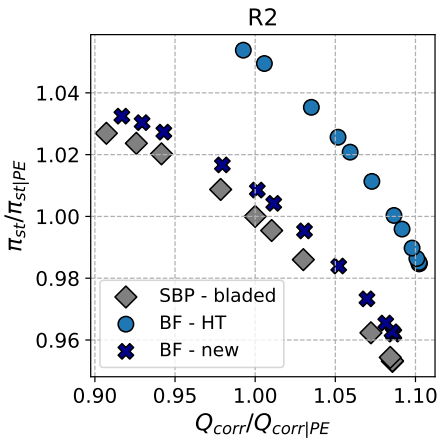

(b) Total-to-static pressure ratio π_{st} of R2.

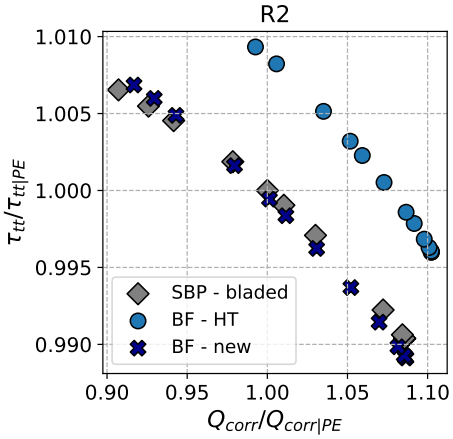

(c) Total-to-total temperature ratio Π_{tt} of R2.

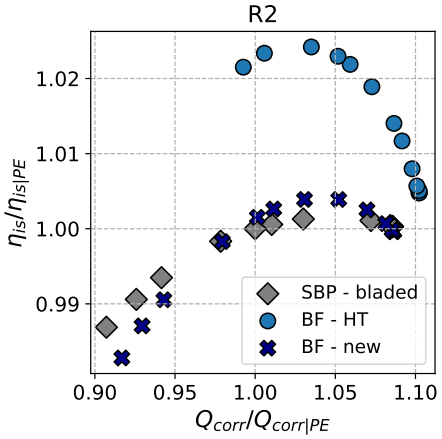

(d) Isentropic efficiency η_{is} of R2.

Figure B.3: Performance metrics for the second rotor row of the CREATE compressor.

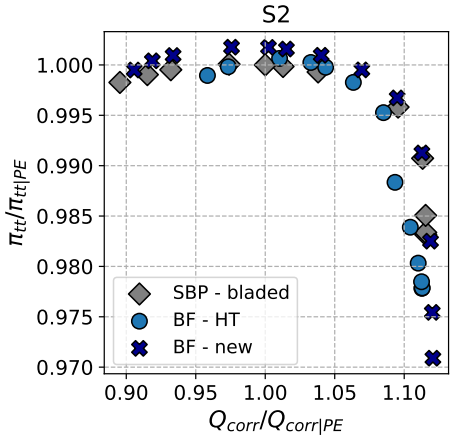

(a) Total-to-total pressure ratio π_{tt} of S2.

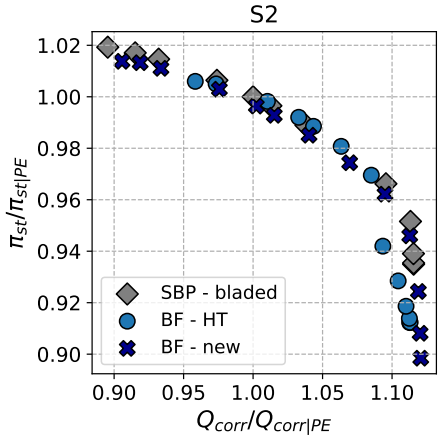

(b) Total-to-static pressure ratio π_{st} of S2.

Figure B.4: Performance metrics for the second stator row of the CREATE compressor.

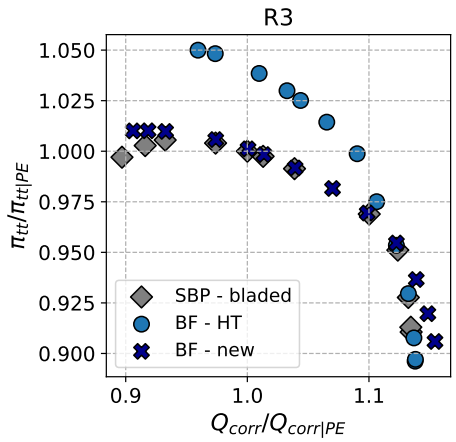

(a) Total-to-total pressure ratio π_{tt} of R3.

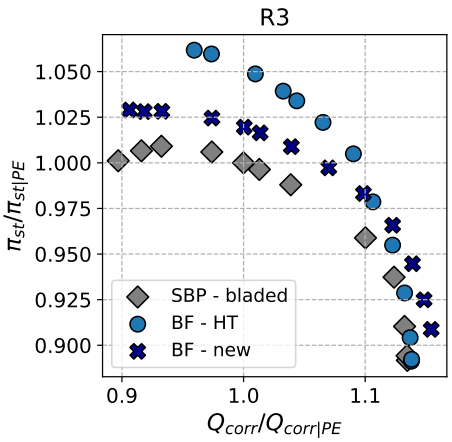

(b) Total-to-static pressure ratio π_{st} of R3.

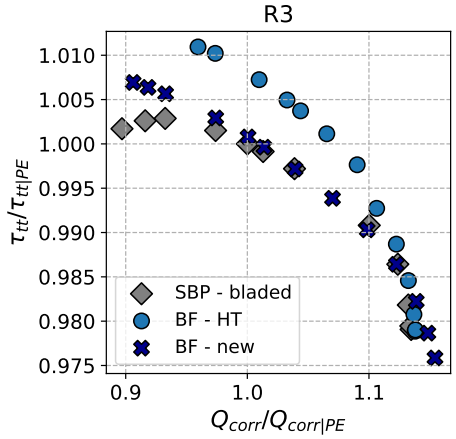

(c) Total-to-total temperature ratio Π_{tt} of R3.

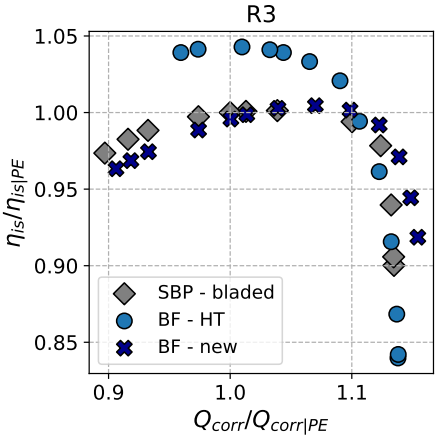

(d) Isentropic efficiency η_{is} of R3.

Figure B.5: Performance metrics for the third rotor row of the CREATE compressor.

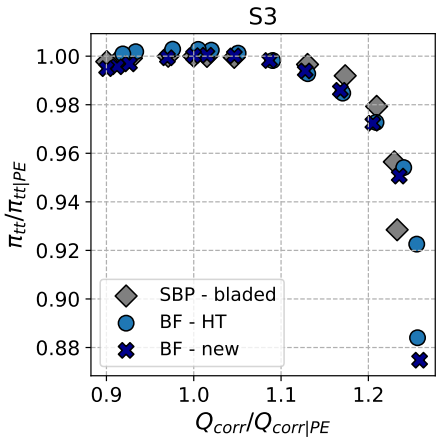

(a) Total-to-total pressure ratio π_{tt} of S3.

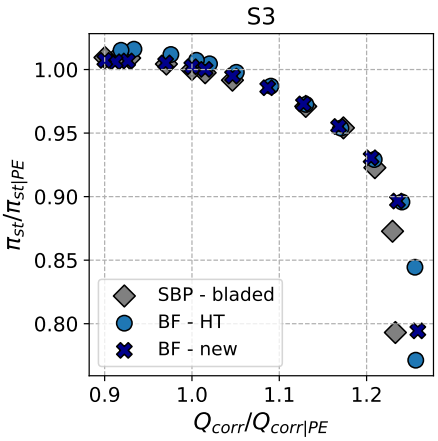

(b) Total-to-static pressure ratio π_{st} of S3.

Figure B.6: Performance metrics for the third stator row of the CREATE compressor.

APPENDIX C

ROW-BY-ROW PERFORMANCE PREDICTIONS OF THE IHPC COMPRESSOR VIA BODY-FORCE METHODOLOGY

This appendix presents a detailed assessment of the modified Body-Force model performance prediction for each bladed row of the IHPC compressor. The figures included illustrate the main performance metrics: total-to-total pressure ratio (π_{tt}), total-to-static pressure ratio (π_{st}), total-to-total temperature ratio (τ_{tt}), and isentropic efficiency (η_{is}), all plotted as functions of the corrected mass flow rate. The data are normalised with respect to the values at the peak efficiency operating point.

Each plot compares the results from three modelling approaches: the reference blade-resolved simulations ($2\pi/4$ - bladed), the Body-Force method using the original Hall-Thollet model (BF - HT), and the Body-Force method incorporating the modified model (BF - new).

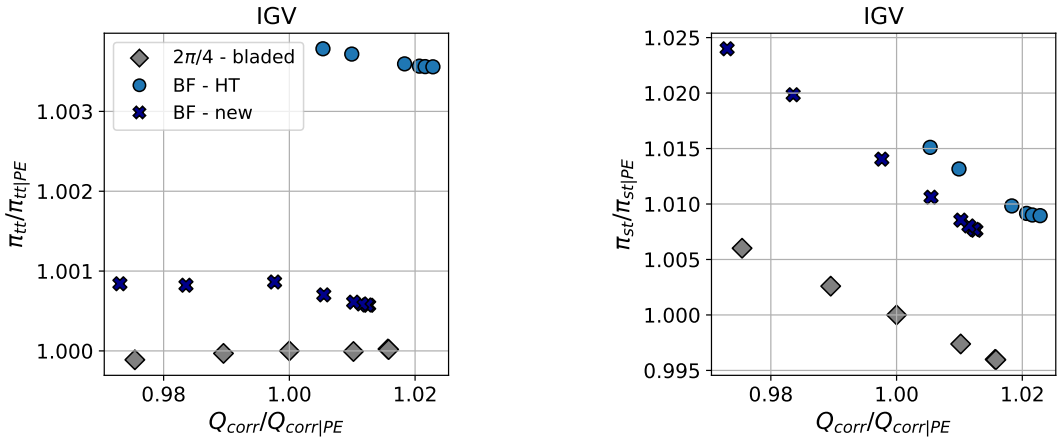

(a) Total-to-total pressure ratio π_{tt} of IGV.

(b) Total-to-static pressure ratio π_{st} of IGV.

Figure C.1: Comparison of performance metrics for the inlet guide vane (IGV) of the IHPC compressor.

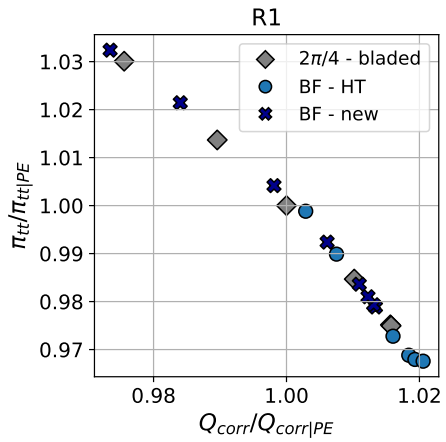

(a) Total-to-total pressure ratio π_{tt} of R1.

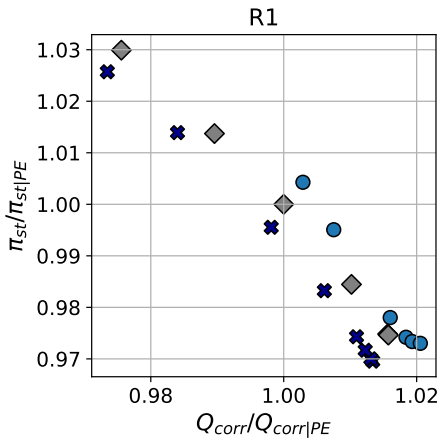

(b) Total-to-static pressure ratio π_{st} of R1.

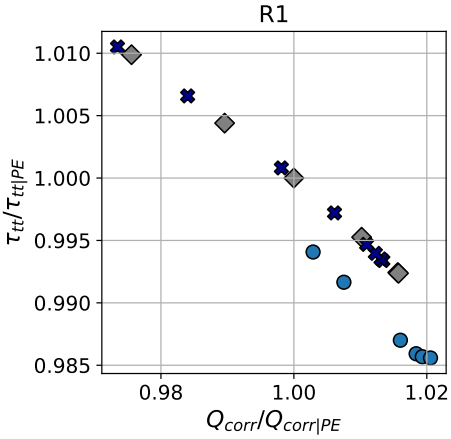

(c) Total-to-total temperature ratio Π_{tt} of R1.

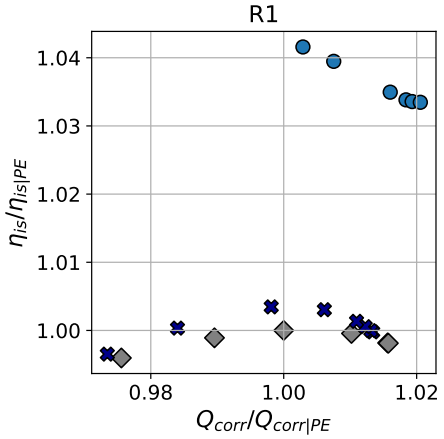

(d) Isentropic efficiency η_{is} of R1.

Figure C.2: Performance metrics for the first rotor row (R1) of the IHPC compressor.

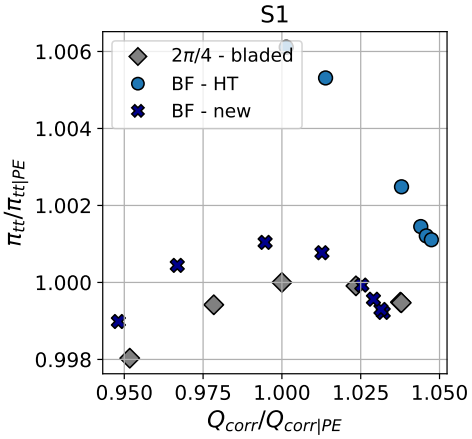

(a) Total-to-total pressure ratio π_{tt} of S1.

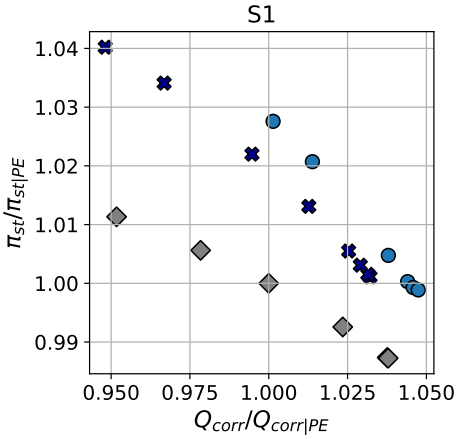

(b) Total-to-static pressure ratio π_{st} of S1.

Figure C.3: Performance metrics for the first stator row (S1) of the IHPC compressor.

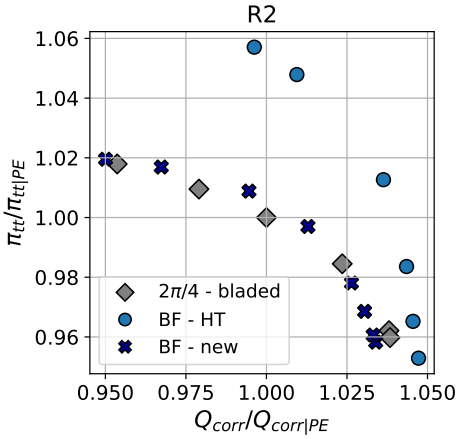

(a) Total-to-total pressure ratio π_{tt} of R2.

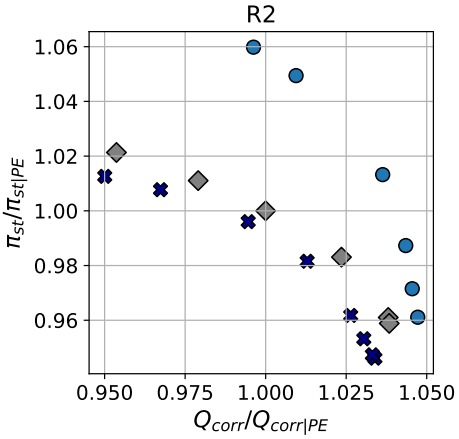

(b) Total-to-static pressure ratio π_{st} of R2.

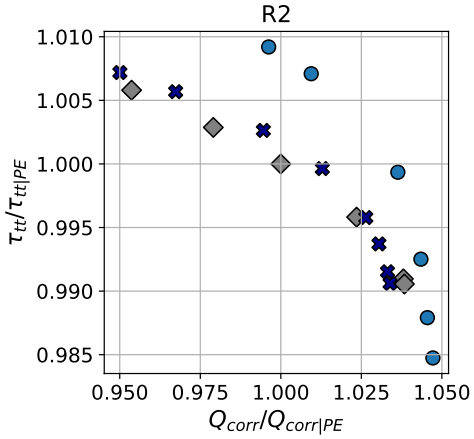

(c) Total-to-total temperature ratio Π_{tt} of R2.

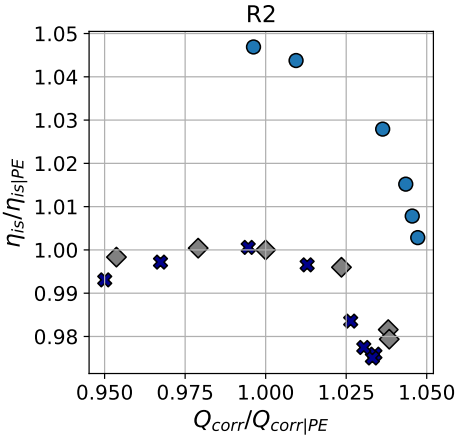

(d) Isentropic efficiency η_{is} of R2.

Figure C.4: Performance metrics for the second rotor row (R2) of the IHPC compressor.

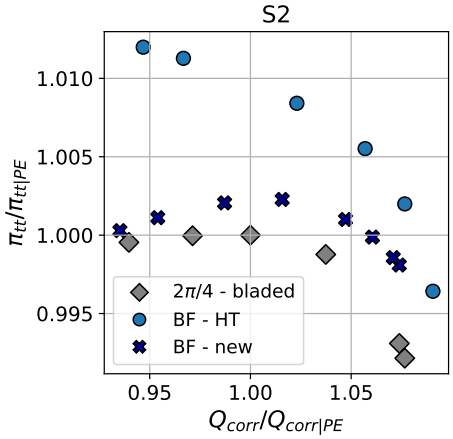

(a) Total-to-total pressure ratio π_{tt} of S2.

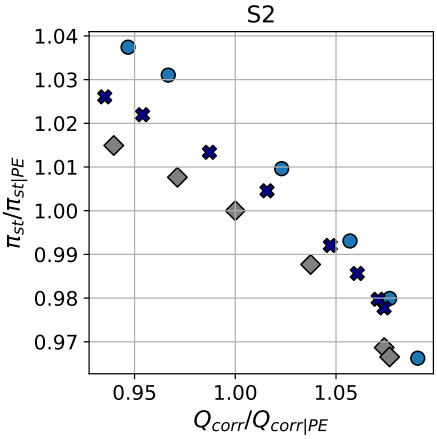

(b) Total-to-static pressure ratio π_{st} of S2.

Figure C.5: Performance metrics for the second stator row (S2) of the IHPC compressor.

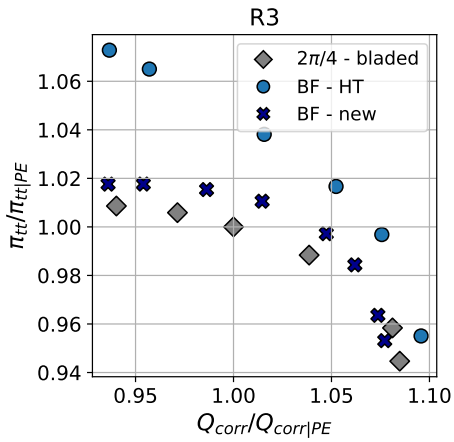

(a) Total-to-total pressure ratio π_{tt} of R3.

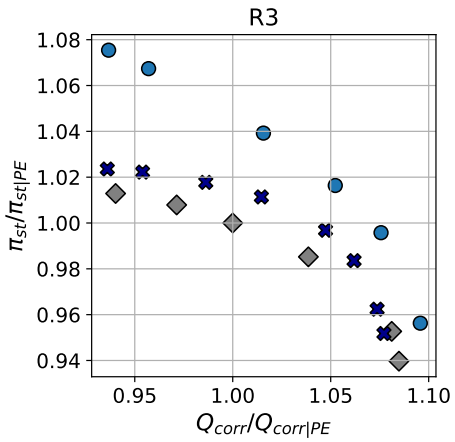

(b) Total-to-static pressure ratio π_{st} of R3.

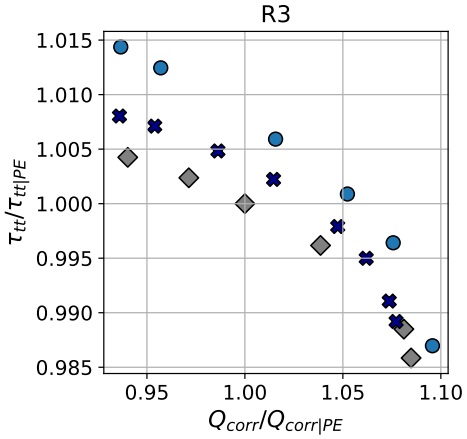

(c) Total-to-total temperature ratio Π_{tt} of R3.

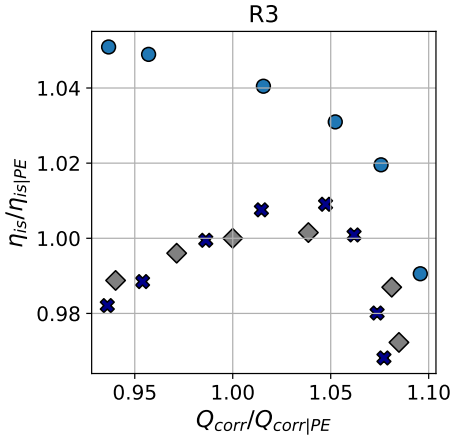

(d) Isentropic efficiency η_{is} of R3.

Figure C.6: Performance metrics for the third rotor row (R3) of the IHPC compressor.

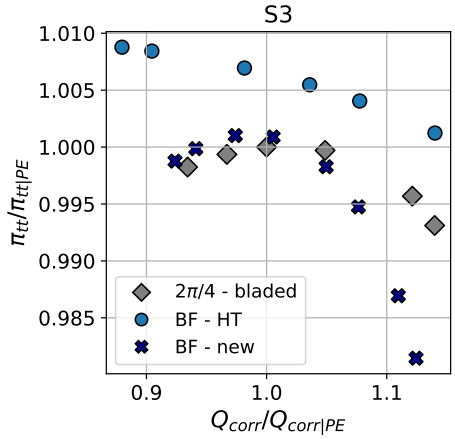

(a) Total-to-total pressure ratio π_{tt} of S3.

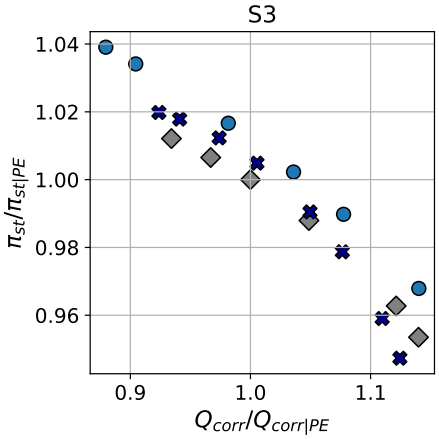

(b) Total-to-static pressure ratio π_{st} of S3.

Figure C.7: Performance metrics for the third stator row (S3) of the IHPC compressor.

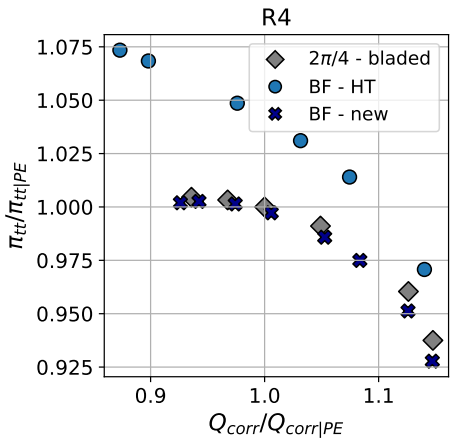

(a) Total-to-total pressure ratio π_{tt} of R4.

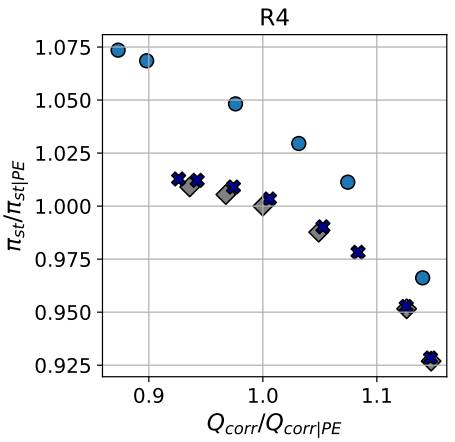

(b) Total-to-static pressure ratio π_{st} of R4.

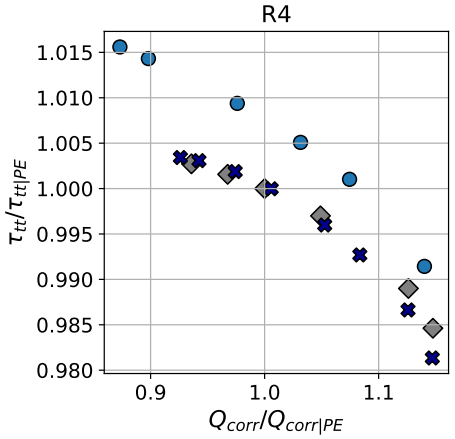

(c) Total-to-total temperature ratio Π_{tt} of R4.

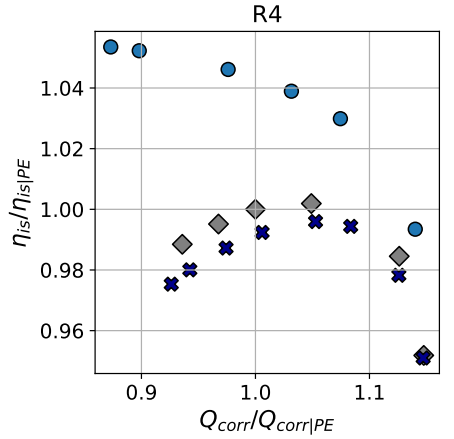

(d) Isentropic efficiency η_{is} of R4.

Figure C.8: Performance metrics for the fourth rotor row (R4) of the IHPC compressor.

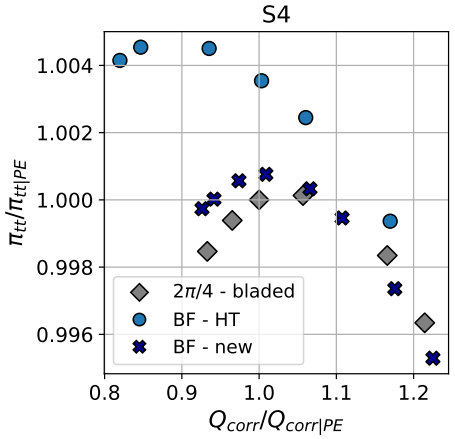

(a) Total-to-total pressure ratio π_{tt} of S4.

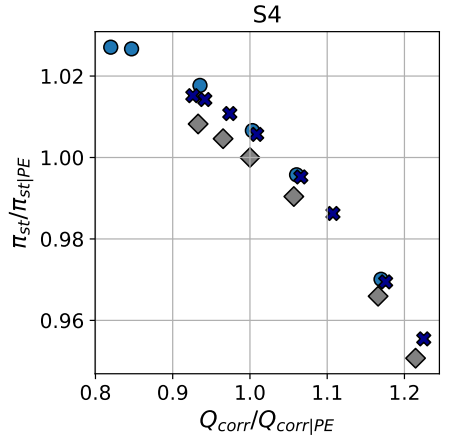

(b) Total-to-static pressure ratio π_{st} of S4.

Figure C.9: Performance metrics for the fourth stator row (S4) of the IHPC compressor.

BIBLIOGRAPHY

[1] I. ARIGA, N. KASAI, S. MASUDA, Y. WATANABE, AND I. WATANABE, *The effect of inlet distortion on the performance characteristics of a centrifugal compressor*, vol. Volume 1: Turbomachinery of Turbo Expo, 04 1982, p. V001T01A039, doi: 10.1115/82-GT-92.

[2] R. H. AUNGIER, *Centrifugal Compressors: A Strategy for Aerodynamic Design and Analysis*, ASME Press, 2000, doi: 10.1115/1.800938.

[3] A. AWES, G. DUFOUR, R. DAON, J. MARTY, R. BARRIER, AND X. CARBONNEAU, *Unsteady Body Force Methodology for Fan Operability Assessment under Clean and Distorted Inflow Conditions*, in AIAA Scitech 2021 Forum, American Institute of Aeronautics and Astronautics, Jan. 2021, doi: 10.2514/6.2021-0388.

[4] S. BARALON, U. HALL, AND L. E. ERIKSSON, *Viscous throughflow modelling of transonic compressors using a time-marching finite volume solver*, in ISABE- International Symposium on Air Breathing Engines, 13 th, Chattanooga, TN, 1997, pp. 502–510.

[5] A. BARETTER, *Analysis of the performance and stability of an axial compressor operating under inlet flow distortion*, PhD thesis, ENSAM Université, 2022, URL `http://www.theses.fr/2022HESAE049/document`.

[6] A. BARETTER, P. JOSEPH, O. ROUSSETTE, F. ROMANÓ, AND A. DAZIN, *Experimental analysis of an axial compressor operating under flow distortion*, vol. Volume 10A: Turbomachinery - Axial Flow Fan and Compressor Aerodynamics of Turbo Expo, 06 2022, p. V10AT29A030, doi: 10.1115/GT2022-82394.

[7] M. A. BENNINGTON, J. D. CAMERON, S. C. MORRIS, C. LEGAULT, S. T. BARROWS, J.-P. CHEN, G. S. MCNULTY, AND A. R. WADIA, *Investigation of tip-flow based stall criteria using rotor casing visualization*, in Turbo Expo, vol. 43161, 2008, pp. 641–651, doi: 10.1115/GT2008-51319.

[8] C. BENOIT, S. PÉRON, AND S. LANDIER, *Cassiopee: a CFD pre- and post-processing tool*, Aerospace Science and Technology, 45 (2015), pp. 272–283, doi: 10.1016/j.ast.2015.05.023.

[9] L. BERNARDOS, T. BONTEMPS, AND M. BALMASEDA, *Mola*. `https://github.com/onera/MOLA`, 2025.

[10] C. BESELT, R. RENNINGS, F. THIELE, AND D. PEITSCH, *Experimental and numerical investigations of rotating instability phenomenon in an axial compressor stator*, in 42nd AIAA fluid dynamics conference and exhibit, 2012, p. 2980, doi: 10.2514/6.2012-2980.

[11] N. C. BISSINGER AND T. BREUER, *Basic principles–gas turbine compatibility–intake aerodynamic aspects*, Encyclopedia of Aerospace Engineering, (2010), doi: 10.1002/9780470686652.eae487.

[12] C. BURBERI, V. MICHELASSI, A. SCOTTI DEL GRECO, S. LORUSSO, L. TAPINASSI, M. MARCONCINI, AND R. PACCIANI, *Validation of steady and unsteady CFD strategies in the design of axial compressors for gas turbine engines*, Aerospace Science and Technology, 107 (2020), p. 106307, doi: 10.1016/j.ast.2020.106307.

[13] L. CAMBIER, S. HEIB, AND S. PLOT, *The Onera elsA CFD software: input from research and feedback from industry*, Mechanics & Industry, 14 (2013), pp. 159–174, doi: 10.1051/meca/2013056.

[14] T. R. CAMP AND I. J. DAY, *A study of spike and modal stall phenomena in a low-speed axial compressor*, Journal of Turbomachinery, 120 (1998), pp. 393–401, doi: 10.1115/1.2841730.

[15] V. CARIES, J. BOUDET, AND E. LIPPINOIS, *Panel method for 3d inviscid flow simulation of low-pressure compressor rotors with tip-leakage flow*, International Journal of Turbomachinery, Propulsion and Power, 10 (2025), doi: 10.3390/ijtpp10010003.

[16] Y. A. ÇENGEL AND J. M. CIMBALA, *Fluid Mechanics: Fundamentals and Applications*, McGraw-Hill Education, New York, 4th ed., 2017.

[17] K. I. CHAN, *An assessment of computational procedures for eleven-stage compressor response to inlet distortion*, PhD thesis, Massachusetts Institute of Technology, 2003, URL `https://dspace.mit.edu/bitstream/handle/1721.1/82766/54070371-MIT.pdf`.

[18] J.-J. CHATTOT, *Actuator disk theory-steady and unsteady models*, Journal of Solar Energy Engineering, 136 (2014), p. 031012, doi: 10.1115/1.4026947.

[19] P. CHENG, M. PRELL, E. GREITZER, AND C. TAN, *Effects of compressor hub treatment on stator stall and pressure rise*, Journal of Aircraft, 21 (1984), pp. 469–475, doi: 10.2514/3.44995.

[20] N. CHIEREGHIN, D. G. MACMANUS, M. SAVILL, AND R. DUPUIS, *Dynamic distortion simulations for curved aeronautical intakes*, Royal Aeronautical Society (RAeS), 2015, URL `https://dspace.lib.cranfield.ac.uk/handle/1826/16075`.

[21] Y. COLIN, B. AUPOIX, J. BOUSSUGE, AND P. CHANEZ, *Numerical simulation of the distortion generated by crosswind inlet flows*, in International Symposium on Air Breathing Engines, 2007, URL `https://www.cerfacs.fr/~cfdbib/repository/TR_CFD_07_129.pdf`.

[22] N. COURTIADE AND X. OTTAVY, *Experimental study of surge precursors in a high-speed multistage compressor*, in Turbo Expo, vol. 44748, American Society of Mechanical Engineers, 2012, pp. 2417–2426, doi: 10.1115/1.4023462.

[23] ——, *Experimental study of surge precursors in a high-speed multistage compressor*, Journal of Turbomachinery, 135 (2013), p. 061018, doi: 10.1115/1.4023462.

[24] W. T. COUSINS, *History, philosophy, physics, and future directions of aircraft propulsion system/inlet integration*, vol. Volume 2: Turbo Expo 2004 of Turbo Expo, 06 2004, pp. 305–320, doi: 10.1115/GT2004-54210.

[25] L. COZZI, F. RUBECHINI, M. GIOVANNINI, M. MARCONCINI, A. ARNONE, A. SCHNEIDER, AND P. ASTRUA, *Capturing Radial Mixing in Axial Compressors With Computational Fluid Dynamics*, Journal of Turbomachinery, 141 (2019), p. 031012, doi: 10.1115/1.4041738.

[26] C. CREA, J. MARTY, R. BARRIER, S. COCHON, AND G. DUFOUR, *Body force modelling of a multi-stage high-pressure compressor under inlet distortion*, International Journal of Turbomachinery, Propulsion and Power, 10 (2025), doi: 10.3390/ijtpp10020012.

[27] ——, *Body force modelling of a multi-stage high-pressure compressor under inlet distortion*, Hannover, Germany, 2025, 16th European Turbomachinery Conference, URL `https://hal.science/hal-05033263/`.

[28] ——, *Effects of inlet distortion on the stability of a transonic multi-stage high-pressure compressor: A URANS-validated body force approach*, Orlando, Florida, Jan. 2026, AIAA SciTech Forum, doi: 10.2514/6.2026-0238.

[29] N. A. CUMPSTY, *Compressor Aerodynamics*, Longman Scientific & Technical, Harlow, UK, 1989.

[30] I. DAY, *Axial compressor performance during surge*, Journal of Propulsion and Power, 10 (1994), pp. 329–336, doi: 10.2514/3.23760.

[31] I. J. DAY, E. M. GREITZER, AND N. A. CUMPSTY, *Prediction of compressor performance in rotating stall*, Journal of Engineering for Power, 100 (1978), pp. 1–12, doi: 10.1115/1.3446318.

[32] P. DE HALLER, *Das verhalten von tragflügelgittern in axialverdichtern und im windkanal*, Brennstoff-Wärme-Kraft (BWK), 5 (1953), p. 24.

[33] J. B. DELANO, *The effect of high solidity on propeller characteristics at high forward speeds from wind-tunnel tests of the naca 4-(3)(06.3)-06 and naca 4-(3)(06.4)-09 two-blade propellers*, NACA Research Memorandum NACA-RM-L6L19, National Advisory Committee for Aeronautics, 1947, URL `https://ntrs.nasa.gov/api/citations/20050019462/downloads/20050019462.pdf`.

[34] J. D. DENTON, *Throughflow calculations for transonic axial flow turbines*, Journal of Engineering for Power, 100 (1978), pp. 212–218, doi: 10.1115/1.3446336.

[35] ——, *Loss mechanisms in turbomachines*, vol. 78897, American Society of Mechanical Engineers, 1993, doi: 10.1115/1.2929299.

[36] A. DEPPE, H. SAATHOFF, AND U. STARK, *Spike-type stall inception in axial-flow compressors*, in Proceeding of 6th Conference on Turbomachinery, Fluid Dynamics and Thermodynamics, Lille, France, 2005.

[37] W. S. DIEHL, *Effect of aerofoil aspect ratio on the slope of the lift curve*, Technical Report NACA TR 261, National Advisory Committee for Aeronautics (NACA), United States, 1922, URL `https://ntrs.nasa.gov/citations/19930080914`.

[38] S. L. DIXON AND C. HALL, *Fluid Mechanics and Thermodynamics of Turbomachinery*, Butterworth-Heinemann, Oxford / Boston, 2013, doi: 10.1016/C2011-0-05059-7.

[39] J. DODDS AND M. VAHDATI, *Rotating stall observations in a high speed compressor-Part I: Experimental study*, Journal of Turbomachinery, 137 (2015), p. 051002, doi: 10.1115/1.4028557.

[40] ——, *Rotating stall observations in a high speed compressor-Part II: Numerical study*, Journal of Turbomachinery, 137 (2015), p. 051003, doi: 10.1115/1.4028558.

[41] X. DONG, D. SUN, F. LI, AND X. SUN, *Stall margin enhancement of a novel casing treatment subjected to circumferential pressure distortion*, Aerospace Science and Technology, 73 (2018), pp. 239–255, doi: 10.1016/j.ast.2017.12.005.

[42] C. DOSNE, *Development and implementation of adjoint formulation of explicit body-force models for aero-propulsive optimizations*, PhD thesis, Institut Polytechnique de Paris, July 2024, URL `https://theses.hal.science/tel-04972890`.

[43] J. DU, F. LIN, J. CHEN, C. NIE, AND C. BIELA, *Flow structures in the tip region for a transonic compressor rotor*, Journal of Turbomachinery, 135 (2013), p. 031012, doi: 10.1115/1.4006779.

[44] J. DURHAM, *Observations of stall cells in a single stage compressor*, Research Memorandum 3376, Aeronautical Research Council, United Kingdom, 1962, URL `https://reports.aerade.cranfield.ac.uk/handle/1826.2/602`.

[45] J. ESCURET AND V. GARNIER, *Numerical simulations of surge and rotating-stall in multi-stage axial-flow compressors*, in 30th Joint Propulsion Conference and Exhibit, 1994, p. 3202, doi: 10.2514/6.1994-3202.

[46] A. FOURMAUX, *Assessment of a low storage technique for multi-stage turbomachinery navier-stokes computations*, vol. Unsteady Flows in Aeropropulsion of ASME International Mechanical Engineering Congress and Exposition, 11 1994, pp. 97–103, doi: 10.1115/IMECE1994-0595.

[47] M. FURUKAWA, K. SAIKI, K. YAMADA, AND M. INOUE, *Unsteady flow behavior due to breakdown of tip leakage vortex in an axial compressor rotor at near-stall condition*, in Turbo Expo, vol. 78545, American Society of Mechanical Engineers, 2000, p. V001T03A112, doi: 10.1115/2000-GT-0666.

[48] S. J. GALLIMORE, *Spanwise mixing in multistage axial flow compressors: Part II-throughflow calculations including mixing*, Journal of Turbomachinery, 108 (1986), pp. 10–16, doi: 10.1115/1.3262009.

[49] ——, *Viscous throughflow modeling of axial compressor bladerows using a tangential blade force hypothesis*, Journal of Turbomachinery, 120 (1998), pp. 662–670, doi: 10.1115/1.2841775.

[50] F. GAO, W. MA, G. ZAMBONINI, J. BOUDET, X. OTTAVY, L. LU, AND L. SHAO, *Large-eddy simulation of 3-D corner separation in a linear compressor cascade*, Physics of Fluids, 27 (2015), doi: 10.1063/1.4928246.

[51] C. W. GEAR, *The numerical integration of ordinary differential equations*, Mathematics of Computation, 21 (1967), pp. 146–156, URL https://www.ams.org/journals/mcom/1967-21-098/S0025-5718-1967-0225494-5/.

[52] GENCI - GRAND EQUIPEMENT NATIONAL DE CALCUL INTENSIF, 2025. https://www.genci.fr/. Accessed: 2025-04-07.

[53] J. W. GIBBS, *On the fundamental formulae of dynamics*, American Journal of Mathematics, 2 (1879), pp. 49–64, doi: 10.2307/2369196.

[54] D. GIL-PRIETO, P. K. ZACHOS, D. G. MACMANUS, AND G. MCLELLAND, *Unsteady characteristics of s-duct intake flow distortion*, Aerospace Science and Technology, 84 (2019), pp. 938–952, doi: 10.1016/j.ast.2018.10.020.

[55] B. GODARD, N. BEN NASR, R. BARRIER, J. MARTY, N. GOURDAIN, AND E. DE JAEGHERE, *Methodologies for Turbofan Inlet Aerodynamics Prediction*, in 35th AIAA Applied Aerodynamics Conference, Denver, Colorado, June 2017, American Institute of Aeronautics and Astronautics, doi: 10.2514/6.2017-3413.

[56] Y. GONG, *A computational model for rotating stall and inlet distortions in multistage compressors*, PhD thesis, Massachusetts Institute of Technology, 1999, URL https://dspace.mit.edu/handle/1721.1/9733.

[57] S. E. GORRELL, J. YAO, AND A. R. WADIA, *High fidelity URANS analysis of swirl generation and fan response to inlet distortion*, AIAA paper, 4985 (2008), p. 13, doi: 10.2514/6.2008-4985.

[58] C. GOUT, *Méthodes numériques pour la simulation aux grandes échelles LES mono-canal d'étages de turbomachines*, PhD thesis, Institut National Polytechnique de Toulouse-INPT, 2022, URL https://theses.hal.science/tel-04248256.

[59] E. M. GREITZER, *Surge and rotating stall in axial flow compressors-Part I: Theoretical compression system model*, Journal of Engineering for Power, 98 (1976), pp. 190–198, doi: 10.1115/1.3446138.

[60] ——, *Surge and rotating stall in axial flow compressors-Part II: Experimental results and comparison with theory*, Journal of Engineering for Power, 98 (1976), pp. 199–211, doi: 10.1115/1.3446139.

[61] ——, *Axial compressor stall phenomena*, Journal of Fluids Engineering, 102 (1980), pp. 134–151, doi: 10.1115/1.3240634.

[62] E. M. GREITZER, C. S. TAN, AND M. B. GRAF, *Internal Flow: Concepts and Applications*, Cambridge Engine Technology Series, Cambridge University Press, 2004, doi: 10.1017/CBO9780511616709.

[63] J. GUO AND J. HU, *Development of body force model for steady inlet distortions in high-speed multistage compressor*, Proceedings of the Institution of Mechanical Engineers, Part G: Journal of Aerospace Engineering, 231 (2017), pp. 1650–1659, doi: 10.1177/0954410016656880.

[64] ——, *A three-dimensional computational model for inlet distortion in fan and compressor*, Proceedings of the Institution of Mechanical Engineers, Part A: Journal of Power and Energy, 232 (2018), pp. 144–156, doi: 10.1177/0957650917719811.

[65] D. HAGELSTEIN, R. A. VAN DEN BRAEMBUSSCHE, R. KEIPER, AND M. RAUTENBERG, *Experimental investigation of the circumferential static pressure distortion in centrifugal compressor stages*, in Turbo Expo, 1997, doi: 10.1115/97-GT-050.

[66] A. HALE AND W. OBRIEN, *A three-dimensional turbine engine analysis compressor code (TEACC) for steady-state inlet distortion*, vol. Volume 4: Manufacturing Materials and Metallurgy; Ceramics; Structures and Dynamics; Controls, Diagnostics and Instrumentation; Education; IGTI Scholar Award of Turbo Expo, 06 1997, p. V004T16A005, doi: 10.1115/97-GT-124.

[67] D. K. HALL, *Analysis of civil aircraft propulsors with boundary layer ingestion*, PhD thesis, Massachusetts Institute of Technology, 2015, URL `http://dspace.mit.edu/handle/1721.1/7582`.

[68] D. K. HALL, E. GREITZER, A. URANGA, M. DRELA, AND S. PANDYA, *Inlet flow distortion in an advanced civil transport boundary layer ingesting engine installation*, Journal of Turbomachinery, 144 (2022), p. 101002, doi: 10.1115/1.4054035.

[69] A. HARTEN, *High resolution schemes for hyperbolic conservation laws*, Journal of Computational Physics, 49 (1983), pp. 357–393, doi: 10.1006/jcph.1997.5713.

[70] W. HAWTHORNE, N. MITCHELL, J. MCCUNE, AND C. TAN, *Nonaxisymmetric flow through annular actuator disks: Inlet distortion problem*, Journal of Engineering for Power, 100 (1978), pp. 604–617, doi: 10.1115/1.3446409.

[71] A. HERGT, J. KLINNER, J. WELLNER, C. WILLERT, S. GRUND, W. STEINERT, AND M. BEVERSDORFF, *The present challenge of transonic compressor blade design*, Journal of Turbomachinery, 141 (2019), p. 091004, doi: 10.1115/1.4043329.

[72] A. HERGT, R. MEYER, AND K. ENGEL, *Effects of vortex generator application on the performance of a compressor cascade*, Journal of Turbomachinery, 135 (2013), p. 021026, doi: 10.1115/1.4006605.

[73] M. HEWKIN-SMITH, G. PULLAN, S. GRIMSHAW, E. GREITZER, AND Z. SPAKOVSZKY, *The role of tip leakage flow in spike-type rotating stall inception*, in Turbo Expo, vol. 50817, American Society of Mechanical Engineers, 2017, p. V02DT46A009, doi: 10.1115/1.4042250.

[74] D. J. HILL AND J. J. DEFOE, *Innovations in Body Force Modeling of Transonic Compressor Blade Rows*, International Journal of Rotating Machinery, 2018 (2018), pp. 1–12, doi: 10.1155/2018/6398501.

[75] ——, *Scaling of incidence variations with inlet distortion for a transonic axial compressor*, Journal of Turbomachinery, 142 (2020), p. 021003, doi: 10.1115/1.4045464.

[76] W. HORN, K.-J. SCHMIDT, AND S. STAUDACHER, *Effects of compressor tip injection on aircraft engine performance and stability*, Journal of Turbomachinery, 131 (2009), p. 031011, doi: 10.1115/1.2988159.

[77] T. HOUGHTON AND I. DAY, *Stability enhancement by casing grooves: The importance of stall inception mechanism and solidity*, Journal of Turbomachinery, 134 (2011), p. 021003, doi: 10.1115/1.4002986.

[78] T. P. HYNES AND E. M. GREITZER, *A method for assessing effects of circumferential flow distortion on compressor stability*, Journal of Turbomachinery, 109 (1987), pp. 371–379, doi: 10.1115/1.3262116.

[79] INTERNATIONAL AIR TRANSPORT ASSOCIATION, *Fly net zero: Iata's commitment to achieving net-zero carbon emissions by 2050*, 2021.
Accessed: 2025-11-26.

[80] INTERNATIONAL CIVIL AVIATION ORGANIZATION, *Icao special environment report – on international aviation cleaner energy transition*, 2023.
Accessed: 2025-11-26.

[81] W. G. JOO AND T. P. HYNES, *The simulation of turbomachinery blade rows in asymmetric flow using actuator disks*, Journal of Turbomachinery, 119 (1997), pp. 723–732, doi: 10.1115/1.2841182.

[82] J. KERNER, *An assessment of body force representations for compressor stall simulation*, Master's thesis, Massachusetts Institute of Technology, 2010, URL `https://dspace.mit.edu/handle/1721.1/57882`.

[83] J. L. KERREBROCK, *Flow in transonic compressors*, AIAA Journal, 19 (1981), pp. 4–19, doi: 10.2514/3.50919.

[84] A. P. KOTTAPALLI, *Development of a body force model for centrifugal compressors*, Master's thesis, Massachusetts Institute of Technology, 2013, URL `https://dspace.mit.edu/handle/1721.1/85697`.

[85] F. KRAVTSOFF, M. SCHVALLINGER, AND X. OTTAVY, *A CFD-based throughflow solver using cascade potential theory for axial compressor flow modeling*, in Turbo Expo, vol. 87103, American Society of Mechanical Engineers, 2023, p. V13CT32A024, doi: 10.1115/GT2023-102875.

[86] B. KUSTERS AND H. SCHREIBER, *Compressor cascade flow with strong shock-wave/boundary-layer interaction*, AIAA Journal, 36 (1998), pp. 2072–2078, doi: 10.2514/2.308.

[87] P. LAMPART, *Tip leakage flows in turbines*, TASK Quarterly. Scientific Bulletin of Academic Computer Centre in Gdansk, 10 (2006), pp. 139–175, URL `https://journal.mostwiedzy.pl/TASKQuarterly/article/view/2110`.

[88] G. M. LASKOWSKI, J. KOPRIVA, V. MICHELASSI, S. SHANKARAN, U. PALIATH, R. BHASKARAN, Q. WANG, C. TALNIKAR, Z. J. WANG, AND F. JIA, *Future directions of high fidelity CFD for aerothermal turbomachinery analysis and design*, in 46th AIAA fluid dynamics conference, 2016, p. 3322, doi: 10.2514/6.2016-3322.

[89] K.-B. LEE, M. WILSON, AND M. VAHDATI, *Effects of inlet disturbances on fan stability*, Journal of Engineering for Gas Turbines and Power, 141 (2019), p. 051014, doi: 10.1115/1.4042204.

[90] A. LESSER, J. ISELER, AND R. NIEHUIS, *Numerical investigation of a highly loaded axial compressor stage with inlet distortions*, vol. Volume 7: Turbomachinery, Parts A, B, and C of Turbo Expo, 06 2011, pp. 381–391, doi: 10.1115/GT2011-46457.

[91] C. LI, T. KE, J. ZHANG, H. ZHANG, AND W. HUANG, *Experimental and numerical investigation of the unsteady tip leakage flow in axial compressor cascade*, Journal of Thermal Science, 22 (2013), pp. 103–110, doi: 10.1007/s11630-013-0599-9.

[92] J. LI, J. DU, S. GENG, F. LI, AND H. ZHANG, *Tip air injection to extend stall margin of multi-stage axial flow compressor with inlet radial distortion*, Aerospace Science and Technology, 96 (2020), p. 105554, doi: 10.1016/j.ast.2019.105554.

[93] J. LI, J. DU, Y. LIU, H. ZHANG, AND C. NIE, *Effect of inlet radial distortion on aerodynamic stability in a multi-stage axial flow compressor*, Aerospace Science and Technology, 105 (2020), p. 105886, doi: 10.1016/j.ast.2020.105886.

[94] J. LI, J. TENG, M. FERLAUTO, M. ZHU, AND X. QIANG, *An improved stall prediction model for axial compressor stage based on diffuser analogy*, Aerospace Science and Technology, 127 (2022), p. 107692, doi: 10.1016/j.ast.2022.107692.

[95] Q. LI, T. PAN, Z. LI, T. SUN, AND Y. GONG, *Experimental study of compressor instability inception in a transonic axial flow compressor*, in Turbo Expo, vol. 45639, American Society of Mechanical Engineers, 2014, p. V02DT44A004, doi: 10.1115/GT2014-25190.

[96] Z. LI, D. SUN, X. DONG, AND X. SUN, *A review on aero-engine inlet-compressor integration and inlet flow distortion in axial compressors*, Fundamental Research, (2024), doi: 10.1016/j.fmre.2024.03.018.

[97] S. LIEBLEIN, *Aerodynamic design of axial-flow compressors 6: Experimental flow in two-dimensional cascades*, NACA Research Memorandum NACA-RM-E55K01a, National Advisory Committee for Aeronautics, Lewis Flight Propulsion Laboratory, 1955, URL `https://digital.library.unt.edu/ark:/67531/metadc65390/`.

[98] Y. LIU, J. DU, J. LI, Z. FAN, M. ZHANG, D. ZHAO, AND M. SELLIER, *Experimental investigation on unsteady pre-stall behaviors of axial compressor with circumferential total pressure distortion*, Aerospace Science and Technology, 158 (2025), p. 109937, doi: 10.1016/j.ast.2025.109937.

[99] J. P. LONGLEY, *Measured and Predicted Effects of Inlet Distortion on Axial Compressors*, in Volume 1: Turbomachinery, Brussels, Belgium, June 1990, American Society of Mechanical Engineers.

[100] J. P. LONGLEY, H. W. SHIN, R. E. PLUMLEY, P. D. SILKOWSKI, I. J. DAY, E. M. GREITZER, C. S. TAN, AND D. C. WISLER, *Effects of rotating inlet distortion on multistage compressor stability*, Journal of Turbomachinery, 118 (1996), pp. 181–188, doi: 10.1115/1.2836624.

[101] J. R. LUCAS, W. F. O'BRIEN, AND A. M. FERRAR, *Effect of BLIType Inlet Distortion on Turbofan Engine Performance*, in Volume 1A: Aircraft Engine; Fans and Blowers, Düsseldorf, Germany, June 2014, American Society of Mechanical Engineers, doi: 10.1115/GT2014-26666.

[102] Y. MA, J. CUI, N. R. VADLAMANI, AND P. TUCKER, *Effect of fan on inlet distortion: Mixed-fidelity approach*, AIAA Journal, 56 (2018), pp. 2350–2360, doi: 10.2514/1.J056858.

[103] Y. MA, N. R. VADLAMANI, J. CUI, AND P. TUCKER, *Comparative studies of RANS versus large eddy simulation for fan–intake interaction*, Journal of Fluids Engineering, 141 (2019), p. 031106, doi: 10.1115/1.4041393.

[104] A. MAGRINI, *Study of Body Force Modelling for Coupled Fan/Airframe Simulations*, PhD thesis, University of Padova, 2021, URL `https://hdl.handle.net/11577/3391182`.

[105] F. E. MARBLE, *Three-dimensional flow in turbomachines*, in Aerodynamics of Turbines and Compressors, vol. 10, Princeton University Press, Princeton, NJ, 1964, pp. 83–166, doi: 10.1515/9781400885985.

[106] J. MARTY AND B. AUPOIX, *Interaction of shrouded stator flow and main flow and its influence on performances of a three-stage high pressure compressor*, Proceedings of the Institution of Mechanical Engineers, Part A: Journal of Power and Energy, 226 (2012), pp. 489–500, doi: 10.1177/0957650911414322.

[107] J. MARTY, R. BARRIER, AND E. GARNIER, *Impact of distortions due to separation in S-duct inlet on compressor stage behavior and performances*, in 23rd AIAA Computational Fluid Dynamics Conference, Denver, Colorado, June 2017, American Institute of Aeronautics and Astronautics, doi: 10.2514/6.2017-3795.

[108] R. S. MAZZAWY, *Multiple Segment Parallel Compressor Model for Circumferential Flow Distortion*, Journal of Engineering for Power, 99 (1977), pp. 288–296, doi: 10.1115/1.3446288.

[109] N. M. MCDOUGALL, N. A. CUMPSTY, AND T. P. HYNES, *Stall inception in axial compressors*, Journal of Turbomachinery, 112 (1990), pp. 116–123, doi: 10.1115/1.2927406.

[110] R. MEYER, S. SCHULZ, K. LIESNER, H. PASSRUCKER, AND R. WUNDERER, *A parameter study on the influence of fillets on the compressor cascade performance*, Journal of Theoretical and Applied Mechanics (JTAM), Vol 50 (2012), URL `https://bibliotekanauki.pl/articles/281953.pdf`.

[111] L. MING, Y. WU, Z. YANG, Z. ZHU, H. OUYANG, AND L. LI, *Large eddy simulation investigation of S-shaped intake distortion and swirl characteristics*, Aerospace Science and Technology, 141 (2023), p. 108578, doi: 10.1016/j.ast.2023.108578.

[112] R. J. MONAGHAN, *A review and assessment of various formulae for turbulent skin friction in compressible flow*, A.R.C. Technical Report C.P. No. 141 (15.464), Aeronautical Research Council, 1953, URL https://reports.aerade.cranfield.ac.uk/bitstream/handle/1826.2/155/arc-cp-0142.pdf.

[113] F. K. MOORE AND E. M. GREITZER, *A theory of post-stall transients in axial compression systems: Part I-development of equations*, Journal of Engineering for Gas Turbines and Power, 108 (1986), pp. 68–76, doi: 10.1115/1.3239887.

[114] A. NASERI, M. BOROOMAND, AND S. SAMMAK, *Numerical investigation of effect of inlet swirl and total-pressure distortion on performance and stability of an axial transonic compressor*, Journal of Thermal Science, 25 (2016), pp. 501–510, doi: 10.1007/s11630-016-0891-6.

[115] NUMECA INTERNATIONAL.
IGG/AutoGrid5™ version 12.2, https://www.numeca.com.

[116] X. OTTAVY, N. COURTIADE, AND N. GOURDAIN, *Experimental and computational methods for flow investigation in high-speed multistage compressor*, Journal of Propulsion and Power, 28 (2012), pp. 1141–1155, doi: 10.2514/1.B34412.

[117] P. OURO, T. STOESSER, AND L. RAMÍREZ, *Effect of blade cambering on dynamic stall in view of designing vertical axis turbines*, Journal of Fluids Engineering, 140 (2018), p. 061104, doi: 10.1115/1.4039235.

[118] J. H. PAGE, P. HIELD, AND P. G. TUCKER, *Effect of inlet distortion features on transonic fan rotor stall*, Journal of Turbomachinery, 140 (2018), p. 071008, doi: 10.1115/1.4040030.

[119] T. PAN, Q. LI, Z. LI, AND Y. GONG, *Effects of radial loading distribution on partial-surge-initiated instability in a transonic axial flow compressor*, Journal of Turbomachinery, 139 (2017), p. 101010, doi: 10.1115/1.4036646.

[120] H. PANTEL, F. FALISSARD, AND G. DUFOUR, *Assessment of Reynolds-Averaged Navier–Stokes/blade element theory body force method for propeller modeling*, AIAA Journal, 62 (2024), pp. 758–775, doi: 10.2514/1.J063302.

[121] S. PAZIREH, *Body Force Modeling of Axial Turbomachines Without Calibration*, PhD thesis, University of Windsor (Canada), 2020, URL https://uwindsor.scholaris.ca/server/api/core/bitstreams/ccf4a1af-d6ef-48ae-9a8c-2c097cdb4196/content.

[122] R. E. PEACOCK, *A review of turbomachinery tip gap effects: Part 1: Cascades*, International Journal of Heat and Fluid Flow, 3 (1982), pp. 185–193, doi: 10.1016/0142-727X(82)90017-0.

[123] H. PEARSON AND A. MCKENZIE, *Wakes in axial compressors*, The Aeronautical Journal, 63 (1959), pp. 415–416, doi: 10.1017/S0368393100071273.

[124] A. PETERS, *Ultra-short nacelles for low fan pressure ratio propulsors*, PhD thesis, Massachusetts Institute of Technology, 2014, URL https://dspace.mit.edu/handle/1721.1/87128.

[125] A. PETERS, Z. S. SPAKOVSZKY, W. K. LORD, AND B. ROSE, *Ultrashort nacelles for low fan pressure ratio propulsors*, Journal of Turbomachinery, 137 (2015), URL `https://dspace.mit.edu/handle/1721.1/87128`.

[126] D. POIRIER, S. ALLMARAS, D. MCCARTHY, M. SMITH, AND F. ENOMOTO, *The cgns system*, in 29th AIAA, Fluid Dynamics Conference, 1998, p. 3007, doi: 10.2514/6.1998-3007.

[127] S. PUTERBAUGH AND M. BRENDEL, *Tip clearance flow-shock interaction in a transonic compressor rotor*, Journal of Propulsion and Power, 13 (1997), pp. 24–30, doi: 10.2514/2.5146.

[128] R. P. M. RADEMAKERS, S. BINDL, AND R. NIEHUIS, *Effects of flow distortions as they occur in s-duct inlets on the performance and stability of a jet engine*, Journal of Engineering for Gas Turbines and Power, 138 (2015), p. 022605, doi: 10.1115/1.4031305.

[129] C. REID, *The response of axial flow compressors to intake flow distortion*, in Proceedings of the 1969 ASME Gas Turbine Conference and Products Show, American Society of Mechanical Engineers, 1969, doi: 10.1115/69-GT-29.

[130] N. REUSS AND C. MUNDT, *Experimental investigations of pressure distortions on the high-pressure compressor operating behavior*, Journal of Propulsion and Power, 25 (2009), pp. 653–667, doi: 10.2514/1.37412.

[131] M. RIGHI, *Three-dimensional through-flow modelling of axial compressor rotating stall and surge*, PhD thesis, Cranfield University, 2018, URL `https://dspace.lib.cranfield.ac.uk/handle/1826/19222`.

[132] M. RIGHI, L. E. FERRER-VIDAL, AND V. PACHIDIS, *Body-force and mean-line models for the generation of axial compressor sub-idle characteristics*, The Aeronautical Journal, 124 (2020), pp. 1683–1701, doi: 10.1017/aer.2020.58.

[133] M. RIGHI, V. PACHIDIS, L. KÖNÖZSY, T. GIERSCH, AND S. SCHRAPE, *Experimental validation of a three-dimensional through-flow model for high-speed compressor surge*, Aerospace Science and Technology, 128 (2022), p. 107775, doi: 10.1016/j.ast.2022.107775.

[134] M. RIGHI, V. PACHIDIS, L. KÖNÖZSY, AND L. PAWSEY, *Three-dimensional through-flow modelling of axial flow compressor rotating stall and surge*, Aerospace Science and Technology, 78 (2018), pp. 271–279, doi: 10.1016/j.ast.2018.04.021.

[135] W. B. ROBERTS, G. K. SEROVY, AND D. M. SANDERCOCK, *Design point variation of three-dimensional loss and deviation for axial compressor middle stages*, Journal of Turbomachinery, 110 (1988), pp. 426–433, doi: 10.1115/1.3262215.

[136] P. L. ROE, *Approximate riemann solvers, parameter vectors, and difference schemes*, Journal of Computational Physics, 43 (1981), pp. 357–372, doi: 10.1016/0021-9991(81)90128-5.

[137] F. ROMANÒ, C. RANNOU, A. BARETTER, J. MARTY, P. JOSEPH, AND A. DAZIN, *How inlet flow inhomogeneities can affect the transition to stall in an axial compressor?*, in Proceedings of the 16th European Turbomachinery Conference (ETC16), Turbomachinery, Fluid Dynamics and Thermodynamics, Hannover, Germany, Mar. 2025.

[138] S. SAITO, M. FURUKAWA, K. YAMADA, K. WATANABE, A. MATSUOKA, AND N. NIWA, *Mechanisms and quantitative evaluation of flow loss generation in a multi-stage transonic axial compressor*, in Turbo Expo, vol. 58554, American Society of Mechanical Engineers, 2019, p. V02AT39A008, doi: 10.1115/GT2019-90439.

[139] D. M. SANDERCOCK AND N. L. SANGER, *Some observations of the effects of radial distortions on performance of a transonic rotating blade row*, NASA Technical Note NASA-TN-D-7824, NASA Lewis Research Center, Cleveland, OH, Dec. 1974, URL `https://ntrs.nasa.gov/api/citations/19750004173/downloads/19750004173.pdf`. Document ID: 19750004173.

[140] J. SANS, J.-F. BROUCKAERT, AND S. HIERNAUX, *Experimental and numerical investigations of the solidity effect on a linear compressor cascade*, in Turbo Expo, vol. 56635, American Society of Mechanical Engineers, 2015, p. V02AT37A034, doi: 10.1115/GT2015-43204.

[141] J. SCHREIBER, *Investigation of experimental and numerical methods, and analysis of stator clocking and instabilities in a high-speed multistage compressor*, PhD thesis, Université de Lyon, Dec. 2016, URL `https://hal.science/tel-01508542`.

[142] J. SCHREIBER, X. OTTAVY, G. NGO BOUM, S. AUBERT, AND F. SICOT, *Numerical simulation of the flow field in a high speed multistage compressor: study of the time discretization sensitivity*, in Turbo Expo, vol. 56642, American Society of Mechanical Engineers, 2015, p. V02BT39A006, doi: 10.1115/GT2015-42114.

[143] Y. SHEORAN, B. BOULDIN, AND P. M. KRISHNAN, *Compressor performance and operability in swirl distortion*, Journal of Turbomachinery, 134 (2011), p. 041008, doi: 10.1115/1.4003657.

[144] M. SHUR, M. STRELETS, A. TRAVIN, J. CHRISTOPHE, K. KUCUKCOSKUN, C. F. SCHRAM, S. SACK, AND M. ÅBOM, *Effect of inlet distortions on ducted fan noise*, in 22nd AIAA/CEAS Aeroacoustics Conference, 2016, p. 2819, doi: 10.2514/6.2016-2819.

[145] J.-F. SIMON, *Contribution to Throughflow Modelling for Axial Flow Turbomachines*, PhD thesis, Université de Liege, 2007, URL `https://orbi.uliege.be/bitstream/2268/314848/1/thesisJFSimon.pdf`.

[146] B. SMITH, *A near wall model for the k-l two equation turbulence model*, in Fluid Dynamics Conference, 1994, p. 2386, doi: 10.2514/6.1994-2386.

[147] M. SONG, H. XIE, B. YANG, AND S. ZHANG, *Influence of tip clearance on flow characteristics of axial compressor*, Processes, 8 (2020), p. 1445, doi: 10.3390/pr8111445.

[148] Z. S. SPAKOVSZKY, H. J. WEIGL, J. D. PADUANO, C. M. VAN SCHALKWYK, K. L. SUDER, AND M. M. BRIGHT, *Rotating stall control in a high-speed stage with inlet distortion: Part I-radial distortion*, Journal of Turbomachinery, 121 (1999), pp. 510–516, doi: 10.1115/1.2841345.

[149] S. SPINNER, D. KELLER, R. SCHNELL, AND M. TROST, *A blade element theory based actuator disk methodology for modeling of fan engines in RANS simulations*, in AIAA Aviation 2020 Forum, 2020, p. 2749, doi: 10.2514/6.2020-2749.

[150] A. SPURR, *The prediction of 3D transonic flow in turbomachinery using a combined through-flow and blade-to-blade time marching method*, International Journal of Heat and Fluid Flow, 2 (1980), pp. 189–199, doi: 10.1016/0142-727X(80)90013-2.

[151] A. STENNING, *Inlet distortion effects in axial compressors*, Journal of Fluids Engineering, 102 (1980), pp. 7–13, doi: 10.1115/1.3240630.

[152] J. A. STORER AND N. A. CUMPSTY, *Tip leakage flow in axial compressors*, Journal of Turbomachinery, 113 (1991), pp. 252–259, doi: 10.1115/1.2929095.

[153] K. L. SUDER, M. D. HATHAWAY, S. A. THORP, A. J. STRAZISAR, AND M. B. BRIGHT, *Compressor stability enhancement using discrete tip injection*, Journal of Turbomachinery, 123 (2001), pp. 14–23, doi: 10.1115/1.1330272.

[154] D. SUN, X. SHEN, D. XU, F. NING, J. LI, AND X. SUN, *Analysis of flow characteristics and flow stability on an axial compressor with inlet temperature ramp distortion*, Aerospace Science and Technology, (2025), p. 110457, doi: 10.1016/j.ast.2025.110457.

[155] W. THOLLET, *Body force modeling of fan-airframe interactions*, PhD thesis, ISAE-SUPAERO, July 2017, URL `http://www.theses.fr/2017ESAE0010/document`.

[156] W. THOLLET, G. DUFOUR, X. CARBONNEAU, AND F. BLANC, *Assessment of Body Force Methodologies for the Analysis of Intake-Fan Aerodynamic Interactions*, in Volume 2C: Turbomachinery, Seoul, South Korea, June 2016, American Society of Mechanical Engineers, doi: 10.1115/GT2016-57014.

[157] P. TIANYU, Y. JIANDONG, L. HANAN, AND L. QIUSHI, *Impact of circumferential inlet distortion on different types of stall inceptions in a transonic compressor*, Chinese Journal of Aeronautics, 37 (2024), pp. 107–117, doi: 10.1016/j.cja.2024.07.018.

[158] H.-O. TO AND R. J. MILLER, *The effect of aspect ratio on compressor performance*, Journal of Turbomachinery, 141 (2019), p. 081011, doi: 10.1115/1.4043219.

[159] M. TRYFONIDIS, O. ETCHEVERS, J. D. PADUANO, A. H. EPSTEIN, AND G. J. HENDRICKS, *Prestall behavior of several high-speed compressors*, Journal of Turbomachinery, 117 (1995), pp. 62–80, doi: 10.1115/1.2835644.

[160] G. D. VAN ALBADA, B. VAN LEER, AND W. ROBERTS JR, *A comparative study of computational methods in cosmic gas dynamics*, Astronomy and Astrophysics, vol. 108, no. 1, Apr. 1982, p. 76-84., 108 (1982), pp. 76–84, doi: 10.1007/978-3-642-60543-7_6.

[161] G. J. WALKER, *Turbulent skin friction on axial compressor blading*, AIAA Journal, 28 (1990), pp. 1201–1202, doi: 10.2514/3.25193.

[162] F. WANG, M. CARNEVALE, L. DI MARE, AND S. GALLIMORE, *Simulation of multistage compressor at off-design conditions*, Journal of Turbomachinery, 140 (2018), p. 021011, doi: 10.1115/1.4038317.

[163] S. WANG, Y. CHEN, AND Y. WU, *Effect of tip clearance on non-synchronous propagating flow disturbances of compressor rotors under high aerodynamic loading conditions*, Advances in Aerodynamics, 6 (2024), p. 17, doi: 10.1186/s42774-024-00178-0.

[164] F. WILLEMS AND B. DE JAGER, *Modeling and control of compressor flow instabilities*, IEEE Control Systems Magazine, 19 (2002), pp. 8–18, doi: 10.1109/37.793434.

[165] D. C. WISLER, *Advanced compressor and fan systems*, General Electric Aircraft Engine Business Group, 1988.

[166] D. XU, C. HE, D. SUN, AND X. SUN, *Stall inception prediction of axial compressors with radial inlet distortions*, Aerospace Science and Technology, 109 (2021), p. 106433, doi: 10.1016/j.ast.2020.106433.

[167] Z. YANG, Y. WU, Z. LIU, S. ZHANG, X. XI, J. TIAN, AND H. OUYANG, *Tip flow on rotating instability on an axial compressor with different tip clearances*, Aerospace Science and Technology, 139 (2023), p. 108364, doi: 10.1016/j.ast.2023.108364.

[168] M. ZAAG, R. BOTEZ, AND T. WONG, *Cessna citation x engine model identification using neural networks and extended great deluge algorithms*, INCAS BULLETIN, 11 (2019), pp. 195–207, doi: 10.13111/2066-8201.2019.11.2.16.

[169] G. ZAMBONINI, *Unsteady dynamics of corner separation in a linear compressor cascade*, PhD thesis, École Centrale de Lyon, Lyon, France, 2016, URL `http://www.theses.fr/2016LYSEC049/document`.

[170] G. ZAMBONINI, X. OTTAVY, AND J. KRIEGSEIS, *Corner separation dynamics in a linear compressor cascade*, Journal of Fluids Engineering, 139 (2017), p. 061101, doi: 10.1115/1.4035876.

[171] W. ZHANG AND M. VAHDATI, *A parametric study of the effects of inlet distortion on fan aerodynamic stability*, Journal of Turbomachinery, 141 (2019), p. 011011, doi: 10.1115/1.4041376.

[172] Y. ZHANG, X. LU, W. CHU, AND J. ZHU, *Numerical investigation of the unsteady tip leakage flow and rotating stall inception in a transonic compressor*, Journal of Thermal Science, 19 (2010), pp. 310–317, doi: 10.1007/s11630-010-0388-7.

SUMMARY

FRENCH SUMMARY

Introduction

La conception des turbomachines aéronautiques est aujourd'hui fortement influencée par des objectifs environnementaux et des réglementations internationales exigeant une réduction drastique des émissions, avec une trajectoire vers la neutralité carbone d'ici 2050. Pour répondre à ces exigences, les architectures de moteurs évoluent vers des configurations plus intégrées et aérodynamiquement avancées, telles que l'ingestion de couche limite (BLI), les entrées en S ou les nacelles ultra-compactes, qui améliorent les performances globales mais génèrent des écoulements d'entrée fortement non uniformes et instationnaires. Ces écoulements peuvent présenter séparations, swirl, écoulements secondaires et fortes variations spatiales et temporelles, qui sont encore renforcées par des conditions opérationnelles réelles : vent de travers, manoeuvres, extraction ou injection d'écoulement de purge, ingestion de gaz chauds ou recirculés. Ces distorsions posent de nouveaux défis aérodynamiques pour les compresseurs, notamment en termes d'opérabilité et de sécurité.

La distorsion d'entrée se traduit par une distribution non uniforme des grandeurs d'écoulement (vitesse, température, pression, direction) au niveau du compresseur, par rapport à l'hypothèse d'entrée uniforme utilisée lors de la conception. Ces non-uniformités, souvent radiales et circumférentielles, qui peuvent être également instationnaires, imposent des charges variables sur les aubes. Cela peut provoquer des surcharges locales, des séparations, une baisse de la capacité de compression et une réduction de la marge de décrochage. Dans les cas sévères, elles peuvent conduire à un décrochage ou un pompage, avec des conséquences importantes sur l'opérabilité, la sécurité et la maintenance. Les compresseurs haute pression (HPC) sont particulièrement sensibles : la distorsion peut se propager sur plusieurs étages et interagir avec des structures complexes (chocs, fuites de bout d'aube, vortex secondaires, traînées), et les effets s'amplifient en raison du couplage non linéaire et du mélange inter-étages. Pour limiter ces impacts, les compresseurs intègrent des solutions de robustesse aérodynamique (profilage des aubes, optimisation géométrique) ainsi que des stratégies de contrôle (bleed, traitements de parois). Toutefois, une prédiction fiable du comportement sous distorsion reste indispensable dès les phases de conception.

La modélisation de la distorsion est complexe en raison de sa propagation dynamique et de sa tridimensionnalité. Les outils de conception préliminaire (mean-line, throughflow) supposent une entrée uniforme et négligent les effets non axisymétriques, sous-estimant ainsi les pénalités de performance et les risques d'instabilité. Les simulations CFD haute fidélité (URANS) permettent de capturer ces phénomènes, mais leur coût computationnel les réserve aux phases avancées de la conception. Des modèles d'ordre réduit ont été développés (com-

presseur parallèle, actuator disk, throughflow étendu), mais leurs hypothèses simplificatrices limitent leur applicabilité au complexe environnement des compresseurs multi-étages, notamment en négligeant le transport de swirl, le couplage inter-étages et l'évolution de la distorsion.

Les modèles Body-Force représentent un compromis efficace entre fidélité et coût : ils modélisent l'effet des aubes par des termes sources de quantité de mouvement et d'énergie dans les équations de Navier-Stokes, évitant ainsi la résolution détaillée des aubes. Cette formulation locale permet d'étudier des entrées distordues via des simulations stationnaires, tout en reproduisant des phénomènes tels que la propagation de distorsion et le transport de swirl, avec une bonne correspondance avec les simulations haute fidélité et les données expérimentales. Toutefois, leur extension aux HPC multi-étages reste complexe : les modèles existants reposent souvent sur des simplifications qui ne se généralisent pas toujours aux régimes HPC et peinent à reproduire les structures secondaires, les fuites de bout d'aube et les interactions non linéaires. L'évolution de la distorsion à travers les étages ajoute également une complexité supplémentaire.

Cette thèse a pour objectif d'étudier les effets aérodynamiques de la distorsion d'entrée sur les compresseurs haute pression et d'évaluer leur robustesse sous des conditions d'entrée non uniformes et réalistes. Elle développe une méthodologie Body-Force existante, constituant une alternative efficace aux simulations blade-resolved, tout en conservant une fidélité suffisante pour capturer le transport de swirl et l'évolution de la distorsion. La formulation améliorée est validée à l'aide de données expérimentales et de simulations de référence, puis appliquée à l'étude de la propagation de distorsion, de la dégradation de performance et de l'impact de modifications géométriques sur la sensibilité à la distorsion, sur une large gamme de configurations. La structure de la thèse suit une progression méthodologique : revue bibliographique (chapitre 1), cas d'étude et méthodologie (chapitre 2), simulations blade-resolved de référence (chapitre 3), évaluation et amélioration du modèle Body-Force en écoulement propre (chapitre 4), application aux distorsions (chapitres 5 et 6), analyse de la robustesse géométrique (chapitre 7) et conclusion générale.

Chapitre 1

Ce chapitre établit le cadre théorique et méthodologique permettant d'étudier les effets de la distorsion d'entrée sur les compresseurs haute pression des moteurs aéronautiques. Il rappelle d'abord les principes de fonctionnement, les caractéristiques de performance et les notions fondamentales liées aux compresseurs, afin de fournir le contexte nécessaire. La distorsion d'entrée est ensuite introduite, en mettant l'accent sur les cas de distorsion radiale et circumférentielle, en raison de leur impact majeur sur la stabilité aérodynamique et le rendement. Le chapitre se conclut par un état de l'art des approches de modélisation numérique, avec une attention particulière portée sur les méthodes Body-Force. Une attention spécifique est accordée au modèle de Hall-Thollet, qui constitue la base méthodologique des simulations utilisées dans cette thèse.

L'examen de la littérature montre que les modèles Body-Force, et notamment le modèle de Hall-Thollet, offrent un compromis intéressant entre précision et coût computationnel. Toutefois, ces modèles reposent sur des hypothèses simplificatrices qui limitent leur applicabilité aux configurations haute pression et multi-étages. Ils nécessitent souvent des calibrations spécifiques à chaque cas, point de fonctionnement et régime, et ne reproduisent pas entièrement

les phénomènes de flux secondaires essentiels. L'état de l'art souligne donc la nécessité de méthodes plus efficaces, adaptables et robustes pour étudier l'impact de la distorsion d'entrée sur la performance des compresseurs. Cette thèse vise à combler ces lacunes en développant un modèle Body-Force amélioré, capable de mieux représenter les effets de distorsion dans les HPC.

Chapitre 2

Ce chapitre présente les deux cas d'étude de cette thèse : les compresseurs haute pression CREATE et IHPC. Chaque configuration est brièvement décrite, en mettant en avant ses caractéristiques de conception et les jeux de données expérimentales associés, qui serviront à valider les simulations. Ces dernières sont réalisées à l'aide du solveur CFD elsA, spécifiquement conçu pour les turbomachines, et reposent sur des paramètres numériques clés, ainsi que sur une stratégie de maillage adaptée.

Les approches de modélisation numérique, notamment les méthodes blade-resolved et Body-Force, sont ensuite comparées, en soulignant leurs différences essentielles. Le cadre numérique utilisé, comprenant le solveur CFD, les conditions aux limites, ainsi que les stratégies de maillage et de post-traitement, est détaillé pour assurer la cohérence des résultats dans les chapitres suivants.

Les configurations choisies couvrent une large gamme de complexités géométriques et aérodynamiques, ainsi que des régimes d'écoulement allant du haut subsonique au transonique. Les jeux de données expérimentales associés, de résolutions et de qualités variables, permettent de valider les calculs blade-resolved et de caractériser le champ d'écoulement dans l'anneau sous différentes conditions. Une attention particulière a été portée au calcul du déficit de distorsion à partir des données expérimentales du compresseur industriel, afin dévaluer l'impact de la distorsion sur la performance.

Chapitre 3

Ce chapitre présente les simulations de haute fidélité (RANS et URANS) blade-resolved, qui constituent les références pour ce travail. Il est divisé en deux parties, respectivement dédiées aux compresseurs CREATE et IHPC. Pour chaque cas, les configurations numériques sont détaillées, précisant leur rôle dans la thèse et leur lien avec les méthodes numériques précédemment introduites. Les résultats des simulations sous conditions de veine lisse sont validés par rapport aux données expérimentales disponibles, afin dévaluer leur précision et fiabilité.

Une large gamme de configurations numériques a été explorée pour chaque machine, allant des simulations monocanal à des calculs plus complexes couvrant toute la section du compresseur, y compris sous conditions de distorsion. Chaque configuration est décrite en termes de domaine de calcul, de caractéristiques du maillage et de conditions aux limites appliquées.

Les simulations blade-resolved ont été validées pour les deux compresseurs, en les comparant aux données expérimentales sous conditions de veine lisse. Bien que de légères différences aient été observées, les résultats montrent une bonne fidélité, reproduisant globalement le comportement des machines expérimentales malgré les simplifications nécessaires dans la configuration des cas numériques.

Enfin, la caractérisation de l'écoulement en conditions de veine lisse a permis didentifier des phénomènes complexes, tels que les vortex de passage, les séparations de coin, les vortex de fuite de bout daube et les structures de choc, qui sont essentiels pour les analyses suivantes.

Chapitre 4

Ce chapitre propose une évaluation critique et une amélioration méthodologique du modèle Body-Force de Hall-Thollet, sélectionné pour cette étude. Il identifie les principales limitations du modèle lorsqu'il est appliqué aux compresseurs haute pression et présente une stratégie pour y remédier. L'accent est mis sur trois améliorations majeures. Tout d'abord, une méthodologie de calibration robuste a été développée, indépendante du point de fonctionnement, de la vitesse d'entraînement et des conditions d'entrée. Ensuite, des corrections ont été introduites près des parois pour améliorer la précision près du moyeu et du carter, tout en atténuant les instabilités de flux à faibles débits massiques. Enfin, des corrélations des pertes secondaires ont été intégrées pour mieux capturer les phénomènes complexes découlement.

Ces améliorations visent à renforcer la précision et la fiabilité prédictive du modèle dans les compresseurs haute pression, ce qui est essentiel pour évaluer les effets de la distorsion d'entrée. La stratégie de calibration repose sur des coefficients scalaires dérivés dune analyse de sensibilité détaillée, clarifiant l'influence de chaque paramètre sur la performance du modèle. Le clipping, inspiré des travaux antérieurs, a été intégré pour améliorer la précision près des parois et réduire les instabilités de flux à faibles débits massiques. Une formulation générale pour l'intégration des corrélations des pertes a également été développée, exprimée en termes de pertes dentropie ou de coefficients de perte de pression totale. Une corrélation spécifique pour traiter les pertes dues aux fuites de flux au niveau du rotor a été introduite, avec des ajustements adaptés aux pales de compresseur modernes. Il a été constaté que lapplication des corrections locales, y compris les ajustements près des parois et les pertes secondaires, doit précéder la calibration globale, car ces corrections influencent directement les coefficients de calibration finaux.

Bien que ces stratégies aient été appliquées à des cas détude spécifiques, leur applicabilité va au-delà des compresseurs étudiés ici. Le modèle Body-Force amélioré et la méthodologie associée forment un cadre flexible et adaptable à une large gamme de configurations de compresseurs haute pression. Bien que les paramètres de calibration puissent varier selon les configurations, lapproche combinant calibration systématique, corrections près des parois et intégration des corrélations des pertes secondaires offre une base solide pour améliorer la précision prédictive dans diverses applications de turbomachines.

En résumé, ce chapitre présente un modèle Body-Force complet et amélioré qui surmonte les principales limitations de la formulation initiale dans les applications de compresseurs haute pression. Les performances du modèle et sa validation seront examinées en détail dans les chapitres suivants.

Chapitre 5

Ce chapitre propose une évaluation approfondie des capacités du modèle Body-Force développé et de son application au compresseur CREATE en conditions de veine lisse et sous diverses conditions de distorsion.

La validation initiale sous conditions de veine lisse montre que le modèle reproduit avec une grande précision les résultats des simulations de référence blade-resolved, tant pour la performance globale du compresseur que pour les quantités locales du champ d'écoulement. Les prédictions sont restées dans une marge d'environ 1% par rapport aux résultats de référence sur l'ensemble de la caractéristique de performance du compresseur, et cette concordance a été maintenue pour chaque étage. Aux points de fonctionnement à rendement maximal et proches pompage, le modèle a également bien reproduit les distributions de l'écoulement axial et radial, bien que de légères divergences aient été observées près des parois, sans impact significatif sur l'analyse globale.

Après avoir validé le modèle sous conditions non distordues, il a été appliqué à deux scénarios de distorsion : radiale et circonférentielle. Le cas de la distorsion radiale a mis en évidence la robustesse du modèle, avec une prédiction précise des effets de la distorsion sans nécessiter de recalibration. La distorsion radiale a surtout affecté les régions proches des parois, mais le modèle a restitué des résultats physiquement cohérents.

L'étude de la distorsion circonférentielle (cas P2D) a renforcé la confiance dans le modèle. Les prédictions de pression totale, température totale et montée en pression étaient dans un écart de 1% par rapport aux données de référence blade-resolved. En plus de la précision, l'analyse a révélé comment le modèle capture les mécanismes physiques clés, comme l'évolution de la distorsion de pression totale, la redistribution du flux induite par le swirl, et les variations de l'apport de travail. L'analyse de stabilité a montré que le dernier stator était la roue d'aubes la plus sensible, et a permis d'identifier les combinaisons de distorsion et de points de fonctionnement les plus susceptibles de conduire à une instabilité. Ces résultats sont en accord avec ceux des simulations blade-resolved.

Un point particulièrement notable est que toutes ces prédictions ont été obtenues sans ajuster les coefficients calibrés ni les valeurs de clipping de la force normale, ce qui témoigne de la robustesse du modèle et de sa capacité à prédire le comportement sous différents points de fonctionnement et conditions d'entrée. Cela souligne la généralisabilité du modèle et sa pertinence pour des applications pratiques dans des environnements d'entrée non uniformes.

Le chapitre se termine par une évaluation des performances computationnelles. Par exemple, pour le cas de la distorsion circonférentielle P2D, le modèle Body-Force a nécessité jusqu'à deux cents fois moins de temps CPU que la simulation équivalente blade-resolved. Des gains similaires ont été observés dans tous les cas, particulièrement pour les simulations non stationnaires, mettant en évidence l'avantage computationnel du modèle réduit.

En conclusion, le modèle Body-Force s'avère être un outil puissant, efficace et fiable pour prédire le comportement des flux dans les compresseurs sous conditions d'entrée complexes et non uniformes, tout en offrant un gain substantiel en termes de temps de calcul.

Chapitre 6

Ce chapitre propose une évaluation approfondie des capacités du modèle Body-Force développé et de son application au compresseur IHPC en conditions de veine lisse et sous conditions de distorsion.

L'étude commence par la validation de la méthodologie Body-Force modifiée sous conditions de veine lisse, sur deux points de fonctionnement : le point de rendement maximale et un point stable proche pompage. Les comparaisons avec les données de référence blade-resolved ont montré que le modèle reproduit avec précision tant les métriques de performance glob-

ales que les caractéristiques locales de l'écoulement, y compris les distributions de pression et de température, les angles de flux et les profils d'entropie selon l'extension radiale. Cette validation réussie confirme la capacité du modèle à capturer les phénomènes aérodynamiques essentiels, tels que les pertes de bout d'aube, les flux secondaires et les interactions de chocs, fournissant ainsi une base solide pour les analyses suivantes sous conditions de distorsion. En particulier, l'analyse montre que le modèle reste fiable lorsqu'il est appliqué à des points de fonctionnement hors conception, démontrant sa capacité prédictive au-delà des conditions de calibration.

La propagation de la distorsion de pression totale imposée à travers le compresseur a ensuite été examinée. La distorsion a été observée à atténuer progressivement tout en induisant une redistribution du champ de flux, affectant à la fois la pression totale et la température, comme cela a été vu pour le compresseur CREATE dans le chapitre 5. La frontière avant de la région distordue est apparue comme la zone la plus critique pour la charge de flux et les considérations de stabilité. Les comparaisons avec les simulations blade-resolved ont confirmé que le modèle Body-Force capture les principales caractéristiques de la distorsion, y compris son évolution azimutale, son atténuation en intensité, et les écarts de flux associés. De légères divergences, principalement liées aux effets locaux de dissipation et de mélange non explicitement résolus par le modèle, n'ont pas compromis la capacité prédictive globale.

Une analyse détaillée de la stabilité sous distorsion a identifié la région près du moyeu comme étant la zone critique pour l'initiation de la panne. L'évolution de la vitesse axiale, de l'angle de flux, de l'entropie et des indicateurs de stabilité a montré que la séparation du flux et la décélération rapide près du moyeu agissent comme des précurseurs de l'instabilité. Les prédictions du Body-Force s'accordent avec les tendances de la littérature, indiquant que la séparation près du moyeu domine la déstabilisation, permettant une évaluation quantitative de la réduction de la marge de panne due à la distorsion.

Enfin, le chapitre a évalué l'efficacité computationnelle de l'approche Body-Force. En permettant des simulations sur l'ensemble de l'annulus à une fraction du coût des méthodes blade-resolved, le modèle facilite des études paramétriques approfondies et des investigations détaillées des effets non-stationnaires qui seraient autrement impraticables. Cette combinaison de précision et de faisabilité computationnelle souligne la valeur du modèle en tant qu'outil prédictif pour l'analyse des compresseurs sous conditions d'entrée non distordues et distordues.

Dans l'ensemble, les résultats de ce chapitre démontrent que la méthodologie Body-Force modifiée est une approche robuste et efficace pour capturer les principales réponses aérodynamiques et le comportement de stabilité d'un compresseur multi-étage à haute vitesse sous des conditions hors conception et des distorsions d'entrée tridimensionnelles complexes. La méthodologie constitue une base solide pour de futures études sur l'opération hors conception et les phénomènes non-stationnaires, comblant ainsi le fossé entre les simulations haute-fidélité et les approches computationnelles viables dans le processus de conception.

Chapitre 7

Ce chapitre explore l'application du modèle Body-Force pour évaluer la sensibilité du compresseur IHPC à des modifications géométriques spécifiques, en particulier celles de la solidité et du rapport d'aspect de la première roue de rotors. L'objectif principal est de tester la fiabilité du modèle pour des études de conception, en se concentrant sur des configurations

à débit propre et en conditions de distorsion circulaire, tout en portant une attention particulière aux régions critiques du moyeu et du carter.

L'étude commence par l'application de modifications géométriques à la première roue de rotors, permettant d'isoler l'impact de chaque paramètre sur le comportement des pales en aval. Les résultats montrent que, pour des configurations sous-soniques ou à faible transonique, telles que celles du compresseur CREATE ou de la première roue de rotors du compresseur IHPC à vitesse partielle, le modèle Body-Force prédit correctement les effets de la solidité. Cependant, dans des conditions où des phénomènes complexes comme les chocs détachés ou les séparations de flux importantes surviennent, le modèle présente des limites, n'étant pas assez précis pour capturer ces effets.

L'étude du rapport d'aspect a donné des résultats plus concrets. Le modèle a montré une bonne capacité à prédire l'impact des modifications géométriques sur un compresseur transsonique complet comme l'IHPC. Sous conditions de débit propre, le modèle a montré sa fiabilité pour prédire les effets aérodynamiques complexes et tridimensionnels induits par ces changements. L'analyse a ensuite été étendue aux conditions de distorsion circulairement déformée, avec une attention particulière portée aux zones critiques du moyeu et du carter, qui sont essentielles pour la stabilité du compresseur.

Les résultats ont révélé que la modification du rapport d'aspect de la première roue de rotors apportait plusieurs avantages : une réduction de la masse et de la longueur du moteur, favorisant un compresseur plus compact et léger, ainsi qu'une amélioration de la stabilité près du carter pour certains points de fonctionnement. Cependant, cette modification a aussi réduit la stabilité près du moyeu, en particulier à rendement maximal et près du décrochage, mettant en évidence le compromis nécessaire entre réduction de masse et optimisation de la stabilité. Ce compromis doit être soigneusement évalué, surtout dans la région du moyeu, où les instabilités sont plus susceptibles de se manifester.

En conclusion, ce chapitre démontre que le modèle Body-Force est un outil fiable pour l'analyse des effets de modifications géométriques dans des compresseurs opérant en régimes sous-soniques ou à faible transsonique. Toutefois, des limitations existent dans des conditions transsoniques complètes, en particulier lorsque des phénomènes de chocs détachés ou de séparations de flux étendues se produisent. Dans de tels cas, les hypothèses du modèle doivent être réévaluées et adaptées à ces conditions plus complexes. Ainsi, bien que le modèle constitue une base solide pour les études de conception, des ajustements ou une validation plus poussée peuvent être nécessaires dans certaines configurations de flux.

Conclusion

Cette recherche s'est concentrée sur l'analyse des effets des distorsions d'entrée dans l'environnement aérodynamique des compresseurs haute pression multi-étages, en développant un cadre de modélisation de faible ordre combinant efficacité computationnelle et précision prédictive. Le modèle Body-Force a été choisi en raison de sa capacité à reproduire les effets tridimensionnels du flux et à capturer la réponse aérodynamique des compresseurs face aux distorsions, une capacité encore peu explorée dans des régimes caractérisés par de forts gradients de pression, des rapports d'aspect faibles et une charge aérodynamique élevée.

Des jeux de données haute fidélité, basés sur des simulations blade-resolved, ont été générés pour deux cas représentatifs : le compresseur CREATE, un banc d'essai bien instrumenté, et le compresseur IHPC, avec une configuration plus industrielle et complexe. Ces

deux cas ont permis de tester la robustesse du modèle dans des conditions réalistes et de valider ses performances en matière de prédiction des effets des distorsions d'entrée.

Le modèle Body-Force a d'abord été validé sous conditions de débit propre, avec une réduction de l'erreur de prédiction de 10%-25% à environ 2% pour les deux compresseurs, tout en reproduisant fidèlement le comportement local du flux. Ensuite, des tests sous différentes conditions de distorsion, incluant des distorsions radiales, circonférentielles et géométriques, ont montré que le modèle prédisait efficacement la transmission de la distorsion, la redistribution du flux et la réduction de la marge de décrochage, avec une bonne concordance avec les simulations de haute fidélité.

L'impact des modifications géométriques, telles que la solidité des pales et le rapport d'aspect, a également été étudié à travers des études paramétriques. Bien que des limitations aient été observées dans des régimes transsoniques ou en présence de séparations importantes de la couche limite, le modèle a montré sa capacité à prédire les effets de distorsion dans une large gamme de configurations géométriques.

Une des principales forces du modèle est son efficacité computationnelle : il est jusqu'à trois ordres de grandeur plus rapide que les simulations blade-resolved, permettant ainsi d'explorer rapidement de nombreux cas paramétriques et de simuler des phénomènes transitoires. Toutefois, des améliorations sont nécessaires pour mieux capturer les régions supersoniques et les effets de la séparation de flux dans des configurations géométriques complexes. Une calibration automatisée et un modèle non stationnaire pourraient également étendre les capacités du modèle, permettant l'analyse de phénomènes instables et de distorsions dynamiques.

En termes d'applications pratiques, le modèle offre une plateforme efficace pour l'optimisation des compresseurs, en particulier pour les études de conception préliminaires, lévaluation de la robustesse aux distorsions et l'intégration aéropropulsive. Il constitue également un outil puissant pour les études de distorsion dans des conditions d'entrée réalistes et pour l'analyse de la réponse dynamique du compresseur.

Les perspectives futures incluent l'intégration des distorsions de swirl et des effets instationnaires, fréquents dans les applications pratiques, afin de mieux comprendre leur impact sur la performance et la stabilité des compresseurs dans des scénarios d'opérabilité réalistes. Ces évolutions permettraient d'améliorer encore la capacité du modèle à prédire le comportement dynamique des compresseurs dans des conditions d'entrée plus complexes.

RÉPUBLIQUE FRANÇAISE
Liberté
Égalité
Fraternité

Université de Toulouse

Titre : Étude des effets de la distorsion sur la stabilité des compresseurs haute pression multi-étages par modélisation Body-Force

Mots clés : BFM, Compresseurs, Distorsion,

Résumé : Le secteur de l'aviation traverse une transformation vers la durabilité, avec des moteurs aéronautiques de plus en plus conçus pour répondre à des objectifs environnementaux ambitieux. Ces défis imposent des exigences strictes sur les systèmes de propulsion, qui doivent améliorer l'efficacité énergétique, réduire les émissions, limiter le bruit et assurer la rentabilité. Les nouvelles configurations, telles que l'ingestion de la couche limite et les nacelles ultra-compactes, optimisent la performance des aéronefs mais génèrent des distorsions d'entrée susceptibles d'affecter gravement les performances des compresseurs, entraînant des risques de séparation du flux, de baisse de performance, voire des instabilités.

Cette recherche se concentre sur les effets des distorsions d'entrée dans les compresseurs haute pression (HPC), en étudiant leur propagation à travers les architectures multi-étages et leur influence sur la robustesse des compresseurs. Les outils de préconception, en raison de leurs hypothèses simplificatrices, ne permettent pas de prédire pleinement les effets des distorsions, tandis que les simulations détaillées sont coûteuses en ressources de calcul. Pour remédier à cela, l'étude adopte et perfectionne un modèle Body-Force, une approche réduite efficace pour simuler la propagation des distorsions dans des configurations simples, et offrant ainsi une alternative pratique aux simulations CFD de haute fidélité.

Le travail débute par l'évaluation d'un modèle Body-Force existant, conçu pour des configurations de compresseurs simples, afin d'en analyser la pertinence pour les HPC. Ce modèle est ensuite amélioré pour accroître sa précision et l'adapter aux exigences spécifiques des compresseurs haute pression. Il est validé par des données expérimentales et des simulations aubes-maillées provenant de deux cas tests distincts. L'application du modèle à ces cas permet d'analyser l'impact des distorsions d'entrée sur la robustesse des compresseurs, notamment la manière dont les motifs de distorsion se propagent à travers les étages et influencent la réduction de la marge de décrochage ainsi que l'apparition des instabilités. Les résultats montrent que le modèle prédit précisément la dégradation des performances, la modification du flux et l'évolution de la marge de décrochage. L'étude fournit également des informations sur l'influence des caractéristiques géométriques sur la sensibilité du compresseur aux distorsions.

L'amélioration du modèle Body-Force constitue un outil puissant pour la conception en phase précoce, permettant une prise de décision éclairée dans le développement de compresseurs robustes et résistants aux distorsions. Grâce à sa grande efficacité computationnelle, le modèle facilite les études paramétriques et les évaluations des distorsions à un coût raisonnable, améliorant ainsi les performances globales du compresseur. Cette recherche apporte des éclairages précieux sur l'impact des distorsions d'entrée sur la robustesse des compresseurs et permet de mieux comprendre comment les moteurs d'avion de demain pourront répondre aux défis environnementaux et opérationnels à venir. En offrant une alternative plus accessible aux simulations CFD coûteuses, elle ouvre la voie à une conception plus rapide et plus flexible des systèmes de propulsion aérospatiaux.

Title: Investigation of the Effects of Inlet Distortion on the Stability of Multi-Stage High-Pressure Compressors via Body-Force Modelling

Key words: BFM, Compressors, Distortion,

Abstract: Aviation is undergoing a transformative shift towards sustainability, with modern aero-engine design focused on meeting ambitious environmental targets. These objectives drive the need for propulsion systems that enhance fuel efficiency, reduce emissions, minimise noise, and maintain cost-effectiveness. In response, engine architectures are evolving towards more advanced configurations, such as boundary layer ingestion and ultra-com-pact nacelles, improving overall aircraft performance. However, these innovations introduce complex flow disturbances at the compressor inlet, resulting in inlet distortion, a non-uniform distribution of velocity, temperature, and pressure, which can lead to significant operational challenges, including flow separation, reduced performance, lower stall margin, and even compressor stall or surge.

This research examines the aerodynamic effects of inlet distortion on high-pressure compressors, with a focus on how distortion patterns propagate through multi-stage architectures and influence compressor robustness. The study addresses the challenge of predicting inlet distortion impacts early in the design process. Conventional tools, assuming uniform inlet conditions, often underestimate performance penalties, while blade-resolved simulations are computationally expensive. To overcome these limitations, the research enhances a Body-Force modelling framework: an efficient, reduced-order approach that captures key flow phenomena like distortion propagation and swirl transport, offering a practical alternative to high-fidelity CFD simulations.

The research begins with the evaluation of an existing Body-Force model, which is well-established for simpler compressor configurations, and develops targeted modifications to enhance its accuracy and applicability to high-pressure compressors. The enhanced model is validated against high-fidelity reference data from both blade-resolved simulations and experimental data from two distinct compressor test cases. By applying the model to these cases, the research assesses the impact of inlet distortion on compressor robustness, focusing on how distortion patterns propagate across multiple stages and contribute to stall margin reduction and the onset of instability. The results demonstrate that the model accurately predicts distortion-induced effects, including performance degradation, altered flow distribution, and changes in stall margins. Additionally, the study provides insights into the model's capabilities in relation to varying geometric features and highlights how these features influence the compressor's sensitivity to distorted inflow.

The enhanced Body-Force model proves to be an efficient tool for early-stage design, facilitating more informed decision-making in the development of robust, distortion-resilient compressors. By simulating inlet distortion effects with high computational efficiency, the model enables early-stage distortion and parametric studies at a reasonable cost, ultimately improving compressor operations. This research provides valuable insights into the impact of inlet distortion on compressor robustness, enhancing the understanding of how future aero-engine designs can address the evolving environmental and operational challenges.